GDAŃSK UNIVERSITY
OF TECHNOLOGY
Faculty of Mecahnical Engineering
and Ship Technology

WIMiO

The author of the PhD dissertation: Krzysztof Wołoszyk
Scientific discipline: mechanical engineering

DOCTORAL DISSERTATION

Title of PhD dissertation: Experimental and numerical investigations of ultimate strength of degradated structures

Title of PhD dissertation (in Polish): Doświadczalne i numeryczne badanie nośności granicznej zdegradowanych konstrukcji

Supervisor *signature*	Second supervisor *signature*
Dr hab. inż. Tomasz Mikulski, prof. PG	Prof. Yordan Garbatov
Auxiliary supervisor *signature*	Cosupervisor *signature*
-	-

Gdańsk, year 2021

Page intentionally left blank

STATEMENT

The author of the PhD dissertation: Krzysztof Wołoszyk

I, the undersigned, agree that my PhD dissertation entitled: Experimental and numerical investigations of ultimate strength of degradated structures may be used for scientific or didactic purposes.[1]

Gdańsk,...................................... ....

signature of the PhD student

Aware of criminal liability for violations of the Act of 4th February 1994 on Copyright and Related Rights (Journal of Laws 2006, No. 90, item 631) and disciplinary actions set out in the Law on Higher Education (Journal of Laws 2012, item 572 with later amendments),[2] as well as civil liability, I declare, that the submitted PhD dissertation is my own work.

I declare that the submitted PhD dissertation is my own work performed under and in cooperation with the supervision of Tomasz Mikulski and the second supervision of Yordan Garbatov.

This submitted PhD dissertation has never before been the basis of an official procedure associated with the awarding of a PhD degree.

All the information contained in the above thesis, which is derived from written and electronic sources, is documented in a list of relevant literature in accordance with art. 34 of the Copyright and Related Rights Act.

I confirm that this PhD dissertation is identical to the attached electronic version.

Gdańsk,...................................... ....

signature of the PhD student

I, the undersigned, agree to include an electronic version of the above PhD dissertation in the open, institutional, digital repository of Gdańsk University of Technology, Pomeranian Digital Library, and for it to be submitted to the processes of verification and protection against misappropriation of authorship.

Gdańsk,...................................... ....

signature of the PhD student

*) delete where appropriate.

---

[1] Decree of Rector of Gdansk University of Technology No. 34/2009 of 9th November 2009, TUG archive instruction addendum No. 8.

[2] Act of 27th July 2005, Law on Higher Education: Chapter 7, Criminal responsibility of PhD students, Article 226.

Page intentionally left blank

GDAŃSK UNIVERSITY
OF TECHNOLOGY
Faculty of Mecahnical Engineering
and Ship Technology

WIMiO

DESCRIPTION OF DOCTORAL DISSERTATION

The Author of the PhD dissertation: Krzysztof Wołoszyk

Title of PhD dissertation: Experimental and numerical investigations of ultimate strength of degradated structures

Title of PhD dissertation in Polish: Doświadczalne i numeryczne badanie nośności granicznej zdegradowanych konstrukcji

Language of PhD dissertation: English

Supervision: Dr hab. inż. Tomasz Mikulski, prof. PG

Second supervision*: Prof. Yordan Garbatov (CENTEC, IST, University of Lisbon)

Date of doctoral defense:

Keywords of PhD dissertation in Polish: usztywnione płyty, korozja, obciążenie ściskające, nośność graniczna, Metoda Elementów Skończonych, pola losowe

Keywords of PhD dissertation in English: stiffened plates, corrosion, compressive load, ultimate strength, Finite Element Method, random fields

Summary of PhD dissertation in Polish: Niniejsza praca poświęcona jest wpływowi korozji na odpowiedź strukturalną elementów konstrukcyjnych. Dziewięć spawanych usztywnionych płyt oraz trzydzieści standardowych próbek na rozciąganie zostało poddanych przyspieszonej korozji morskiej. Po zakończeniu testów korozyjnych, próbki zostały dokładnie pomierzone w kontekście skorodowanych powierzchni. Małe próbki zostały poddane obciązeniu rozciągającemu w celu identyfikacji własności mechanicznych, w zależności od stopnia skorodowania. Przeprowadzone zostały analizy MES z zastosowaniem wygenerowanych pól losowych i wyniki zostały zwalidowane w oparciu o dane eksperymentalne. Usztywnione płyty poddane zostały obciążeniu ściskającemy i odpowiedź strukturalna została przeanalizowana, uwględniając początkowe imperfekcje płyt, poziom skorodowania, naprężenia pospawalnicze oraz nieliniowości materiałowe. Modele numeryczne z różną dokładnością odwozorwania korozji zostały zwalidowane w oparciu o dane eksperymentalne. Jedynie kiedy nierównomierny rozkład grubości w wyniku korozji wraz z jednoczesnym spadkiem własności mechanicznych jest uwzględniony, odpowiedź strukturalna może zostać poprawnie zasymulowana. Formuła parametryczna służąca do szybkiego szacowania nośności granicznej skorodowanych usztywnionych płyt została opracowana. Przykłady analizy niezawodności uwzględniające rozwój korozji w czasie eksploatacji zostały pokazane.

Summary of PhD dissertation in English: The presented work investigates the corrosion influence on the structural behaviour of structural elements. Nine welded large-scale stiffened plates, and 30 standard small specimens have been subjected to the accelerated marine immersed conditions. After corrosion testing, the specimens have been accurately measured in terms of surface characteristics. The coupon specimens were furtherly subjected to tensile loading to develop the mechanical properties conditional on the severity of corrosion degradation. The FE analyses employing the technique of random field modelling were developed and validated against experiments. The stiffened plates were subjected to the compressive loading, and the structural response has been analysed, accounting for initial imperfection, corrosion degradation, welding-induced residual stresses, and material non-linearity. The numerical models of different accuracy of

corrosion degradation models were validated with the experimental results showing that only when non-uniform thickness reduction with subsequent changes in mechanical properties is taken into account, the structural behaviour could be accurately simulated. An analytical formulation allowing for a fast estimation of the structural capacity of corroded stiffened plates and the reliability formulation taking into account the time-dependent development of corrosion degradation has been developed.

ACKNOWLEDGEMENTS

First and foremost, I want to express my gratefulness to my supervisors: Prof. Yordan Garbatov and Prof. Tomasz Mikulski, for their advice, knowledge and guidance. Furthermore, special thanks go to Prof. Yordan Garbatov for his patience, support and constant encouragement. He was my supervisor and my mentor who helped me with my first steps in the academic world.

I also want to thank Prof. Mikulski, who let me work in his department and provide a great atmosphere to scientific work there. The gratitude also goes to my colleagues from the department for their support and valuable comments during seminars. I want to especially thank Dr Marian Bogdaniuk, Dr Wojciech Puch and Prof. Czesław Szymczak. Many thanks go to Paweł Bielski and Leszek Samson, that helped with experiments and shared their knowledge and expertise. We had many discussions about my work, and they helped me see the problem from different perspectives. I also want to thank Hanna Pruszko for her support and encouraging discussions. Outside the University, many thanks go to Mesut Tekgoz, from Lisbon, who shared his experience and for his friendly attitude during my visits there.

I also want to thank Dr Jakub Kowalski for his help with the major part of experiments and for allowing me to perform them in his laboratory. Further, thanks for sharing the knowledge and expertise as well as valuable discussions. Many thanks also to Dariusz Birr and Marian Adamczyk, for their help in lab. I want to express my gratitude to Prof. Janusz Kozak for his input with the development of supports for the testing machine and his support during his tenure as a Dean of Faculty.

Many thanks go to Dr Hossein Ghaemi for his engagement in collaboration with Prof. Yordan Garbatov. Thanks to his support, visits of Prof. Garbatov to our University were initiated and very well prepared, which helped me develop the PhD thesis.

I want to also wish my gratitude to Prof. Jarosław Górski, who helped me get acquainted with reliability analysis and random field theory. Many thanks also to Prof. Juliusz Orlikowski for his valuable input regarding the design of the corrosion tests. I want to express my thankfulness to Prof. Paweł Kłosowski for allowing me to test the coupon specimens in his laboratory.

The National Science Centre, Poland, has supported the part of the work presented in the Thesis (grant No. 2018/31/N/ST8/02380, entitled “Experimental and numerical investigations of progressive collapse of ageing structures exposed to corrosion and locked cracks”). The ANSYS software used in the simulations presented in this paper was available as part of the partnership cooperation agreement between ANSYS Inc., MESco sp. z o.o., and the Gdansk University of Technology. Agisoft Metashape Professional Educational License software provided by the Gdansk University of Technology was used for photogrammetric purposes. Part of the calculations was carried out at the Academic Computer Centre in Gdańsk.

Last but not least, I want to express my gratitude to all my family for their support and encouragement. Special thanks go to my wife Asia and daughter Hania for their constant motivation to work and unconditional support.

Page intentionally left blank

TABLE OF CONTENTS

1. INTRODUCTION

Ship structures need to be safe as well as economically justified. Further, the possible loss of human life and cargo and environmental pollution due to the ship sinkage should lead to even higher precautions considering the ship's safety. The ship size increased rapidly during the recent 50 years [1], leading to many structural challenges. The ability to describe the hull structural behaviour is an essential feature for ship structural design and the ultimate strength analysis. Thus, the longitudinal strength assessment involves the hull girder's structural capacity estimation and evaluates the maximum loads that may act on it. Additionally, from the beginning of the design process, one should consider the intact state of the structure and its possible deterioration since ship structures are operating in a severe environment. The proper estimation of the deterioration level in the design stage may decrease operational expenditure since it may optimise future surveys.

The ship's hull structures are composed of stiffened plating. The external pressure acts directly on the plating, which is supported by stiffeners. The stiffener distance is usually between 500 mm up to 1,000 mm, and there are supported by primary supporting members (transverse and longitudinal girders).

The typical dimensions of the ship hull (the ratio between length and breadth is significant) lead to the be considered as a "free-free beam" when considering the global response of a hull girder. The loads acting on a ship hull are related to, i.e. deadweight and lightweight, buoyancy, wave-induced loads leading to bending and torsional moments, and shear force in the ship hull cross-sections.

The acting loads produce a flexural deflection of the ship hull girder that can distinguish in two primary forms of sagging and hogging. In sagging, the deck plate is subjected to longitudinal compression and the bottom to tension. Thus, the deck plate and deck stiffened panels may fail by buckling. Oppositely, in hogging, the deck plates are subjected to a tensile load, and bottom plates are subjected to a compressive load, and in this case, the bottom plates and panels may buckle. The sagging and hogging conditions are occurring one after another. It needs to be highlighted that in such conditions of oscillating stresses, the problem of fatigue cracking will also be very important. In this case, the dominant will be the range of acting stresses, especially the tensile ones. However, fatigue is a phenomenon where dominant are the cycles of medium-value stresses (significantly below the yield stress value), leading to the high cumulative number of occurrence during a typical ship exploitation period. This leads to cracks in the structural elements and growth of them during the next cycles of stresses.

The ship's structural design's basic idea is that its strength must be higher than the applied loads. If opposite, the ship may fail, leading to catastrophic consequences, including loss of ship, cargo, and crew life. In some specific ship types, such as tankers, the oil spill's environmental consequences are also significant. One of the recent accidents was one of the container ship MOL Comfort [2]. The casualty report [2] indicates that the buckling of the bottom plating, due to hull girder loads exceeding the hull girder strength, was the primary factor that leads to structural failure, and furtherly entire mid-ship section collapsed.

Buckling is a phenomenon where structural members such as plate, stiffened plate, when subjected to the compressive loads, deflect in the out-of-plane direction when the load exceeds the buckling limit [3]. After buckling occurrence, the deflections increase together with the increment of the axial load and displacement, which results in a reduction of in-plane stiffness. The reason is that the deflected member shows lower resistance to in-plane compressive loads when compared to the flat member.

Apart from the reduction of in-plane stiffness of the structural member, premature yielding could also occur. The bending of the deflected member causes this phenomenon since the deflection causes the eccentricity with regards to the axial compressive loading. The yielding occurrence furtherly reduces the stiffness.

In a formal sense, buckling is a bifurcation phenomenon that changes the in-plane deflection into in-plane and out-of-plane deflection at the same time. Nevertheless, this can be achieved when the structural component is perfectly flat and free of any initial imperfections. However, this is not the case of ship structures, which are mostly welded, and the welding process induces distortions and residual stresses from the beginning of the service life.

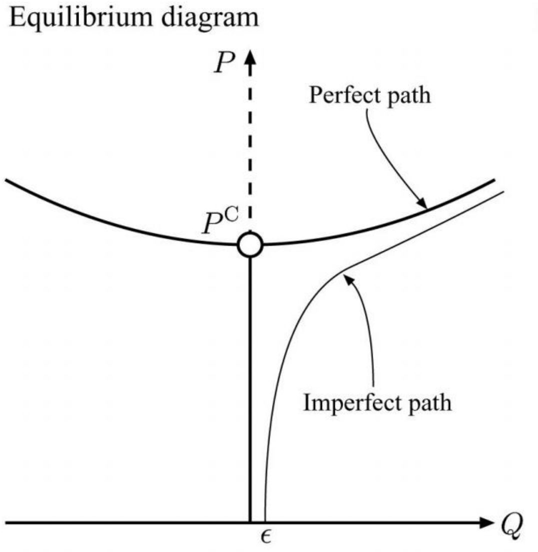

Figure 1.1. Nonlinear response of the buckled plate [4].

A comparison of compressive force as a function of mid-lateral displacement between perfect and imperfect plate is presented in Figure 1.1. In the case of the perfect plate, the force arises up to the bifurcation point, and stiffness suddenly drops, leading to a gradual increase of lateral displacement with an almost constant force value. When considering a real plate with initial imperfections, the stiffness is reduced from the beginning and lateral displacement increase with the rise of compressive force. In that case, the bifurcation point is not explicit, and the imperfect path is continuous. With the further development of compressive force, the yielding will occur, leading to the damage of the plate and obtaining the maximum possible force that the plate can carry. Thus, we can introduce the ultimate strength phenomenon.

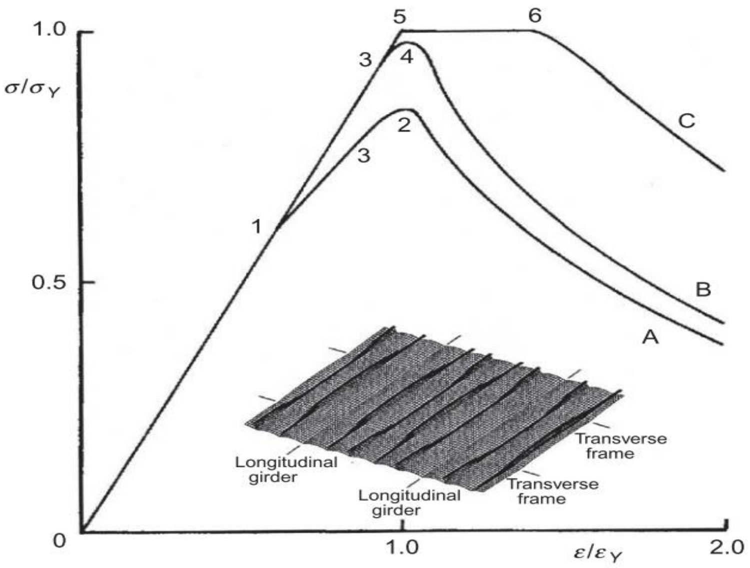

Figure 1.2. The average stress-strain relationship for compressed stiffened panel [3].

A typical stress-strain relationship of a stiffened panel subjected to compressive load shown in Figure 1.2. The curve C shows the structural behaviour of stiffened panel when both the plate and the stiffener has a low slenderness ratio. In this case, the yielding starts at Point 5, which is below the buckling level, and furtherly yielding spreads in the entire cross-section reaching Point 6. After reaching that point, the stiffened panel cannot carry more load, and the load-carrying capacity drops down. The ultimate strength in this particular case is equal to the plastic strength. Curve B shows the structural behaviour, where the entire panel buckles to full collapse. At Point 3, the yielding initiates, and the overall buckling occurs at Point 4, which is the ultimate strength of the stiffened panel. Path A represents the force-displacement curve typical for the slender plates. In that case, the plate undergoes buckling at Point 1, and stiffness decreases due to the lateral deflection increase. The yielding starts to occur at Point 3, furtherly leading to the moment where ultimate strength is reached at Point 2. Based on the presented cases with different slenderness, it could be summarised that the ultimate strength could be originated either from plastic collapse, either from local or global buckling.

When analysing the ship structures, one needs to be aware that the hull structure will differ from an as-built state with the increase of age. Due to the operation in the harsh marine environment, the steel elements will be subjected to severe corrosion degradation. At the ship design stage, the corrosion risk is managed by the thickness addition required by classification societies (e.g. Common Structural Rules [5]), and the strength criteria are satisfied for the net thickness. The values of corrosion addition are based on the statistical analysis of thickness loss measurements specific to the member location and environment, and there are taken as 95% quantile of predicted corrosion depth, assuming the 25-year exploitation period. Regular inspections are carried out throughout the ship service life, and members identified as worn are replaced. Nevertheless, the methods used to estimate structural behaviour are typically developed for intact structures and assume that the corrosion will lead to uniform thickness reduction. When considering the other degradation effects acting simultaneously, such as fatigue cracking, the strength deterioration maybe even magnified.

The structural problems may be crucial for aged ships. In the last report on maritime transport [6], the mean age of the current merchant fleet has been summarised. The mean age of all ships is equal to 20.98 years, including bulk carriers (9.07 years) and tanker ships (18.53 years). In general cargo ships, almost 60% of operating ships are above 20-years old, and most of them already exceed the typical period of exploitation. Based on the statistics of capacity loss, it is evident that the probability of loss is increasing with the ship age, as presented in the recent statistics concerning bulk carriers [7] (see Figure 1.3). Although most of these losses were caused due to human error (which lead to, e.g. grounding), rather than pure structural failures, the aged ship will be less resistant to such accidents.

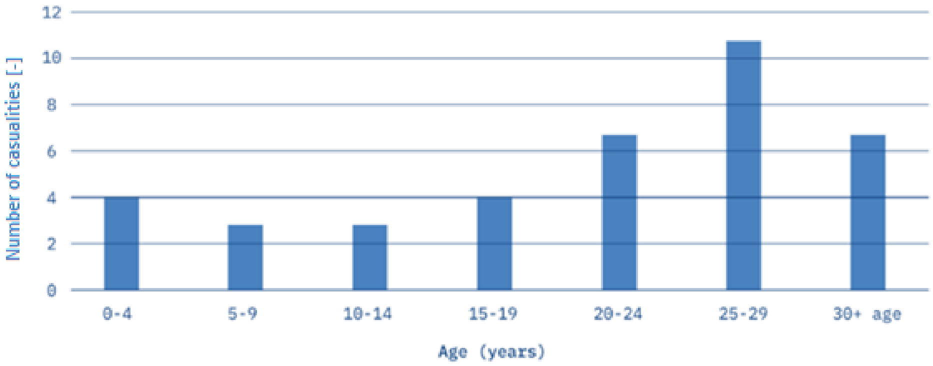

Figure 1.3. Bulk carriers losses by age (period 2010-2019) [7].

According to Zayed et al. [8], even up to 90% of hull damages are primarily or indirectly caused by corrosion. An example of tanker ship loss, which was primarily caused by excessive corrosion, was breaking a ship’s hull in two parts, e.g. Prestige in 2002 (see Figure 1.4). In theory, regular surveys should not lead to such situations. However, as can be found in [9], always exist the probability that some of the deteriorated structural elements will be omitted during inspections. In bad conditions for carrying the measurements, such as the double bottom, such probability could be considerable.

Figure 1.4. Breaking of tanker ship Prestige [10].

For the safety of ship structures, it is crucial to understand a hull girder's behaviour when subjected to extreme loading. Especially, it is essential to identify the structural behaviour of ageing structural components since their behaviour may be significantly different from the intact structure. The primary ageing mechanism that needs to be taken into account is corrosion degradation.

In the presented thesis, the ultimate strength of the corroded structural elements is investigated. Stiffened plates and standard coupon specimens have been subjected to the accelerated marine immersed conditions. Further, accurate measurements of the corrosion characteristics have been performed. Based on tested coupon specimens, the mechanical properties were obtained conditional on the severity of corrosion degradation. The FE analysis of small-scale specimens was performed employing random field modelling and validated against experimental results. The compressive tests were performed regarding the intact and corroded stiffened plates accounting for initial imperfections, welding-induced residual stresses, and material non-linearity. The FE computations were performed too, taking into account different models of corrosion degradation. Finally, an analytical formulation allowing for a fast estimation of the structural capacity of corroded stiffened plates and the reliability formulation taking into account the time-dependent development of corrosion degradation has been developed.

2. STATE OF THE ART

Nowadays, the ultimate strength assessment is a fundamental task in the ship and offshore structural design, and it is initially assessed during the first phases of the design process, where fast and accurate prediction methods are required.

The three main categories of existing methods related to the ultimate strength assessment can be classified [11] as direct methods (linear method, empirical formulations), progressive collapse methods (Smith method), numerical methods (Idealized Structural Unit Method (ISUM), nonlinear Finite Element Method (nonlinear FEM) and experimental methods.

2.1. Numerical methods of ultimate strength

2.1.1. Single-step approach

The first attempts at the ultimate strength assessment of ship structures were accomplished by Caldwell [12]. The simplified direct formulation, taking into account material yield and buckling, was introduced. In a further development, Paik and Mansour [13] assumed a stress distribution through the ship section limited to simple structural geometries only. Paik et al. [14] presented the improved Paik-Mansour method assuming stress distribution in the hull section predominantly. The heights of the collapsed and yield areas are determined employing force equilibrium in a section using the iterative procedure. Compared with the other approaches (Smith’s method, ISUM, and FEA), the method yields good results for a wide range of hull types [11]. The main advantage of this approach is low CPU time and simplicity; thus, it can be widely used in the initial stages of the design process.

2.1.2. Progressive collapse approach

Alternatively, the incremental-iterative approach was developed by Smith [15], taking into account the longitudinal elastoplastic response of individual structural components. Nowadays, both direct and progressive approaches have been improved and introduced to the IACS Common Structural Rules for Bulk Carriers and Oil Tankers [5].

The Progressive Collapse method, also called the Smith method, discretises the ship cross-section into appropriate elements, usually stiffened plates (stiffeners with attached plating). The structural behaviour of each component is predicted in the form of a load-shortening curve. Next, the incremental procedure is introduced to obtain the hull's moment-curvature response to combined horizontal and vertical bending.

This method is based on three main assumptions [15]:

- The plane section remains plane;
- Panel buckling is interframe;
- Individual elements resist the planeloads separately.

The method has been widely accessed to predict the capacity of an intact ship section [16].

Since then, the method has been continually developed. An improved method was proposed by Yao and Nikolov [17] and applied to analyse the behaviour of double hull oil tanker [18] and bulk carrier [19]. Another significant improvement was developed by Benson [20,21], extending the method's application to compartment level failure modes.

Li et al. [22] proposed an approximate method for ship hull girder ultimate strength by combining the progressive collapse approach with the hull's beam theory.

The Smith method produces better results than direct methods; it is more straightforward and less time-consuming than the FE analysis. However, the critical point of this approach is to get the proper stress-strain curves of stiffened plate elements.

2.1.3. Nonlinear FEM solution

The most widespread numerical method is nonlinear FEM. One of the first applications was presented by Kutt et al. [23]. With the increase of computational power, vast FE programs have been applied to the ship's structural analysis, such as ABAQUS, ANSYS, MARC, ADINA.

A typically used methodology to assess the ultimate strength of various structures, including ship hulls, is a static solver with an equilibrium convergence iterator using the Riks arc-length method or Newton Raphson method [24]. The static solver neglects the time-dependent mass and inertia effects; this is usually a valid assumption for small loading frequencies (less than a quarter of the lowest natural frequency of a structure).

However, for more significant models such as ship hull girders, convergence problems can occur and make results unachievable. In such cases, explicit dynamic solvers, such as LS Dyna, are applied. ISSC 2015 [11] reported a benchmark study employing various methods, indicating that only the explicit dynamic solver can analyse all hull girder studied cases. ISSC 2018 [25] reported an extension of the previous benchmark study showing that apart from that, various participated analysts that had the same initial parameters of the studied model; the results were subjected to relatively large scatter. The conclusion was that more validation work and comparison with experimental results are needed to provide more reliable results.

The nonlinear FEM is widely used for the analysis of plates [26–28], stiffened plates [29,30], and stiffened panels [31–33] when considering different effects.

2.1.4. Idealised Structural Unit Method

The Idealised Structural Unit Method (ISUM) was initially proposed by Ueda [34] and furtherly developed by Paik et al. [35]. It allows for rapid assessment of the ship's hull ultimate strength to smaller constituent parts (beam-column unit, unstiffened plate unit, stiffened plate unit, hard unit, and virtual unit). More sophisticated elements were proposed in [36,37]. Paik et al. [38] presented a summary of ISUM theory and applications. Some applications to the analysis of the ultimate strength of a hull girder could be found in [39].

2.2. Experimental methods

Apart from the development of numerical tools is evident; experimental investigations are still the most valuable input for predicting the ultimate strength of different structural components. The experimental results are typically used to validate different numerical methods. The most valuable is, of course, the full-size experiments, e.g. destroyers Preston and Bruce [40] and destroyer Albuera [41]. However, due to very high costs and problems with the load application, the reduced scale experiments are more frequently conducted, usually in the form of a box girder. Apart from hull girder tests, the experiments of reduced models, i.e. stiffened panels, stiffened plates, and plates, are frequently performed.

2.2.1. Plates

The simplest structural element that composes the ship hull cross-section is the un-stiffened plate. The primary role of plates is to support the external sea pressure and internal cargo pressure and transfer the load into the stiffeners and primary supporting members. Such members can be subjected to different types of loads, such as longitudinal, transverse, and lateral loads. In many cases, the most crucial is a combination of them. The plate slenderness and plate aspect ratio are the primary factors that govern the plate elements' ultimate capacity.

A series of experiments of plates subjected to different types of loading could be found, for example, in [42–44]. Based on that, different empirical formulations were proposed.

2.2.2. Stiffened plates and panels

The stiffened plate is the fundamental structural component that resists the longitudinal loads. It is composed of a longitudinal stiffener with attached plating. The most crucial elements are those located near the bottom as well as the deck. The stiffened plates are spanned between the very rigid transverse frames. The composition of several stiffened plates located between two longitudinal frames is defined as a stiffened panel. The investigation of the ultimate strength of both of these components allows predicting the ultimate strength of the entire hull girder and providing information about factors influencing structural behaviour.

The majority of experiments analysing the ultimate strength of stiffened plates and panels was carried out in [45–48]. Recently, a series of experiments concerning stiffened panels subjected to axial compression with a total number of 24 specimens was carried out in [49–51]. Different column slenderness ratios were investigated as well as stiffener types were analysed. Experimental investigation of the ultimate strength of wide stiffened panels was also done in [52]. Other recent experiments concerning both stiffened plates and panels could be found in [53–56].

2.2.3. Box girders

The simplest small-scale model of ship hull girder is the so-called box girder. This model allows applying the bending loads closest to real ship structural conditions than stiffened plates and panels. However, the number of stiffeners and ideal geometrical similarity is usually hard to be satisfied when compared to the full-scale ship. Thus, the transfer of obtained results into the real scale is still challenging. Nevertheless, such experiments are highly useful in validating numerical codes, especially considering FE analyses.

One of the first attempts of the box girder's experimental analysis was performed by Dowling et al. [57]. Studies investigating small-scale box girders as ship hull models were conducted, e.g. a series of experiments in [58] performed a pure bending test of a box girder with one span, then pure bending tests of mild and high tensile steel, respectively [59,60]. Box girders with different spacing between frames were also investigated in [61]. Progressive collapse tests on a 1/10-scale wood-chip carrier have been performed in [62].

A hull model of three longitudinal box girders on a deck subjected to pure bending was tested [63]. A container ship hull subjected to hogging to find possible failure modes and ultimate strength using similar conversion relationships was investigated [64,65]. The torsional ultimate strength test of a ship-type hull girder with a large deck opening was performed [66].

2.3. Factors influencing the ultimate strength of welded structures

Usually, when analysing the structural response of different members, the idealised structure is taken into account. However, in experiments, the ultimate strength is affected by many factors and subjected to considerable uncertainties. Furtherly, during the ship exploitation phase, different ageing mechanisms will cause the loss of initial structural capacity. An appropriate analysis of parameters influencing the intact and aged structural members is the only one to yield good results of the ultimate strength of an entire structure.

The ultimate strength of the ship hull is affected mostly by:

- Material properties;
- Initial distortions and residual stresses due to low-quality welding;
- Large deformations caused by collision or grounding;
- Structural degradation effects, such as cracks and corrosion degradation;
- Type of the subjected load, quasi-static or dynamic.

Various experimental and numerical investigations have been carried out showing the impact of each of these factors on the load-carrying capacity of plates, stiffened plates, and stiffened panels. The most important of these investigations are presented here.

2.3.1. Welding-induced residual stresses

The welding process induces initial distortions and residual stresses in stiffened panels, thus affecting ultimate strength. These phenomena are complex and difficult to estimate during the design process. The effects of both residual stresses and distortions cause a reduction in the load-carrying capacity of stiffened plates near the collapse load, smoothing the load-shortening curve in the relevant region [67].

In a benchmark study in [68], some scatter in the strength reduction is observed due to the residual welding stresses. Empirical techniques are also applied to account for inelastic effects in stiffened plates under an axial compressive load, such as the Johnson-Ostenfeld correction

[67]. A potential 25% decrease of ultimate strength was found in [69]. Some experiments were also carried out in [53, 54, 55].

Gannon et al. [73] performed a FEl analysis of welded stiffened plates and compared the results with analytical formulations and IACS Rules, concluding that the residual stresses reduce the ultimate strength by 11 % with a consequent reduction in the hull girder ultimate bending moment of 3.3 %. Khan and Zhang [74] analysed the stiffened panels and observed a reduction of 11-13 % of the ultimate strength due to the residual stresses, especially for thick and slender members. Gannon et al. [75] performed a 3D FE analysis of the tee- and angle-stiffened plates and compared the results with IACS CSR formulations, where a 12.5 % reduction of the ultimate strength was observed. They also concluded that lateral distortions vary with the welding sequence. Gannon et al. [76] studied the welding influence on the ultimate strength of flat-bar stiffened plates, detecting a maximum 16.5 % reduction of the load-carrying capacity. The IACS [77] formulation was also analysed, concluding that the capacity of flat-bar stiffened panels was overestimated. Some other works investigating this problem could also be highlighted [78–80]. Nevertheless, it needs to be pointed out that the possible reduction of the ultimate strength will be highly dependent on both welding quality and plate and column slenderness ratios of the particular stiffened plate.

Approximate longitudinal stress distribution in a welded stiffened plate is shown in Figure 2.1 [81]. The stresses are assumed to be constant along the longitudinal direction. A tensile zone exists in the plate; at the weld location, the stress equals the yield stress, σ_y spreads at the width of $2\eta t$. The rest of the plate shows a compressive zone with a width of $b - 2\eta t$ where the residual stress is defined as:

$$\sigma_r = \frac{2\eta\sigma_y}{\frac{b}{t}} - 2\,\eta \qquad (2.1)$$

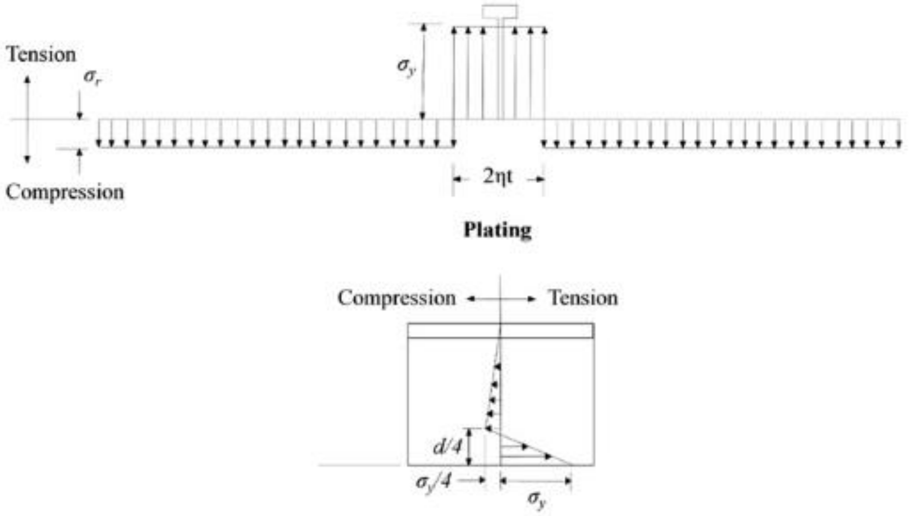

Figure 2.1. Longitudinal residual stress distribution in welded stiffened plates [81].

The η value varies from 3 to 4.5 due to the geometry and welding conditions [82]. This distribution is consistent with the measurements provided in [83] and by very recent experimental investigations in [84].

Tekgoz et al. [85] studied the influence of residual stresses using the methodology presented above, with an idealised stress field and modifying the stress-strain curve of the material utilising FE simulations, showing that the second method swiftly produces good results.

Apart from the classic stress distribution approach, the thermo-mechanical analysis was also used to analyse the stress distribution and distortions in welded joints. Tekgoz et al. [86] studied a single stiffener fillet welded to a plate and investigated the impact of a welding sequence on the residual stresses and, subsequently, on the ultimate strength. It was found that the welding sequence is a decisive factor.

Welding-induced residual stresses reduce the strength of an intact structure and are often taken into account [29]. However, based on different studies, it is evident that the residual stresses are significantly reduced after multiple loading cycles, which is called a shakedown effect [87]. Thus, when investigating the strength of structures after some exploitation period, the residual stresses can be neglected.

2.3.2. Welding-induced distortions

The second effect related to welding is the distortions of the plate elements. Similarly to the welding-induced stresses, the influence of initial distortions was investigated by many researchers up to now. The statistics related to the ship plating distortions could be found, e.g. in [88–90].

One of the first studies was conducted by Dow and Smith [91], who analysed buckling and post-buckling behaviour of rectangular steel plates under compressive loads and concluded that localised imperfection resulted from the welding-induced distortion is one of the most critical factors affecting the load-carrying capacity. Some other early studies related to this topic could be found in [92,93], where the impact of the initial distortions on the strength of welded plate elements has been studied. It was found that when the level of imperfections is significant, the strength of plates subjected to uniaxial compressive load can be significantly reduced. The reduction was observed for plates with different levels of slenderness. The investigations of the impact of the initial imperfections on the ultimate capacity of other structural members were also carried out, including stiffened plates in [94] and panels in [95,96], and the conclusions were similar. However, due to the presence of stiffeners, the reduction was not so significant when compared to the unstiffened plates. Some simplified methods for incorporating the initial imperfections in the ultimate strength predictions were proposed [97].

The initial distortion distribution is simplified for a design application. A half-sine wave distribution is usually assumed along the length and across the width [68]. The extreme imperfections are expressed as a fraction of plate slenderness given by:

$$\beta = \frac{b}{t}\left(\frac{\sigma_y}{E}\right)^{0,5} \tag{2.2}$$

where *E* is the elastic modulus. Smith et al. [93] found that the δ_0/t typically varies from $0.05\beta^2$ to $0.15\,\beta^2$ with an extreme value of $0.4\,\beta^2$. The distortions are also classified into three levels:

$$\frac{\delta_{opl}}{t} = \begin{cases} 0.025\,\beta^2, & for\ slight\ level \\ 0.1\,\beta^2, & for\ average\ level \\ 0.3\,\beta^2, & for\ severe\ level \end{cases} \tag{2.3}$$

Gannon et al. [73] analysed the hull girder ultimate strength applying a severe level of the initial imperfections and the Smith method showing that the reduction of hull girder ultimate strength can reach 6%. Similar conclusions were made by Estefen et al. [98], where initial imperfections to the FE model of the Suezmax tanker were applied.

Nowadays, the most commonly used method to predict thin-walled structures' behaviour under compressive load is the non-linear finite element method; however, some closed-form solutions are useful too. There are various methods to take into account the initial imperfections. The first one is the implicit one; thus, some imperfections are taken into account during formula development, using rules and norms, such as the ultimate strength approach as stipulated by the Common Structural Rules [5]. The second method is to perform the linear buckling analysis firstly, and the shape of the first mode is to be used for the further non-linear calculation. The third method applies some priorly assumed shape and level of the initial imperfections directly to the FE model. The commonly used method here is the Smith method [45]. Finally, one can measure the actual value and shape of any particular structural element's initial imperfections, employing various methods. The measurement of the initial imperfections is the essential work that needs to be done when evaluating the ultimate strength of different structural members experimentally. Furtherly, there need to be applied to the FE model.

2.3.3. Local denting

Both residual stresses and initial imperfections are somehow inherent in the process of manufacturing. Good control of welding quality can mitigate them. Nevertheless, during ship exploitation, the ultimate strength could be reduced too. Local damage can cause a reduction of the ultimate capacity.

A series of numerical investigations were performed in [99,100] on damaged plates. The conclusion was that the antisymmetric shape of the damage in adjacent plates has the most significant effect on the load-carrying capacity, and the amplitude of local damage is less critical. Paik et al. [101] investigated dented plates with different dent shapes, sizes, and locations. Small dents do not affect ultimate compressive strength regardless of the dent depth. However, with the increase of the dent diameter, the compressive strength reduction is significant, and the dent depth then also becomes an essential factor. The location of the plate also influences the load-carrying capacity. Ultimate strength analysis of highly damaged plates was also conducted in [102]. The effect of the dent depth and size were studied. The reduction of load-carrying capacity was up to 25 %. It was found that with the increase of the dent size concerning plate breadth, the thicker plates give lower ultimate strength discharge.

Witkowska and Guedes Soares [103] investigated locally damaged panels. The modelled damage was of local dents caused by the impact of a falling or striking object. Three different models were analysed: a single dented plate, a transverse panel, and a large 9-plate panel. It was concluded that the single pate model gives good results, but when intact plates surround it, the results are disappointing. The strength reduction observed was minor but not negligible. Other work dedicated to dented stiffened panels was carried out in [104], and the conclusions were very similar. The experimental and numerical study of small-scale panels carried in [105,106] showed a good agreement between the FE analyses and experimental testing. Some other works concerning this topic could also be highlighted in [107–109].

2.3.4. Locked cracks

Ships and offshore structures are subjected to different degradation effects, such as corrosion and cracks. The latter could be a result of fatigue damage or impact loads. The fatigue cracks are often undetected, and they can have a severe impact on the strength reduction of structural components.

The effect of locked cracks and their influence on the load-carrying capacity has been investigated experimentally and numerically. The first attempts to assess the importance of a transverse crack to the buckling capacity of plates were made in [110–113], showing the importance of this problem. In all cases, the buckling strength was significantly lower compared to non-cracked plates. Further studies were performed analysing the elastoplastic collapse, considering the geometry and material nonlinearities. In the studies performed in [114], both numerical and experimental analyses were carried out, concluding that the presence of cracks can significantly reduce the ultimate strength of plates by up to 50%. Additionally, the conservative estimation of strength reduction is related to the cross-sectional area reduction due to a crack. However, due to the cycling load, which may change from tensile to compressive, in some cases, the cracks may close, and then their behaviour is somehow similar to a non-cracked plate. Additionally, a nonlinear FE analysis was a useful tool for predicting cracked plates' behaviour subjected to compressive load.

A comprehensive review related to cracked ship structural elements' ultimate strength was presented in [115]. A limited number of experimental studies were conducted concerning cracked plates in [114,116] and cracked stiffened plates [117]. Shi et al. [117] investigated the influence of different crack locations on structural load-bearing capacity experimentally. The loss of ultimate strength due to various crack locations was found to be significant. It was also found that the crack may result in a reduction of the cross-sectional area that subsequently changes the plate slenderness and affects the failure mode. Further, the numerical assessment was carried out in [118] and validated with the experimental results. The combined effect of locked cracks and openings was experimentally investigated in [119], showing that the presence of these two phenomena could result in a significant loss of plate capacity.

Additionally, it is hard to model the boundary conditions in the experimental domain, and these may differ from the joining conditions of real ship structural components. Recently, more attention has been paid to numerical analyses. The ultimate strength of different structural elements subjected to cracks was investigated, including plates [120–124], stiffened plates

[123,125], stiffened panels [126], box girders [127], and ageing ship hulls [128]. Based on these studies, the most important governing factors on structural capacity reduction can be identified. The governing parameters that may be identified concerning the impact of the crack are the crack length, crack location, crack orientation, and the shape of the crack tip. In all studies, for transverse cracks, the reduction is higher with the crack length increase. In the longitudinal orientation of locked cracks, no significant effect is observed in most studied cases. However, some studies recognised that the longitudinal orientation of the crack is also relevant. In the case of the crack tip shape, it was shown in [129] and [130] that it would not influence the ultimate strength in general. However, the stress concentration around the crack tip will be influenced by the FE mesh density and tip shape.

Nevertheless, the factors that typically influence the ultimate strength of plates will potentially interact with the crack parameters, such as the plate slenderness ratio, plate aspect ratio, and welding-induced imperfections and residual stresses. The combined effects of cracking and initial imperfections were studied in [124]. It was concluded that for small cracks, the ultimate strength is reduced for the higher levels of initial distortions. However, in the case of long cracks, the crack damage effect plays a dominant role.

Based on the different studies, empirical formulations were developed too. Babazadeh and Khedmati [129] derived empirical formulations for the ultimate strength reduction of transversely cracked plates due to the crack length, plate slenderness ratio, and plate aspect ratio. In contrast, Paik et al. [114] derived the formula as a function of the plate slenderness ratio and crack length.

2.3.5. Corrosion degradation

Ships and offshore structures operating at sea are subjected to a highly corrosive environment. The non-uniform corrosion degradation is a factor that can significantly affect the load-carrying capacity of different structural members [131–133], mainly due to cross-sectional area reduction. One can identify the most common types of corrosion, like pitting and general corrosion [134]. The examples of these two corrosion types that could be found in ship structures are presented in Figure 2.2. These two types of corrosion need to be treated separately in terms of modelling and analysis.

The impact of pitting corrosion on the strength of plates was investigated in [135]. The collapse test of artificially pitted plates subjected to a compressive load has been performed in that work. The observed reduction of capacity was significant, and the smallest cross-sectional area has been proposed as a factor that characterises the ultimate strength reduction of pitted plates. Similar experiments have been done for plates subjected to a shear load [136]. Further, numerical and experimental investigations related to the strength of plates subjected to pitting corrosion have been performed in [137–143]. A semi-spherical shape of pits has been chosen, and the pitting distribution was either regular or not. In some cases, the pits were distributed with the use of random techniques [144].

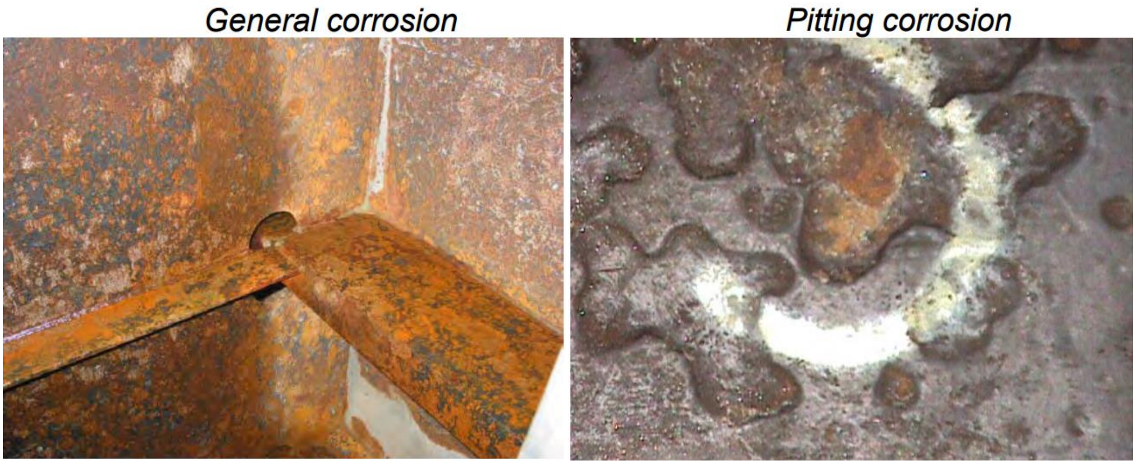

Figure 2.2. The comparison between general and pitting corrosion [145].

The majority of works related to the influence of pitting corrosion into the strength of structural elements are focused on the simple plate elements. However, studies related to stiffened plates or panels can also be found. The experimental study of the ultimate strength of artificially pitted plate with two stiffeners has been carried out in [146], investigating different pit locations, depths, and diameters. It was observed that the pitting would cause not only strength reduction but the failure mode will be changed as well when compared to the intact specimen [147]. Numerical studies related to the ultimate strength of pitted stiffened plates were carried out in [148], and a simplified formulation based on the corroded volume loss has been proposed. Some other numerical investigations could be found in [149–151]. One can conclude that in the case of the stiffened plates and panels, the experimental studies are limited but are needed to validate the numerical codes.

It has to be pointed out that in most of the experimental studies, artificial pitting is created, and there is a lack of studies that deal with natural pitting corrosion. Nevertheless, the corrosion observed during the ship service life is mainly general [152], although the pitting one is hazardous. General corrosion is observed, e.g. in cargo holds as well as in ballast tanks.

When investigating the general corrosion [152], the one causes metal degradation in two levels. The uniform thickness loss taken as a mean corrosion diminution value from a specific plate region can be considered first. In the second level, there are observed local irregularities of the corroded surface of the plate. It can be considered two main models representing the general corrosion, the uniform and non-uniform one [153]. The model of uniform degradation produces fast results, and it is easily applicable to different numerical and closed-form methods. Due to that reason, it is applied in the Classification Society Rules, e.g. [5]. In the case of non-uniform modelling, the application of this model is not easy and rather possible to be applied only in sophisticated FE codes with the application of the very refined mesh. However, it was found that the non-uniformity of the corroded surface can be captured when evaluating the mechanical properties of small-scale coupons subjected to tensile loading.

The discussion about the reduction of mechanical properties of steel specimens with the subsequent corrosion degradation is vital. Several studies have been done during the last couple of years, mainly experimentally and in the numerical domain. Garbatov et al. [154] tested corroded plate specimens with different corrosion severity. They concluded that the mechanical properties reduction is significant for the specimens with a higher than 20% degradation level. Not only yield strength and the Young modulus are reduced, but also the elongation is significantly reduced. Kashani et al. [155] analysed the stress-strain behaviour of non-uniformly corroded steel circular bars. In this case, the degree of degradation was up to 20%. The yield strength reduction was up to 30 %, and the mean strain at failure reduction was even up to 80 %. Zhan et al. [156] tested 267 corroded steel bars corroded in different conditions (in a laboratory and natural environment). They concluded that the mechanical properties have significantly deteriorated, and the yield plateau of the steel bar became shorter or even disappeared with the development of the corrosion. In the study performed in [157], 30-years old, naturally corroded steel reinforcing bars were examined. Besides the tensile tests, they measured the corrosion distribution along the bars. They concluded that the reduction of the mechanical properties is governed by the minimal cross-section area of the specimen. Additionally, Li et al. [158,159] performed tensile tests of pre-stressed and corroded specimens, and the effect of the mechanical properties reduction was magnified with comparison to only corroded specimens.

In ship and offshore structures, thin-walled structures such as plates and slender beam are more often used. The mechanical properties of corroded flat specimens were investigated in [160–164], and the conclusions were similar to those obtained for bars. The reduction was observed not only in severe corrosion conditions but also in lower corrosion degradation. In the case of very thin plates, such as one millimetre of thickness, the reduction of the mechanical properties was up to 70% from their initial values [161].

Most researchers agreed that if the corrosion will produce a perfectly uniform surface, it would not significantly affect the mean stress-strain response of a small-scale specimen. Thus, the reduction of mechanical properties is caused by the corroded surface's local non-uniformity [165–168]. This hypothesis is supported by the experimental results presented in [169], where specimens after cleaning showed higher mechanical properties than the corroded non-cleaned ones. In the marine environment and especially for ship structures, non-uniform corrosion is the most common one, and this phenomenon cannot be neglected.

Based on the experimental results, several mathematical models for predicting mechanical properties of corroded bars and flat specimens were developed in [170,171]. Li et al. [172] developed a simplified constitutive model for corroded bars based on experimental and numerical studies. Garbatov et al. [154] developed a model for corroded coupon specimens. Other mathematical models for estimating different mechanical properties of flat bars based on experimental investigations can be found in [143,173–175]. Although a couple of models were developed, more work is still needed towards developing a more unified approach regarding mechanical property change in terms of corrosion degradation.

With the development of more advanced measuring techniques, detailed measurements of 3-D corrosion morphology are possible. Examples of such measurements can be found in [176–178]. Based on that, the mechanical properties of corroded specimens or fatigue properties can be evaluated [178–180], and even the structural response of beam elements may be analysed [181]. Wang et al. [160] compared experimental results with the nonlinear FE analysis, where the corrosion surface was scanned and implemented in the finite element model. The agreement between experimental and numerical results was good.

The research related to the ultimate strength of corroded structural members of a larger-scale was also carried out using numerical and experimental techniques.

The ultimate strength of corroded plates subjected to compressive loading was investigated numerically, applying uniform in [182,183] and non-uniform corrosion models in [184–187]. In all cases, the observed strength reduction was significant. However, the non-uniform models presented higher strength reduction when compared to the uniform models. The influence of random corrosion thickness distribution on the ultimate strength of rectangular steel plates was also investigated in [153]. Applying the Monte Carlo Simulation, a plate thickness distribution was generated, taking the degree of degradation into account. Next, the model was used for a reliability analysis [188].

Garbatov et al. [189] investigated numerically and experimentally the ultimate strength of stiffened plates with different corrosion levels. The ultimate strength reduction was significant. Furtherly, the combined effect of the uniform thickness loss and subsequent mechanical properties reduction was incorporated in the numerical model of Woloszyk et al. [190], showing excellent agreement with the experimental results presented in [189]. However, in this case, the degree of degradation levels was very high (above 40 %). Usually, the plates with that level of corrosion are replaced in real structures. The experimental work of not so severely corroded stiffened plates is lacking. Other works related to corroded stiffened plates and panels' ultimate strength could be found in [191,192].

Saad-Eldeen et al.[193–199] performed a series of experiments of corroded box girders subjected to pure vertical bending. The corrosion was generated in a real seawater condition, but it was fastened by applying an electric current [200]. The observed reduction of box girders capacity was very significant. Additionally, due to the non-uniform corrosion distribution, the structural behaviour was highly asymmetrical. An ultimate strength prediction based on experimental results and dimensional theory was performed in [201]. The uncertainty of the results with the comparison with Classification Society rules was at 8.3 %. It was found that corrosion may strongly reduce the ultimate strength of a ship hull.

The literature review of corrosion influence on the hull girder section modulus was shown in [202]. The results of the recent studies in [203–210] are shown in Table 2.1. The observed loss of hull girder section modulus varies from 4% to 20%, mainly due to the assumptions and models used in the analysis.

Table 2.1. The reduction of global hull girder strength after 20 years of exploitation [202].

Ship(s)	Loss of hull girder section modulus at 20 years old	Basis
A single hull tanker [205]	About 7%	Analysis
A single hull VLCC [203]	About 20% in mean value, 6% in standard deviation	Analysis
Double hull tankers [207]	About 10%	Analysis
A handy-size bulk carrier [208]	4.2%	Analysis
A double hull tanker [206]	12% (average corrosion)	Analysis
A conversion single-hull FPSO [204]	7.5%	Analysis
Single hull tankers [209]	About 8% in mean, 2% in standard deviation	Analysis
A single hull tanker [210]	About 10%	Analysis
A fleet of 210 single-hull tankers [209]	3.2 % in mean value and 1.9% in standard deviation	Measurements

To conclude, corrosion degradation is one of the most significant factors influencing the ultimate strength of plates and stiffened plates. It could also be noticed, the experimental studies are very limited, and more comprehensive research is needed to validate the numerical models.

3. MOTIVATION AND OBJECTIVES OF THE THESIS

Based on the presented status of the current state of the art related to the ultimate strength of ship structural components, especially subjected to corrosion degradation, it was identified, and some basic models are already established, but the knowledge is still very limited. Notably, the experimental investigations of naturally corroded structural elements (with in situ conditions or accelerated ones) are lacking.

The preliminary results presented in [35] showed that corrosion degradation significantly impacts the ultimate strength. The derived numerical model demonstrated a good agreement with experimental results, where the uniform thickness reduction with the following mechanical properties changes was taken into account, identifying that a more robust model for intact and ageing conditions may be developed.

The central research hypothesis is as follows: **“The decrease of the structural capacity of corroded compressed stiffened plates results from a non-uniform thickness loss with the subsequent reduction of mechanical properties depending on the severity of degradation in any particular point of the analysed plate”**. The following hypothesis has been verified using both experimental and numerical investigations.

The stiffened plate subjected to a compressive load has been chosen as a research objective. This type of structural element is the simplest part of a ship's cross-section. The entire progressive collapse behaviour of a hull girder can be estimated based on the responses of the individual stiffened plates, which is a basis of the Smith method [15], adopted in the Rules of Classification Societies [5]. When considering typical aspect ratios of the stiffened plates, a single stiffened plate's structural behaviour is relatively independent of the adjacent stiffened plates, and stresses acting in the transverse direction can be neglected. The exception from this rule could be the structure of a single side of the typical bulk carrier, which is stiffened transversely, leading to high aspect ratios and high slenderness ratios of the stiffened plate elements. In that case, the entire panel's behaviour needs to be analysed due to the orthotropic stress state existence. Both plate and column slenderness ratio of the considered specimens are similar to found in operating ships typically.

The results presented in [35] considered higher levels of corrosion degradation (above 40 %). This type of corrosion level is rather hard to be reached, since the Classification Societies force to replace the structural elements with a degradation level above 20 %. Additionally, the applied corrosion process was the electrochemical one, leading to different surface characteristics compared to natural conditions. Thus, in the presented thesis, degradation levels up to 21 % have been chosen as a research objective.

In the beginning, the corrosion tests have been designed to provide the accelerated conditions of the marine immerse corrosion degradation process. Nine welded large-scale stiffened plates and 30 standard small specimens (considering different initial plate thickness) have been subjected to the accelerated marine immersed conditions. The time-dependent corrosion rate was estimated and analysed. Corrosion degradation has been controlled using different measurement techniques, including mass measurements and ultrasonic thickness measurements. After corrosion testing, the specimens have been accurately measured in terms of surface characteristics and thickness measurements.

The coupon specimens were furtherly subjected to tensile loading to develop the stress-strain curves and mechanical properties conditional on the severity of corrosion degradation. The finite element analyses employing the technique of random field modelling were developed and validated, taking into account the results of experimental testing.

The stiffened plates were subjected to the compressive loading, and the structural response has been analysed, accounting for initial imperfection, corrosion degradation, welding-induced residual stresses, and material non-linearity. Special attention was paid to the force-displacement response and deflections and strain in particular points of the stiffened plate. The results provided information about the impact of immerse marine corrosion on the ultimate strength of stiffened plates, and a comparison has been performed with the experimental testing of intact specimens. The numerical models of different accuracy of corrosion degradation models were validated with the experimental results, and a research hypothesis has been verified.

Based on the obtained results, a simple formulation, allowing for a fast estimation of the structural capacity of corroded stiffened plates, is developed. Finally, the reliability formulation taking into account the time-dependent progress of corrosion degradation has been developed.

The output of the study significantly contributes to enhancing the knowledge about the behaviour of ship structural components subjected to corrosion degradation.

Herein, the scope of the work in particular chapters is introduced.

Chapter 1 introduces the necessary information about ship structural analysis, particularly about the analysis of buckling and the ultimate strength of ship structural members.

Chapter 2 reviews the current state of the art related to the impact of different factors on the ultimate strength of various structural members, with particular attention to degradation effects, including corrosion.

Chapter 3 provides the motivation and objectives of the presented thesis.

Chapter 4 briefly introduces marine corrosion and describe the designed experimental set-up for accelerated corrosion testing. The testing results, including obtained corrosion rates and specimens dimensions, are also discussed here.

Chapter 5 consists of initial numerical investigations performed before the experimental analysis, indicating the factors that need to be considered.

In Chapter 6, the experimental set-up, including pre-testing analysis, is presented. Furtherly, the results of experimental testing of stiffened plates and small-scale coupons are presented, including intact and corroded conditions.

Chapter 7 provides a review of existing modelling techniques regarding corrosion degradation and introduces a new concept of corrosion modelling using random fields.

In Chapter 8, the numerical investigations of corroded specimens subjected to tensile loading are presented and validated with the experiments.

In Chapter 9, the numerical analysis of intact and corroded stiffened plates can be found. Different corrosion modelling techniques are applied and validated with the results of experimental testing.

The simplified formulation that allows for a fast estimation of the ultimate strength of corroded stiffened plates is introduced in Chapter 10.

Chapter 11 presents the reliability analysis and formulations related to the corrosion-dependent reliability of stiffened plates and ship hull girder.

Conclusions and future works are outlined in Chapter 12.

Chapter 13 presents a list of papers that were published concerning the work presented in the thesis. Additionally, the references to the published papers have been added in the headings of relevant subsections.

4. EXPERIMENTAL SET-UP OF CORROSION DEGRADATION AND ANALYSIS

4.1. Marine corrosion degradation

Experimental testing is needed to evaluate the influence of corrosion degradation on the strength of various structural elements [169,189,198]. One can test members taken from real structures after some time of exploitation or create an artificial corroding environment in the laboratory. In the first case, the initial properties of structural members and corrosion conditions are usually missing. In the second case, the governing variables can be controlled.

In the case of small-scale specimens, the corrosion testing procedures are well-developed [211]. There are no strict rules for large-scale specimens, and existing guidelines are relatively modest [212]. In this way, one needs to choose the proper environmental conditions to be simulated in the experimental domain.

The most common type of corrosion degradation for constructional steel is the so-called ‘uniform’ corrosion. In this case, the material loss is relatively uniform, where the surface is rough and irregular. The corrosion then is measured via material weight-loss after some exposure time.

In the presented chapter, the main factors influencing corrosion degradation of steel structures are discussed, and corrosion test set-up for large-scale specimens is presented. The simplified methodology for calculating the corrosion rate and acceleration factor compared to the natural marine conditions is evaluated. The corrosion measuring techniques are discussed, and an optimum number of thickness measurements, depending on the exposure time, is obtained.

4.1.1. Governing factors

Corrosion degradation is influenced by many factors, mainly: biological, chemical, and physical [213]. In the case of biological factors, their importance seems to be less significant, and thus there will be not discussed further.

The main influencing chemical factors in corrosion degradation are the oxygen and sodium chloride content in the seawater conditions.

The dissolved oxygen concentration undoubtedly influences the corrosion rate of carbon steel. The maximum saturation of oxygen in water is a function of the temperature and salinity [214]. Near the ocean surface, dissolved oxygen content usually reaches the maximum saturation level due to contact with the atmosphere [215]. Two sets of conditions, however, could lead to supersaturated conditions. The first one is the production of oxygen due to the photosynthesis of the microscopic marine plants. During intense periods, the seawater could be even supersaturated, reaching 200% of dissolved oxygen comparing to the equilibrium conditions. The second case that the saturation is above the maximum level is the increased air bubbles due to the wave actions. In this case, the supersaturating does not exceed 110 %.

The linear relation between the corrosion rate and content of the dissolved oxygen for mean ocean temperature and salinity could be found in [216]:

$$r(O_2) = 0.0286 \cdot [O_2] + 0.086 \tag{4.1}$$

The corrosively of the water increases proportionally with the increase of the salinity. This phenomenon is caused due to the increase in water conductivity. However, if the salinity exceeds 3 %, the water corrosively decreases [217]. With the increase of salinity, the oxygen solubility is reduced, and thus 3.5 % of salinity results in the highest corrosion rate. Thus, the 3.5 % salinity is to be set up in testing conditions.

The seawater's pH is usually very constant and is between 8.1 and 8.3 [218]; thus, its effect on the corrosion rate is negligible. Even for higher ranges of pH, the corrosion rate seems to be independent.

The main physical factors that influence the corrosion rate are temperature, water velocity, and water pressure. Water pressure is not essential since the testing tank will be relatively shallow.

Based on the measurement data [219], the influence of temperature (T) into the corrosion rate in seawater could be modelled by linear relationship:

$$r(T) = 0.00356 \cdot T + 0.0392 \left[\frac{mm}{y}\right] \tag{4.2}$$

However, the linear relationship is valid up to some moment, which is related to a decrease in the maximum oxygen saturation with the temperature increase.

In the case of water velocity, it has a significant impact on the corrosion rate. In high water velocities, oxygen more easily reaches the metal surface, and protective films are significantly reduced. Additionally, the corrosion products are more frequently removed. The relationship between the flow velocity (v) may be modelled with the use of an exponential function [219]:

$$r(v) = 0.934\left(1 - Exp\big(-0.446(v + 0.282)\big)\right) \tag{4.3}$$

Even a minimal water velocity may significantly speed-up the corrosion process compared to the stagnation conditions.

4.1.2. Time-variant corrosion degradation

The proper models need to be used to predict the corrosion development for elements located in the ship cross-section. Based on the measurement data of real structures, different corrosion models have been recently developed, e.g.:

- Melchers [131,213];
- Yamamoto and Ikegami [220];
- Guedes Soares and Garbatov [201, 202];
- Paik et al. [223];
- Qin and Cui [224].

One of the commonly used models, developed by Guedes Soares and Garbatov, is presented in Figure 4.1.

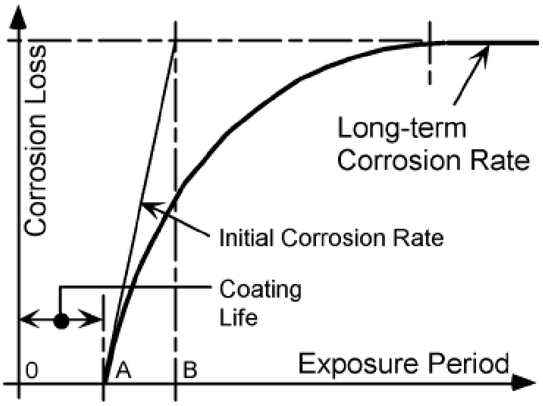

Figure 4.1. Corrosion degradation model, [222].

First, with the coating on, there is no corrosion. Next, after the coating wears off, corrosion rapidly increases. In the long term, during the exposure period, the corrosion stops at a specific value. The model parameters, such as typical coating life, long-time corrosion rate, etc., need to be calibrated using available data from ship measurements. The Classification Societies require such measurements of corrosion diminutions to check that there were not crossed allowable limits. If corrosion is too extensive, the replacement of structural parts is requested.

Some examples of corrosion model parameters for particular ship sections could be found in literature, e.g., deck plates of ballast and cargo tanks of tankers [225], crude oil tanks [132], bulk carrier decks [226]. Some examples of fitting the observed corrosion data of bottom plating of bulk carriers into the corrosion model are presented in Figure 4.2.

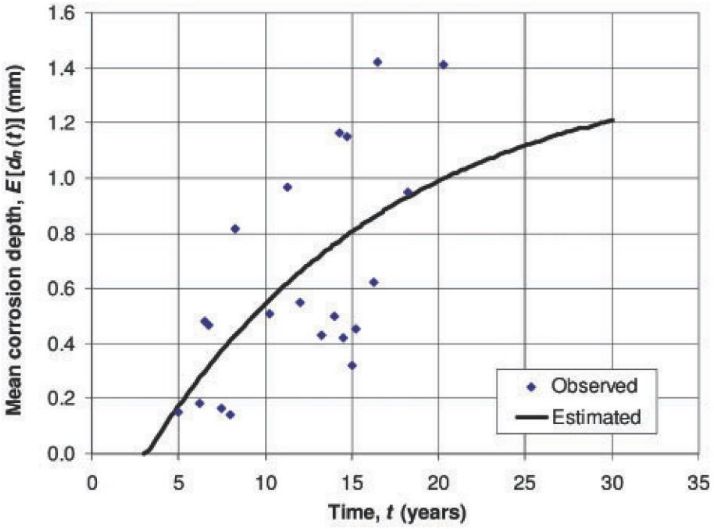

Figure 4.2. Example of fitting of observed corrosion data of bottom plating of bulk carriers into the corrosion model [216].

4.2. Experimental set-up of corrosion degradation [P1]

Based on the analysis from the previous section, the leading natural factors that influence the corrosion rate are temperature, the content of dissolved oxygen in water, water velocity, and salinity. The control of these three factors may result in accelerated corrosion degradation of the specimens.

A very high rate of corrosion degradation, reaching even a couple of mm/year, may result from electrochemical corrosion. In this case, the water and specimens are subjected to a DC power input source. However, the resulting corrosion morphology is very different from those obtained in the case of natural conditions. [227] presented a comparative analysis between electrochemically and naturally corroded specimens. Due to the different corrosion mechanisms, the surfaces of the corroded specimens diverged significantly. Additionally, the mechanical properties were also different depending on the type of corrosion for the same degradation level.

Since the corrosion test aims to simulate marine environmental conditions, one should avoid the electrochemically stimulated corrosion degradation process. Thus, only natural parameters could be controlled to magnify the corrosion rate.

4.2.1. Specimens dimensions

The specimens subjected to the corrosion degradation process are stiffened plates of a 1.265 m length and 0.4 m width with a stiffener of a 0.1 m height. The samples were automatically arc welded, and there are made from the mild steel S235. The stiffened plates were tested for three different initial thicknesses: 5, 6, and 8 mm. With these dimensions, the plate slenderness ratio (see Eq. 2.2) is with the scope of typically observed values in ship structures [228].

Both plate slenderness (see Equation 2.2) and column slenderness ratios are the primary factors that govern the ultimate strength of stiffened plates [228]. The column slenderness ratio is equal to:

$$\lambda = \frac{l}{\pi\sqrt{\frac{I}{A}}}\sqrt{\frac{Re}{E}} \tag{4.5}$$

where l is the plate length, I is the moment of inertia of the plate with the attached stiffener, and A is the cross-sectional area of the stiffened plate.

The resulting plate slenderness and column slenderness ratios of the tested specimens, considering the actual values of mechanical properties, are presented in Table 4.1. When comparing these values with the typically observed in ship structures [228], the plate slenderness ratio can be considered relatively high, and column slenderness is within the mean range.

Table 4.1. Characteristics of tested stiffened plates.

Thickness	Plate slenderness ratio [-]	Column slenderness ratio [-]
5	2.91	0.499
6	2.55	0.522
8	2.13	0.576

For each thickness, four specimens were fabricated. Plates and stiffeners composing the stiffened plates were cut from one sheet of steel; thus, the material is the same for each specimen of the same thickness. The sample specimen during the welding process is presented in Figure

4.3. One stiffened plate of each thickness was furtherly tested in intact condition, whereas the other three were tested after corrosion in the range between 0 % up to 21 % of degradation level. The target degradation levels of stiffened plates are presented in Table 4.2.

Table 4.2. Target corrosion levels for stiffened plates.

Thickness	Target degradation level [%]	Target mean thickness level [mm]
5	7	4.65
	14	4.3
	21	3.95
6	7	5.58
	14	5.16
	21	4.74
8	7	7.44
	14	6.88
	21	6.32

Additionally, the standard coupon specimens will be tested to provide information about mechanical properties for different degrees of corrosion degradation. A total number of 30 specimens (10 for each thickness) were corroded. The target levels of corrosion degradation were as follows: 3%, 6%, 8%, 10%, 12%, 14%, 16%, 18%, 20%, 21%. Due to an increasing level of uncertainty, the intervals of the degradation level were smaller for severely corroded specimens.

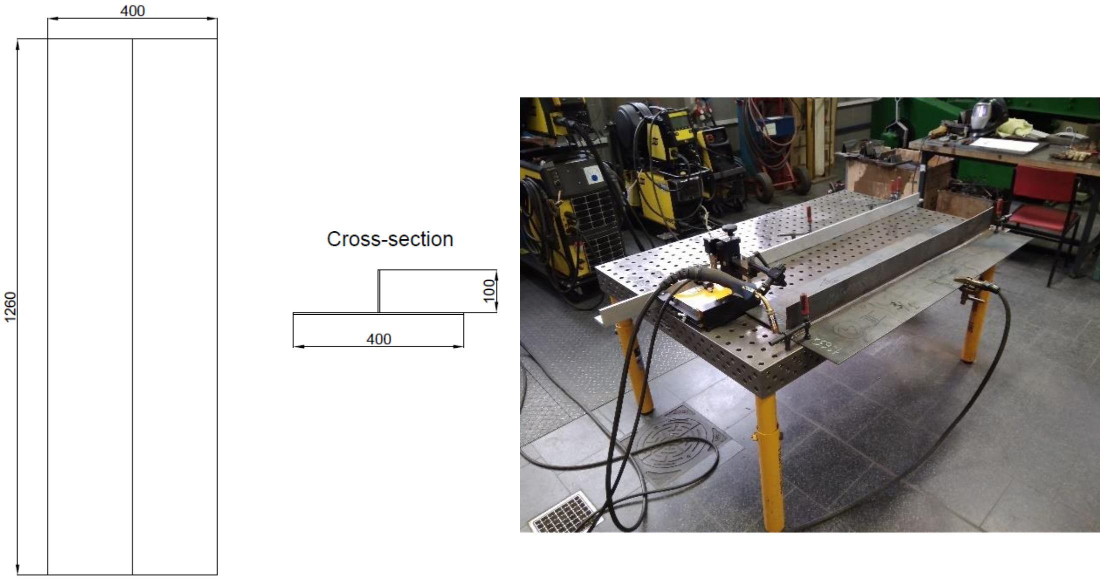

Figure 4.3. Specimens dimensions (left) and specimens during the welding process (right).

4.2.2. *Corrosion tank*

Due to the scale of specimens, the corrosion tank needs to provide sufficient space for water circulation. A 900 l tank with the external dimensions of 2000 x 1100 x 750 mm is chosen for the experiment. The big-scale specimens were placed alongside the tank edge, as presented in Figure 4.4, whereas small-scale tensile specimens were placed on the specially designed grillage structure. The tank is made from GRP laminate. The advantages of this solution are the excellent corrosion resistance and lower weight compared to metal tanks, at a similar price.

Figure 4.4. Corrosion tank with placed specimens.

4.2.3. *Oxygen content control*

As discussed in the previous section, the content of the dissolved oxygen on the surface of the seawater usually reaches the maximum value. However, in testing conditions, one can quickly obtain supersaturated conditions using an aerator [229]. Such aerators are commonly used in fish ponds [230]. Due to that, the corrosion rate could be significantly magnified. With an efficiency of 70 l/min, the aeration pump is chosen to aerate the water circulating in the tank. It is assumed that it should create conditions with a constant supersaturating of about 300 %. The actual value of the dissolved oxygen content will be analysed in laboratory conditions during testing. It could be done with the use of a special oxygen meter.

4.2.4. *Temperature control*

The tank is placed in a closed room when the temperature oscillates at about 20 °C. However, to speed up the corrosion rate, water heating may be applied. Excessive heating (above 40 °C) of such an amount of water requires heaters with enormous power, leading to high energy consumption. Due to that, the heaters with moderate energy consumption of a total power of 600W are used. The maximum temperature of 34 °C could be obtained, and the temperature is continuously controlled to keep the same level during the whole corrosion test.

4.2.5. *Water velocity control*

As noticed previously, even minimal water velocity may produce faster corrosion degradation. To control the circulation water velocity, a circulation pump, as presented in Figure 4.5, is used. The maximum efficiency of the pump is about 20,000 l/h. With these dimensions of the tank, the water circulates with a velocity of approximately 0.03 m/s.

Figure 4.5. A circulation pump was used during corrosion testing.

4.2.6. *Salinity control*

Natural saltwater should be applied to provide the proper salinity conditions. Such salt comes from the process of water evaporation from the real seawater. The salinity level is controlled during the corrosion degradation process. Equipment based on the water density is used to measure the salinity level. As the salinity increases, the water density increases as well. However, the density will be temperature-dependent, and a proper calibration table needs to be used to provide the value of salt level.

4.2.7. *Estimation of corrosion acceleration factor*

The corrosion rate in any conditions may be calculated based on Eqns 4.1 to 4.3. However, the influence of all discussed factors could be combined into one equation [215]:

$$r = 0.012 \cdot 2^{\frac{T-25}{T}} \cdot \{[0_2] + 2.72\} \cdot \left(1 + \sqrt{v}\right) \tag{4.6}$$

In both cases, the results are somewhat similar, and due to simplicity, Eqn 4.4 will be used to estimate the corrosion rate.

The mean values of environmental factors in real ocean conditions (in the surface layer) are presented in Table 4.3 [231]. The coupon not subjected to any flow velocity is assumed as a reference. In the surface layer, approximately fully aerated conditions are existing. Additionally, both surfaces of the specimens will be corroded in the testing tank, double the corrosion rate in testing conditions. In ships, usually, only one surface is corroded significantly. The simulated testing conditions and corrosion rates calculated using Eqn 4.4 are presented in Table 4.3.

Table 4.3. Environmental conditions.

Factor	Real conditions	Testing conditions
Salinity [‰]	34.3	35
Temperature [ºC]	15.5	34
Oxygen saturation [%]	100	300
Water velocity [m/s]	0	0.03
Corroding surfaces	1	2
Corrosion rate [mm/y]	0.0787	0.736

Based on the corrosion rates in real and testing conditions, the acceleration factor can be calculated:

$$a = \frac{r_{test}}{r_{real}} = 9.35\ [-] \tag{4.7}$$

In this way, the same corrosion degradation, which in normal conditions is obtained after 20 years, will be obtained after approximately two years.

One can notice that there is a possibility to increase the corrosion rate even more significantly. There is already an optimum value in both real and testing conditions in the case of water salinity. The supersaturating conditions are also hard to be achieved. The parameters that could be increased are the temperature and water velocity. However, this will require more financial and energy resources. The proposed methodology is somehow a compromise between the costs and time of the corrosion test.

Additionally, one needs to be aware that corrosion degradation is a very complicated process, and estimated corrosion rates are subjected to high uncertainties [232]. Thus, the corrosion rate needs to be monitored continuously during the whole corrosion process.

4.2.8. Corrosion measuring techniques

During the corrosion test, degradation levels are to be obtained. Measurements need to be performed to monitor the corrosion rate. There are various methods to measure corrosion degradation [215], such as:

- Weight measurements of corrosion coupons;
- Electric Resistance;
- Electrochemical Impedance Spectroscopy (EIS);
- Acoustic Emission methods.

The simplest and very precise is the first method, which is based on the weight measurements. The small coupons made from the same sheet of metal as big-scale specimens are taken and analysed after some time. The corrosion degradation is obtained as a reduction of the current mass compared to its initial one. However, the specimens need to be cleaned from corrosion products, which could disturb the measurements. The detailed analysis of the mass measurements, conducted for the need of the present study, of coupons with and without the corrosion products shown that the difference could reach the level of 0.5 %. To reduce the uncertainty related to the measuring equipment, one can choose an exact laboratory weight with an accuracy of 0.1 g.

The Electric Resistance method is very widely used, especially for measuring the material loss in the interior of plants and pipelines. The electric resistance probe is made from the same material and calculates the corrosion rate by measuring the electrical resistance. With the corrosion development, the electrical resistance increases due to the reduction of the cross-section area. The main disadvantage of this method is a low corrosion rate, and the resistance variations are small. Thus, instrumentation with considerable accuracy needs to be used.

Electrochemical impedance spectroscopy has been proven to be an excellent method for measuring corrosion rates. The probe sends the electrical signal with a wide range of frequencies. Then, the impedance characteristics are measured, creating a full spectrum. Depending on the shape of the EIS, the parameters of the corrosion can be obtained. Nevertheless, this methodology requires knowledge of the operator and proper equipment.

The acoustic emission methods can be used in thickness measurements and for defects detection. In the thickness measurements, the probe sends an acoustic signal with a known velocity and measures the time required to capture the signal again. Based on that, the thickness of the element can be determined. The ultrasonic thickness gauge used in the current study consisting of the probe and measuring device is presented in Figure 4.6. The accuracy of such equipment is usually around $\pm 0.05\ mm$ in the case of thin steel plate elements. However, when the surface of the analysed element is irregular, like in severely corroded plates, the measurements can be significantly disturbed [233]. Additionally, such equipment requires proper calibration before the measurements.

Figure 4.6. Typical ultrasonic thickness gauge.

In the present study, two types of measurements are being carried out. The first one is based on the weight measurements of coupon specimens, which is the most accurate. The specimens are taken out and measured from time to time to monitor the actual corrosion degradation. However, the mass measurements are giving information about the mean corrosion depth. The ultrasonic thickness measurements were carried out to see the thickness deviations around the specimen. For minimizing the possible measuring error, the optimum number of thickness measurements can be defined, which is discussed in the next section.

4.2.9. The optimum number of thickness measurements

All measuring techniques are subjected to some uncertainty levels. With the corrosion growth, the surface becomes more and more irregular. By measuring the thickness in a couple of points only, one cannot obtain the correct value of the degree of degradation. However, proper statistical tools could be justified to provide the optimum number of thickness measurement points, leading to a proper estimation of the degradation level.

The nonlinear time-dependent model of Guedes Soares and Garbatov [221] is used for corrosion degradation estimation. The corrosion depth in the function of time can be estimated as follows:

$$d(t) = \begin{cases} d_\infty \left[1 - \exp\left(-\frac{t - \tau_c}{\tau_t}\right)\right], & t > \tau_c \\ 0, & t \le \tau_c \end{cases} \tag{4.6}$$

where d_∞ is the long-term corrosion depth, τ_c is the coating life and τ_t is the transition time.

The following values can be fitted based on real measurements, and the actual values can be found in [234]. Since the tested plates are exposed to seawater, their corrosion will be similar to the corrosion of deck plates of ballast tanks. The transition time is equal to 17.5 years in this case, and the long-term corrosion depth is calibrated to obtain the same mean corrosion rate, as calculated via Eqn 4.4 for real conditions (0.0787 mm/year). The long-term corrosion depth is estimated equal to 2.36 mm. The corrosion depth is a function of time in the real conditions, as presented in Figure 4.7.

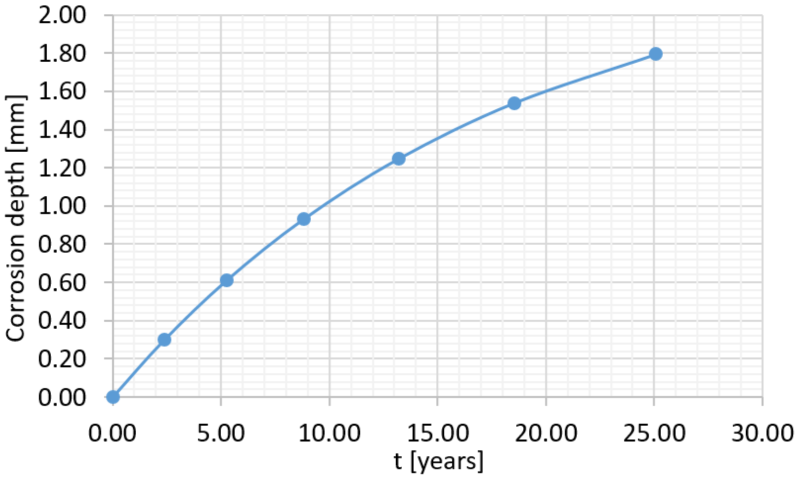

Figure 4.7. Corrosion depth as a function of time.

For testing conditions, the transition time will be the one for real conditions divided by the acceleration factor. For the calculated acceleration factor (9.35), it will be equal to 1.87 years. For all specimens, 21% of corrosion degradation needs to be obtained. In the case of 5 mm specimens, the target corrosion depth is 1.05 mm. This corrosion depth will be obtained after 11 years in real conditions and 399 days in testing conditions. In the case of an 8 mm specimen, the target is a 1.68 mm corrosion depth, and it will be achieved after 22 years in real conditions and 798 days in testing conditions.

The corrosion depth, as given in Figure 4.7, represents the mean value. According to [234], the standard deviation value of corrosion depth will be time-dependent and can be determined as (for coating life equal to 0 years):

$$StDev(t) = 0.384\ Ln(t + 10.54) - 0.71 \tag{4.7}$$

It can be noticed that with the time increment, the standard deviation increase as well.

Based on the mean value and standard deviation of corrosion depth in the time domain, assuming that the Normal distribution of the corrosion depth is known, the needed number of thickness measurements conditional to the confidence level and assumed margin of error could be obtained [235]. Considering n number of measurements, the measured value m should lie within the following margin:

$$\bar{d}(t) - \frac{u_\alpha \sigma(t)}{\sqrt{n}} \leq m \leq \bar{d}(t) + \frac{u_\alpha \sigma(t)}{\sqrt{n}} \tag{4.8}$$

where u_α is the percentile of the N(0,1) distribution with the assumed confidence level α, $\bar{d}(t)$ and $\sigma(t)$ are mean value and standard deviation of corrosion depth, respectively.

In this case, the $(u_\alpha \sigma(t))/\sqrt{n}$ is the standard error ($\Delta d(t)$) of the estimation, when divided by $\bar{d}(t)$, it is expressed as $Err = \Delta d(t)/\bar{d}(t)$. For the assumed standard error and confidence level, the required number of measurements is estimated to:

$$n = \left(\frac{u_\alpha \sigma(t)}{\mathrm{Err}}\right)^2 \tag{4.9}$$

The thickness measurements need to be taken a couple of times during testing to ensure the proper estimation of the degradation level. The number of measurements will vary with time since the standard deviation is growing. For finding the number of the optimum measurements, three different confidence levels (90%, 95%, and 97.5%) and standard errors (5%, 10%, 15%) are investigated. The number of measurements as a function of the testing time with different values of decisive factors is presented in Figure 4.8. The example of a 5 mm plate is presented here.

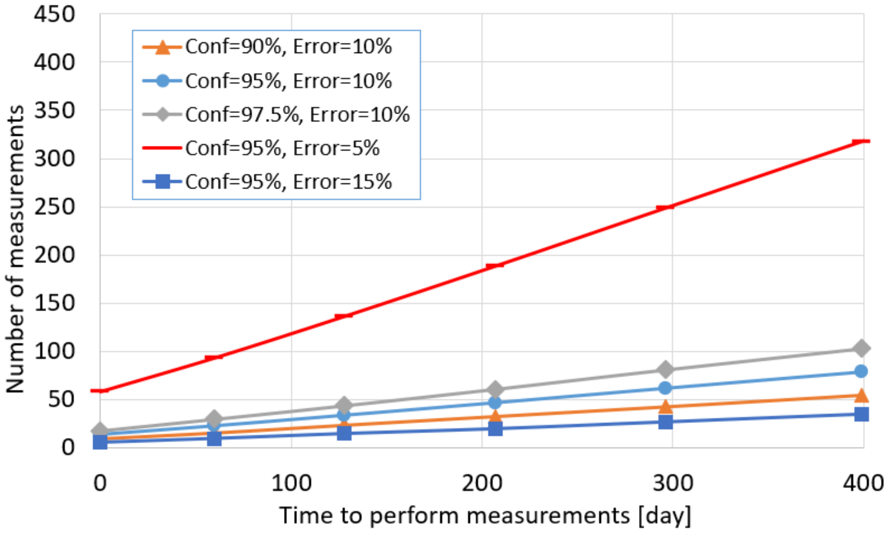

Figure 4.8. The number of measurements as a function of testing time.

One can notice that the relationship between the number of measurements and testing time is almost linear. The last day of measurements (a day 399) is related to obtaining the target value of corrosion degradation for a 5 mm plate thickness. Two additional plots are presented to see the influence of the decisive factors in the number of measurements. Figure 4.9 shows the influence of the assumed error in the number of measurements. Figure 4.10 presents the influence of the confidence level.

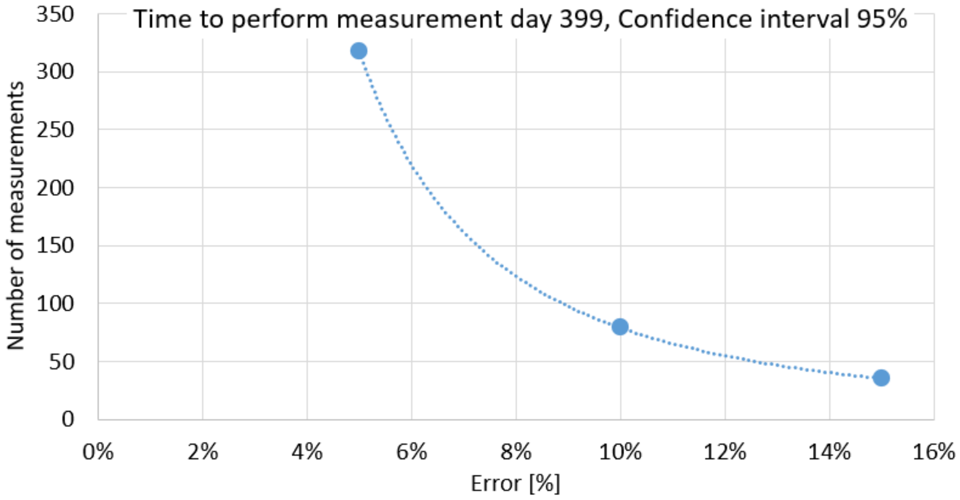

Figure 4.9. Measurements as a function of standard error.

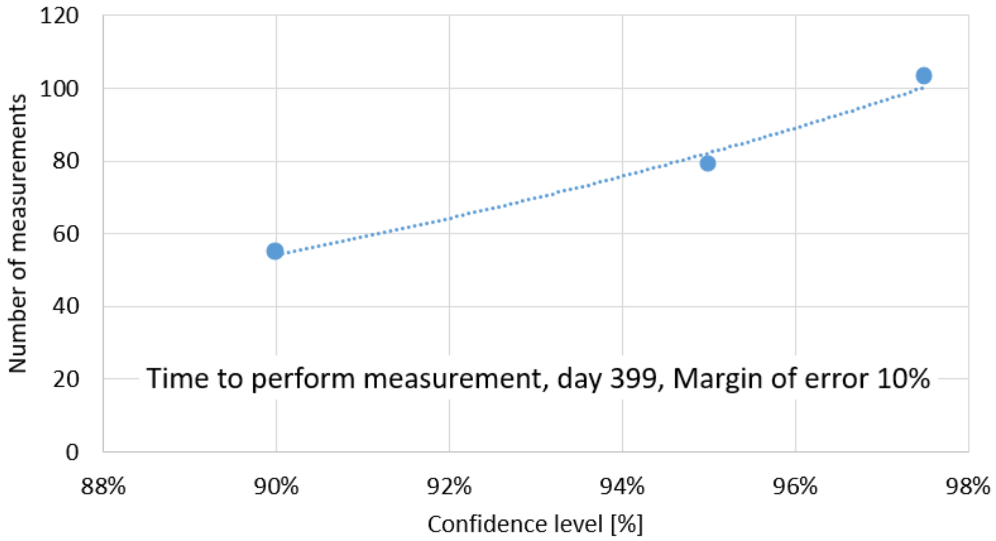

Figure 4.10. Several measurements as a function of confidence level.

As can be seen, both relationships are nonlinear. With the decrease of the standard error, the measuring effort significantly increases. In this case, the relationship is highly nonlinear. As for the confidence level, the measuring effort increase for higher values of this variable. However, the relationship is only slightly nonlinear.

Based on this analysis, a confidence level of 95% and an error value of 10% was chosen as an optimum value that will maximize the measurement precision with the possible minimum measuring effort. The measuring program with an estimated corrosion depth range is presented in Table 4.4. Similar measuring programs are designed for 6 mm and 8 mm specimens.

Table 4.4. Measuring program for 5 mm specimen.

Measurement time [days]	$\bar{d}$ [mm]	$\bar{d}-\Delta d$ [mm]	$\bar{d}+\Delta d$ [mm]	n [-]
0	0.00	0.00	0.00	14
60	0.20	0.18	0.22	23
128	0.40	0.36	0.44	34
207	0.61	0.55	0.68	47
296	0.83	0.75	0.91	62
399	1.05	0.94	1.15	79

After each measuring period, the corrosion depth needs to be recorded. Based on that information, the measuring program needs to be updated accordingly since the corrosion could be higher or lower from the assessed one.

The proposed testing set-up shows that the test could be performed without very specialized equipment, making the proposal economically efficient. Nevertheless, the corrosion rate can be significantly magnified (up to 10 times). The proposed methodology's main advantage is controlling only natural factors, avoiding the electric current usage, resulting in a corrosion mechanism similar to the real seawater conditions. The optimum number of measuring points for thickness measurements of specimens is derived using the simple statistical methodology.

4.3. Accelerated corrosion testing results

The current section provides the results of corrosion testing for both small-scale specimens as well as stiffened plates. The total duration of the corrosion test was equal to 428 days. During testing, some actions were carried out to fit with the planned duration of corrosion tests. As mentioned in the previous section, several possible ways of increasing corrosion rate were available.

The oxygen content measurements were carried out, showing that the approximated level of supersaturation has been lower than the assumed one and was closer to 200%. The quite effective way to speed up the process was the possible temperature increase. However, the glass-reinforced plastic could yield at a temperature above 40ºC. Thus, to speed up the corrosion process, it was decided to introduce a second circulation pump after approx. Two hundred ten days and third circulation pump after 300 days.

Considering the actual value of oxygen saturation at the beginning of testing, the estimated mean corrosion rate was equal to 0.537 mm/year, which was very close to the observed value. After introducing a second circulation pump, the estimated corrosion rate increased to 0.57 mm/year and furtherly with the next circulation pump up to 0.595 mm/year. However, the local flow of the water near the specimens was even faster than medium ones, and the application of two additional circulation pumps led to a higher increase of corrosion rates, as reported in Tables 4.5 and 4.6, for small-scale and large-scale specimens, respectively.

Considering the carried out actions, there will be a notable increase in the corrosion rates for small-scale and large-scale specimens during testing. Consequently, the corrosion depth versus time plots will be slightly different from those presented in Figure 4.7.

4.3.1. Small-scale specimens

In Table 4.5, the most important statistics related to corrosion characteristics of small-scale specimens are presented. As can be noticed, the corrosion rates of 5 mm specimens were subjected to relatively low scatter, whereas the corrosion rates of both 6 mm and 8 mm specimens were subjected to scatter significantly higher. Furtherly, the mean corrosion rates of 6 mm specimens were higher than the predicted value. However, the mean corrosion rate of 5 mm specimens was significantly lower. It can be noticed that the final degradation levels are slightly different from the assumed target levels, and there are originated from the mass deviation being a result of specimens chemical cleaning, which is discussed furtherly.

Table 4.5. Corrosion statistics of small-scale specimens.

Number	Mass [g]		Final DoD [%]	Elapsed days	Corrosion depth [mm]	Corrosion rate [mm/year]		
	Initial	Final				Specimen	Mean	St. Dev.
5.1	502	471	6.3	253	0.313	0.452	0.649	0.224
5.2	506	467	7.8	319	0.388	0.444		
5.3	510	408	20.1	368	1.004	0.996		
5.4	510	403	20.9	396	1.046	0.964		
5.5	510	492	3.5	180	0.175	0.355		
5.6	508	428	15.7	386	0.787	0.745		
5.7	506	455	10.2	328	0.508	0.565		
5.8	510	441	13.5	393	0.673	0.625		
5.9	508	417	17.9	396	0.893	0.824		
5.10	510	452	11.3	396	0.567	0.522		
6.1	622	571	8.2	267	0.494	0.675	1.009	0.288
6.2	628	560	10.8	267	0.649	0.887		
6.3	620	528	14.8	267	0.891	1.218		
6.4	624	525	15.9	286	0.953	1.216		
6.5	632	521	17.6	319	1.054	1.206		
6.6	624	502	19.5	362	1.170	1.180		
6.7	622	495	20.4	320	1.226	1.398		
6.8	620	539	13.1	267	0.786	1.074		
6.9	622	602	3.2	117	0.192	0.598		
6.10	622	581	6.6	229	0.398	0.635		
8.1	814	643	21.0	372	1.679	1.647	1.025	0.448
8.2	808	648	19.8	362	1.584	1.597		
8.3	820	673	17.9	372	1.430	1.403		
8.4	822	691	15.9	372	1.271	1.247		
8.5	820	706	13.9	377	1.108	1.073		
8.6	810	713	12.0	377	0.959	0.928		
8.7	820	754	8.0	356	0.639	0.655		
8.8	808	722	10.6	372	0.847	0.832		
8.9	820	773	5.7	328	0.455	0.506		
8.10	824	799	3.0	243	0.238	0.357		

In Figure 4.11, the corrosion depth versus time for all 5 mm specimens is presented. Notably, the relation of corrosion depth was slightly nonlinear, and at the beginning, the corrosion rate was lower than at the end of the corrosion process. The reasons for that could be several. Firstly, as was discussed, two additional circulation pumps have been added, increasing the corrosion rate. However, this will justify the other part of the curves. There is visible the period of approx. Forty days without any corrosion for most of the specimens. This could be related to the initial very thin layer of the black iron oxide, which comes from the rolling process and could act as an initial barrier from corrosion. In the case of 6 mm and 8 mm specimens, this layer has not been visible. Finally, it is visible from the graph that the deviation of corrosion rate has been relatively low at the major part of the corrosion process. However, after introducing additional circulation pumps, the deviation increased significantly with time.

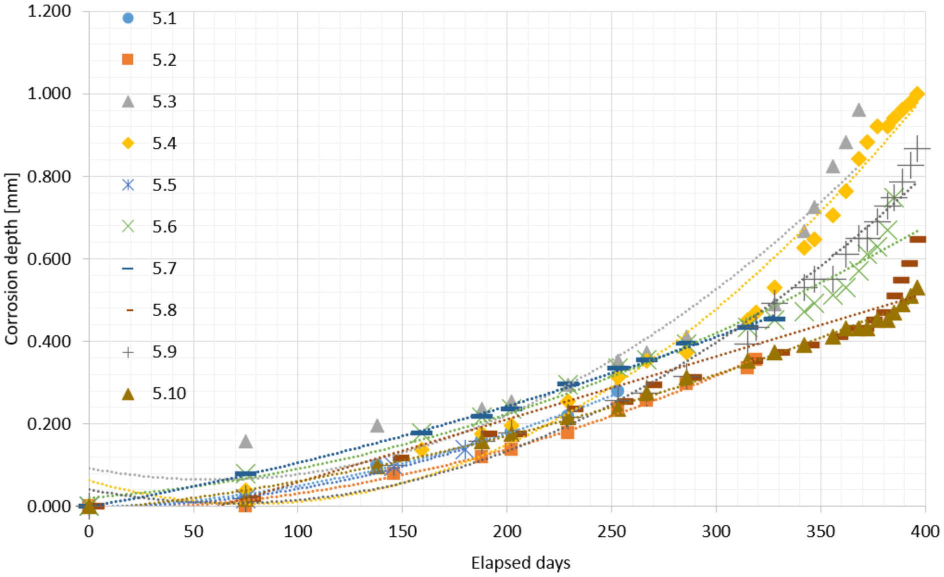

Figure 4.11. Corrosion diminutions of 5 mm specimens vs time.

The corrosion depth for 6 mm specimens is presented in Figure 4.12. In general, the corrosion depth follows the linear trend with the time increment; however, for some specimens, the rate increased after 200 days. From the beginning of the corrosion process, there was a significant deviation of the corrosion depth, which increased with time. In the case of 6 mm specimens, the corrosion diminution has been observed from the very beginning of the corrosion process.

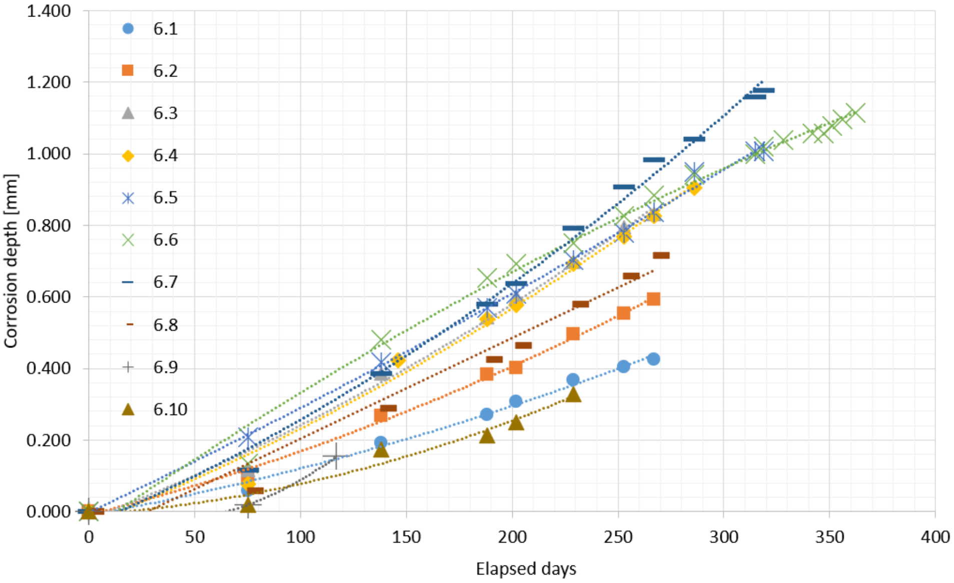

Figure 4.12. Corrosion diminutions of 6 mm specimens vs time.

The relation between corrosion depths of 8 mm specimens and testing time has been presented in Figure 4.13. Similarly to the 6 mm specimens, the corrosion has been active from the beginning of the process, and the relationships are very close to linear ones. However, after introducing the third circulation pump, there was a significant increment of the corrosion rate for many specimens. The corrosion rate has also been significantly scattered, which increased with degradation development. The standard deviation is significantly higher for 8 mm specimens than for both 5 mm and 6 mm specimens (see Table 4.5).

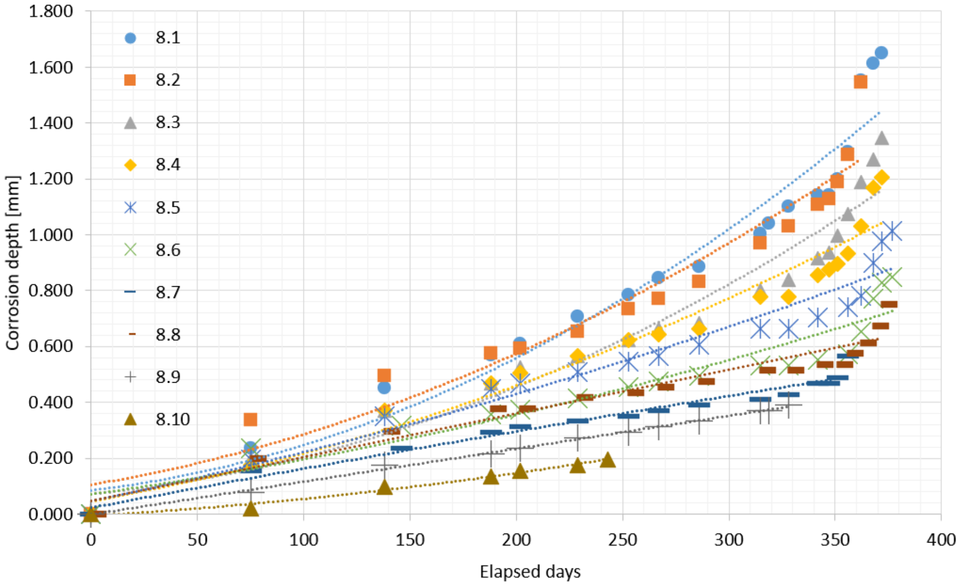

Figure 4.13. Corrosion diminutions of 8 mm specimens vs time.

4.3.2. Large-scale specimens

The corrosion statistics for large-scale specimens are presented in Table 4.6. It could be noticed that the mean corrosion rate of 5 mm and 6 mm specimens is very close to the initially predicted one. In 8 mm specimens, the mean corrosion rate was higher than the initially assessed one. It could be concluded that due to the introduction of two additional circulation pumps, the observed mean corrosion rate was close to the initially assessed one, although the oxygen content has been lower from assumed initially. Due to the cleaning of specimens from corrosion products and the specified priorly moments of mass measurements, the final degradation level deviates from the target one specified in Table 4.2.

Nevertheless, the deviation did not exceed the 0.5 % of degradation level. Finally, it could be noticed that the corrosion rates deviate between specimens. A similar level of approx. 30% of COV is observed for both 5 mm and 6 mm specimens. However, the deviation in the case of 8 mm specimens reaches a significant level of 50%.

Table 4.6. Corrosion statistics of large-scale specimens.

Thickness [mm]	Number	Mass [kg]		Final DoD [%]	Corr. depth [mm]	Elapsed days	Corrosion rate [mm/year]		
		Initial	Final				Specimen	Mean	St. Dev.
5	1.5	25.07	23.25	7.24	0.362	264	0.501	0.774	0.266
	2.5	25.04	19.77	21.05	1.053	372	1.033		
	4.5	25.00	21.60	13.60	0.680	315	0.788		
6	1.6	30.77	26.63	13.46	0.808	382	0.772	0.745	0.311
	3.6	30.72	24.46	20.37	1.222	428	1.042		
	4.6	30.79	28.74	6.67	0.400	347	0.421		
8	1.8	40.43	34.86	13.80	1.104	382	1.055	1.146	0.521
	2.8	40.48	37.72	6.84	0.547	295	0.677		
	3.8	40.55	31.49	22.34	1.787	382	1.707		

The propagation of corrosion degradation with time for all large-scale specimens is presented in Figure 4.14. In both 5 mm and 6 mm specimens, the observed development of corrosion degradation followed a nonlinear trend, and the corrosion rate increased significantly after installing additional circulating pumps. In the case of 8 mm specimens, the trend was rather a linear one. There has been significant scatter for 8 mm specimens, where the corrosion processes of 1.8 and 2.8 specimens were similar, and the 3.8 specimen occurred to corrode almost two times faster. In other thicknesses, the differences between specimens in terms of corrosion rate were not that radical.

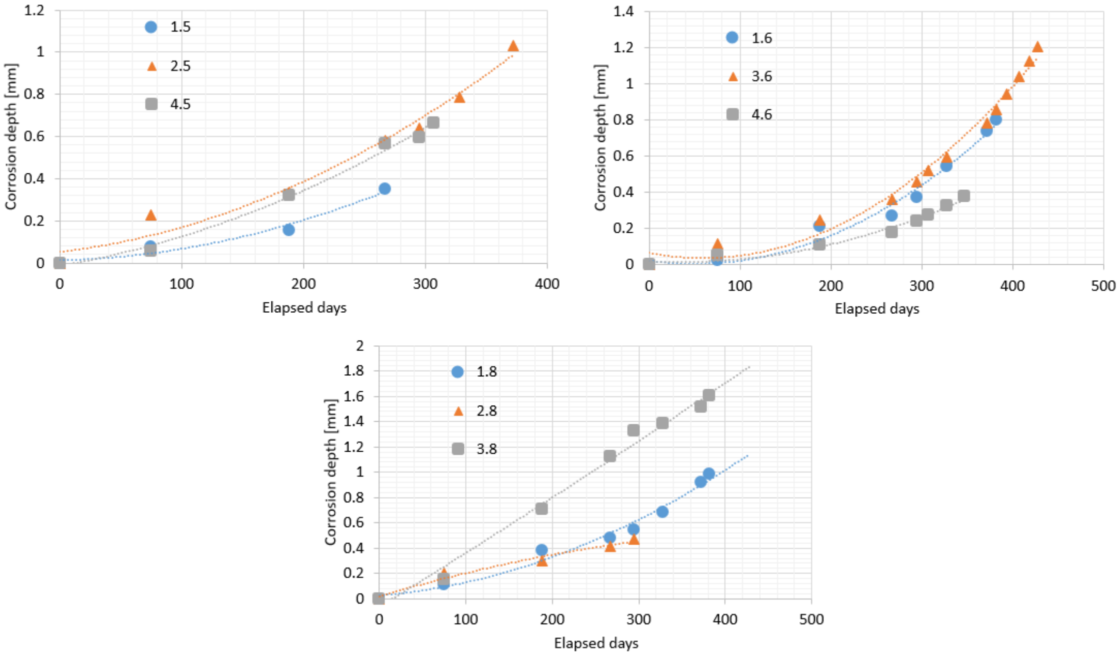

Figure 4.14. Corrosion diminutions of large-scale specimens vs time.

4.3.3. *Correlation between corrosion degradation of large-scale and small-scale specimens*

The primary reason to corrode the small-scale coupons was to investigate the changes in mechanical properties. However, this type of specimens is commonly used to estimate the corrosion rate of larger elements. The mass measurements of such elements are easier and faster. Thus, in the presented section, the correlation between corrosion rate and corrosion trends between large-scale and small-scale specimens is discussed, and the feasibility of this methodology is analysed.

The comparison between the corrosion rates of large-scale and small-scale specimens is presented in Table 4.7. It could be noticed that the mean corrosion rates of small-scale and large-scale specimens are different. The highest deviation is observed for 6 mm specimens where corrosion of coupons was almost 50% faster than stiffened plates. In both 5 mm and 8 mm thicknesses, the mean values of the corrosion rate of large-scale specimens were higher by 19% and 12%, respectively. It could be considered as rather similar values. The Coefficient of Variation is relatively similar for both scales. Thus, the lowest is observed for 5 mm and 6 mm specimens and the highest for 8 mm specimens.

Table 4.7. Statistical descriptors of the small-scale specimens.

Thickness [mm]	Corrosion rate [mm/year]					
	Large-scale specimens			Small-scale specimens		
	Mean	St. Dev.	COV [%]	Mean	St. Dev.	COV [%]
5	0.774	0.266	34.4	0.649	0.224	34.4
6	0.745	0.311	41.8	1.009	0.288	28.5
8	1.146	0.521	45.5	1.025	0.448	43.7

The estimation of the corrosion rate of larger components based on the corrosion of coupons has limited reliability, especially when considering 6 mm plates. One possible reason could be the non-homogeneity of the physical factors of the water in the tank. Although the temperature and salinity are rather constant, the water circulation and oxygen saturation could variate through the tank. One can notice that with the installation of two additional circulation pumps, the increase of corrosion rate was observed for almost all stiffened plates. Due to their large scale, there are not so sensitive to local variations of factors. However, in small-scale specimens, an increment of the corrosion rate was not captured for all of them. It is impossible to provide constant water velocity and oxygen saturation in the tank due to the localized sources of water inlet together with the pipe, where air bubbles are created. In the case of in-situ measurements, the homogeneity of conditions will be better, and the correlation between the corrosion rate of large-scale and small-scale specimens. Nevertheless, the deviations will be noted too.

The general conclusion is derived then, that in case of corrosion testing in laboratory conditions, where the tank is of limited dimensions, the corrosion rate of small-specimens will be not satisfying to estimate the corrosion rate of plates of a larger scale. Eventually, some re-designing of the set-up could provide more homogenous conditions concerning both oxygen saturation and water velocity.

4.4. Analysis of corroded specimens

4.4.1. Small-scale specimens

Corrosion products need to be removed to analyse the surfaces of corroded specimens. Thus, cleaning with the use of a chemical solution has been applied (see Figure 4.15). The solution consisted of hydrochloric acid, which provided a clean surface and corrosion inhibitor Tardiol D, which prevented further atmospheric corrosion of cleaned specimens. The final mass of the specimen has been measured after the corrosion process, revealing that the corrosion products could disturb the measurement of the degradation level up to 1.5 %.

Figure 4.15. The example of a specimen before (left) and after (right) cleaning.

Furtherly, after the cleaning process, the detailed microscopic measurements of corroded surfaces has been carried out. The microscope Keyence VHX-7000 used for that purpose can be seen in Figure 4.16.

Figure 4.16. Specimen during scanning.

The detailed 3D reproduction of the corroded surfaces has been obtained with the mesh size of 2 μm x 2 μm. An example of such a scanned corroded surface could be seen in Figure 4.17. It is noted that only the gauge length of the specimen has been scanned because this part is relevant during tensile testing, whereas mounting parts are not important. Additionally, the range of the possible area that could be captured via a microscope has been limited.

Figure 4.17. An example of a scan of the corroded surface (specimen 6.3).

The scans of corroded surfaces were furtherly transferred using Matlab software into the FE mesh (with regards to scanning mesh, the FE mesh is of the size of 0.5 mm x 0.5 mm), discussed in Section 8.5. The sample thickness map of corroded specimens is presented in Figure 4.18, where both top and bottom surfaces are presented. The rest of the thicknesses maps of specimens can be found in Appendix 1 of the Thesis.

Generally, it could be noticed that the specimens immersed in water bring different corrosion fields when compared to other corrosion types, such as atmospheric corrosion [236]. In this experiment, the regions of either low or large corrosion diminutions are rather widespread, purely demonstrating that no pitting corrosion is observed. However, even in such small specimens, the observed variances show that the general corrosion is also non-uniform. Nevertheless, by observing different specimens, one cannot establish one common pattern, which implies that nature is fully stochastic.

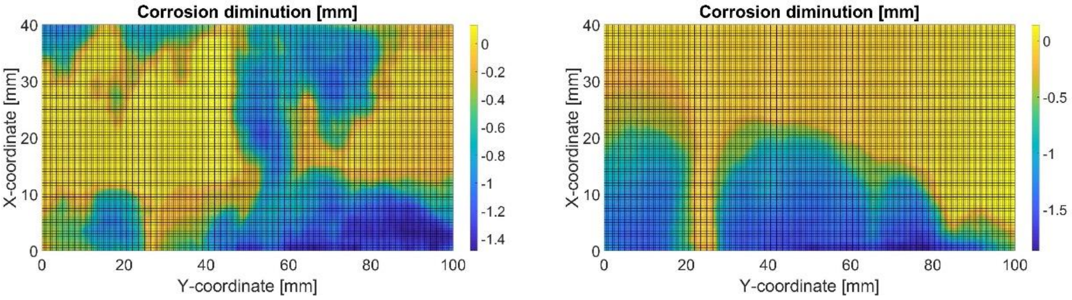

Figure 4.18. Corrosion diminutions of the top (left) and the bottom (right) surface of the 6.3 specimens.

The corrosion surface's statistical descriptors are obtained based on the information gathered from the scanning of the specimens, as presented in Table 4.8. The specimens are sorted with the ascending order of Degree of Degradation. It needs to be noted here that the DoDs reported there could be different from those presented in Table 4.5. In Table 4.5, the total mass loss of the entire specimen is used for DoD calculation. However, for strength analysis, only corrosion characteristics of the specimen without mounting parts are relevant. Thus, the calculated DoD, presented in Table 4.8, was based on the obtained corrosion characteristics from the 3D scans. The DoD from Table 4.8 will be used in all strength calculations presented in the other part of the Thesis. Nevertheless, in most cases, the differences in calculated DoDs are not exceeding 2%. Furtherly the following statistics are presented: maximum residual thickness

(t_{max}), maximum corrosion depth of upper surface ($d_{u,max}$), mean corrosion depth of upper surface ($d_{u,mean}$), a standard deviation of corrosion depth of upper surface ($d_{u,StDev}$), similar statistics related to the bottom surface ($d_{b,max}$, $d_{b,mean}$, $d_{b,StDev}$), minimum residual thickness (t_{min}) and minimum cross-sectional area (A_{min}).

Table 4.8. Statistical descriptors of the small-scale specimens.

No	DoD [%]	t_{max} [mm]	$d_{u,max}$ [mm]	$d_{u,mean}$ [mm]	$d_{u,StDev}$ [mm]	$d_{b,max}$ [mm]	$d_{b,mean}$ [mm]	$d_{b,StDev}$ [mm]	t_{min} [mm]	A_{min} [mm²]
5.5	3.2	5.00	0.741	0.087	0.177	0.587	0.072	0.085	3.82	191.5
5.6	5.9	5.00	1.597	0.207	0.184	1.038	0.089	0.211	3.11	180.9
5.2	7.4	4.98	1.530	0.321	0.516	0.345	0.051	0.047	3.21	174.3
5.1	8.0	5.00	1.264	0.230	0.342	0.664	0.170	0.117	3.24	179.0
5.7	13.1	4.94	1.629	0.170	0.358	1.857	0.484	0.540	1.76	157.6
5.9	15.4	5.00	2.508	0.538	0.839	1.233	0.231	0.242	1.40	156.9
5.8	15.4	5.00	2.269	0.588	0.814	0.798	0.182	0.103	2.39	162.4
5.4	15.5	5.00	2.017	0.444	0.622	0.983	0.331	0.231	2.26	147.8
5.10	16.0	4.99	1.996	0.757	0.730	0.470	0.042	0.033	2.92	164.2
5.3	24.3	5.00	2.016	0.884	0.680	1.661	0.332	0.308	2.20	116.6
6.9	2.2	6.00	0.46	0.047	0.106	0.423	0.084	0.068	5.22	231.1
6.10	6.3	6.00	1.04	0.302	0.294	0.339	0.078	0.080	4.64	214.1
6.1	6.8	6.00	1.32	0.338	0.376	0.176	0.069	0.018	4.75	211.5
6.2	9.6	6.00	1.49	0.555	0.509	0.262	0.018	0.038	4.38	189.6
6.4	12.3	6.00	1.46	0.630	0.421	1.302	0.107	0.303	3.42	183.6
6.3	14.1	6.00	1.61	0.397	0.438	1.900	0.447	0.529	2.69	178.6
6.8	14.7	6.00	1.70	0.517	0.421	1.864	0.366	0.380	2.66	187.6
6.5	16.6	6.00	0.75	0.018	0.060	1.938	0.975	0.595	4.06	172.4
6.6	17.6	6.00	2.21	1.025	0.606	0.938	0.029	0.101	3.33	177.6
6.7	21.3	5.95	2.17	0.333	0.330	2.032	0.947	0.385	2.31	174.4
8.10	1.7	8.00	0.602	0.083	0.191	0.288	0.051	0.079	7.26	300.8
8.9	4.0	8.00	0.262	0.060	0.045	0.940	0.262	0.237	6.93	287.6
8.4	12.3	8.00	2.713	0.774	0.691	3.080	0.208	0.359	2.51	234.3
8.6	13.8	7.86	1.498	0.275	0.240	1.966	0.827	0.598	4.99	239.8
8.7	14.1	8.00	1.574	1.058	0.453	0.512	0.071	0.051	6.03	260.8
8.2	14.8	8.00	2.832	0.935	0.773	1.144	0.248	0.116	4.56	238.1
8.5	15.6	8.00	1.996	0.461	0.597	1.931	0.785	0.469	4.33	234.1
8.8	16.9	7.81	1.107	0.249	0.126	1.909	1.100	0.681	5.51	249.0
8.3	18.4	8.00	1.752	0.148	0.214	2.814	1.324	0.741	4.40	215.2
8.1	28.4	7.79	2.750	0.913	0.627	3.073	1.362	0.709	3.03	188.3

It could be noticed that with the increase of corrosion degradation, the maximum and mean values of the corrosion depth are increasing. The ratio between maximum and mean corrosion depth for all corrosion fields ranges between 1.49 up to 41.8, with the mean value equal to 6.29. This generally shows that locally specimens are much strongly corroded when compared to the mean corrosion diminution. There was no found any correlation between this value and degradation level.

The standard deviation increases as well with the corrosion development. When analysing the ratio between standard deviation and the mean value of corrosion depth, which informs about the particular corrosion field's irregularity, the value deviates between 0.26 up to 3.48. The mean value of this ratio is equal to 1.16. The lowest mean value was obtained for 8 mm specimens, which was below 1. In both 5 mm and 6 mm specimens, these values were higher, showing that corrosion was more irregular for those specimens. No correlation between that ratio and corrosion degradation level was found.

Although both surfaces were equally subjected to the corrosion process, the mean corrosion depth is significantly higher for one of the surfaces in almost most cases. Only a few specimens were similarly corroded on both sides (5.1, 5.4, 5.5, 6.3). However, for most of the specimens, the mean corrosion depth of one side was approximately three times smaller compared to another side.

The interesting fact is that the maximum residual thickness was equal to the initial thickness of the specimen for almost all of the specimens. Although the corrosion was general, there were places untouched by the degradation process.

It is noted that both minimum cross-sectional area and minimum residual thickness are decreasing with the corrosion development. There are observed extreme values for some specimens regarding initial thickness in minimum thickness (5.7, 5.9, 6.3, 6.7, 6.8, 8.1, 8.4). The minimum thickness is below half of the initial thickness for those specimens, which shows strong irregularity of the observed corrosion fields. In the case of minimum cross-sectional area, it is observed that for all specimens, that value is lower when compared to the cross-sectional area resulting from mean corrosion depth. For all specimens, the mean difference between the minimum cross-sectional area and one that resulted from uniform loss is equal to 10.5 %, where 1.1 % and 29.8 % are extreme differences. It is noted that with the increase of the degradation level, this difference is increasing too. Additionally, there are observed higher differences with the increase of initial specimen thickness.

4.4.2. Large-scale specimens

In the case of large-scale specimens, detailed microscopic measurements were not possible. Thus, only general thickness distribution has been captured via ultrasonic measurements. The corrosion products have been removed manually to avoid the destruction of corroded surfaces. After some time of the specimens drying, the corrosion products started to detach from the surface, and only additional manual removing was sufficient to provide a clear surface and perform the ultrasonic measurements. Similarly to the small-scale specimens, the final mass was captured without corrosion products, and the degradation level was up to 2%

smaller compared to non-cleaned specimens – some examples of corroded stiffened plates after presented in Figure 4.19.

Figure 4.19. Corroded stiffened plates examples - 2.5 (left), 4.6 (mid) and 3.8 (right).

Seventy-eight points in a plate and 24 points in the stiffener has been measured from both sides to measure the thickness distribution accurately. Thus, the 208 measurement points for each stiffened plate were captured, taking into account the regular distance between grid points. One can notice that this is above the number indicated in Table 4.4. However, even for not severely corroded plates, accurate information about thickness distribution and the possible application of thickness distribution into the numerical model.

In Table 4.9, the statistics concerning the gathered information from ultrasonic measurements are presented. It was identified that local non-uniformity of the surface of the corroded specimen could lead to significant overestimation of the thickness in a particular point. In general, the highest local irregularities were observed for 8 mm specimens. For most strongly corroded 3.8 specimen, this difference reaches the level of 0.5 mm, which is way above the acceptable error of ultrasonic equipment itself (0.1 mm). In the case of 5 mm specimens, there were relatively flat regions of the plate that made possible accurate measurements. In that case, the differences between mass measurements and ultrasonic ones were within the acceptable level of error. When one considers the mean thickness value from both sides of the plate, it is higher for all of the specimens when compared with accurate mass measurements. The closest results are obtained for a minimum value of thickness from two sides of the plate, and those are taken into account in further analysis. In this view, in real ships, the measurements are carried out usually only on one side of the plate; thus, significant overestimations could be obtained.

Additionally, in situ measurements, the lower number of thickness points is collected, which could be another source of uncertainty.

Table 4.9. Statistics of ultrasonic measurements.

Specimen	Residual thickness [mm]				
	Mean - mass	Mean – 1st side	Mean – 2nd side	Mean from 2 sides	Minimum from 2 sides
1.5	4.638	4.735	4.682	4.709	4.633
2.5	3.948	4.051	4.121	4.086	3.891
4.5	4.320	4.410	4.318	4.364	4.248
1.6	5.192	5.428	5.355	5.391	5.220
3.6	4.778	5.081	5.034	5.057	4.894
4.6	5.600	5.865	5.753	5.809	5.668
1.8	6.896	7.301	7.312	7.306	7.135
2.8	7.453	7.557	7.633	7.595	7.522
3.8	6.213	6.719	6.691	6.705	6.501

The thickness distribution maps have been obtained based on the measurements, with the interpolated values between the grid's points. It is noted that the distribution is nonuniform for all of the specimens.

The distributions for stiffened plates of initial 5 mm thickness are presented in Figures 4.20-4.22. The distribution for a 1.5 mm stiffened plate, which corresponds to 7% of DoD, is presented in Figure 4.20. In this case, the higher corrosion diminutions are observed on the right side of the plate, and the lower thickness is in the bottom part of the stiffener. In Figure 4.21, the residual thickness for a 4.5 mm stiffened plate is presented. In general, the lowest thickness is observed near the stiffener in the welding zone, and the stiffener itself significantly deteriorates. The thickness distribution for a plate with a 21% degradation level (2.5) is presented in Figure 4.22. It is noted that similarly to the previous specimen, the high corrosion depths are observed near the welding zone of the specimen. Additionally, the right side of the plate is strongly corroded in comparison to the left one. The stiffener itself is quite uniformly corroded.

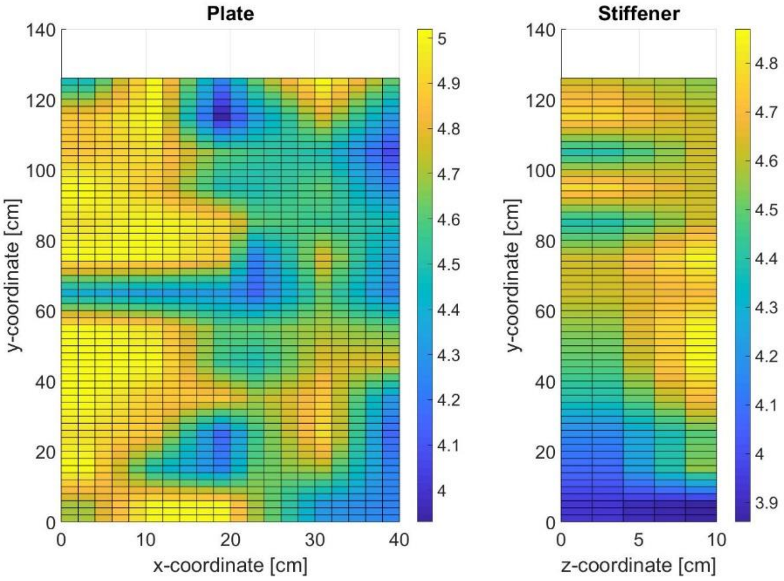

Figure 4.20. Thickness distribution in 1.5 specimen (7% of DoD) [mm].

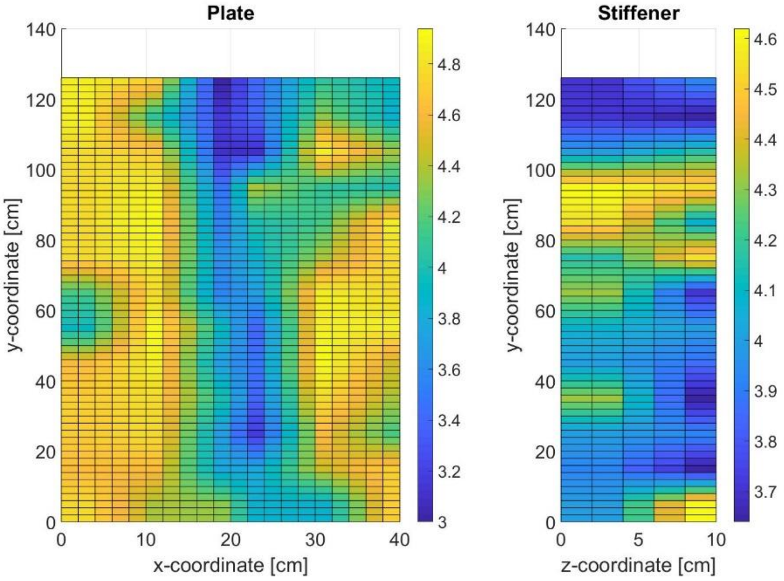

Figure 4.21. Thickness distribution in 4.5 specimen (14% of DoD).

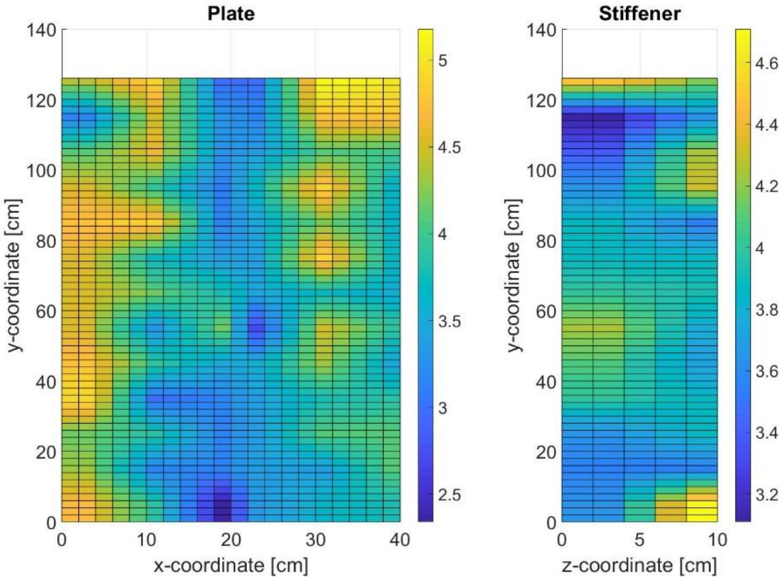

Figure 4.22. Thickness distribution in 2.5 specimen (21% of DoD).

The distributions for plates with an initial thickness of 6mm are presented in Figures 4.23-4.25. It is noted that the thickness distributions for plates with 7% and 14% of DoD (Figures 4.23 and 4.24, respectively) are quite similar. The highest corrosion diminutions are concentrated near the welding region and some places on the plate edges. In the case of stiffeners, in the 4.6 specimen (Figure 4.23), the middle part is rather non-corroded, opposite to upper and lower regions. In specimen 1.6 (Figure 4.24), the stiffener is corroded mostly near the welding, and higher corrosion depths are observed near the free edge. In the 3.6 specimen (see Figure 4.25), extensive corrosion for both plate and the stiffener is observed near the welding zone and upper part of the specimen.

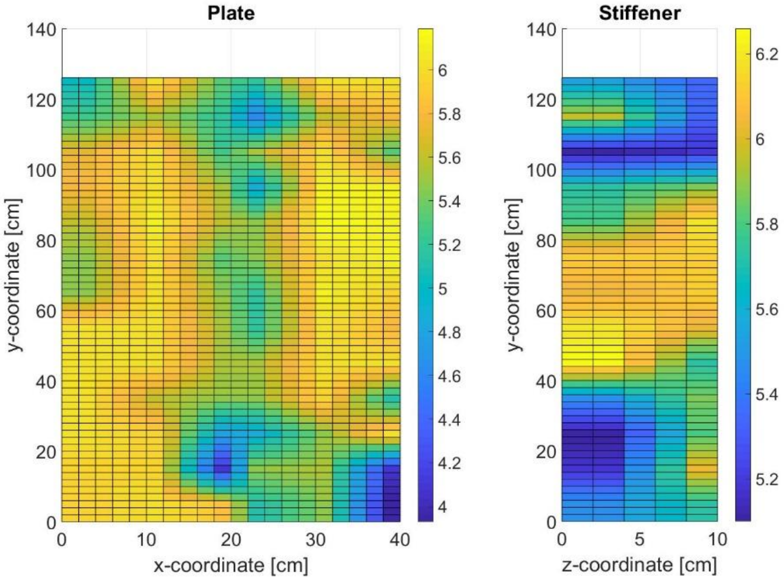

Figure 4.23. Thickness distribution in 4.6 specimen (7% of DoD).

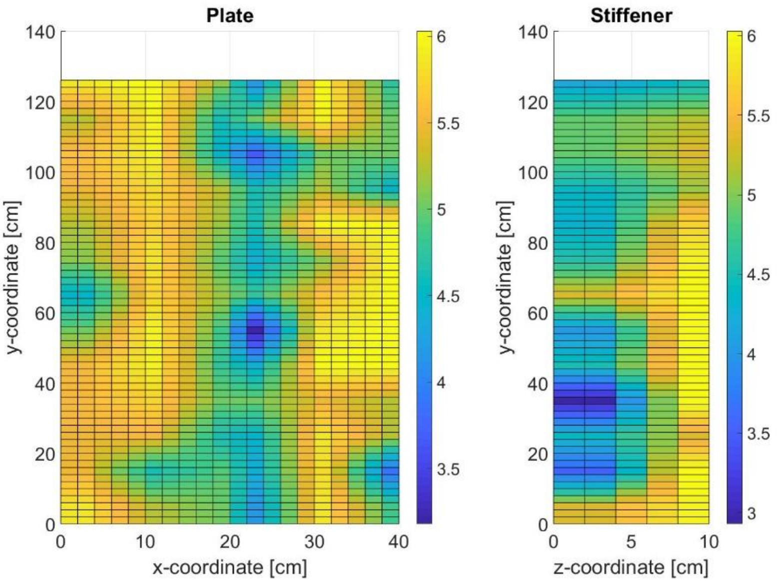

Figure 4.24. Thickness distribution in 1.6 specimen (14% of DoD).

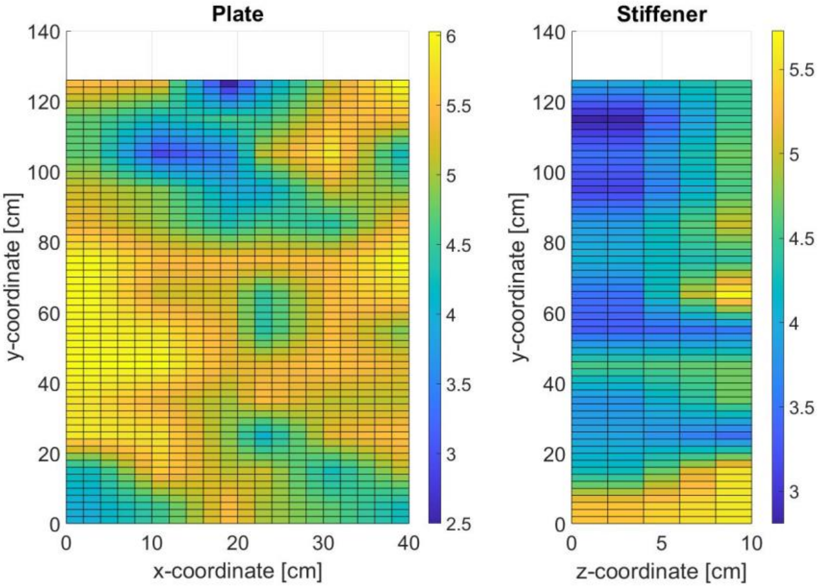

Figure 4.25. Thickness distribution in 3.6 specimen (21% of DoD).

The thickness distributions for initially 8 mm stiffened plates are presented in Figures 4.26 - 4.28. The distribution of thickness for 2.8 specimen is presented in Figure 4.26. It is noted that the higher corrosion diminutions for both plates and the stiffener are near the bottom and top of the specimen. In the specimen with 14% of degradation level (see Figure 4.27), the high corrosion diminutions are observed near the plate's welding zone and right side. High corrosion depths are observed in the lower part of the stiffener, which is quite uniformly corroded. In the most strongly corroded specimen (see Figure 4.28), the severely corroded regions in the plate are the bottom, top and left side. In the case of the stiffener, there is a quite irregular field; however, near the bottom are the highest corrosion deteriorations observed.

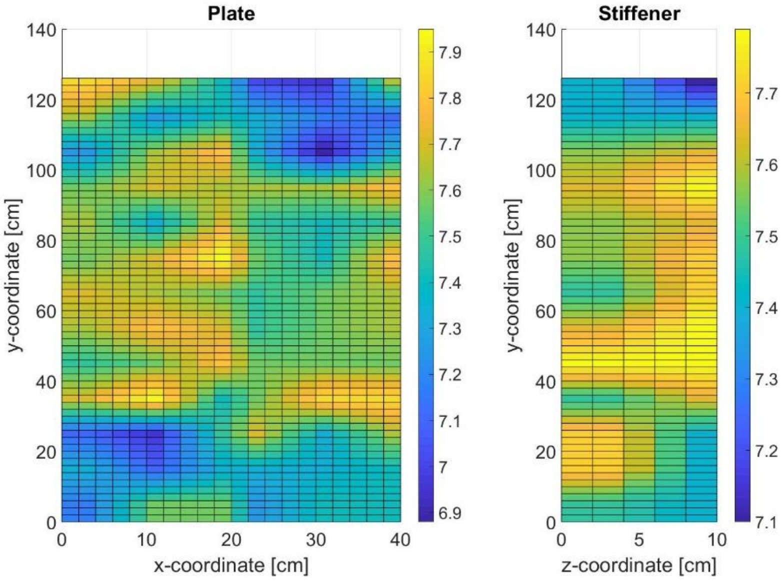

Figure 4.26. Thickness distribution in 2.8 specimen (7% of DoD).

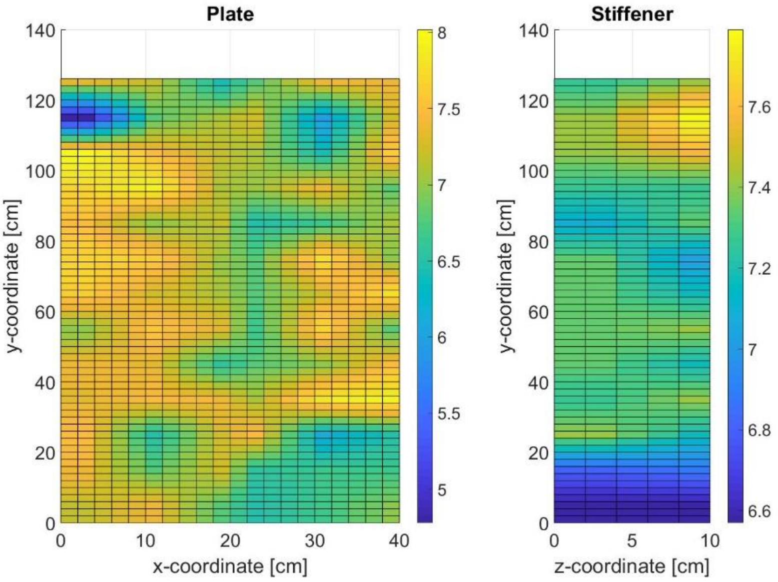

Figure 4.27. Thickness distribution in 1.8 specimen (14% of DoD).

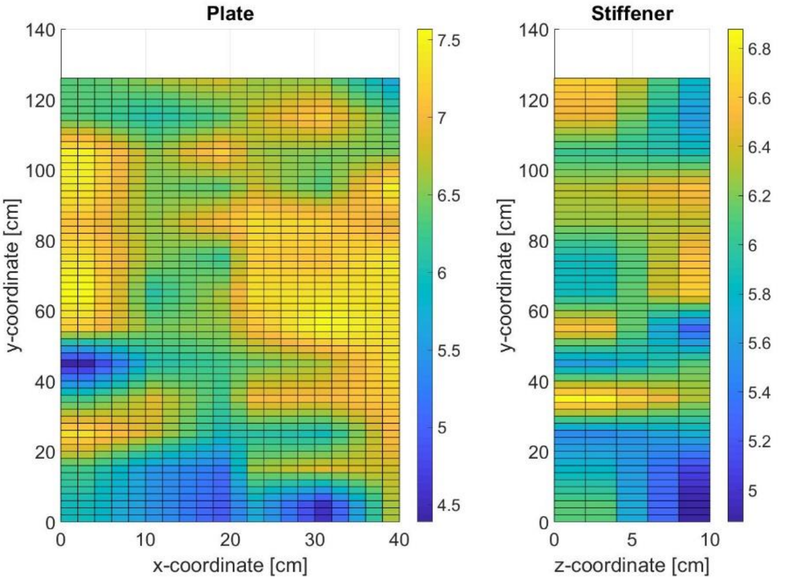

Figure 4.28. Thickness distribution in 3.8 specimen (21% of DoD).

In comparison to small-scale specimens, in this case, one can capture some corrosion patterns common to most of the specimens. In general, the zone which was subjected to the highest corrosion depths was the welding region. Additionally, in many specimens, both the plate and the stiffener's free edges were strongly corroded.

The statistics of the thickness for both plate and the stiffener are presented in Table 4.10. The mean corrosion depths for both plate and the stiffener are close to each other; for most of the specimens, the difference is not higher than 5% of the initial thickness. The standard deviation of thickness in the plate is higher for almost all cases (the exception is specimen 1.6) compared to the stiffener, which is an understandable observation since it has a much higher area than the stiffener.

Table 4.10. Statistics of the thickness of large-scale specimens.

Plate number	Mean thickness [mm]			Standard Deviation [mm]		
	Plate	Stiffener	Total	Plate	Stiffener	Total
1.5	4.66	4.54	4.63	0.295	0.269	0.292
2.5	3.90	3.86	3.89	0.628	0.350	0.570
4.5	4.29	4.07	4.25	0.568	0.317	0.521
1.6	5.27	5.02	5.22	0.639	0.855	0.700
3.6	5.06	4.25	4.89	0.720	0.787	0.807
4.6	5.65	5.75	5.67	0.496	0.369	0.469
1.8	7.11	7.24	7.14	0.516	0.278	0.470
2.8	7.51	7.58	7.52	0.234	0.167	0.220
3.8	6.62	6.04	6.50	0.671	0.520	0.682

The standard deviation increases with the increment of corrosion depth, consistent with the previously assumed model (Equation 4.7). The comparison between the assumed model and obtained experimental values is presented in Figure 4.29. It needs to be noted that in this case, standard deviation from Eq. 4.7 is presented concerning the corrosion depth and not a time; thus, the relationship is linear instead of logarithmic.

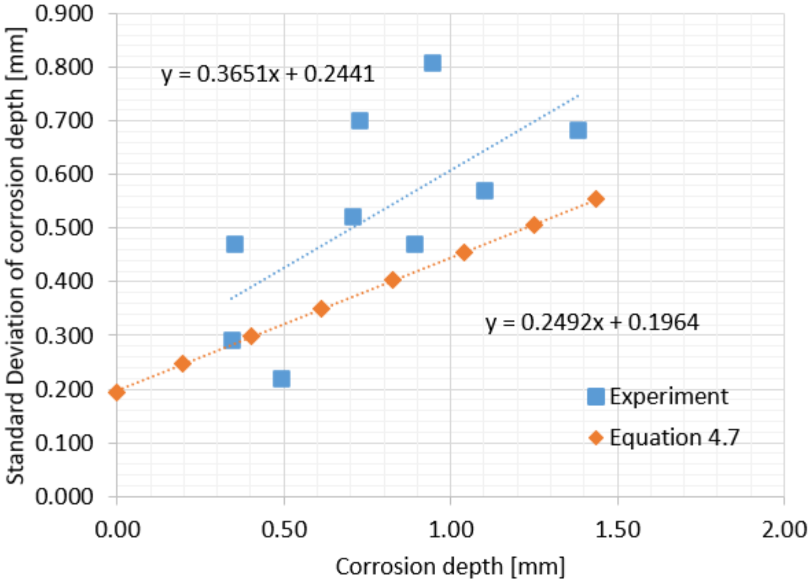

Figure 4.29. The standard deviation of corrosion depth vs corrosion depth – comparison between model and measurements.

It is noted that the standard deviation obtained from measurements is higher in comparison to the assumed one. This could result from more detailed measurements performed in this thesis, whereas the model is based on the in situ measurements performed in real operating ships. In the latter case, not so many measuring points are captured. Nevertheless, the inclination of both curves is very similar, and there can be used for the estimation of standard deviation with corrosion development.

5. INITIAL NUMERICAL INVESTIGATIONS, UNCERTAINTY ASSESSMENT [P2]

Priorly to the experimental and numerical analysis of the ultimate strength of corroded structural elements, the governing parameters need to be determined. For investigating that, the initial numerical investigations of corroded stiffened plates are carried out.

Uncertainties are involved in the structural analysis due to the environment randomness, geometric and material properties variations and the inaccuracies in the loads and strength predictions [237]. Uncertainties can be classified into four main groups [238]: inherent uncertainties, measurement uncertainties, statistical uncertainties, and model uncertainties.

Inherent uncertainties are caused by the uncertainty of nature, like wind and wave loadings [239]. There cannot be reduced by obtaining more information.

Measurement and statistical uncertainties are caused by the imperfection of instruments and limited data for specific quantities (e.g. material uncertainty, fabrication uncertainty, degradation uncertainty, geometry, and structural uncertainty). There can be reduced by obtaining more information.

Model uncertainties are due to idealizations made in physical formulations for load and structural strength. The development of model uncertainty was initiated by Ang and Cornell [240], where they proposed the model of random variable X as the actual value of some quantity equals to $X = BX_p$. The X_p is value predicted by mathematical model and B is the model uncertainty, which is the random variable and can be determined with the comparison of the model predictions with experimental results. Furtherly, the concept of the model uncertainty was extended by Ditlevsen [241].

The uncertainty analysis of an intact stiffened panel was performed by Garbatov et al. [242]. The results show that inaccuracies of material properties predictions significantly influence the load-carrying capacity of the stiffened panel. An advanced uncertainty analysis was performed by Teixeira et al. [183], where an approach to assessing the ultimate strength of plates with random initial distortions, material and geometrical properties, and random corrosion degradation was presented.

The present chapter investigates the influence of corrosion degradation and different maintenance actions on the uncertainties in the ultimate strength estimate of stiffened plates, which was not previously studied. Additionally, a simple model uncertainty formulation related to FEM modelling is developed based on the work presented in [190].

The uncertainties investigated in this chapter are material uncertainties (i.e. yield stress, ultimate tensile stress, and Young modulus), geometry and structural uncertainties (such as thickness, which is also related to corrosion degradation uncertainty for the corroded plates), and fabrication uncertainties (initial imperfections). These uncertainties can be classified as measurement and statistical uncertainties, which reveal that obtaining more information about them can reduce the uncertainty of the ultimate strength estimates.

5.1. Finite element and corrosion modelling

The study is performed using the Stochastic Finite Element Method [243], where the random variables are generated using random sampling techniques. The response defined by the Ultimate Strength is investigated with the use of a proper statistical methodology.

5.1.1. Mechanical properties

Mechanical properties are estimated based on the experimental tests, where the small-scale specimens are subjected to different maintenance actions as reported in [244] and [169], where the total number of 74 specimens has been tested.

The ultimate strength of corroded stiffened plates is analysed under four different conditions: intact one, uncleaned corroded, corroded - sandblasted and corroded - sandpaper cleaned.

The analysed stiffened plates are 1000 mm long and 400 mm wide with a height of the stiffener of 100 mm. The as-build initial thickness is taken equal to 4.5 mm.

For each condition, besides the intact one, two Degrees of Degradation, DoD are analysed: 20% and 40%. The corrosion degradation is considered uniformly distributed with mechanical properties as a function of DoD. For each level of the DoD and cleaning method, the mechanical properties are different.

The statistical descriptors of mechanical properties are based on the regression curves estimated from experimental results. The standard deviation of each parameter is determined as a standard error of the estimate from the regression curve. However, the thickness variation is based on the thickness measurements performed before the experiment. The statistical descriptors of the mechanical properties and thickness for each case are presented in Table 5.1.

Table 5.1. Statistical descriptors of mechanical properties.

	Yield Stress [MPa]		Ultimate Stress [MPa]		Young Modulus [GPa]		Thickness [mm]	
Case	Mean value	Standard Deviation	Mean value	Standard Deviation	Mean value	Standard Deviation	Mean value	Standard Deviation
Intact	235.0	7.11	656.2	52.7	196.0	23.05	4.5	0.062
Corroded (DoD = 20%)	236.9	7.11	592.1	43.4	175.3	23.05	3.6	0.077
Corroded (DoD = 40%)	220.6	7.11	516.6	36.9	154.6	23.05	2.7	0.090
Sandblasted corroded (DoD = 20%)	237.6	10.62	613.6	26.7	189.6	17.67	3.6	0.062
Sandblasted corroded (DoD = 40%)	231.2	10.62	560.9	24.0	183.2	17.67	2.7	0.076
Sandpaper cleaned	261.0	3.97	632.7	40.2	168.2	12.25	3.6	0.106

corroded (DoD = 20%)								
Sandpaper cleaned corroded (DoD = 40%)	266.6	3.97	621.9	36.9	140.4	12.25	2.7	0.133

5.1.2. Initial imperfections modelling

The initial imperfections of the stiffened plate are modelled as suggested by Smith et al. [93] as a function of the slenderness ratio β (Eq. 3.2) with the consideration of three levels as presented in Eq. 3.3. Additionally, the maximal longitudinal imperfection, c_0/l is defined as:

$$\frac{c_0}{l} = \begin{cases} 0.00025\, l, & for\ slight\ level \\ 0.0012\, l, & for\ average\ level \\ 0.0038\, l, & for\ severe\ level \end{cases} \tag{5.1}$$

The longitudinal and plate initial imperfections are correlated, i.e. when the longitudinal imperfections have a slight level, plate imperfections have also a slight level.

The initial imperfections are modelled as the Log-normally distributed, where the slight level corresponds to a lower confidence level, medium to a mean value, and the severe one corresponds to the upper confidence level. Since the initial imperfections are created during the fabrication process, there are estimated for the same plate slenderness ratio for all cases (i.e. the initial thickness and mechanical properties). It is assumed that there are not changing during degradation and cleaning processes.

However, depending on any particular case, the initial imperfection may be positive or negative (see Figure 5.1). Additionally, a uniform probability mass function of the initial imperfection sign is considered (0.5 probability for positive imperfections (+1) occurrence and 0.5 probability for negative imperfections (-1) occurrence).

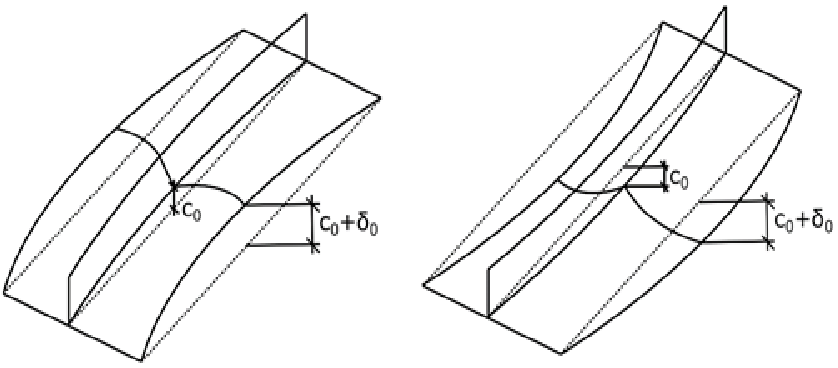

Figure 5.1. Positive (left) and negative (right) initial imperfections.

5.1.3. Finite Element Modelling

The commercial software Ansys [245] is used to generate finite element models. The nonlinear static solver employing the Arc-length method is used to obtain the load-carrying capacity of any particular studied case. The eight-node SHELL181 elements are used to model both plate and stiffener.

There are two types of nonlinearities considered here: material nonlinearity (material is considered a bilinear one) and geometric nonlinearity (large deformations).

The boundary conditions are modelled as fixed ones on the shorter edges (it is assumed that the transverse girders are stiff enough to create fixed boundary conditions) and free on the longer edges (see Figure 5.2).

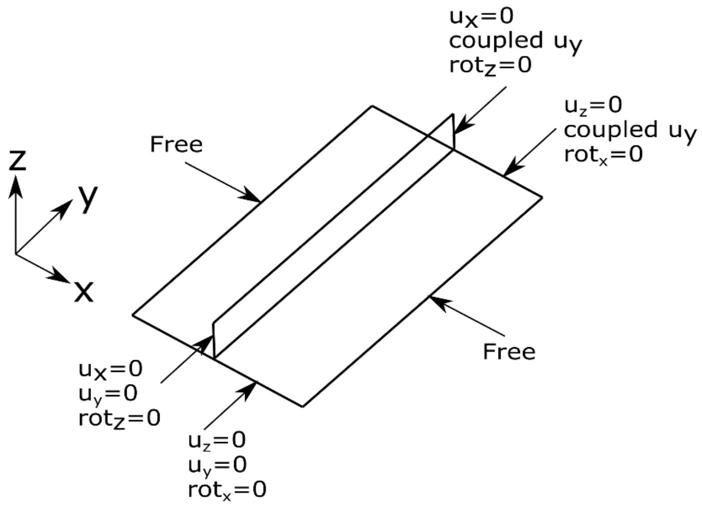

Figure 5.2. Applied boundary conditions.

The stiffened plates are subjected to a compressive load to obtain the force-displacement curve of each case and resulting in the ultimate strength. The initial imperfections are implemented by changing the z-coordinate of each finite element node.

The mesh density convergence study has been performed (Figure 5.3). As it can be noticed, when the mesh density is very fine, the ultimate force is converging to the accurate value. Finally, the element size of 0.02 m is chosen due to the convergence problem with the smaller size of finite elements leading to about 0.8 % difference from the predicted accurate value.

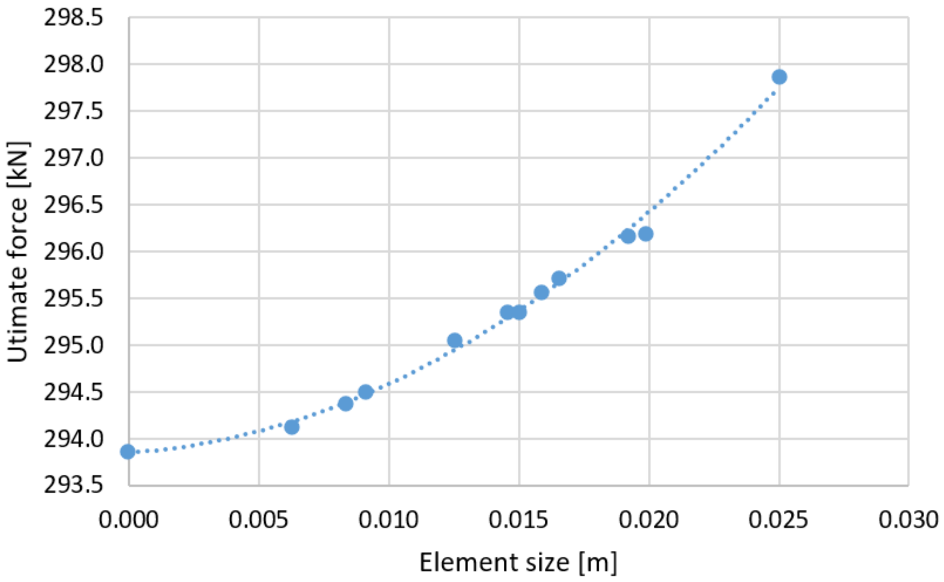

Figure 5.3. Mesh convergence study.

The corrosion wastage is modelled as uniform corrosion degradation based on the DoD level with subsequently mechanical properties change (as presented in Table 5.1). The force-displacement curves for maximum, minimum, and medium ultimate strength for an intact case are presented in Figure 5.4.

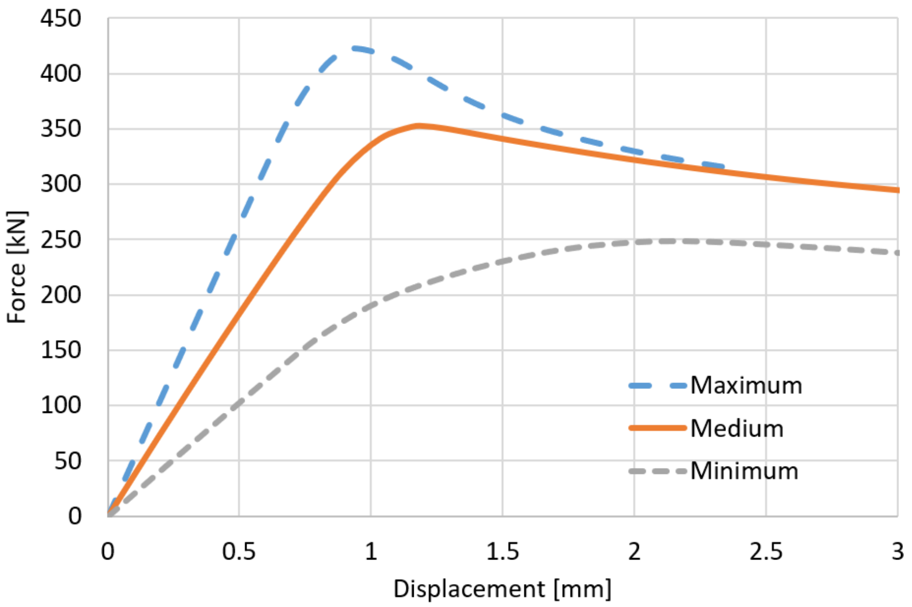

Figure 5.4. Force-displacement curves in an intact case.

5.1.4. Monte Carlo simulations

The Monte Carlo method is used [246] to generate random samples due to the complexity and non-linearity in the ultimate strength estimation. However, with the classic Monte Carlo (MC) method, the number of samples to produce the proper PDF function of each variable is relatively high. Due to that reason, the development of the classical MC method, i.e. Latin Hypercube Sampling [247], is used. For each case, the 1000 sets of random variables are produced, leading to a robust analysis. The resulting ultimate capacity is the random variable as a function of several random input variables (i.e. mechanical properties, thickness, and initial imperfections):

$$\widetilde{\sigma_U} = f\left(\widetilde{Re}, \tilde{E}, \widetilde{Rm}, \tilde{t}, \widetilde{\delta_0}, \widetilde{c_0}\right) \tag{5.4}$$

5.1.5. *Results and discussion*

The means of the ultimate strength as a function of different particular input parameters may be compared to analyse the influence of each particular input parameter on the ultimate strength. The analysis is presented for the intact case. However, for the corroded cases, the results of sensitivity analysis are very similar. The mechanical properties and initial imperfections are ranked into six levels as follows:

$$\begin{gathered} Mean\ +\ i \cdot StDev < \ c \leq \ Mean\ + \\ +\,(i+1)StDev\ , i \in [-3;\ 2] \end{gathered} \tag{5.5}$$

For analysing the importance of any particular input parameter, the null-hypothesis concerning the difference between the pair of means is considered here $H_0\colon \tau_1 = \tau_2;\ \tau_2 = \tau_3; etc.$ When there is no significant difference between any particular pair of means, the null hypothesis is accepted; otherwise, it is rejected. For hypothesis testing, the Fisher LSD test is used with a 95% confidence level. The results of the analysis are presented in Figures 5.5 – 5.9.

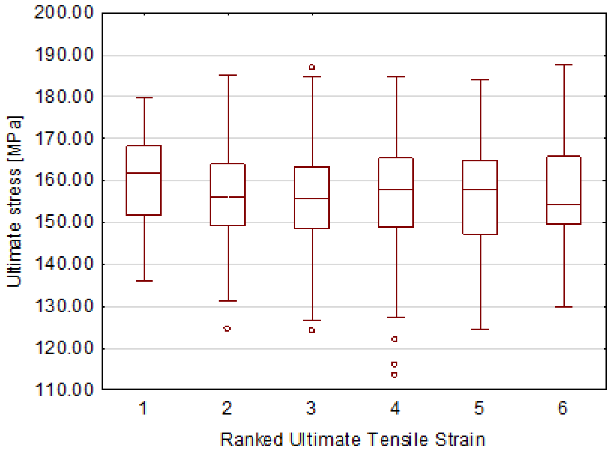

	1	2	3	4	5	6
1	**A**	**A**	**A**	**A**	**A**	**A**
2	**A**	**A**	**A**	**A**	**A**	**A**
3	**A**	**A**	**A**	**A**	**A**	**A**
4	**A**	**A**	**A**	**A**	**A**	**A**
5	**A**	**A**	**A**	**A**	**A**	**A**
6	**A**	**A**	**A**	**A**	**A**	**A**

Figure 5.5. Box plot of null hypothesis acceptance/rejection of Ultimate tensile stress.

As can be noticed, except for the ultimate tensile stress, the uncertainties induced by different parameters influence the resulting ultimate stress. It may be concluded that the ultimate tensile stress may be treated as a deterministic value in future analysis. With the increase of other mechanical properties (Yield Stress and Young Modulus), the ultimate stress is also increasing.

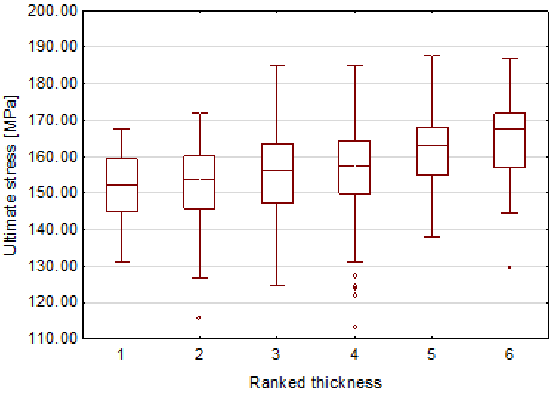

	1	2	3	4	5	6
1	A	A	R	R	R	R
2	A	A	R	R	R	R
3	R	R	A	A	R	R
4	R	R	A	A	R	R
5	R	R	R	R	A	A
6	R	R	R	R	A	A

Figure 5.6. Box plot of null hypothesis acceptance/rejection of thickness.

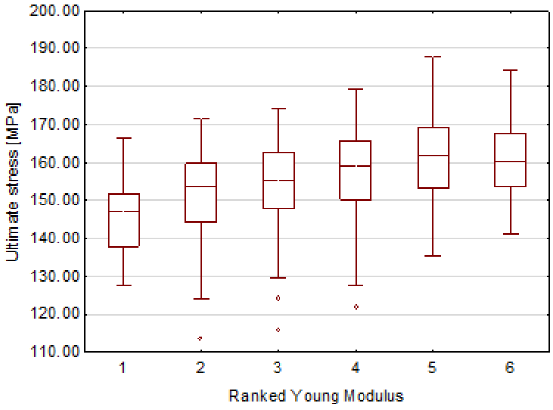

	1	2	3	4	5	6
1	A	A	R	R	R	R
2	A	A	R	R	R	R
3	R	R	A	R	R	R
4	R	R	R	A	R	A
5	R	R	R	R	A	A
6	R	R	R	A	A	A

Figure 5.7. Box plot of null hypothesis acceptance/rejection of Young Modulus.

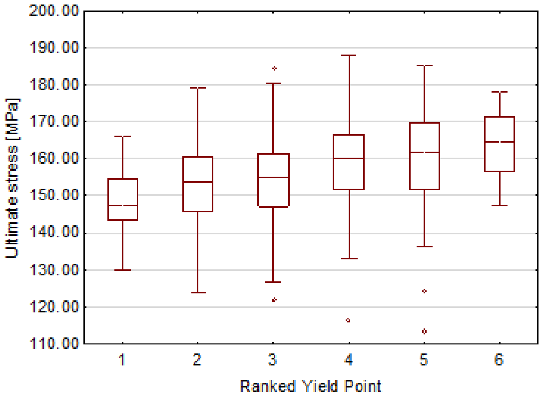

	1	2	3	4	5	6
1	A	A	R	R	R	R
2	A	A	A	R	R	R
3	R	A	A	R	R	R
4	R	R	R	A	A	R
5	R	R	R	A	A	A
6	R	R	R	R	A	A

Figure 5.8. Box plot of null hypothesis acceptance/rejection of yield Point.

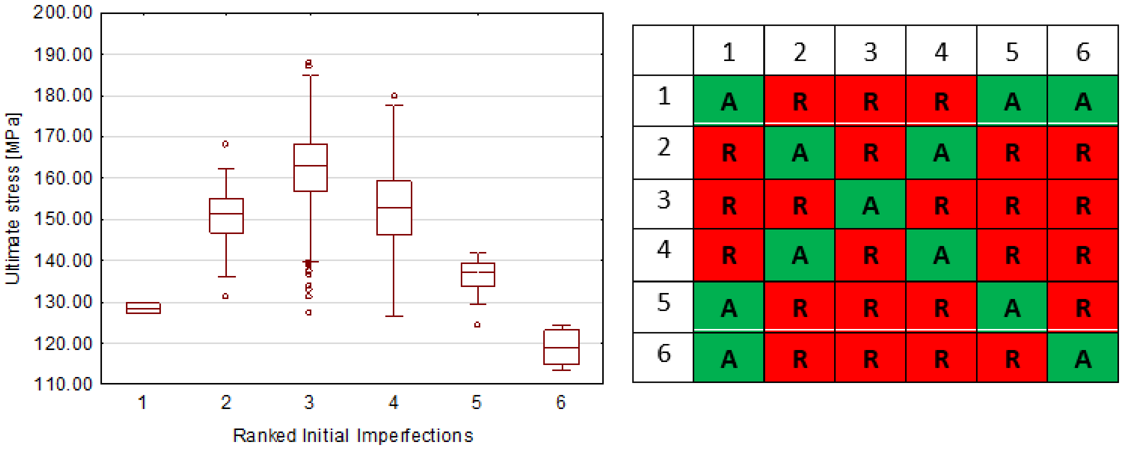

	1	2	3	4	5	6
1	A	R	R	R	A	A
2	R	A	R	A	R	R
3	R	R	A	R	R	R
4	R	A	R	A	R	R
5	A	R	R	R	A	R
6	A	R	R	R	R	A

Figure 5.9. Box plot of null hypothesis acceptance/rejection of Initial Imperfections.

In the initial imperfections, the maximum absolute value of the initial imperfections (rank 1 and 6) indicates a minimum value of the ultimate strength. Generally, initial negative imperfections (ranks 1-3) give higher impacts regarding the positive initial imperfections (ranks 4-6).

Since the uncertainty of the input parameters influences the uncertainty of the ultimate strength, with a reduction of the input variable uncertainties, the resulting uncertainty decreases. Due to that, it is essential to reduce these uncertainties.

The initial imperfections are related to the welding process. By controlling the welding process (i.e. current welding parameters, welding sequence, etc.), the initial imperfections may be reduced. The influence of the welding sequence on the initial imperfections was investigated in [248], showing that proper planning of the welding sequence can significantly reduce the initial imperfections. Nevertheless, even simple manufacturing methods may be used, such as pre-setting the welding parts or pre-bending to get straight constructions after welding. However, it is almost impossible to get a perfectly straight construction after welding. Assuming that the severe initial imperfections may be avoided by proper control of the welding process, the related uncertainty may be much smaller.

Concerning mechanical properties, there is still limited knowledge about the influence of corrosion degradation on mechanical properties and related uncertainties. However, to reduce uncertainty, more robust experimental work is needed, especially in the DoD range from 0% to 30%, typically seen in ship structures during the service life.

It can be noticed that the thickness uncertainty is growing with the increase of DoD. It is caused by the non-uniformity of the surface, which makes thickness measurements more disturbed. During the ship service life, corrosion degradation is measured, and, however, it is hard to collect information from a significant number of points. Due to that, there is hard to decrease the level of thickness uncertainty.

To analyse which input parameters are the most critical ones, their uncertainty level can be compared with the sensitivity of ultimate strength concerning any particular parameter. The results of the present analysis are presented in Table 5.2 and Figure 5.10.

Table 5.2. Sensitivity analysis.

Parameter	Uncertainty level	The sensitivity of ultimate strength
Yield stress	Medium	Medium
Young modulus	High	Medium
Ultimate tensile stress	High	None
Thickness	Low	High
Initial imperfections	High	Very high

As can be noticed, the most critical input data are the initial imperfections. After that, the second most influencing parameters are Young modulus, Yield stress, and thickness.

Based on that analysis, it can be seen that the proper estimation of initial imperfections and mechanical properties (except the ultimate tensile stress) is a very important issue.

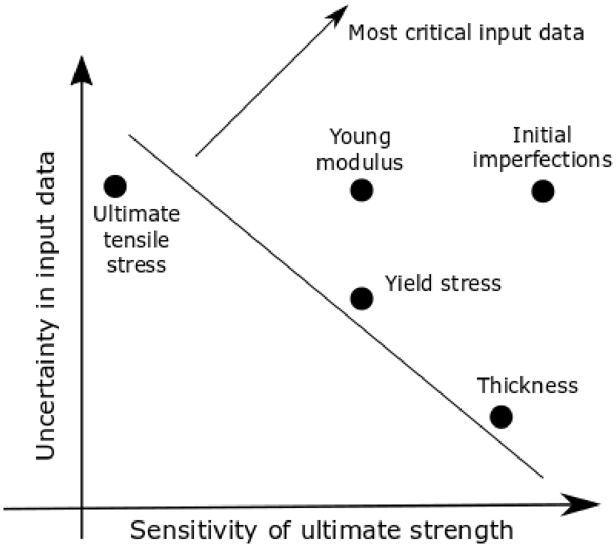

Figure 5.10. Sensitivity analysis.

5.1.6. Uncertainty assessment

The histograms of the ultimate strength for the intact and corroded cases are presented in Figure 5.11. The Normal probability plots for different cleaning methods are shown in Figure 5.12.

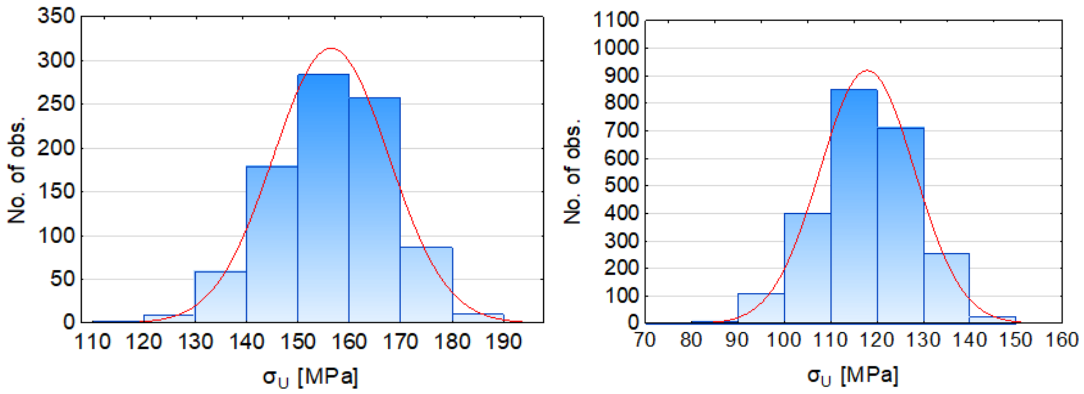

Figure 5.11. Ultimate stress in non-corroded case (900 observations) (left) and corroded case of DoD equal to 20 % (2,300 observations) (right).

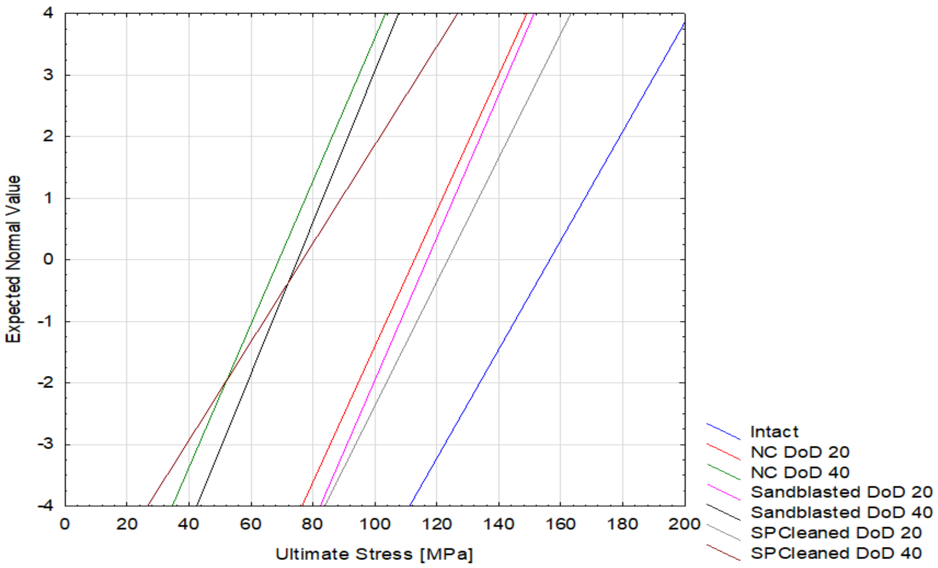

Figure 5.12. Normal probability plots of ultimate strength.

The mean values and standard deviations of the resulting ultimate stresses are presented in Table 5.3.

Table 5.3. Ultimate stress for all cases.

	Mean [MPa]	Minimum [MPa]	Maximum [MPa]	Standard Deviation [MPa]	COV [%]
Intact	156.4	113.5	187.8	11.3	0.07
Non-cleaned DoD = 20 %	112.7	82.7	139.5	9.0	0.08
Sandblasted DoD = 20 %	116.9	90.2	141.3	8.6	0.12
Sand Paper Cleaned DoD = 20 %	123.5	90.7	147.7	9.8	0.07
DoD = 20 %, All cases	117.8	82.7	147.7	10.2	0.11
Non-cleaned DoD = 40 %	69.0	15.8	88.6	8.3	0.08
Sandblasted DoD = 40 %	75.0	25.3	93.9	8.0	0.16
Sand Paper Cleaned DoD = 40 %	76.6	28.1	101.9	12.0	0.09
DoD = 40 %, All cases	73.5	15.8	101.9	10.1	0.14

As can be noticed, the ultimate strength is related to the DoD rather than the type of maintenance action. However, there is a slightly higher ultimate strength for maintained samples (sandblasted and sandpaper cleaned) than the corroded non-cleaned ones. It could be a result of surface smoothening, which may reduce the local stress concentration points. Additionally, sandpaper cleaning gives higher ultimate strength than sandblasting.

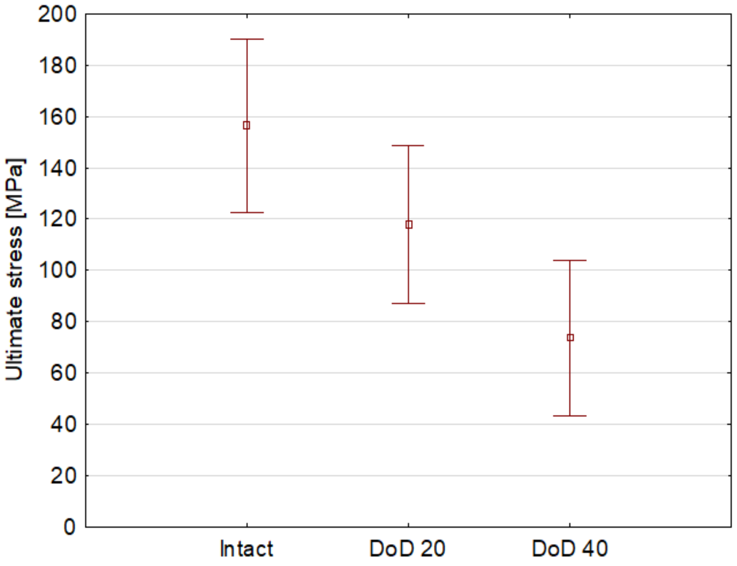

Figure 5.13. Ultimate stress as a function of DoD.

The uncertainty level (i.e. coefficient of variation) changes from 0.07 to 0.16, showing dependency from both – DoD and the type of maintenance actions. With the growth of DoD, the uncertainty level is also growing. The sandpaper cleaning method produces the highest uncertainty level due to the high uncertainties in the mechanical properties.

The Coefficient of Variation analysis reveals that the ultimate stress is reduced with the growth of DoD, but also the uncertainty level grows up.

Figure 5.13 shows the mean values of the ultimate stress with a lower and upper confidence level (with the 95% confidence level).

5.1.7. Simple model uncertainty formulation

The study results presented in [190] are used to develop the model uncertainty here, where the comparative analysis of the ultimate strength of corroded stiffened plates obtained via experiment and the numerical model was performed. The results of the ultimate stress concerning DoD are presented in Figure 5.14.

As shown in Figure 5.14, the ratio between numerical and experimental results for each DoD is estimated.

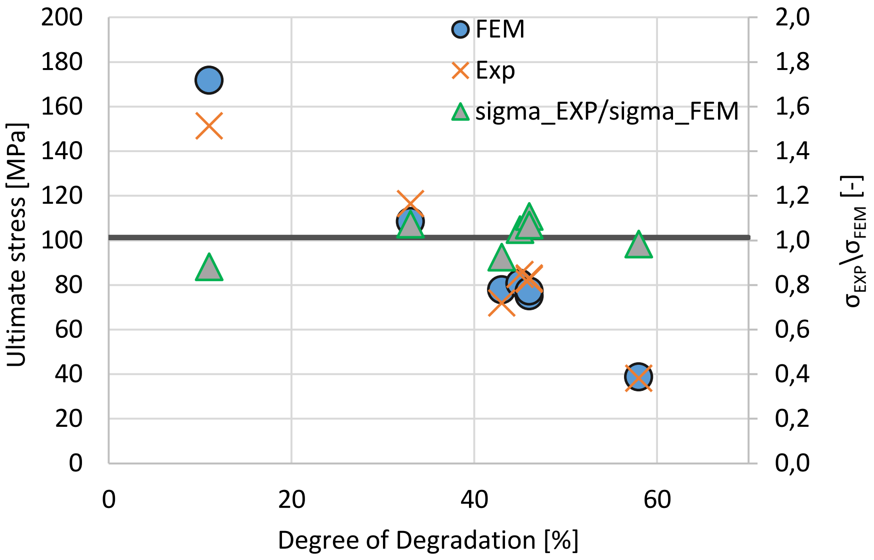

Figure 5.14. Ultimate stress as a function of DoD.

Based on these values, the model uncertainty is derived. The ratio between experimental and numerical results may be modelled as the constant value for each DoD, calculated as the mean value of the ratios between experimental and numerical results (presented as a black line in Figure 5.14). The standard deviation is calculated as the standard error of the estimate between particular ratios and a constant regression curve.

The resulting model uncertainty is defined as:

$$\frac{\widetilde{\sigma_{EXP}}}{\sigma_{FEM}} \sim N\{1.012; 0.0925\} \tag{5.6}$$

5.1.8. Conclusions

Based on the presented preliminary numerical studies, several conclusions may be derived, crucial for the planned numerical and experimental investigations. The parameters that mostly influence the ultimate capacity of corroded stiffened plates are the level of initial imperfections, mechanical properties (yield stress and Young modulus), and corrosion degradation level. The following parameters need to be measured before the experimental analysis to reduce the uncertainty level. The ultimate tensile strain has almost no impact on load-carrying capacity.

Based on the uncertainty assessment, it could be concluded that without the knowledge of governing parameters, the validation of a numerical model will be subjected to high uncertainty.

The ultimate strength is more dependent on the corrosion degradation level than the cleaning method. Due to that, the most crucial is to determine the behaviour of corroded plates themselves. The influence of the cleaning method is a secondary problem; nevertheless, worth being investigated.

Finally, as shown in Figure 5.14, previous studies were focused on severely corroded plates. The investigation of the structural behaviour of stiffened plates with the degradation level between 0 % and 25 % are lacking. The presented work aims to fill this gap.

The presented work has been done before the planning of the experimental analysis; thus, the geometrical plate dimensions are slightly different from those found in further chapters of the thesis.

6. EXPERIMENTAL SET-UP FOR MECHANICAL ANALYSIS

6.1. Support-specimen interaction analysis [P3]

The boundary conditions modelling in the finite element analysis of the ultimate strength assessment of the ship structures is the crucial point that can affect results [25]. The problem is vital in both experimental and numerical domains. One can choose simply supported or fixed boundary conditions in compressive tests of plates and stiffened plates. Both approaches could be seen in many studies. The fixed boundary conditions were used in [119,189], whereas the simply supported plates were used in [117,146]. In the case of real ship structures, the stiffened plates are spanned between the rigid transverse girders, which should yield fixed supports. However, there are not infinitely fixed supports since some rotation of end cross-sections may be seen. Gordo and Guedes Soares [49] performed compressive tests on scaled stiffened panels. Depending on the span of stiffeners and rigidity of transverse frames, the collapse shapes showed that in some conditions, the plates behave like almost entirely restrained, and in others, there were more closed to simply supported. Additionally, the problem with proper support design was analysed during these studies, and some stiffened panels collapse modes have been affected by the non-totally fixed behaviour of the supporting structure.

The critical buckling force is related to the boundary conditions [249]. Using simply supported boundary conditions can lead to underestimating ultimate capacity, leading to a conservative design. On the other hand, when the fixed boundary conditions are assumed, the ultimate strength may be overestimated, and the design solution will be insufficient.

Regardless of the assumed boundary conditions, they should be appropriately generated, especially when the experimental results validate the numerical model. Numerous studies regarding a proper simulation of boundary conditions in impact strength experiments of beams have been performed in [250]. They concluded that the support design is an essential governing parameter that may impact the experimental results.

In the present section, the support-specimen interaction is analysed, where the boundary conditions are assumed to be fixed ones. The maximum gap of the specimen mounting, which leads to proper boundary conditions simulation, is defined. A nonlinear contact analysis employing the Finite Element Method is performed. The analysis results are used to design the supports that will be furtherly used in compressive experiments of stiffened plates.

6.1.1. Finite Element Modelling

A bilinear elastic-plastic material model with hardening is used to model both support and specimen structures. This model will be sufficient, especially that the ultimate tensile stress revealed a non-important parameter in the ultimate strength analysis, as shown in the previous chapter. The support structure is designed to be made from high-tensile steel with a yield point of 355 MPa and the ultimate tensile stress, which is 490 MPa. The specimens are made from normal strength steel with a yield point of 235 MPa, and the ultimate tensile stress is 355 MPa.

Like the previous study, the FE analysis is performed using the commercial software ANSYS [245]. The calculations are performed using the nonlinear implicit static solver accounting for both material and geometrical nonlinearities.

The FE model consists of the following parts:

- FE model of the specimen generated by SHELL181 elements;
- FE model of the support generated by SOLID185 elements;
- CONTA170 and CONTA175 finite elements model the contact between the support and specimen.

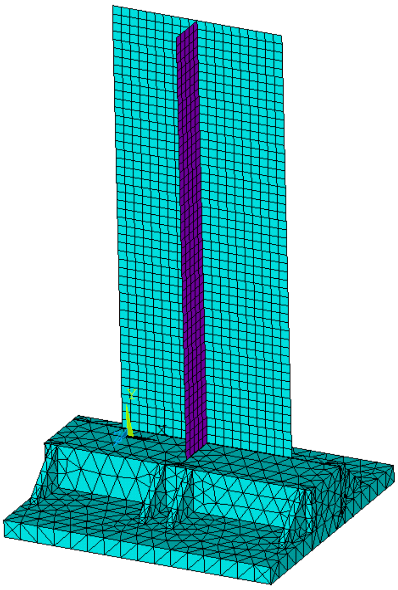

Figure 6.1. Finite Element model of support and specimen.

The specimen is composed of a plate of a length of 1.1 m and 0.4 m wide with a 0.1 m height stiffener. However, the 0.1 m length part of the specimen is clamped in the support, so the effective length of the specimen is 1 m. The thickness of both plate and stiffener ranges from 5 up to 10 mm. The model is presented in Figure 6.1. The mesh density of the specimen is obtained by mesh convergence study, and it is found that the finite element size of 0.02 m gives satisfying results (see Section 5.1.3). The contact finite element analysis requires a denser mesh of the contact surface (specimen) concerning the target surface (support). In the support structure, the tetrahedral elements are used with a finite element size of 0.04 m since the main goal of the present analysis is to reproduce the geometry and stiffness of the support structure and analyse its impact on ultimate strength.

The initial imperfections of the specimen are considered as presented in Section 5.1.2, taking into account the mean level of them.

The support structure is fixed on its bottom surface as it will be attached to the testing machine head. In the case of specimen boundary conditions, both stiffener and plate lower edges are restrained in a way that is a result of the modelled contact pair. The boundary conditions of the upper edges of the plate and stiffener are considered in two cases. In the first case, it is modelled as simply supported. This case is used as a reference to observe the behaviour of support-specimen interaction. In the second case, both the stiffener and plate's upper edges are clamped, simulating the real experimental test conditions. Additionally, all longitudinal displacements of the upper edges are coupled as they will be during experimental testing.

6.1.2. Results and discussion

The gap between the support clips and the specimen is presented in Figure 6.2.

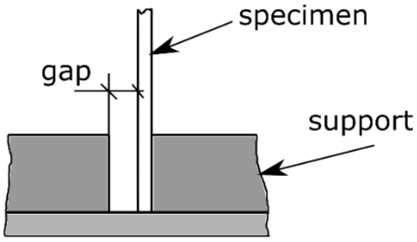

Figure 6.2. The gap between the specimen and the supporting clips.

The fixed boundary conditions can be simulated when the gap size equals zero. However, in the experimental domain, it is tough to guarantee this due to the unfairness of both specimen and support clips. The ultimate strength analysis with a gap size from 1 mm up to 20 mm is performed to analyse the maximum gap that may be allowed. The calculations are performed with a specimen thickness of 5 mm. The upper edges of the specimen are simply supported. The post-collapse shapes for different gap sizes are presented in Figures 6.3 and 6.4.

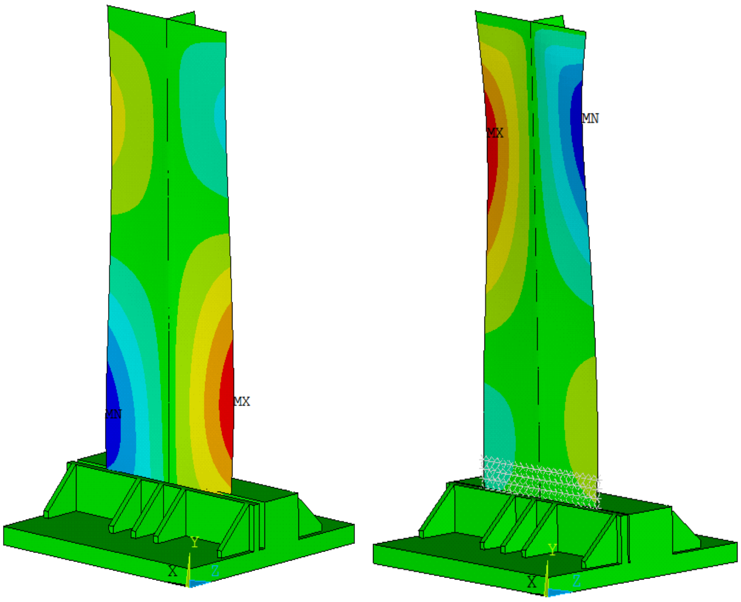

Figure 6.3. Deformation of specimens with a gap size of 20 mm (left) and 5 mm (right).

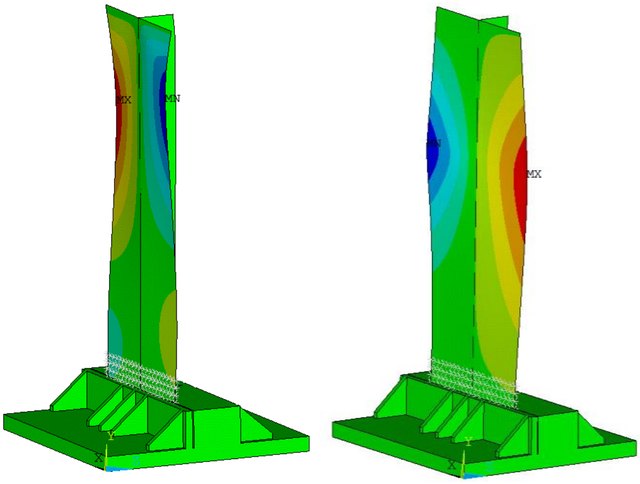

Figure 6.4. Deformation of specimens with a gap size of 4 mm (left) and 2 mm (right).

The deformed shape of the specimen with a gap size of 20 mm shows that the rotation of the lower edge of the specimen is not restrained. The maximum deflections of the plate in the lateral direction are near the lower support. In the case of a gap size of 5 and 4 mm, some rotation of the specimen's lower edges is observed, and two half-sine waves in the longitudinal direction on the deformed shape are formed. In the case of a 2 mm gap size, there is only one half-sine wave in the longitudinal direction of the deformed shape, showing that the rotation of the lower edge of the specimen is restrained. It can be noticed that for all cases, the failure mode is a plate-induced failure. The specimen's ultimate compressive force in a function of the gap size is presented in Figure 6.5.

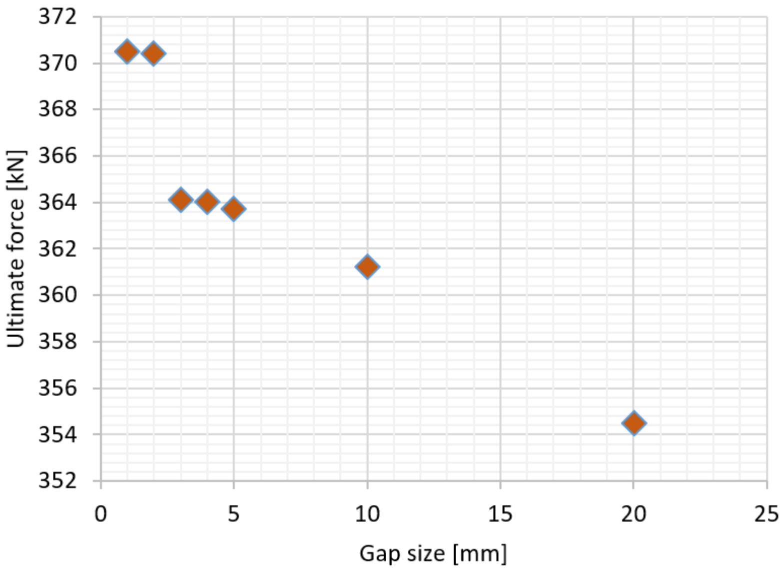

Figure 6.5. Ultimate force in the function of gap size.

It may be easily observed that for the first two points corresponding to 1 and 2 mm gap sizes, the ultimate force is very similar, and the value corresponds to fixed boundary conditions simulation. The next group, a gap of 3 up to 10 mm, shows a lower ultimate capacity, which corresponds to partially fixed conditions that allow for some rotation. With the gap size of 20 mm, the plate behaves like an almost simply supported one, and the ultimate force is the lowest.

However, there is not a significant reduction in the ultimate capacity (about 5 % comparing 20 mm and 2 mm gaps), but in the experiment, the edges will be supported in both upper and lower edge, and this effect may be magnified if not a proper supporting structure is designed. It can be noticed that the change in the ultimate force corresponds well with the deformation shapes presented in Figures 6.3 and 6.4.

The force-displacement curves for different gap sizes are presented in Figure 6.6. The displacement is the shortening of the specimen in a longitudinal direction.

In the first phase of the loading, all specimens behave similarly, and the curve inclination is equal to the Young modulus of the material. After reaching the bifurcation point (around 0.5 mm of displacement), the plates start to buckle, and the inclination of the curves is changing. As can be seen, the smaller inclination of the force-displacement curve is obtained for the more significant gap size, which corresponds to the closely simply supported conditions. The most significant inclination of the force-displacement curve is observed for the gap size of 2 mm, which corresponds to fixed boundary conditions.

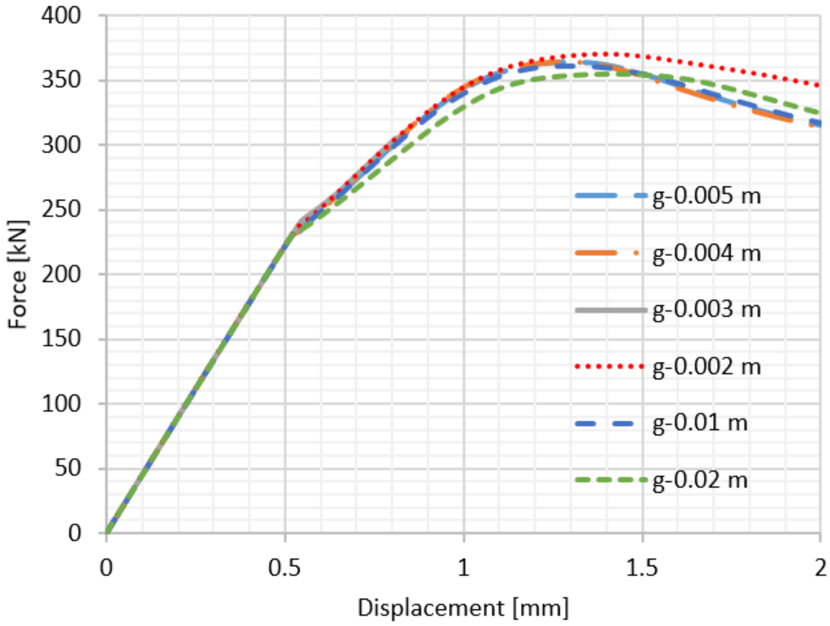

Figure 6.6. Force-displacement curves.

Figure 6.7 shows normal axial stresses in specimens for gap sizes of 5 mm and 2 mm. It can be noticed that the high-stress areas are corresponding to the places of high deflections. In the case of a 5 mm gap, the high-stress regions are near the specimen's upper edge, and in the case of a 2 mm gap, there are located in approximately two-thirds of the specimen. Additionally, it could be observed that in a specimen presented in Figure 6.7, left, there are plastic regions very close to the upper edges of the specimen.

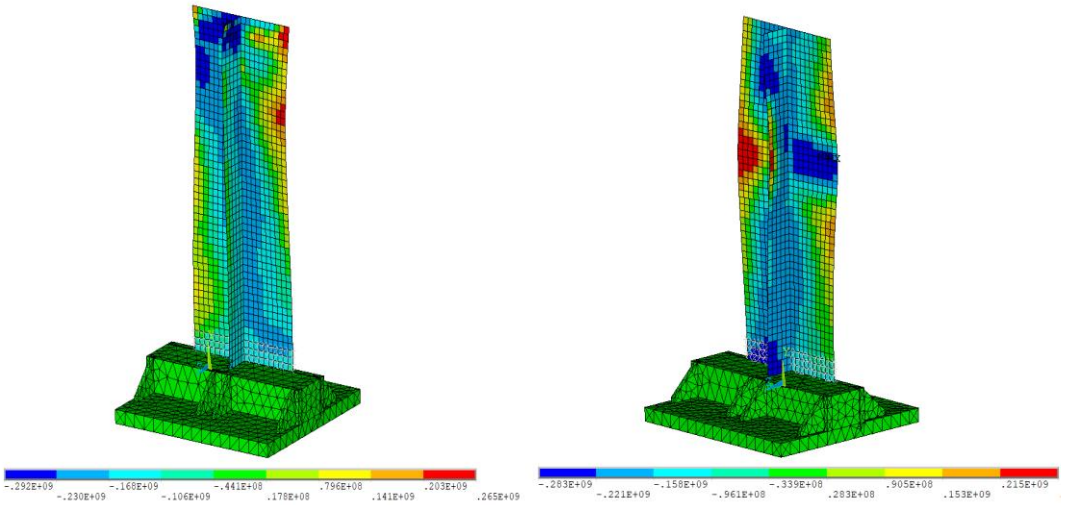

Figure 6.7. Normal stresses in the specimen with the 5 mm gap (left) and 2 mm gap (right).

To analyse the stiffened plate's behaviour in experimental conditions, the gap size was assumed to be 2 mm, and the upper edges of the specimens are fixed. The analysis results are presented in Figure 6.8, where deformations after the collapse and normal stresses are shown, respectively.

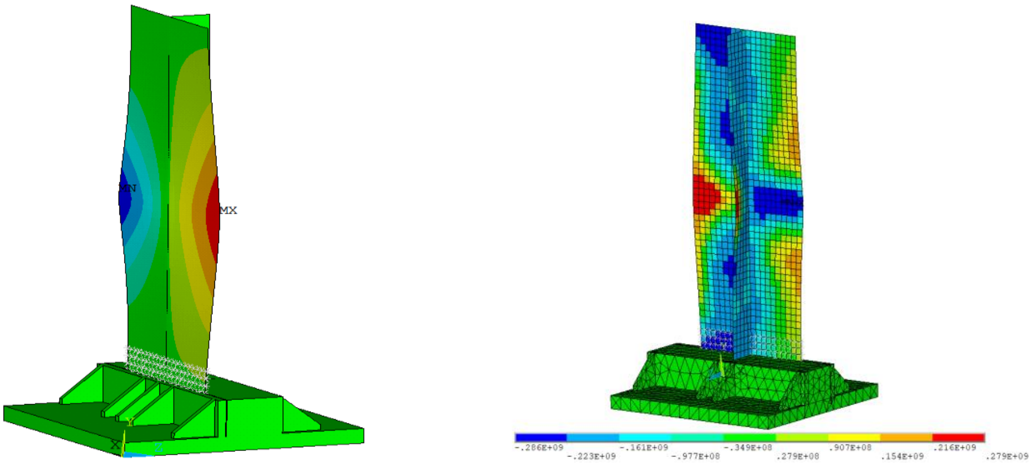

Figure 6.8. Deformation (left) and normal stresses (right) of the specimen with a 2 mm gap and fixed upper edge.

The results show that the support behaves appropriately. The maximum deflections are in the middle-length of the specimen, and the behaviour of the lower and upper edges of the specimen is very similar. The mode of failure is plate-induced buckling. A similar observation may be seen in normal stresses. Figure 6.8, right, shows a very symmetric stress distribution concerning the horizontal axis. The plastic regions occur in the mid-length of the specimen and near the supports.

For ultimate strength predictions before the experimental testing, the specimens with a different plate and stiffener thicknesses were analysed, namely 5, 6, 8, and 10 mm. It is assumed that the supports behave properly, and the upper edges are fixed as it will be done during the experiment.

The results of normalized ultimate stress (ultimate stress concerning yield point) are presented in Figure 6.9. The deformation forms of the stiffened plates are presented in Figure 6.8 (5 mm specimen) and Figure 6.10 for other thicknesses.

As can be noticed, the normalized ultimate stress is significantly reduced with the reduction of plate thickness. In the case of a 10 mm plate thickness, the failure mode is dominated by yielding, and in the case of 5, 6, and 8 mm plates, the failure mode is the plate-induced buckling, and it is caused by the plate buckling at the initial loading stage. In the post-collapse shape of the specimen with a 10 mm thickness, the one-side deformations in the mid-length are defined, which induces a failure mode of column buckling.

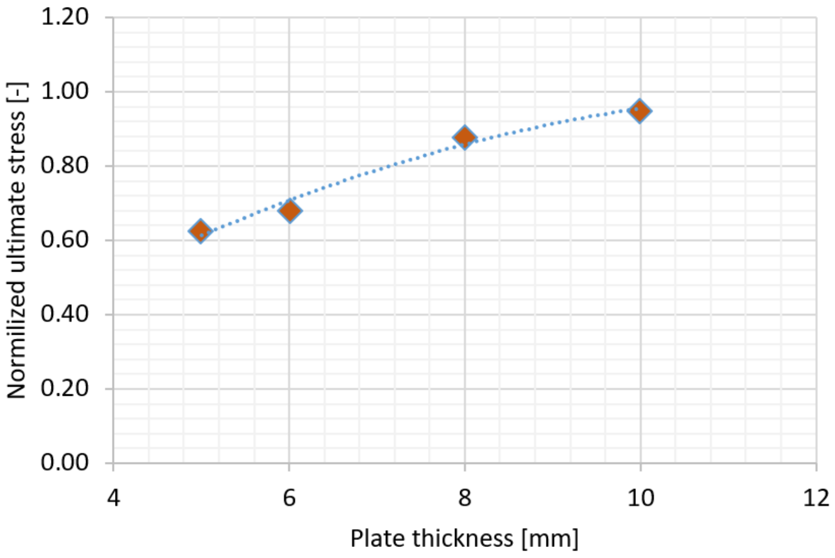

Figure 6.9. Ultimate force in the function of specimen thickness.

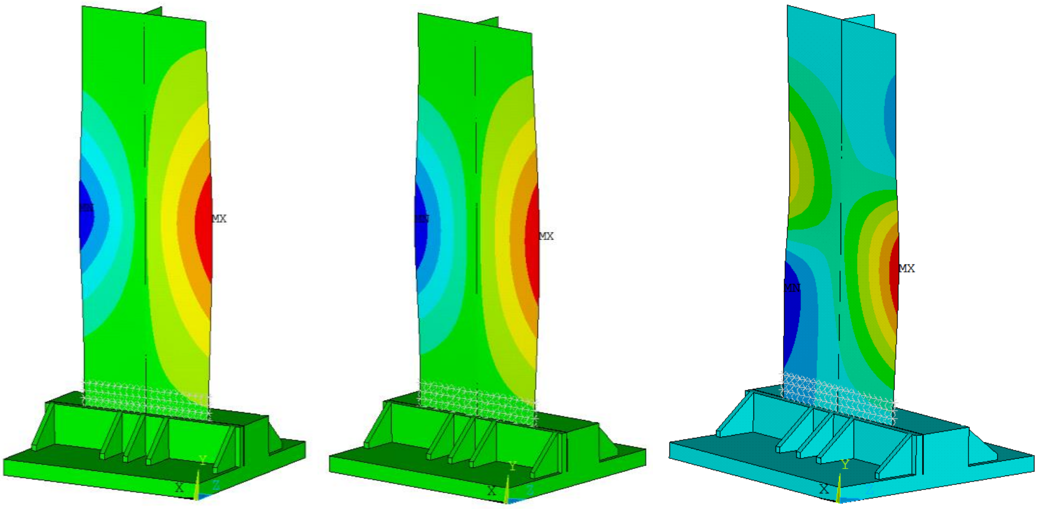

Figure 6.10. Deformation of the specimens with a thickness of 6 mm (left), 8 mm (mid), and 10 mm (right).

6.1.3. *Support design*

The support structure is designed as presented in Figure 6.11 to provide the proper fixed boundary conditions. The main feature of the presented supports is adjustability. Thanks to the steel mounting blocks controlled by the set of screws, the gap between support and plate could be reduced to a minimum leading to full fixation. Additionally, this allows for testing the stiffened plates with different thicknesses by using one support set.

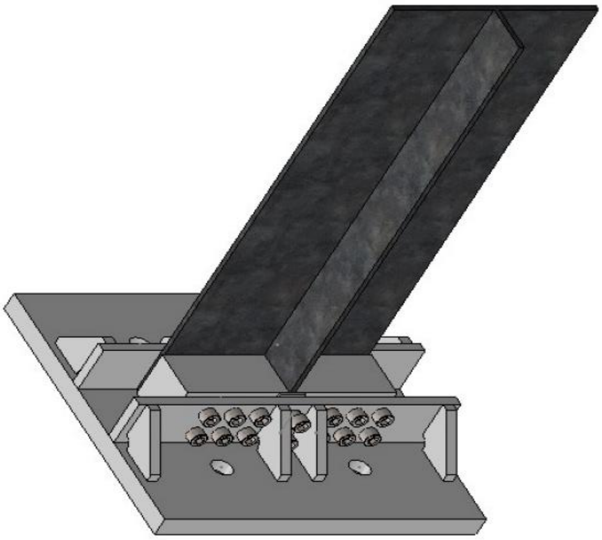

Figure 6.11. Designed support.

The maximum acceptable gap between specimen and support in simulating the fully clamped supports cannot exceed 2 mm. Crossing the acceptable gap may impact the ultimate capacity and the pre and post-collapse regimes, and the stress distribution around the specimen.

The study was also used to identify the most appropriate places to mount the strain-gauges for recording the structural behaviour during the experiments.

6.2. Experimental set-up [P4]

The experiment aims to carry out the ultimate strength tests of the intact and corroded stiffened plates and investigate the influence of corrosion on reducing the strength of stiffened plates with different initial thicknesses. The dimensions of tested stiffened plates were described in detail in Section 4.1.2. As it was pointed out, in intact conditions, the total number of three specimens (one for each thickness) were tested. The rest nine specimens were tested after being corroded.

The main objective of the experiment is to investigate corrosion influence, and thus, other possible influencing parameters, mainly mechanical properties and welding induced stresses and distortions, should be possibly similar for all plates. The following actions were carried out:

- Material properties were obtained via standard coupon testing in both intact and corroded conditions;
- Initial distortions were measured for each specimen using photogrammetry technique;
- Welding parameters were the same for the group of specimens with a similar thickness (the automatic welding was provided);

The quantities that were obtained as an output of the experiment are as follows:

- The most important response was the force-displacement curve for each tested specimen;
- Strains were obtained via strain gauges in points that were typed based on the preliminary numerical simulations
- Local plate displacements;
- Post-collapse forms of deformation.

6.2.1. Supporting structure

The supporting structure designed according to the results of preliminary numerical analysis, as presented in Section 6.1, is shown in Figure 6.12. Nevertheless, the plate displacements near the supports will be measured to confirm that the clamped boundary conditions were achieved.

For the longitudinal unloaded edges, the difference of the ultimate strength of stiffened panels under various constraints is relatively small [35]; hence, the longitudinal edges of the testing coupons were kept free during testing.

Figure 6.12. The designed support structure and tested specimen (bottom part).

6.2.2. Testing machine

The main features of the testing machine are:

- compression loading – up to 4000 kN;
- tension loading - up to 2000 kN

The maximum compressive load for the thickest plate should not exceed 1,000 kN; thus, the machine, as presented in Figure 6.13, should provide the loading to destroy the specimens. The loading is transmitted via the bottom supporting structure, connected with the head of the hydraulic jack-up. The pressure in hydraulic jack-up is controlled manually, and it is raising very slowly to provide the quasi-static conditions.

Figure 6.13. Testing machine with the mounted specimen (left).

6.2.3. Gauges configuration

The actual outcome of the testing machine is the force value. To monitor the longitudinal shortening of the specimen, the longitudinal displacement has been measured via displacement transducers in two independent places, between the floor and bottom support (the upper support is not moving during the experiment) and between bottom support and upper support. The additional displacement transducers have been installed to monitor the lateral deflections of the plate near the support, which was furtherly used to investigate the supporting performance. One displacement gauge has also been installed to measure the lateral displacement in the middle of the specimen, which is allowed to investigate the possible column buckling. The main physical quantities measured during the experiment were strains in the middle cross-section and the specimen. The mid-cross-section has been identified in pre-experimental analysis as a place of possible highest strains during the collapse of the stiffened plate. The strain gauges measured only axial strains along with the specimen since it was identified that the transverse strains play a minor role. The full compensation of the temperature has been provided to reduce the uncertainty level. The drawings showing the distribution of both strain gauges and displacement transducers on the specimen is presented in Figure 6.14, and the actual realization during experiments is presented in Figure 6.15. Video recording has been provided to register the development of deflected shape during testing.

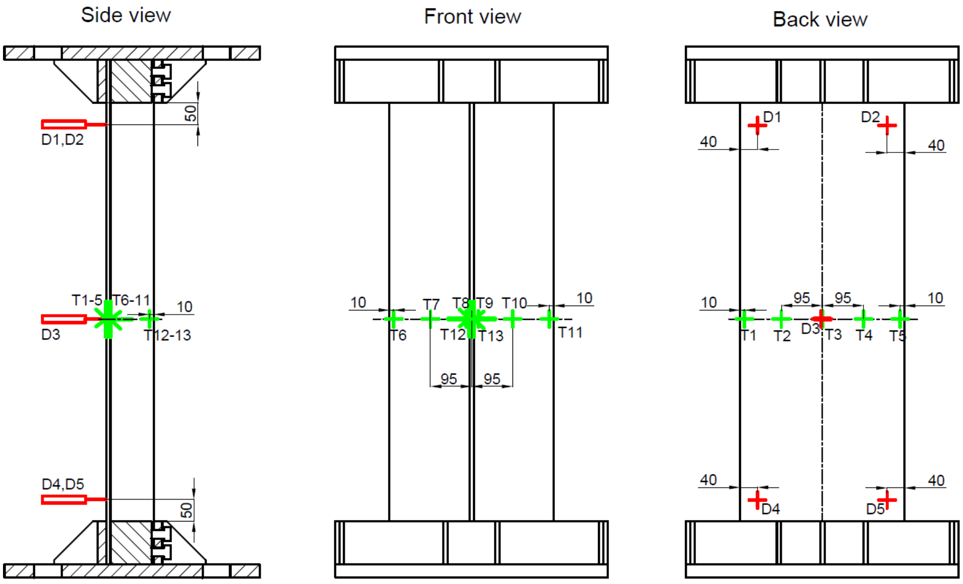

Figure 6.14. Distribution of strain gauges and displacement transducers.

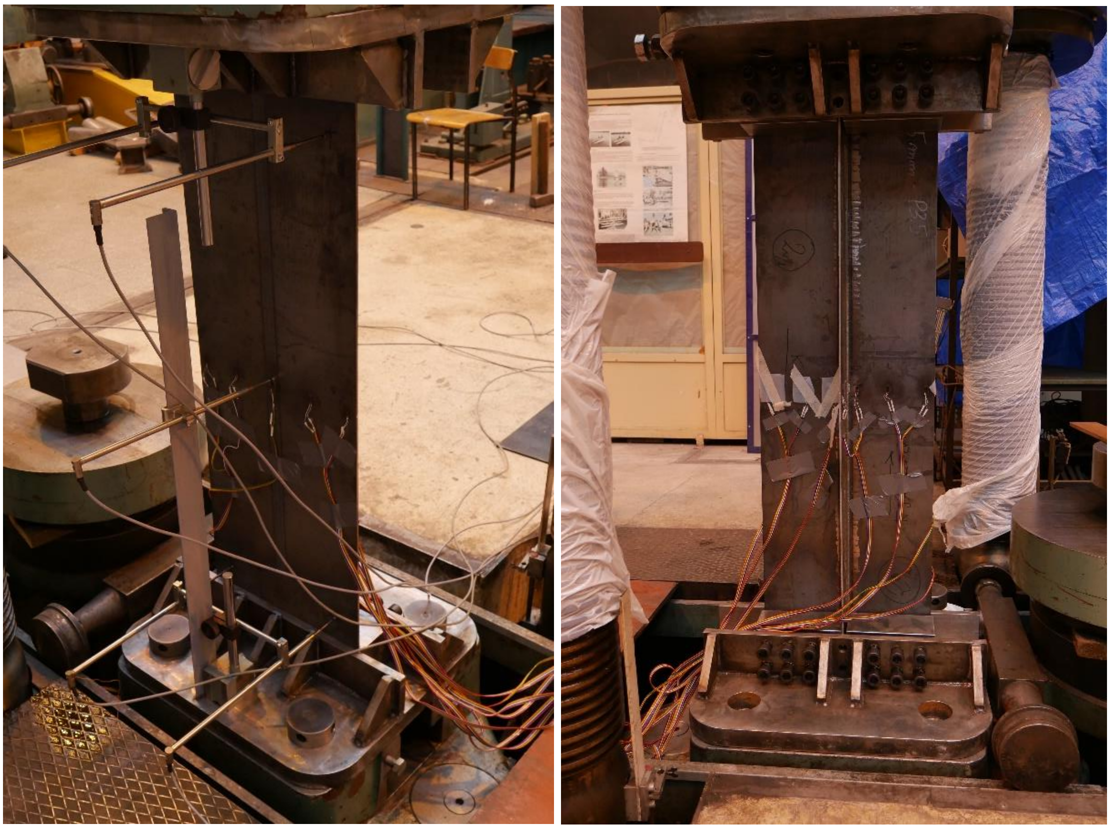

Figure 6.15. Back (left) and front (right) view on the specimen with installed gauges.

6.3. *Measurement of welding-induced residual stresses [P5]*

As mentioned previously, the welding parameters were identical to each group of plate thickness to have a similar level of residual stresses and initial imperfections. Additionally, the automatic arc-welding has been applied to reduce the uncertainty of the welding parameters. The applied thermal energy, together with a time of welding for each specimen, has been presented in Table 6.1.

Table 6.1. The welding parameters.

Thickness [mm]	Specimen number	Weld number	Introduced energy per mm of weld [kJ/mm]	Time of welding [s]
5	5.1	1	0.69	256
		2	0.57	230
	5.2	1	0.82	245
		2	0.52	246
	5.3	1	0.56	223
		2	0.52	208
	5.4	1	0.41	250
		2	0.52	207
6	6.1	1	0.93	279
		2	0.95	285
	6.2	1	0.79	290
		2	0.93	278
	6.3	1	0.93	279
		2	0.94	265
	6.4	1	0.95	284
		2	0.94	282
8	8.1	1	1.60	342
		2	1.68	349
	8.2	1	1.29	310
		2	1.21	311
	8.3	1	1.52	337
		2	1.59	349
	8.4	1	1.44	326
		2	1.58	338

The typical specimen has been presented in Figure 4.3. The welding sequence is presented in Figure 6.16 (left).

The welding- induced distortions and residual stresses in stiffened panels affect ultimate strength. These phenomena are complex and difficult to estimate during the design process. The effects of both residual stresses and distortions cause a reduction in the load-carrying capacity of stiffened plates near the collapse load, smoothing the load-shortening curve in the relevant region [67].

To determine the level of welding-induced residual stresses, the non-destructive testing in the mid-cross section of the 5 mm and 8 mm stiffened plates has been carried out employing specialized equipment, which utilizes the Barkhausen effect [251]. The laboratory that performed the measurements had the Polish Office of Technical Inspection (UDT) certificate for that methodology as well as a certificate from the Polish Register of Shipping. The measuring points are presented in Figure 6.16 (right).

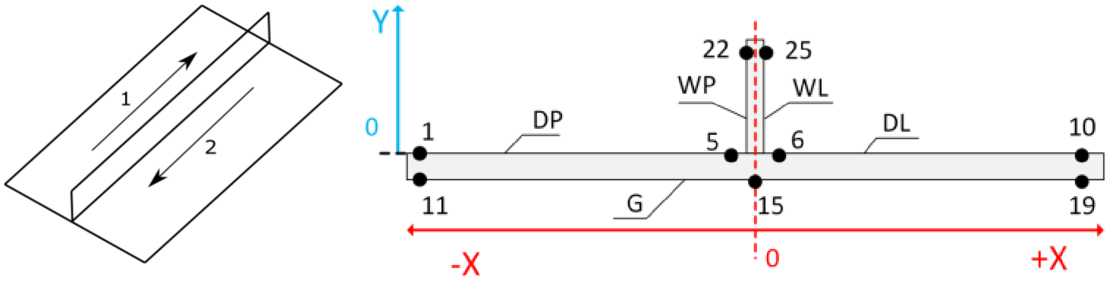

Figure 6.16. Applied welding sequence (left) and the measuring points of welding residual stresses in the mid-cross section of the specimen (right).

At each point, the stresses in both longitudinal (Sx) and transverse (Sy) directions were measured. The residual stresses in the plate element for 5 mm and 8 mm specimens are presented in Figure 6.17, considering both upper (DP, DL) and lower (G) surfaces of the plate. It needs to be noted that the residual stresses near the welding zone (points 5 and 6) were measured approx. 2.5 cm from the symmetrical axis due to the width of the gauging probe. However, the residual stresses in the longitudinal direction in the welding zone are reaching the yield stress level of the material. Thus, this residual stress level in that region is assumed as equal to yield stress.

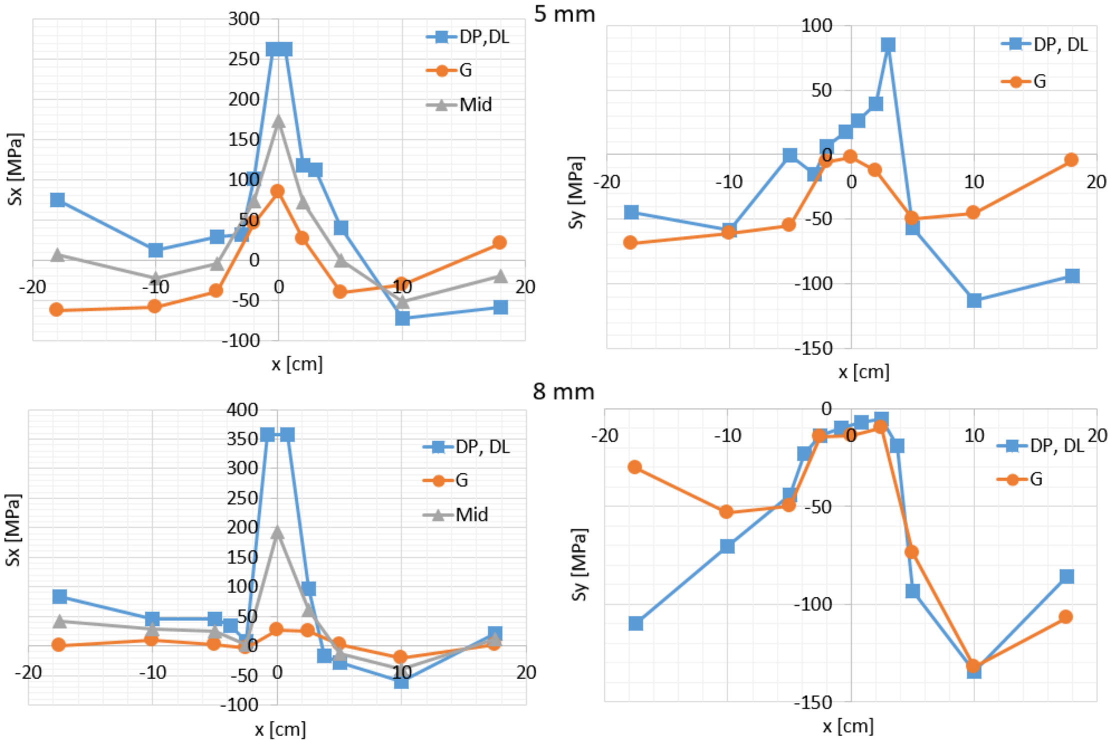

Figure 6.17. Residual stresses in the plate element of 5 mm (top) and 8 mm (bottom) thickness.

It can be noticed that the distribution of the welding-induced residual stresses in the longitudinal direction is similar to the typically observed one in [78] in the case of both 5 mm and 8 mm specimens. The region of high tensile stresses is observed near the welding zone, whereas the compressive stresses are observed away from that region. However, when considering a 5 mm stiffened plate, there are significant differences between residual stresses on the top and bottom surface, mainly caused due to the high slenderness ratio. This indicates that the plate areas near the specimens' free edges are subjected to the local bending since the beginning of the loading process. Additionally, the bending direction is opposite on both sides of the stiffener. The welding-induced stresses distribution is consistent with the observed shape of the initial imperfections, which is discussed in the next section. Furtherly, it can be noticed that the distribution of compressive stresses is asymmetrical, which is a result of the applied welding sequence. Thus, a similar observation can be drawn in terms of an 8 mm stiffened plate. However, in that specimen, the bending stresses are less significant, caused by the lower plate slenderness ratio than the 5 mm plate. In the case of the transverse direction stresses, the compressive ones exist in the regions away from the welding zone, whereas, in the welding zone, the transverse stresses are close to zero in the case of both specimens.

As discussed in [78], the parameter that determines either the residual stresses will significantly impact the ultimate strength is the ratio between the mean compressive stresses and yield stress of the material. The higher the compressive stresses are, the potential decrease of the ultimate strength is also higher. The estimated compressive stresses are 7.0 % and 4.4 % of yield stress for 5 mm, and 8 mm stiffened plates. The estimated compressive stresses may be classified as relatively low values of the residual compressive stresses and, as indicated in [78], without significantly impacting the ultimate strength. Similar observations can be found in [252], and additionally, it was shown that the flat-bar stiffened plates would be less sensitive to the welding-induced residual stresses when compared with tee-bar or L-bar stiffened plates.

Based on the analysis of the welding-induced residual stresses, it may be concluded that there are rather non-significant, which may be due to the automatic welding and proper selection of the welding parameters. Additionally, where one considers a stiffened panel, the plate elements between stiffeners are restrained, resulting in higher residual welding-induced stresses. In the case of a single stiffened plate, the longitudinal edges are free, which leads to a bigger initial imperfection with lower residual stress at the same time.

Based on the above, the welding-induced residual stresses are not taken into account in the numerical analysis.

6.4. Initial imperfections measurements and analysis [P6]

The initial imperfections of the specimens have been measured in the non-corroded state since there will not change with corrosion development. The technique that has been employed involves image-based photogrammetry.

Although photogrammetry originates mostly from geodetic applications, it founded a firm place in archaeological, paleontological and antique techniques [253]. Koelman [254] employed photogrammetry to capture complete ship hulls for further analysis. It was noted that from an industrial point of view, the method was fairly simple and adequate while exhibiting numerous advantages over alternative methods. Inclusion of texture in the measured material, in addition to the standard geometry point cloud, was proven to be a major asset allowing human-aided recognition of ship parts - a feature absent in akin laser scanning method.

An experimental setup was prepared to perform the measurements of imperfections. Four cameras were attached to a frame, which was placed over a heavy steel table. The camera stand was originally designed within the “Mechanics of anterior abdominal wall in optimizing hernia treatment” national grant (National Science Centre, Poland). The table was covered with a dark blanket, and a measured specimen was lying on that blanket. During the measurement, a series of four images were taken simultaneously using a remote shutter, then the plate was slide to the next position (together with the blanket), and photos were taken. The process was repeated until the whole plate surface was captured in the images.

All cameras that created a fixed camera array, were equipped with remote control shutters, which allowed contactless and simultaneous image acquisition. Real dimensions of the measured object need to be captured. To achieve this, scale bars or referencing markers are usually used. In this case, however, it was not advised because surface topology was the essential part of capturing. To overcome these obstacles, markers (crosses) were drawn directly on the surface of the plates using a felt-tip pen (Fig. 6.18). Distances between the markers were measured in the real world and later introduced to the model during the post-processing stage. However, not the most precise, this approach allowed to capture the full original surface of the object. Because of space limitations and practical reasons, the camera rig was immobilised, and the plates were slide under the rig during image acquisition.

Figure 6.18. Example of image capture.

An image capture example is shown in Figure 6.18 by the camera during the measurement. Steel reflexes are reduced by using potato flour. In the corners of the plate, there are white cross markers. The distance between the markers along the plate was measured and then used to scale the photogrammetric model.

The majority of image processing was executed in two pieces of software: Agisoft Metashape, a commercial package for photogrammetry, and RawTherapee, an open-source image-editing software. Each photo includes some part of a measured object and background -

partially static (camera stand, room), partially not (dark blanket). A relevant object area was selected in each photo, and the rest masked out, including out-of-focus object surfaces, edges, and background (irrelevant). In-focus areas were identified mostly visually.

During the camera alignment phase, relative positions of cameras are calculated, and a sparse point cloud of the measured object is created (Figure 6.19). Camera alignment was then optimised to ensure that these points overlap in respective projection planes. The High settings were used, which means that full-resolution photos have been used to perform camera alignment and build the initial sparse point cloud. Masked-out areas were excluded from the process.

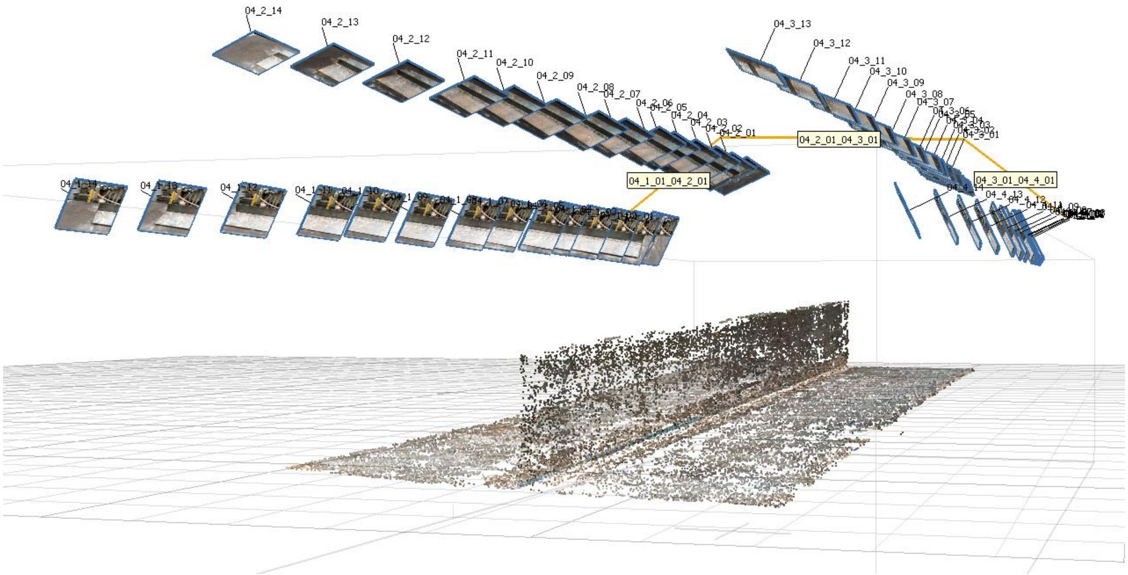

Figure 6.19. Initial sparse point cloud and estimated positions of cameras.

After the sparse cloud is created, the dense cloud is built based on the aligned cameras projections. Basing on the dense cloud, a surface is created, consisting of triangular mesh elements. During the surface generation, it was decided to choose aggressive depth filtering, which means that a smooth, continuous surface was desired. The final step of photogrammetric reconstruction was texturing of the surface. In this study, all the textures were consistently sharp, which allowed for identifying their features without problems. Figure 6.20 shows the textured photogrammetric model with the white cross markers included and used as scale bars. Two scale bars (along each long edge) were used, and the variance between them was computed. It turned out to be negligible, so no additional scaling methods were utilised.

Figure 6.20. Textured photogrammetric model.

The geometrical model created in Agisoft Metashape can be exported, whether as point cloud coordinates or an STL surface. These models are usually not directly appropriate for FE analysis because of their excessive size and numerous inconsistencies.

To overcome these obstacles, an algorithm in Matlab is used in creating organised nodal lines while representing global imperfections and preserving local imperfections of the measured plates. Automation of the process was required since there was a need to prepare 12 geometrical models - each in different mesh size variants - for FE analysis. For this purpose, it was started with importing the dense point cloud and getting rid of the edges, which - being boundary areas - are the most prone for reconstruction error (Figure 6.21). The main plate and the stiffener are also separated at this stage and are processed individually in all subsequent steps.

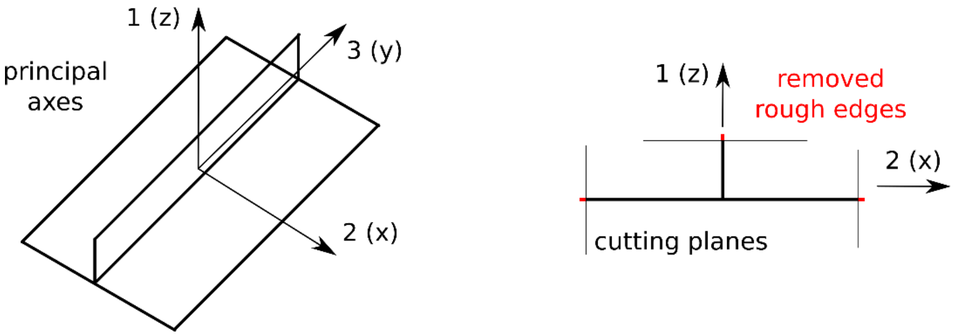

Figure 6.21. Computed principal axes of inertia for plate orientation (left) and trimmed rough edges providing smooth surface (right).

Afterwards, the mesh grid lines were created, and each point from a point cloud was assigned to a field isolated by the grid lines. In each isolated field, a centre of mass was calculated, and a best-fit-plane was found based on the distribution of imported points. Based on the centre-normal pairs, coordinates of the corner nodes positioned along the grid lines can be calculated. Since most target mesh nodes (except for the plate edges) are common for the four neighbouring element corners, their elevations are averaged from all the neighbours (Figure 6.22). This way, it is possible to preserve a smooth, continuous character of the surface while including the originally measured imperfect features of the specimen.

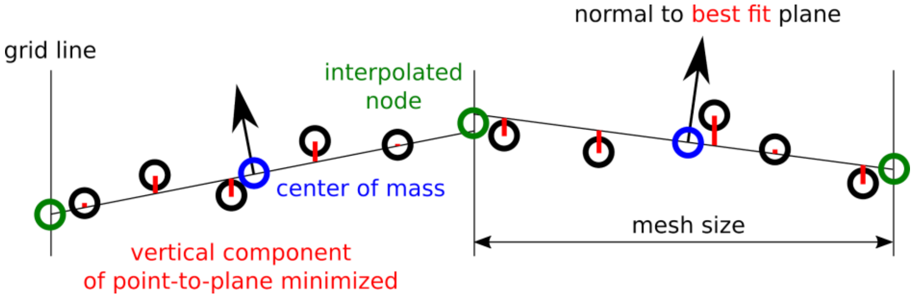

Figure 6.22. Grid nodes (green) are interpolated from corner nodes of all adjacent areas (2D view).

As a final result of the procedure, a well-organised node-set is created, closely representing the measured plate dimensions. In this case, two separate meshes are generated -

one for the main plate, the other one for the stiffener. They are tied together in the central axis. An example of such a process has been presented in Figure 6.23. The measured imperfections (two opposite bulges) are easily noticeable.

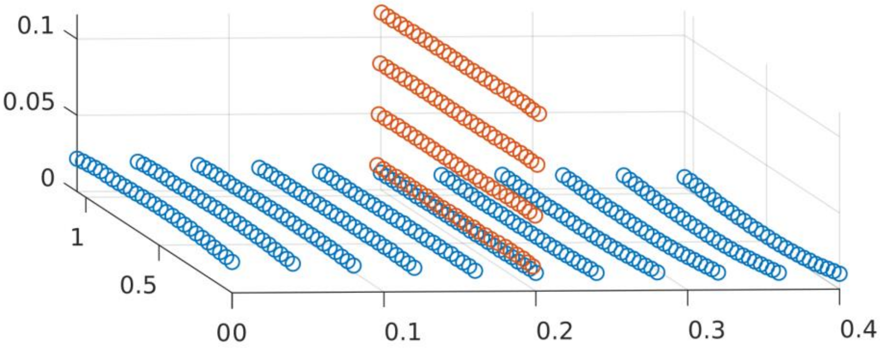

Figure 6.23. The outcome of the organised downsampling procedure.

Based on the measurements, one can indicate the common shape of initial plate imperfections, where the stiffener imperfections are denoted as c_0. Where the positive sign is in the b_1 and b_2 imperfections, the shape is similar to the one presented in Figure 6.24. The minus sign denotes that the curvature of imperfection is the opposite.

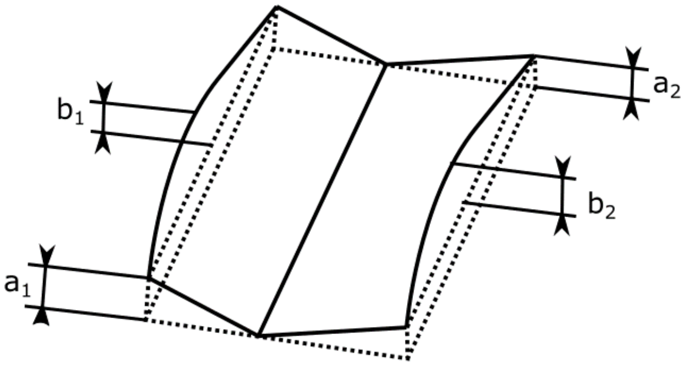

Figure 6.24. Values of obtained initial imperfections.

The values for initial imperfections are presented in Table 6.2.

Table 6.2. The values of initial imperfections measurements.

Plate thickness	No	a_1 [mm]	a_2 [mm]	b_1 [mm]	b_2 [mm]	c_0 [mm]
5 mm	1	2.37	5.19	-7.98	5.37	1.19
	2	3.45	3.05	-8.91	9.02	3.35
	3	2.78	3.37	-6.98	4.49	2.95
	4	2.33	3.49	-5.34	3.95	0.00
	Mean	2.73	3.77	-7.30	5.71	1.87
6 mm	1	3.73	3.66	3.69	-4.10	2.18
	2	4.01	4.17	3.58	-4.95	0.72
	3	4.62	3.12	2.19	-5.01	0.85

	4	4.36	3.21	0.63	-5.19	0.60
	Mean	4.18	3.54	2.52	-4.81	1.09
8 mm	1	3.77	5.50	-3.01	-2.43	0.22
	2	4.31	5.07	-0.25	-0.11	0.44
	3	4.25	4.73	1.39	1.46	0.77
	4	6.13	4.88	-2.16	-3.21	0.37
	Mean	4.61	5.05	-1.01	-1.07	0.45

The shape of the initial imperfections is consistent with other literature examples [255]. One can notice that when the plate is thicker, the general sideways imperfections are bigger (a_1, a_2, whereas the local plate imperfections are tend to be smaller (b_1, b_2). Similarly, the stiffener imperfections are smaller, with the increase of plate thickness. In the case of 5 mm and 6 mm plates, the local plate imperfections are of the opposite signs on both sides of the stiffener. In the case of an 8 mm plate, the plate imperfections are of the same sign. It is also notable that although the welding conditions were the same for each thickness of stiffened plates, the imperfections are subjected to significant scatter.

The typical shapes of initial imperfections for different thicknesses of stiffened plates are presented in Figure 6.25. One can notice that with the increase of the plate thickness, the global imperfections are more dominant, whereas the local imperfections are less significant.

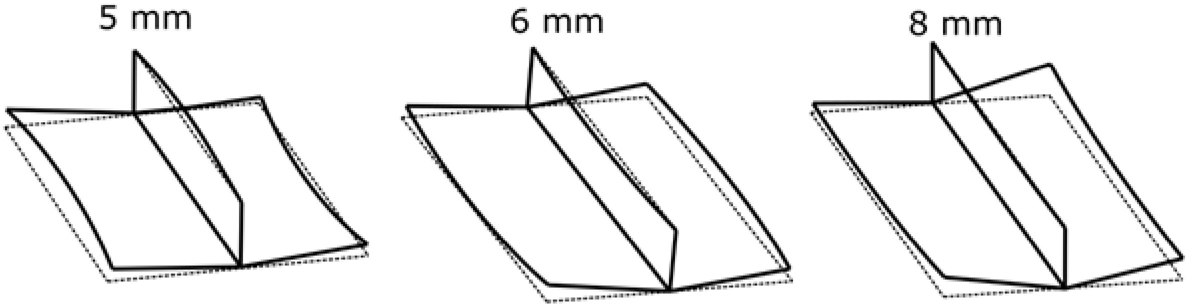

Figure 6.25. Initial imperfections of specimens (scale factor 5x).

6.5. Tensile testing of coupons

6.5.1. Intact specimens

In the present study, the six or seven coupon specimens from each thickness of standard size (see Figure 6.26) were taken from different places of steel sheets (1.25 m x 2.5 m) and analysed. The typical Zwick-Roell machine with the hydraulic engine was used to carry out the tensile test and to obtain the values of elasticity modulus; the mechanical extensometer was adopted (see Figure 6.27). The tests were performed following the ISO standard for tensile testing [256] of flat coupons.

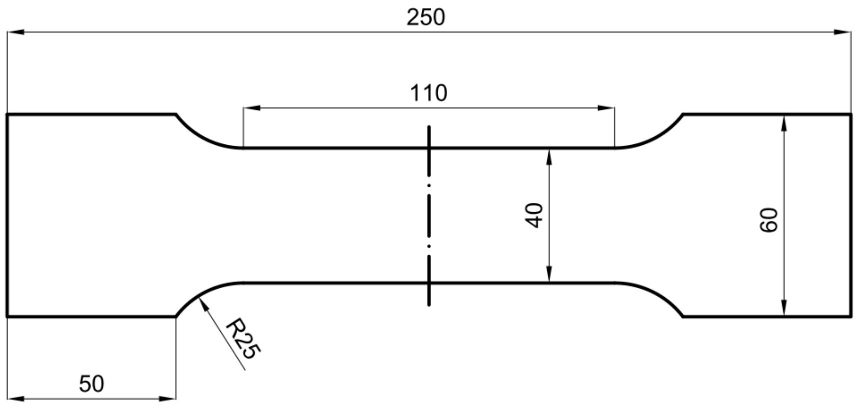

Figure 6.26. Dimensions of standard coupon specimens.

Figure 6.27. Testing machine (left) and mounted specimen with installed extensometer (right).

The stress-strain curves for specimens of different thickness are presented in Figures 6.28 – 6.30.

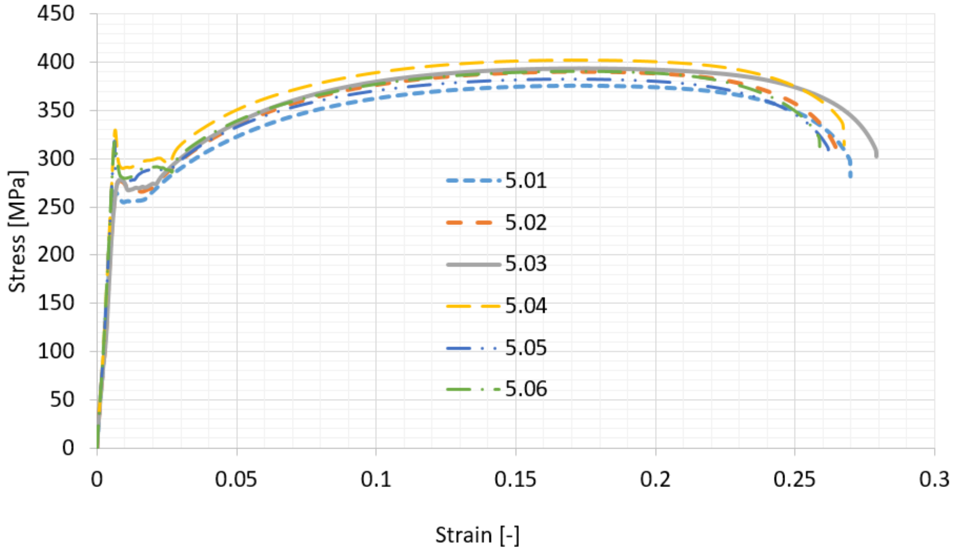

Figure 6.28. Stress-strain curves of 5 mm specimens.

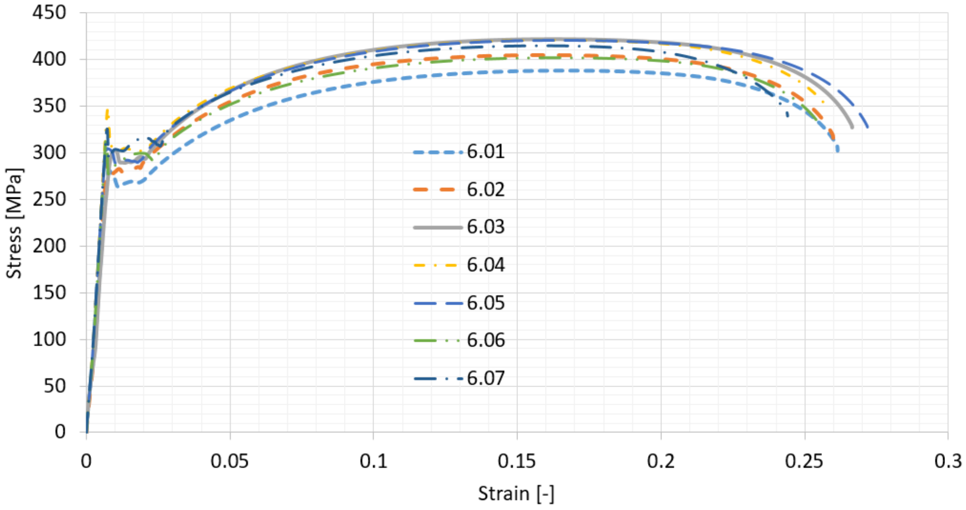

Figure 6.29. Stress-strain curves of 6 mm specimens.

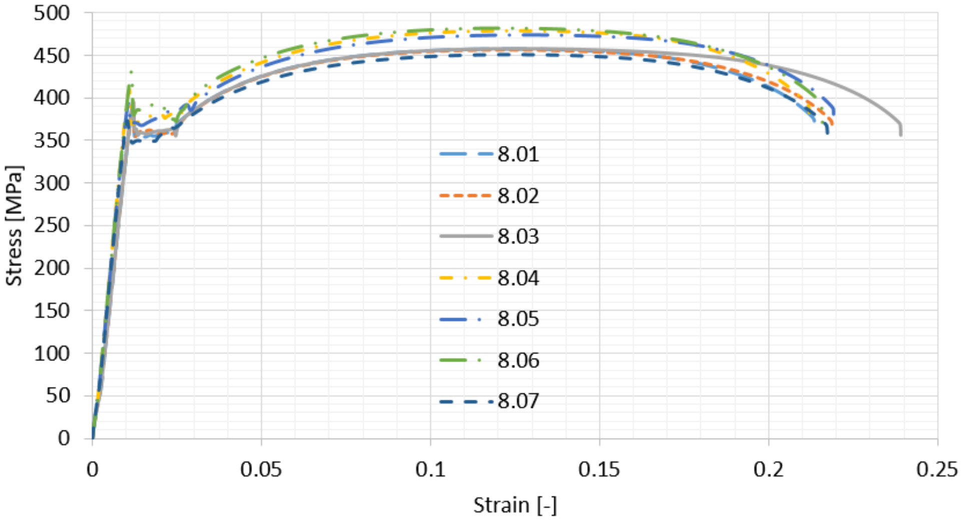

Figure 6.30. Stress-strain curves of 8 mm specimens.

The summary of the results of performed tensile tests is presented in Table 6.3. It could be noticed that in the case of each thickness, the mechanical properties are subjected to a significant level of uncertainty. In yield stress, the highest uncertainty is observed for a 5 mm plate, and the Coefficient of Variation is equal to 4.5 %.

Table 6.3. Results of tensile tests.

Thickness [mm]	Parameter	Young modulus E [GPa]	Yield stress R_e [MPa]	Ultimate tensile stress R_m [MPa]	Total elongation δ [-]
5	Mean	197.42	272.25	389.19	0.266
	St Dev	10.43	12.31	9.15	0.01
	COV [-]	0.053	0.045	0.024	0.027
6	Mean	196.38	284.36	410.30	0.260
	St Dev	7.57	12.57	12.66	0.01
	COV [-]	0.039	0.044	0.031	0.034
8	Mean	199.08	360.61	465.15	0.219
	St Dev	6.84	11.83	12.55	0.01
	COV [-]	0.034	0.033	0.027	0.041

6.5.2. Corroded specimens

After cleaning and measuring the corroded specimens, there were subjected to tensile testing. As a result, the stress-strain curves for each specimen has been obtained. The stress values were calculated with regards to the mean thickness value, which was calculated based on the degradation level, as reported in Table 4.8.

The stress-strain curves for 5 mm specimens were presented in Figure 6.31. This graph shows evident degradation of mechanical properties, including yield stress, ultimate tensile stress, and total elongation. Further, the yield plateau is smaller with corrosion development and even disappearing for strongly corroded specimens compared to intact specimens (see Figure 6.28).

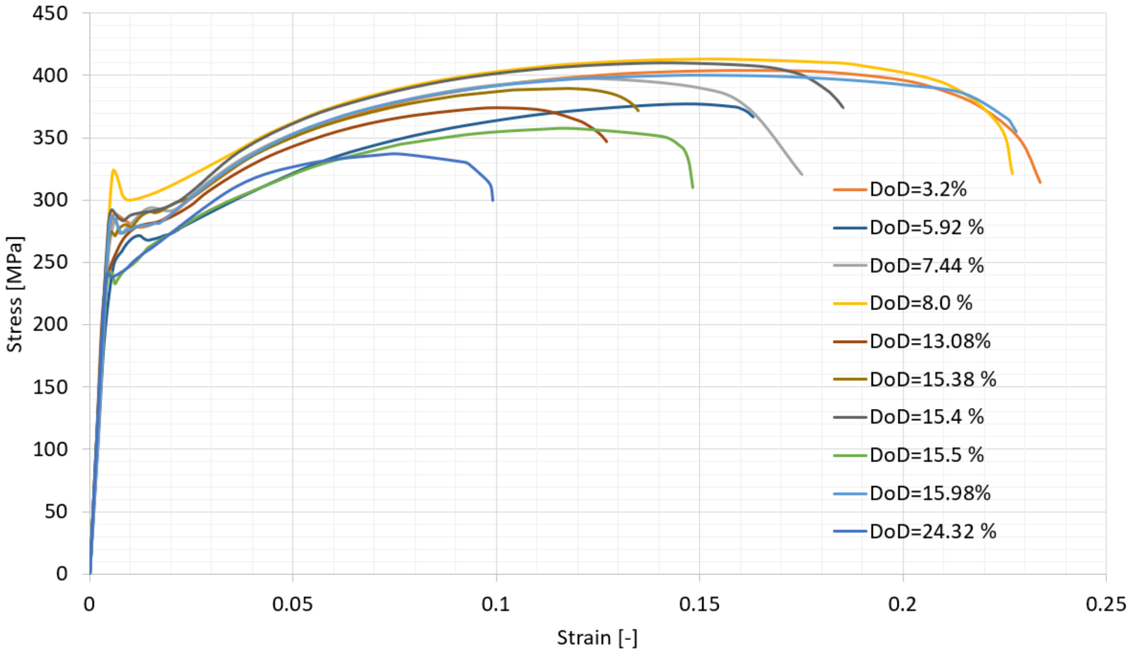

Figure 6.31. Stress-strain curves for 5 mm specimens subjected to corrosion degradation.

Similar observations could be captured for other groups of thicknesses. The stress-strain curves for 6 mm specimens are presented in Figure 6.32, whereas for 8 mm specimens are presented in Figure 6.33. The most evident differences in changes in yield stress could be noticed in Figure 6.33. In the case of the 6 mm specimens, those changes are smaller. Nevertheless, a lack of yield plateau for strongly corroded specimens and a significant drop of total elongation is purely visible in both cases.

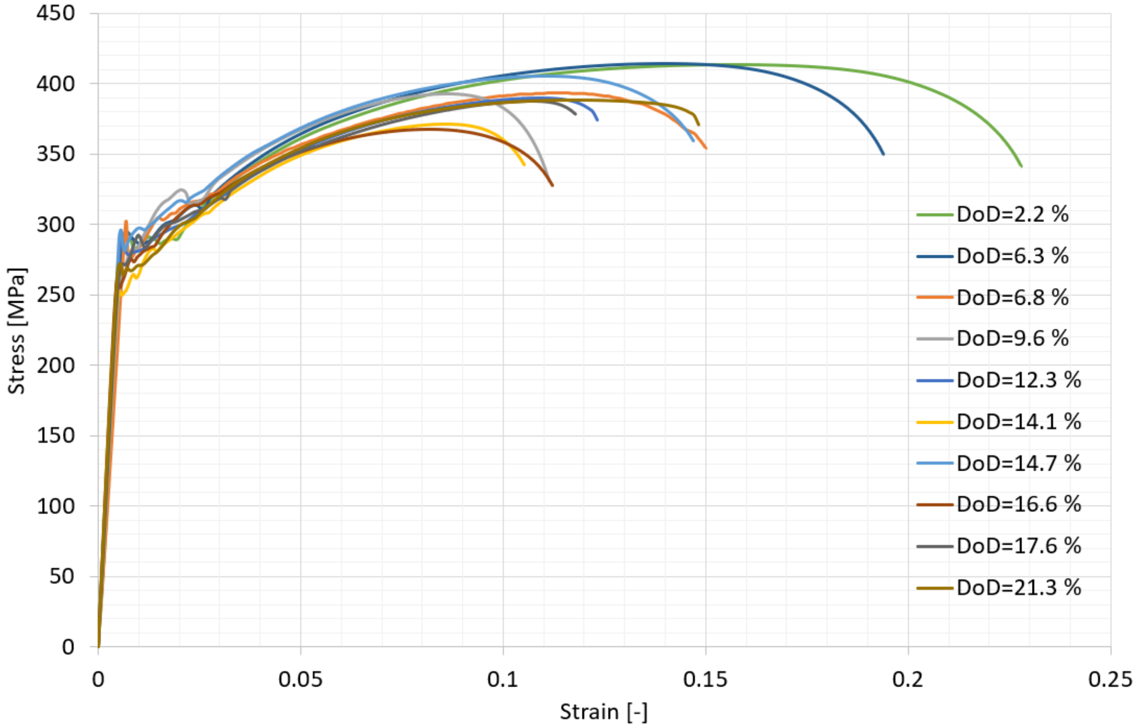

Figure 6.32. Stress-strain curves for 6 mm specimens subjected to corrosion degradation.

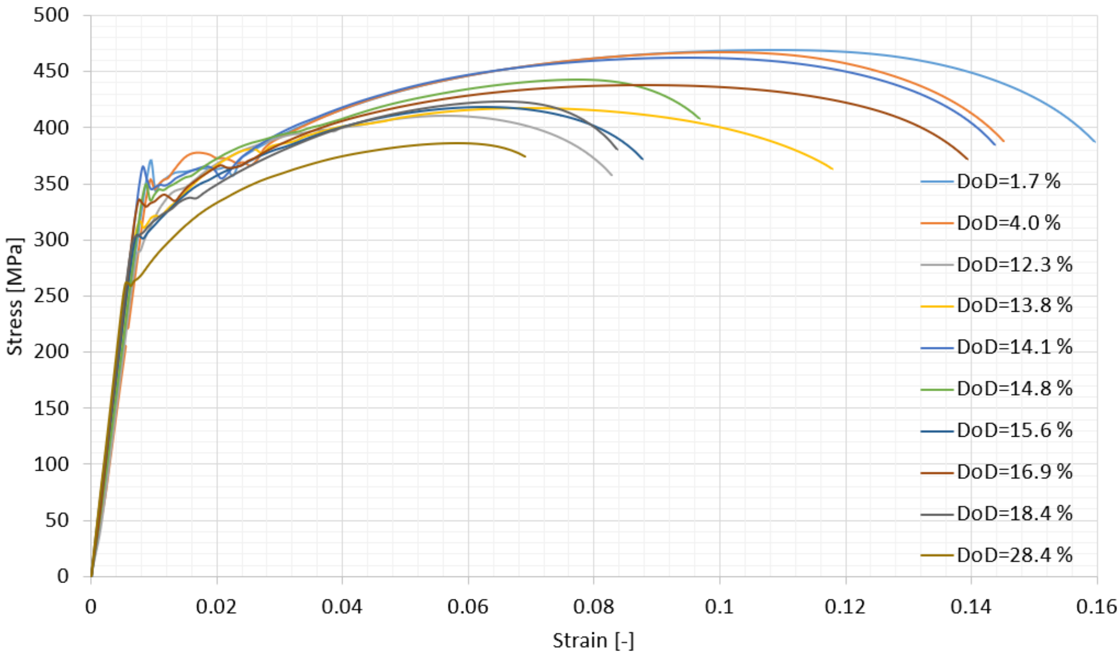

Figure 6.33. Stress-strain curves for 8 mm specimens subjected to corrosion degradation.

To develop the constitutive models for changes in mechanical properties with the corrosion development, the results for each thickness are plotted in function of the Degree of Degradation. The corrosion dependent mechanical properties for 5 mm specimens were presented in Figure 6.34. From the beginning, there is observed a large scatter of mechanical properties values. There are two sources of this phenomena. Firstly, significant scatter was observed for intact values of mechanical properties, as reported in the previous section. Secondly, since the corrosion process gives corroded characteristics of the specimens of stochastic origin, the mechanical properties are dependent on those.

Nevertheless, regardless of the high level of uncertainty, the evident reduction of mechanical properties is observed, and linear regressions are plotted. However, there was no correlation between variables in Young's modulus, and there were obtained very high values, bigger than the initial one, which should be considered false. The same observation is obtained for other thickness (Figures 6.35 and 6.36).

There are several possible reasons for such a situation. In the case of yield stress, ultimate stress and total elongation, these characteristics are somehow indicating the entire specimen's behaviour. However, in Young’s modulus, the strain is measured in the middle half of the length of the specimen via an extensometer. In the case of the prismatic specimen, this is purely valid, whereas, in the case of a corroded specimen, this is not showing the entire specimen's behaviour. As reported in corrosion scans, there are cases with areas of higher thickness in the middle of the probe, which will lead to relatively low values of strains when the mean thickness is considered a reference. Notably, the places of failure of the specimens were, in most cases, away from the middle (see Appendix 2). Thus, the obtained values of Young’s modulus cannot be taken as true, and this value is considered as a constant, initial one within the corrosion development.

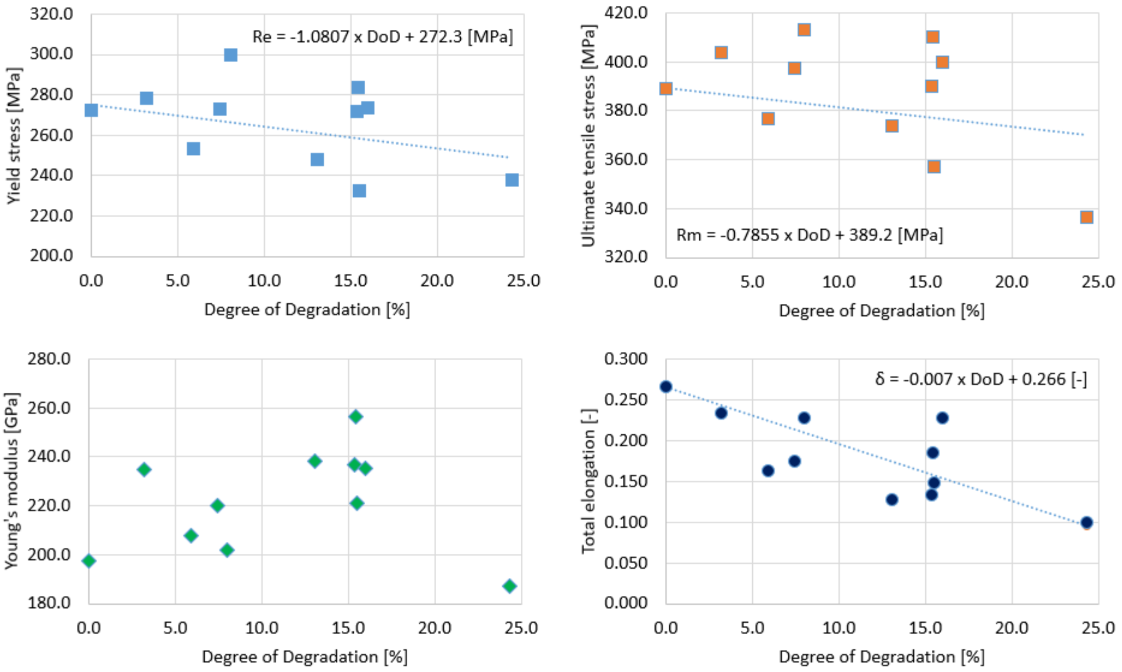

Figure 6.34. Corrosion dependent mechanical properties for 5 mm specimens.

The changes in mechanical properties for 6 mm specimens are presented in Figure 6.35. It is noted that there was observed a similar reduction of yield stress, whereas ultimate tensile stress degraded faster with comparison to 5 mm specimens. Similarly, the observed scatter of mechanical properties values are also quite high; however, it is slightly lower than Figure 6.34.

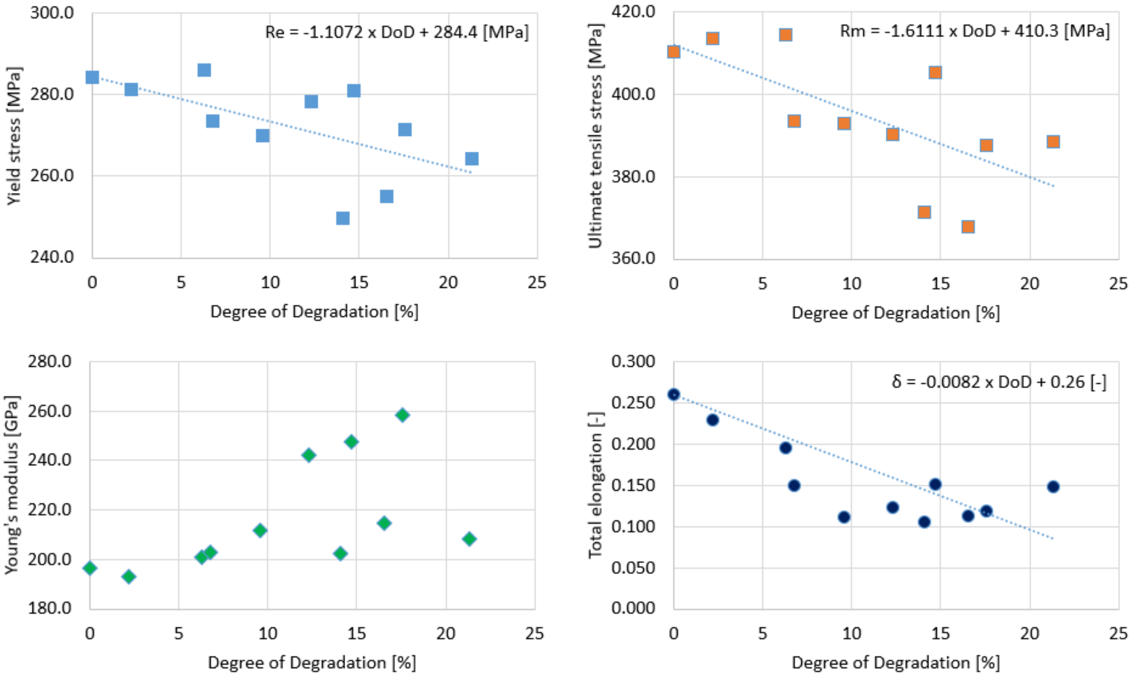

Figure 6.35. Changes in mechanical properties for 6 mm specimens.

The corrosion-dependent mechanical properties for 8 mm specimens are presented in Figure 6.36. Notably, the observed reduction of mechanical properties is significantly higher than other thicknesses, regardless of the higher initial values of yield stress and ultimate tensile stress (see Table 6.3). Furtherly, the observed scatter much lower, and values are closer to regression curves. Partially, this could result from the lowest uncertainty level of mechanical properties in the intact state, as reported in Table 6.3, compared to other specimens.

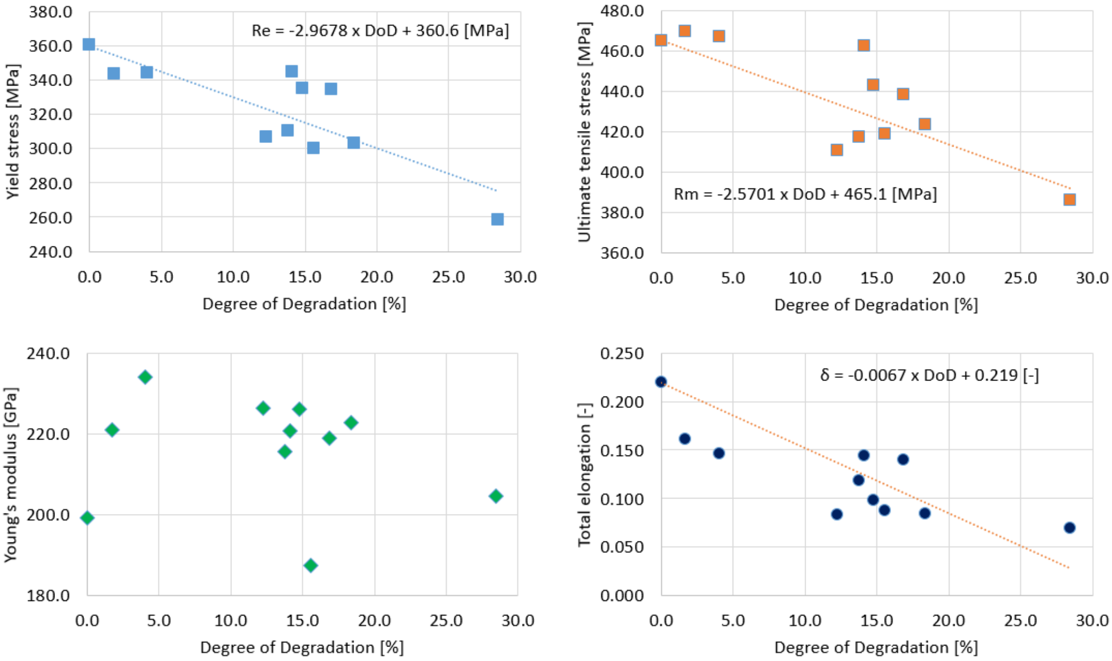

Figure 6.36. Changes in mechanical properties for 8 mm specimens.

Based on the presented results, one could draw the hypothesis that the thicker plate is, the higher reduction of mechanical properties is observed. However, it will be rather premature to make conclusions and more investigations will be needed at this staged. It could result from slightly different corrosion characteristics obtained for a different group of thicknesses (see Section 4.4.1).

The relationships that have been obtained in Figures 6.34-6.36 will be used for the other part of the Thesis for numerical modelling. As indicated, Young's modulus will be considered as an initial value for each thickness.

After failure, the specimens are presented in Appendix 2, where additional results of FE analysis are presented too (discussed in the other part of the Thesis). As indicated previously, for most cases, the position of failure was away from the middle. The positions are consistent with the areas of lower thickness within the specimen (see Appendix 1).

6.6. Compressive testing and pre and post-collapse analysis of stiffened plates.

6.6.1. Intact specimens [P5]

The experimental results for three specimens of different stiffness are presented in the form of force-displacement curves, as can be seen in Figure 6.37. With the increase of plate thickness, the inclination of the force-displacement curve is higher due to the rise of the specimen in-plane stiffness (the extent to which the element can resist deformation or deflection under the subjected load. The ultimate capacity point has been reached for a longitudinal shortening of 5 mm in 6 mm and 8 mm specimens. In the 5 mm stiffened plate case, the maximum force has been reached at the level of 7 mm of the longitudinal displacement. As can be noticed, in the case of all specimens, up to the 1 mm displacement, the behaviour is not stable, which could be the result of specimens fixing in the support at the beginning of the loading process. Although the adjustable fixing system has been designed, the total fixation before the load application is unachievable due to both support and specimen's unfairness. Furtherly, in the case of a 5 mm specimen, the exact bifurcation point can be noticed, with an axial force of 240 kN. This was also being observed, where excessive lateral deformations of the plate occurred. When considering 6 mm and 8 mm specimens, the exact bifurcation point cannot be traced. However, the moment of the buckling occurrence has been observed during testing. In general, the post-collapse behaviour has been similar between the specimens. The load force was not dropped suddenly after reaching the point of the maximum force. The ultimate strength is summarised in Table 6.4.

Table 6.4. Values of ultimate force for different thicknesses.

Thickness [mm]	Ultimate force [kN]
5	380.2
6	552.3
8	953.9

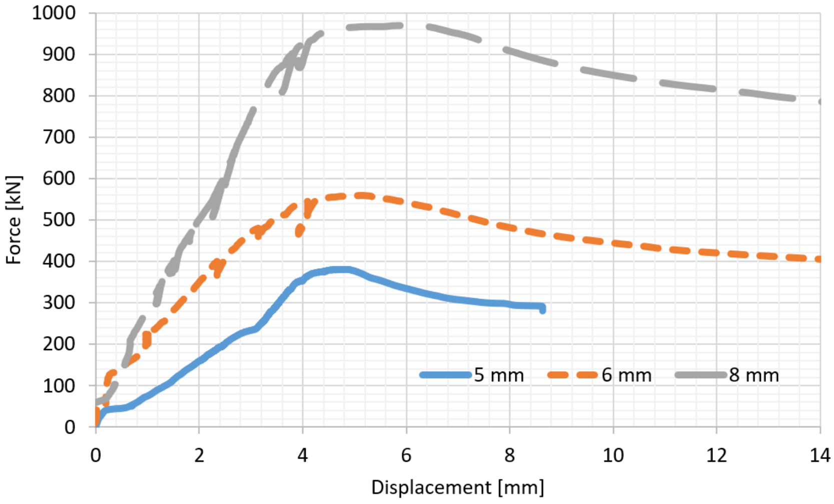

Figure 6.37. Force – displacement curves for tested specimens.

During experimental testing, it has been revealed that the longitudinal displacement measured as a displacement of the lower support overestimates that value. Thus, the relative displacement between upper and lower support has been used to measure longitudinal shortening of the stiffened plate.

The longitudinal membrane strains in the mid-cross-section are evaluated, and the strain gauges' measurements are analysed. The membrane strains are calculated as a medium value between two surface strains. The distributions for all specimens are presented in Figure 6.38. Two steps of the incremental load are chosen, one in the elastic stage and the other when the ultimate capacity is reached. For all specimens, the transition of longitudinal loads is non-uniform.

The welding region transmits most of the load, with a much higher rigidity than the rest of the specimen. The stiffened plate's free edges have the highest imperfection level, and in-plane stiffness is low from the beginning. However, the plate in the welding region is relatively flat, and due to the connection with stiffener, which forms a T-shape, it is much more resistant to out-of-plane bending.

Additionally, the highest initial imperfections are in the region of the side edges, which leads to a local plate bending from the beginning of the loading process. In the case of 5 mm and 6 mm specimens, the longitudinal strain distribution is relatively symmetrical. However, in an 8 mm specimen, the strain on one side of the plate is higher than on the other side. Both welding-induced stresses may cause this in combination with the non-symmetrical distribution of the initial imperfections.

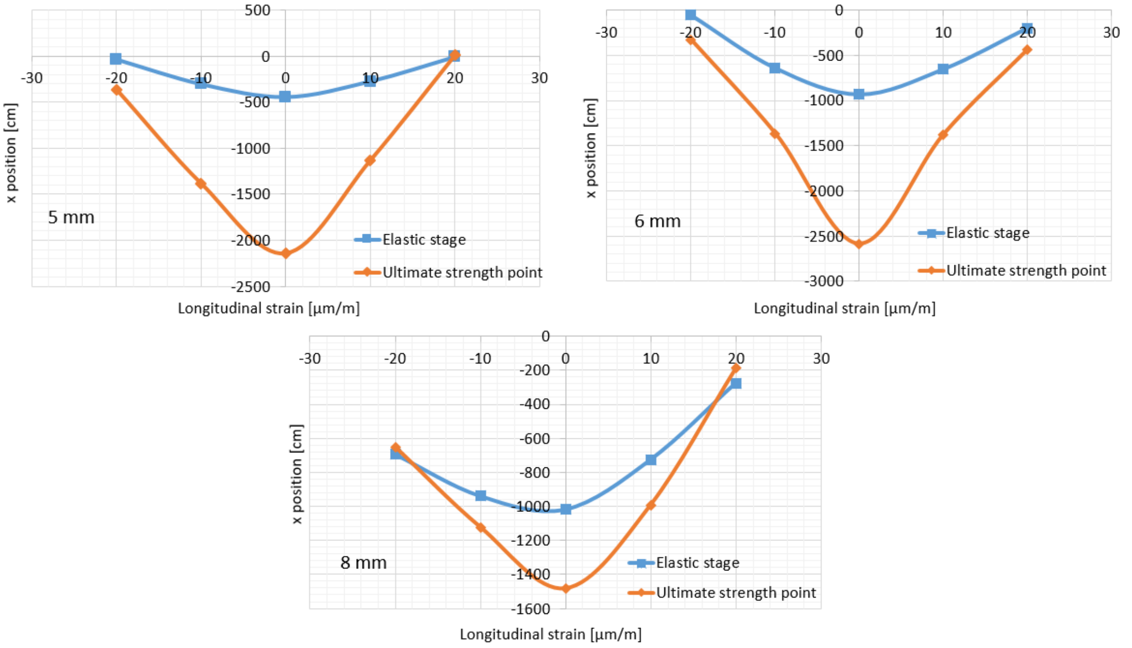

Figure 6.38. Longitudinal strain distributions, mid-cross-sections of the specimens.

Figure 6.39 shows the lateral mid-displacements of specimens as a function of longitudinal displacement. The longitudinal displacement increases up to a point where ultimate capacity is reached in all specimens. The negative displacement indicates that there is increasing in the stiffener. After reaching the ultimate strength, the displacements are decreasing, and the final values go the opposite sign in the case of 5 mm, and 8 mm stiffened plates. This behaviour indicates that in all cases, the collapse is caused by the secondary effects (i.e., local plate buckling and stiffener tripping), and the global column buckling has not occurred. It is also notable that in the case of 6 mm and 8 mm specimens, the displacements are much higher than those of the 5 mm specimen.

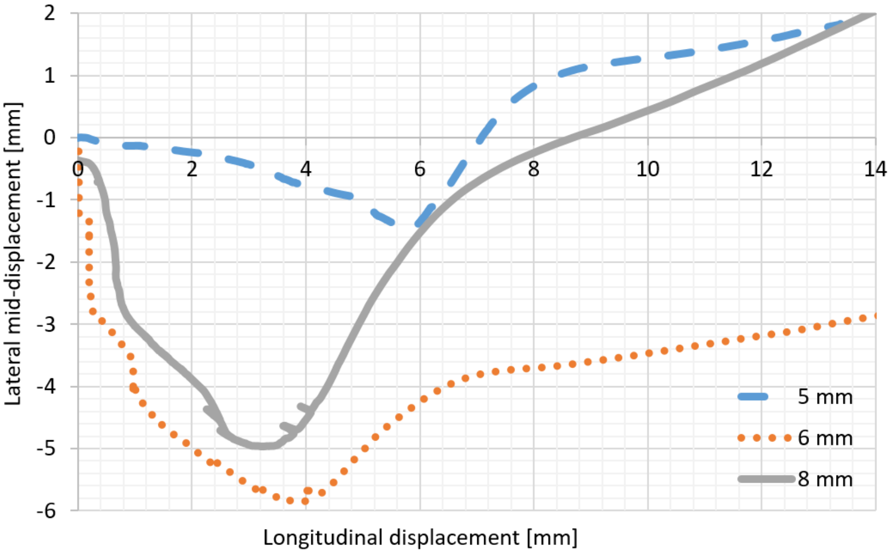

Figure 6.39. Lateral mid-displacements of the specimens.

The buckling modes of the stiffened plates are identified, and post-collapse shapes are analysed, as presented in Figure 6.40. The deflection forms of specimens are somewhat similar. Firstly, during the experimental testing, the plate buckled in both sides of the stiffener, having deflections in opposite directions. Furtherly, the plate buckling forced the rotation of the cross-section, and the stiffener tripping occurred. Finally, the critical cross-section crossed the yield point of the material, and the stiffened plate was unable to carry more load. Thus, the complex elastoplastic collapse mode has been observed, where the plate buckling followed by stiffener tripping was the trigger to cause the loss of the structural capacity. The global column buckling did not occur in the analysed cases, which was also observed in analysing the lateral mid-displacement of the specimens (see Figure 6.39). When one considers 5 mm and 6 mm thick specimens, the critical cross-section, where the highest deflections occurred, has not been located in the middle of the specimen, as estimated in pre-experimental numerical analysis. There are several reasons for that. Firstly, the actual shape of the initial imperfections is revealed to be non-symmetrical. In further investigations (Section 9.1.3), it was found that when one considers that the mechanical properties are non-uniform within the single specimen (which was observed by tensile testing of coupons from one plate), this could cause the change of the post-collapse form. When considering an 8 mm stiffened plate, it is noticed that the critical cross-section has been placed almost in the middle, which is consistent with the pre-experimental investigations.

Figure 6.40. Post-collapse shape for 5 mm (left), 6 mm (mid) and 8 mm (right) specimen.

6.6.2. *Corroded specimens*

The strain was not captured in corroded specimens to avoid destroying an irregular surface obtained after corrosion tests. The proper application of strain gauges will require the precise grinding of the surfaces in the installation regions. It was also indicated that the analysis of strain distribution for intact specimens would be enough to validate the numerical model. Additionally, to investigate corroded specimen behaviour in more detail, two displacement transducers were moved from the position near the support towards the section located in the mid-length of the specimen. In the case of intact specimens, there was more crucial to evaluate the actual boundary conditions for further validating the numerical model. However, for corroded structures, the possible asymmetric behaviour of specimen due to the unfair thickness distribution was more important. The distribution of displacement transducers for testing of corroded specimens is presented in Figure 6.41.

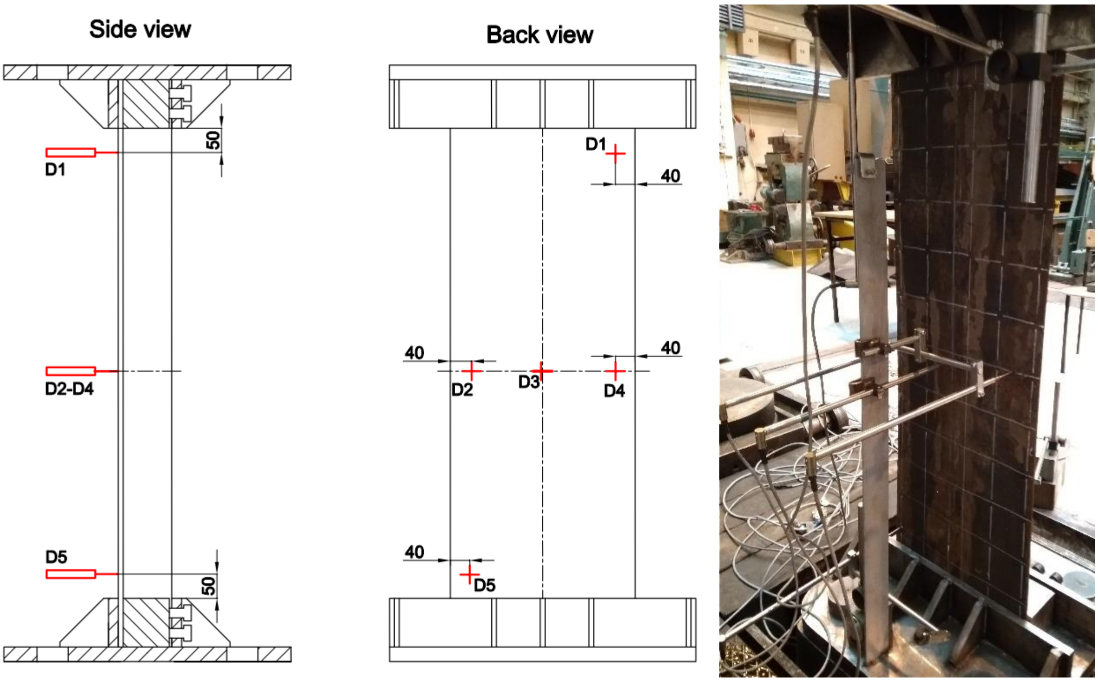

Figure 6.41. Distribution of displacement transducers for testing of corroded specimens.

The total number of nine corroded specimens has been tested, three for each thickness with different levels of corrosion degradation. The obtained values of the ultimate compressive force are presented in Table 6.5.

Table 6.5. Values of ultimate force for different thicknesses.

Thickness [mm]	Ultimate force [kN]			
	Intact	DoD = 7%	DoD = 14%	DoD = 21%
5	380.2	312.5	271.8	210.1
6	552.3	469.3	426.0	278.2
8	953.9	836.6	662.8	532.1

It could be noticed that the ultimate strength value significantly decreases with corrosion development. In Figure 6.42, the relative decrease of ultimate force concerning initial value depending on the DoD level is presented. It could be noticed that the decrease in strength is very similar for different thicknesses and follows the linear trend. In the case of mean thickness reduction of 21 %, the approx. 46% strength reduction has been observed. Although the plate slenderness will increase with thickness reduction, the decrease of ultimate capacity will be less dramatic if only thickness reduction plays a role. Thus, the reduction of mechanical properties (see Section 6.5.2), together with the non-uniform distribution of thickness in the stiffened plate, are the factors that are likely to contribute to that.

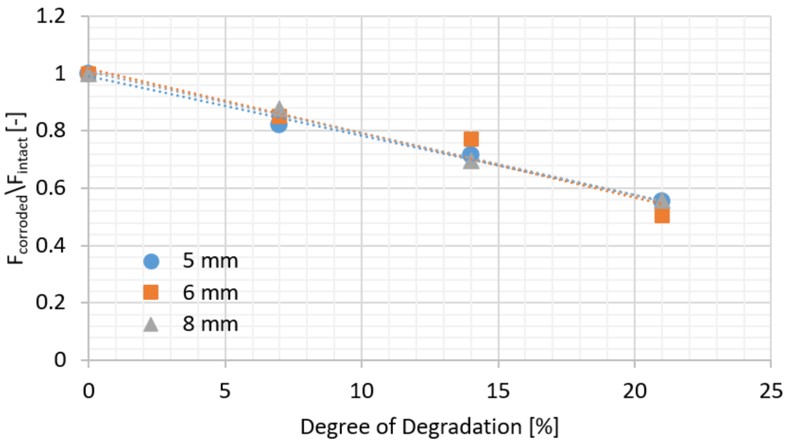

Figure 6.42. Relative strength reduction vs degradation level.

In Figure 6.43, the force-displacement curves for specimens of initially 5 mm thickness are presented. It is noted that the curves are quite similar. In the beginning, the slope of the curve is relatively low, which could be the result of fixing the specimen in the supports. Interestingly, the initial stiffness for an intact case is lower when compared to corroded cases. This could be the results of non-ideal measurements of longitudinal displacements. The initial slope is reduced within the range between 7% up to 21% of degradation level. However, for an intact case, the longitudinal displacement was measured only on lower support, which overestimated this value, as discussed before. It is noted that the moment of ultimate capacity has been reached for different longitudinal displacements between 3 up to 5 mm. Apart from that, there are not visible major differences in pre-collapse behaviour. In terms of post-collapse behaviour, the strongly corroded specimens seem to collapse more prominently, which could be seen in the case of a decrease of force after the ultimate point is reached. In the case of DoD=21 %, the post-collapse behaviour of the specimen was not traced due to the computer's error that captured the experimental data. Nevertheless, the most important value of ultimate capacity and pre-collapse stage has been captured.

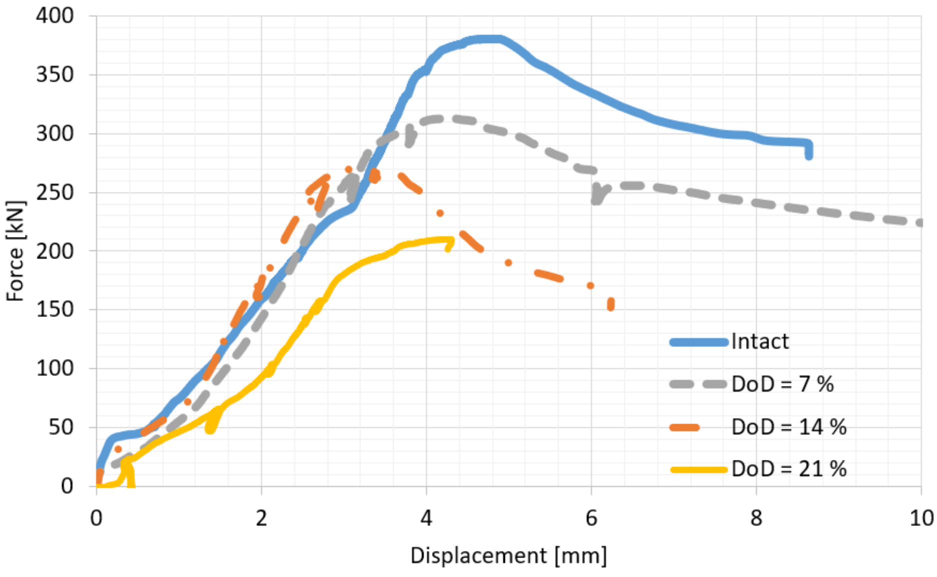

Figure 6.43. Force-displacement curves for 5 mm specimens.

In Figure 6.44, the force-displacement curves for specimens of initially 6 mm thickness are presented. Apart from initial differences cause by fixing of the specimens in the supports (specimens with 14% and 21% of corrosion loss), the force-displacement relationship is quite similar regardless of the degradation level. The ultimate strength is obtained at a similar point between 4 mm and 5 mm of longitudinal displacement. The initial slope of the curves decreases with the corrosion development In all curves. Both pre-and post-collapse regimes are rather similar.

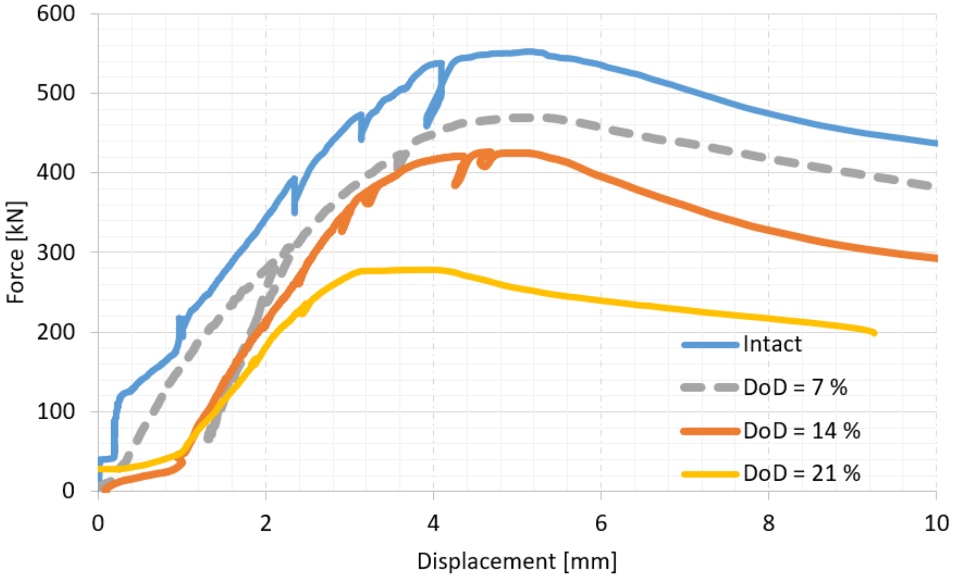

Figure 6.44. Force-displacement curves for 6 mm specimens.

The force-displacement curves for 8 mm specimens are presented in Figure 6.45. It is noted that the initial stiffness of the specimen was lower with the corrosion development, which is visible in terms of the initial slope of the force-displacement curves. The only difference is noted for a specimen with a degradation level of 7%, where some change in pre-collapse behaviour occurred. Nevertheless, both pre-and post-collapse behaviours were rather similar and were not strongly dependent on the level of corrosion degradation. The point of ultimate capacity has been reached between 4 mm and 6 mm of the longitudinal displacement.

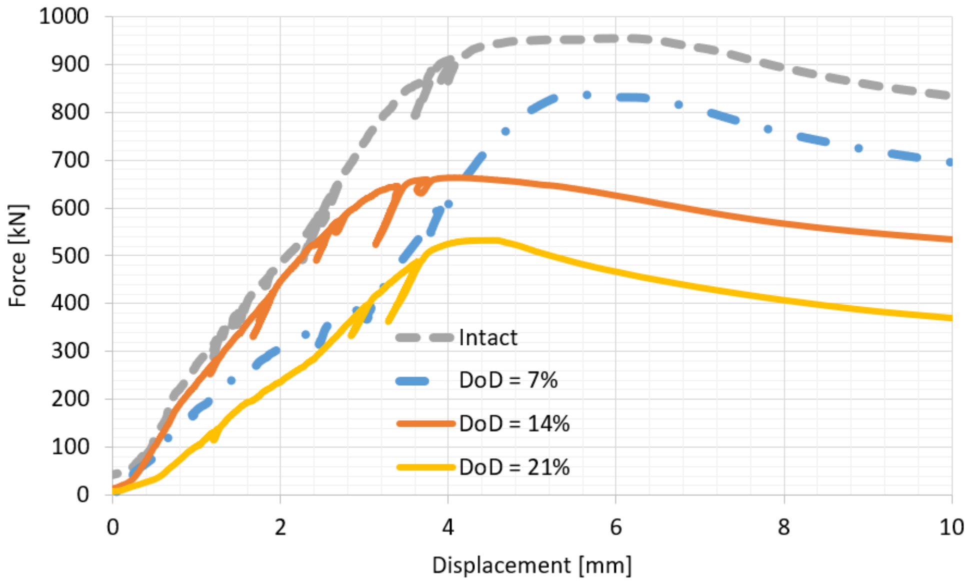

Figure 6.45. Force-displacement curves for 8 mm specimens.

The post-collapse shapes for 5 mm specimens are presented in Figure 6.46. It is noted that in the case of specimens with DoD of 7% and 21%, the collapse has been caused by the local plate buckling followed by stiffener tripping, similarly to intact specimens. The cross-section of the highest plastic deformations was away from the mid-length of the specimen due to the uneven distribution of the thickness of the plate and the stiffener for each degradation level. Further, in the specimen with a DoD of 14 %, the region of high plastic deformations was not that localised and has been more extended along with the specimen, which indicates that local mode of failure occurred, but global buckling too.

Figure 6.46. Post-collapse shapes for 5 mm specimens with degradation level of 7% (left), 14% (mid) and 21% (right).

The observations of post-collapse shapes for 5 mm specimens are consistent within measurements of mid-lateral displacements of the specimens (see Figure 6.47, left, top). It is noted that for both curves (DoD = 7% and DoD = 21%), the lateral mid-displacements increase slightly up to the point of ultimate capacity and then decrease due to the major role of local buckling. For the curve of DoD = 14%, not only local buckling occurred. Thus, the lateral mid-displacement increased after reaching the ultimate point, and there was significantly higher compared to other specimens.

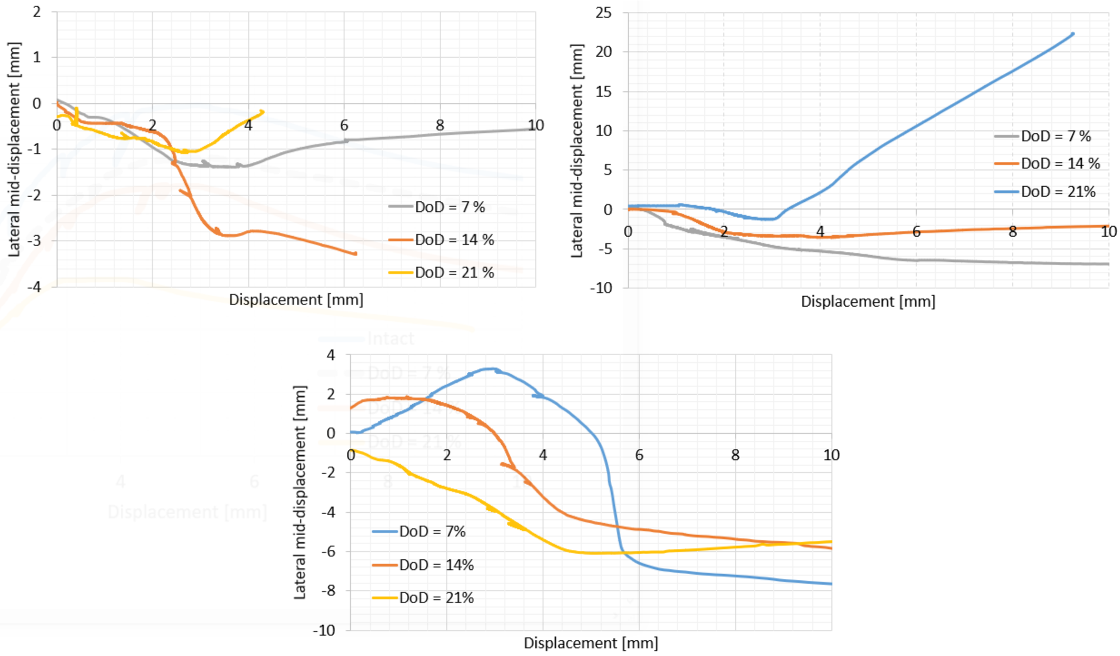

Figure 6.47. Lateral mid-displacements in corroded specimens of 5 mm specimens (left, top), 6 mm specimens (right, top) and 8 mm specimens (bottom).

The post-collapse shapes for 6 mm specimens are presented in Figure 6.48. In the case of 7% and 14% of degradation level, similarly to previous specimens, the collapse has been caused by local plate buckling followed by stiffener tripping. For those specimens, the regions of highest plastic deformations were obtained away from the middle of the specimen. Additionally, in a specimen with a 7% degradation level, the global buckling also contributed to the collapse mode, which could be noticed in the graph of lateral mid-displacement (see Figure 6.47). In that case, the displacement increased slightly after the collapse. In the case of a specimen with a degradation level of 7%, it was almost near the lower support. In the case of a most severe corroded specimen, the global column buckling was the primary cause of the collapse. It is visible by the significant localized plastic deformations in the middle of the stiffener. Furtherly, a significant increase in lateral mid-displacement is noticed in Figure 6.47 for this specimen. Additionally, apart from global mode, the local plate bucking was observed near the upper support.

Figure 6.48. Post-collapse shapes for 6 mm specimens with degradation level of 7% (left), 14% (mid) and 21% (right).

Figure 6.49 shows the post-collapse shapes of 8 mm stiffened plates. It is noted that the collapsed section in the case of 7% and 21 % of the degradation level was almost near the lower support. This was caused due to the high thickness diminutions in that region. The observed failure mode has been the local plate buckling followed by stiffener tripping for all specimens, similarly to other groups of thicknesses. However, for all specimens, some level of global buckling occurred too. The observations are supported by the measurements of lateral mid-displacements (Figure 6.47, bottom). It is noted that the displacements varieties up to the level of ultimate point, and there are slightly increasing after reaching the moment of highest compressive force.

Figure 6.49. Post-collapse shapes for 8 mm specimens with degradation level of 7% (left), 14% (mid) and 21% (right).

The results of lateral displacements in other points are discussed in detail in Section 9.4.2, where the numerical model is validated against experimental results.

Based on the results for corroded specimens, it could be concluded that the failure mode was similar to intact specimens. Nevertheless, for some specimens, global column buckling occurred subsequently with local plate buckling and dominated the failure in the case of one specimen. However, due to uneven distribution of thickness, the region of the stiffened plate, where the highest plastic deformations occurred, was rather away from the middle, and in many cases, was very close to the support. The corrosion caused a major decrease in ultimate strength, which was observed for different plate thicknesses.

7. MODELLING OF CORRODED PLATE SURFACES

The corroded plate surface modelling is one of the most challenging problems related to the analysis of corroded structural elements using different numerical techniques.

A brief review of existing models has been already done in Section 2.3.5. Nevertheless, the current chapter provides a full description of the methods used in the presented thesis. Finally, it needs to be highlighted that the discussed modelling techniques are related solely to the general corrosion degradation, and pitting corrosion is not in the scope of the presented investigations.

7.1. Uniform corroded surface degradation

The primary and simplest model of general corrosion degradation is the uniform one, which assumes that the thickness loss of the plate due to the corrosion is identical in the entire surface. The mean value of corrosion loss could be estimated with the use of models presented in Section 4.1.2.

This type of modelling has many advantages. It is easily applicable to different types of analysis, including closed-form formulations and more advanced methods, such as FE modelling. In all cases, only thickness parameter varieties. Due to that reason, it is used in the Rules of Classification Societies [5], where fast approaches are needed. In that case, the structural behaviour in the design stage is predicted with the deduction of so-called corrosion additions. The corrosion additions are estimated based on the region on ship cross-section and type of cargo, based on the measurements done in operating ships.

Apart from the great applicability of this type of modelling, it has several major disadvantages that cannot be disregarded. Firstly, the surfaces of corroded plates are rather irregular. Thus, when evaluating the strength of structural elements with the uniform thickness distribution, it could lead to non – conservative design. Secondly, it could be seen from experimental testing that areas of lower thickness surrounded by the areas of higher thickness will lead to different structural behaviour compared to plates of constant thickness. Lastly, as discussed previously, in the micro-scale, the localized dense irregularity can cause the degradation of the mechanical properties of the corroded steel elements.

In the last discussed disadvantage, the possible extension of this model was developed in [190], which was the work consisting of preliminary investigations done before this thesis. In this work, the model of stiffened plates consisting of an averaged plate thickness reduction and mechanical properties changes was developed and validated using experimental tests [189], showing a good agreement. The applicability of a similar model was proven in [181], where the flexural performance of corroded beams was investigated. The experimental studies were conducted, including estimating mechanical property changes resulting from the corrosion degradation development of small-scale coupons. The FE shell model consisting of coupled thickness changes and the mechanical properties changes was adopted showing good with the experimental results. Apart of that, it seems that more validation work is still needed.

7.2. Non-uniform corroded surface degradation

The more advanced corrosion model, and at the same time, more close to the reality, is the non-uniform degradation of the corroded surface. However, we can introduce two types of non-uniformity, i.e. global and local ones.

The global non-uniformity comes from the different rates of the corrosion process within the single structural element, and it is typically captured via ultrasonic measurements. The local non-uniformity, on the other hand, is very localized and cannot be captured via typical ultrasonic measurements since the observed non-uniformities (even below 1 mm) are of a lower scale than the typical size of gauging probe. Additionally, to capture that, the very detailed surface cleaning and advanced scanning techniques are the only possible way [177–179], which is hard to obtain in in-situ conditions. Further, to incorporate that in the numerical model, the very dense FE mesh will be needed, leading to the very big effort of both computations and model preparation, which is non-efficient in engineering practice [160]. Thus, as described in the previous section, the changes in mechanical properties can capture that effect in a much simple way. To summarizing, depending on the corrosion environment and process, we can get the relatively uniformly corroded element, but with the very non-uniform localized corrosion. From another perspective, the corrosion loss could be subjected to significant scatter, but the corroded surface can be relatively flat. The summary of the proposed distinction between different corrosion types and models is presented in Figure 7.1.

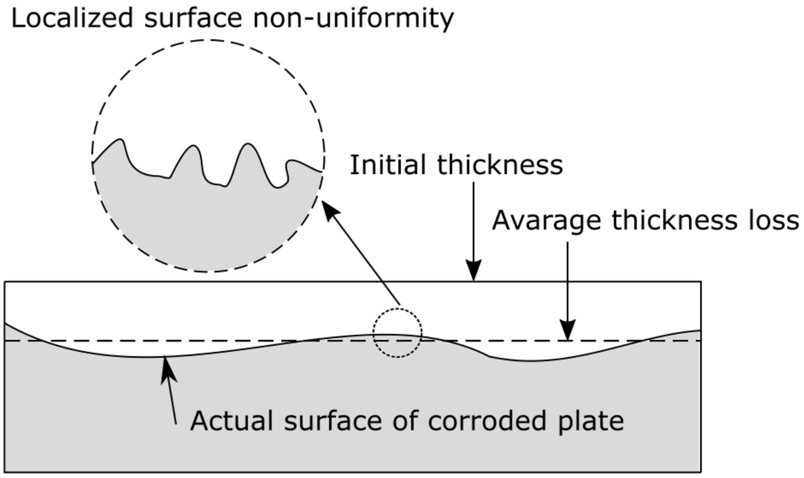

Figure 7.1. Corrosion types and models.

Due to the stochastic origin of the corrosion degradation process, the approach that was found to be most suitable in the presented thesis is the generation of corroded surfaces with the use of random field modelling. The methodology is flexible and allows for the generation of corrosion surfaces in both levels, i.e. global and local ones, and it is described in detail in the next section.

7.3. Random Field modelling

Due to the complexity of methods for measurements of different structural imperfections, such as corrosion degradation, initial distortions, etc., random field modelling [257] seems to be a powerful tool for modelling such imperfections. The examples of random field modelling to reflect the geometric and material imperfections can be found in [258–260]. The possibility of stochastic modelling of the corrosion field was also presented in [261]. Additionally, the random field approach can provide many samples that are usually hard to obtain, especially for relatively large structures such as ships or offshore platforms. Thus, it can be exploited in the reliability analysis [237].

The spatial distribution of irregularities of the corroded surface may be modelled by the random field approach as the one that is the most suitable for this purpose due to the set of an infinite number of spatially correlated random variables. For engineering purposes, one needs to find a random field with a finite number of random variables, and with this respect, the Gaussian random field can be defined entirely by its mean $\mu(\boldsymbol{x})$, variance $\sigma^2(\boldsymbol{x})$ and autocovariance function $C(\boldsymbol{x},\boldsymbol{x}')$.

Different discretization methods of the random field are available. In the present study, the Karhunen – Loeve expansion [262] simulates the random field for a specific mesh density. Other discretization methods may be found in [262,263]. The Karhunen – Loeve expansion is widely used in stochastic Finite Element methods due to some useful properties, including the positive covariance matrix, a limited number of random variables, and, undoubtedly, convergent. According to this expansion method, the random field can be expressed as follows:

$$H(\boldsymbol{x},\theta) = \mu(\boldsymbol{x}) + \sum_{i=1}^{\infty} \sqrt{\lambda_i}\,\xi_i(\theta) f_i(\boldsymbol{x}) \tag{7.1}$$

where λ_i and $f_i(\boldsymbol{x})$ are the eigenvalues and eigenvectors of the covariance function $C(\boldsymbol{x},\boldsymbol{x}')$ where $\boldsymbol{x}$ and $\boldsymbol{x}'$ are two coordinates defined for a specific mesh density. In the random field defined in a 2D surface, each vector will consist of two components.

The parameter $\xi_i(\theta)$ is defined as a set of uncorrelated random variables with a mean value and covariance function of:

$$E[\xi_i(\theta)] = 0 \tag{7.2}$$

$$E\left[\xi_i(\theta)\xi_j(\theta)\right] = 1 \tag{7.3}$$

Assuming that $H(\boldsymbol{x},\theta)$ is a zero-mean Gaussian process, $\{\xi_1(\theta),\xi_2(\theta),\dots\}$ is a vector of uncorrelated random variables sampled from a zero-mean normal distribution.

Truncating the series from Eq. 1 after the n$^{\text{th}}$ term, one can obtain an approximated solution of $H(\boldsymbol{x},\theta)$:

$$\widehat{H}(\boldsymbol{x},\theta) = \mu(\boldsymbol{x}) + \sum_{i=1}^{N} \sqrt{\lambda_i}\,\xi_i(\theta) f_i(\boldsymbol{x}) \tag{7.4}$$

The corresponding autocovariance function is given by:

$$\widehat{C_{HH}}(\boldsymbol{x},\boldsymbol{x}') = \sum_{i=1}^{N} \sqrt{\lambda_i}\, f_i(\boldsymbol{x})\; f_i(\boldsymbol{x}') \tag{7.5}$$

When the mean value and variance are constant, the autocovariance function depends only on an absolute distance between points x and x'; the field is homogenous. Different types of autocovariance function can also be used. In the presented study, the square exponential autocovariance is used:

$$C(\boldsymbol{x},\boldsymbol{x}') = \exp\left(\frac{(\boldsymbol{x}-\boldsymbol{x}')^2}{c_0^2}\right) \tag{7.6}$$

where $(\boldsymbol{x}-\boldsymbol{x}')$ is the absolute distance and c_0 is the correlation length (also known as a damping parameter). The correlation length is the most influencing parameter changing the spatial variation of the field. When c_0 increases, the correlation is extended, and the field becomes smoother, and when c_0 decreases, the correlation is reduced, and the field is more irregular. The example of different level of correlated fields is presented in Figure 7.2, where the fields are with an identical mean value and variance but different correlation lengths.

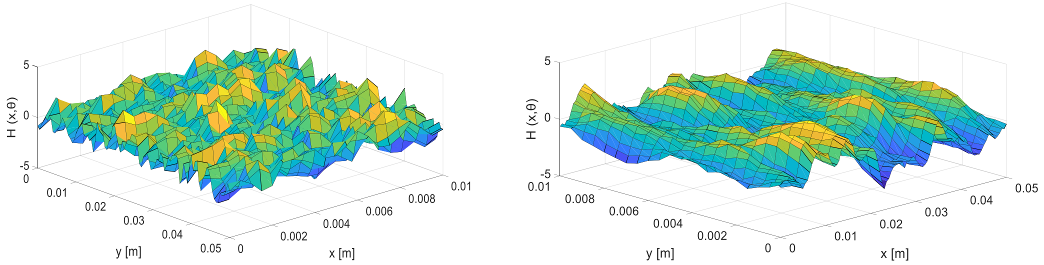

Figure 7.2. Random field with reduced (left) and extended (right) correlation.

The random fields are generated using MatLab software [264] and specially developed code [265], generating a Gaussian random field for a specified mesh density and different correlation lengths. The calibration of the correlation length is based on the real corrosion degradation measurements.

However, as can be seen in some studies, such as in [160], where detailed measurements of the corroded surface were carried out, the maximum corrosion depth is much higher than the mean value, which leads to the log-normal distribution of the corrosion depth. For proper modelling, the normal field is transformed into a log-normal field in the case of the present study as:

$$L(\boldsymbol{x}) = \exp\big(\mu + \sigma H(\boldsymbol{x})\big) \tag{7.7}$$

where μ and σ are the scaling parameters of the log-normal field, and they are calibrated to produce a proper mean value and standard deviation of the random field. The random field transformation example is presented in Figure 7.3, where the normal random field is with a zero mean value and variance equal to one. The scaling parameters of the log-normal distribution are equal to zero and 0.5, respectively. It can be noticed that negative values of the normal field are flattened in the log-normal field, whereas positive values are sharpened.

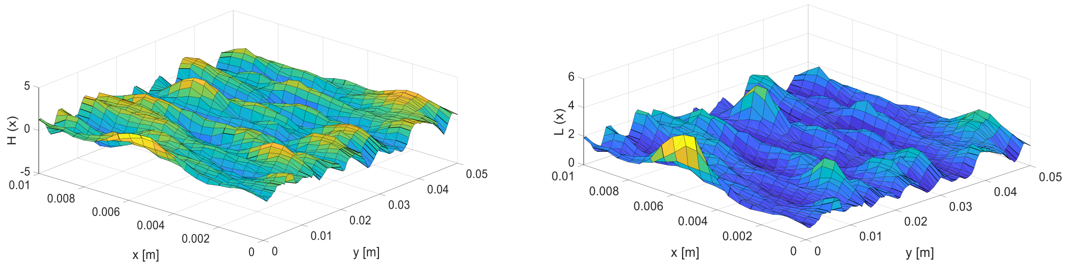

Figure 7.3. Normal (left) and log-normal (right) random field.

7.4. Corrosion degradation modelling with the use of random fields

7.4.1. Local corrosion degradation

The random field of the corroded specimen surface can be generated for the assumed standard deviation and mean value of the corrosion depth. The corrosion degradation may be one or two-side developed depending on the environmental conditions and structural component location and position. In both cases, some corrosion degradation descriptors are distinguished. The adopted approach in the present study is presented in Figure 7.4, and a typically generated random field of corrosion is presented in Figure 7.5. The initial thickness t_0 is the as-built thickness of corroded specimen and t_{max} is the maximum residual corroded plate thickness. The difference between those two variables divided by the initial thickness is the uniform degree of degradation:

$$DoD_u = \frac{t_0 - t_{max}}{t_0} \tag{7.8}$$

In the present study, the two-side corrosion degradation is analysed, and the corrosion descriptors are presented in Figure 7.4. One can distinguish the initial thickness of the specimen as t_0 and the maximum residual thickness after corrosion degradation as t_{max}. Based on that, the uniform degree of degradation is derived as:

$$DoD_u = \frac{t_{ini} - t_{max}}{t_{ini}} \tag{7.9}$$

At any particular point of the corroded specimen, one can distinguish the corrosion depth in the upper surface (h_u) and in the bottom surface (h_b). Similarly, there is a mean and maximum corrosion depth in both surfaces, $\overline{h_u}$ and $\overline{h_b}$ as well as Δh_u and Δh_b, respectively. The minimum residual thickness is calculated as:

$$t_{min} = t_{max} - \Delta h_u - \Delta h_b \tag{7.10}$$

By calculating the total volume of the corroded specimen, $V_{corroded}$, the non-uniform corrosion degradation level can be calculated as:

$$DoD_n = \frac{t_{max} \cdot A - V_{corroded}}{t_0 \cdot A} \tag{7.11}$$

The total degradation level is equal to:

$$DoD = DoD_u + DoD_n \tag{7.12}$$

The cross-sectional areas A_i (see Figure 7.4) are calculated along with the specimen and the minimum cross-sectional area A_{min} is obtained.

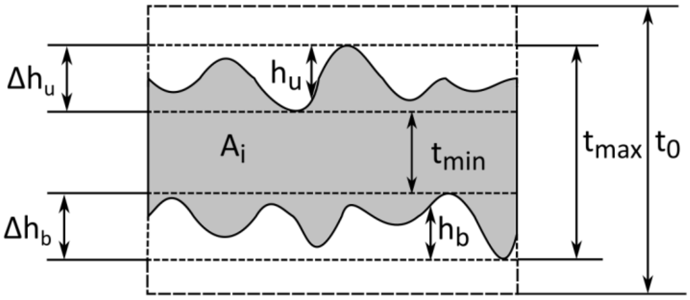

Figure 7.4. Corroded specimen cross-section.

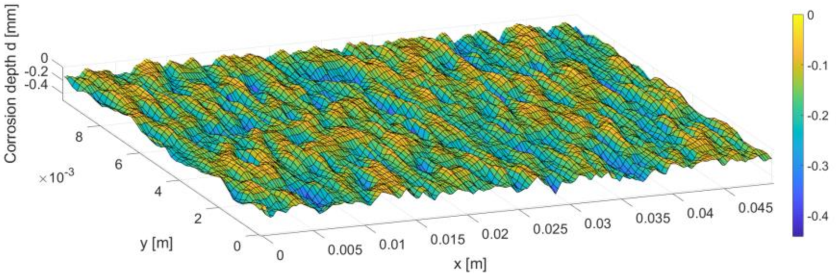

Figure 7.5. Example of the randomly generated corroded surface.

One can choose different corrosion descriptors as a reference value for the mechanical properties estimation, i.e. the average thickness, maximum thickness, minimum cross-sectional area, initial thickness, etc. Only detailed measurements of the mass and detailed scanning of cleaned specimens can provide reliable information to identify the corrosion degradation descriptors, as it was performed in the current study. Thus, the mean thickness was used for the estimation of mechanical properties in Section 6.5.2. However, in real operational conditions, such measurements are impossible. Since the proposed model can be used for real structures, the most common factor for identifying the severity of the degradation is the residual thickness during service life employing the ultrasonic method [266]. In the study presented in [233], analysis of ultrasonic measurements for the rough surface in the back wall of the analysed specimen is shown (a situation was very often seen during inspections). The output is subjected to a high uncertainty level, magnified by the corroded surface's irregularities.

Additionally, they showed that the ultrasonic method tends to show higher thickness values than average corroded plate thickness. This was also observed in the presented work (see Section 4.4.2), where even the minimum value of ultrasonic thickness measurements from two sides brings higher values than the mass measurement. When this method evaluates structural capacity during service life, it seems more reasonable to take either maximum residual thickness as a reference factor in the estimation of mechanical properties or the mean thickness value with the addition of bias between the ultrasonic method and precise mass measurements.

7.4.2. Global corrosion degradation

Similarly to the local corrosion degradation, where random fields with rather low correlation levels are generated, the thickness of the corroded plate on a larger scale could also be modelled using a random field approach.

The statistical information of mean values and standard deviation of corroded plate thickness is needed. To estimate the level of corrosion depth uncertainty, which will be the same as the uncertainty level of residual plate thickness, one can use the real corrosion depth measurements.

The examples of such application into numerical analysis and more detailed information is provided in Section 9.3.

8. NUMERICAL ANALYSIS OF CORRODED SPECIMENS SUBJECTED TO TENSILE LOAD

In the presented chapter, the non-linear FE method is employed to evaluate the tensile behaviour of corroded specimens. The corrosion degradation is modelled with the use of a random field approach. The validation of the proposed methodology is based on the existing literature, experimental results [160,161], and tensile tests presented in Section 6.5.2. This shows the applicability of the presented approach for specimens subjected to different corrosion environments (atmospheric corrosion in [160,161] and marine immersed corrosion in own studies) as well as with different thicknesses (very thin plates in [161] and thick plates in [160] and own studies).

In Section 8.1, the description of FE modelling is provided, and sensitivity studies related to governing parameters of the random field of corrosion are presented in Section 8.2. In both of these sections, the mechanical properties and specimen dimensions are taken from experimental tests of [160]. Nevertheless, the obtained results and presented calibration procedures are identical for the other validation cases.

The comparison between numerical and experimental results is presented in Section 8.3 (experiment from [160]), 8.4 (experiment from [161]), and 8.5 (own experiments). In Section 8.6, the model for changes in mechanical properties for design purposes is proposed. In Section 8.7, the conclusions related to all of these cases are provided. In the case of 8.3 and 8.4 sections, the maximum residual thickness t_{max} is used as a reference one to calculate the mechanical properties, in order to keep the consistency with the referenced studies. However, in case of Section 8.5, the mean thickness t_{mean} is used as a reference one, as it was done in Section 6.5.2.

8.1. Non-linear FE modelling [P7]

To simulate the tensile test of steel specimens, ANSYS LS-DYNA [267] software is employed. The multilinear stress-strain relationship of the material and SOLID 164 elements are used with the explicit dynamics solver. Apart from the tensile testing quasi-static origin, the explicit solver is used to pass the convergence problem [268], originating from corrosion degradation and the necking phenomenon. In the standards of tensile testing [256], the engineering stress-strain curve is established. However, in the FE analysis, one needs to define the true stress-strain ($\sigma_{true} - \varepsilon_{true}$) relationship as:

$$\varepsilon_{true} = \ln(1+\varepsilon) \tag{8.1}$$

$$\sigma_{true} = \sigma(1+\varepsilon) \tag{8.2}$$

where σ and ε are engineering stress and strain, respectively.

The above formulations are valid up to the ultimate tensile strength point. Where the necking phenomenon starts to occur, and the power-law based procedure is introduced [269]:

$$\sigma_{true} = K\varepsilon_{true}^{n} \tag{8.3}$$

where n and K are the strain hardening parameter and strength coefficient, respectively.

Figure 8.1 shows the specimen scheme and the FE model. The area of the specimen's corroded part is of a size of 50x25 mm, and thus the mesh is very dense in this region. In the case of mounting and transitional parts of the specimen, their finite-element size is not relevant since they mainly distribute the longitudinal load. For simulating the experimental conditions, the mounting parts are fixed, and one of them is subjected to a longitudinal displacement. The displacement is realized via small increments in the time domain in the explicit solver.

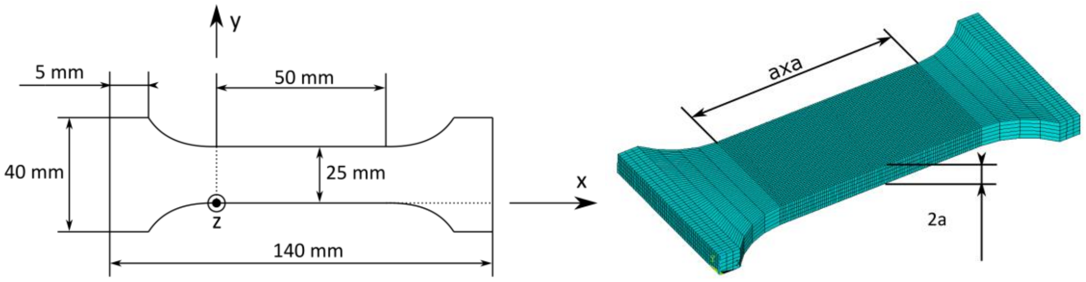

Figure 8.1. Specimen scheme (left) and FE model (right).

To identify the proper element size, mesh convergence studies are carried out. The analysis results with an element size, a from 0.5 mm up to 5 mm, are presented in Figure 8.2. The most refined mesh provides accurate results. However, with the element size of 1 mm, the results are also accurate. Nevertheless, further analysis showed that the 0.5 mm mesh size should be chosen to provide a good representation of the corrosion field, especially for the weaker correlations. It is important to mention that significant differences in total elongation between coarse and refined mesh reaching 40 % in the case of 5 mm mesh are observed, which may be due to the complexity of the necking behaviour. During necking, the strain is highly non-uniform within the mid-cross-section, and the highest strain is visible in the middle. In FE modelling, only the strain in the middle of any particular element can be captured. When the element size is relatively big, the strain distribution is reasonably accurate, and the middle elements show a smaller strain than the accurate one. Thus, the failure criteria are defined with a higher mean elongation, and the total elongation is higher when compared to an accurate one. With mesh refinement, the total elongation tends to an accurate value.

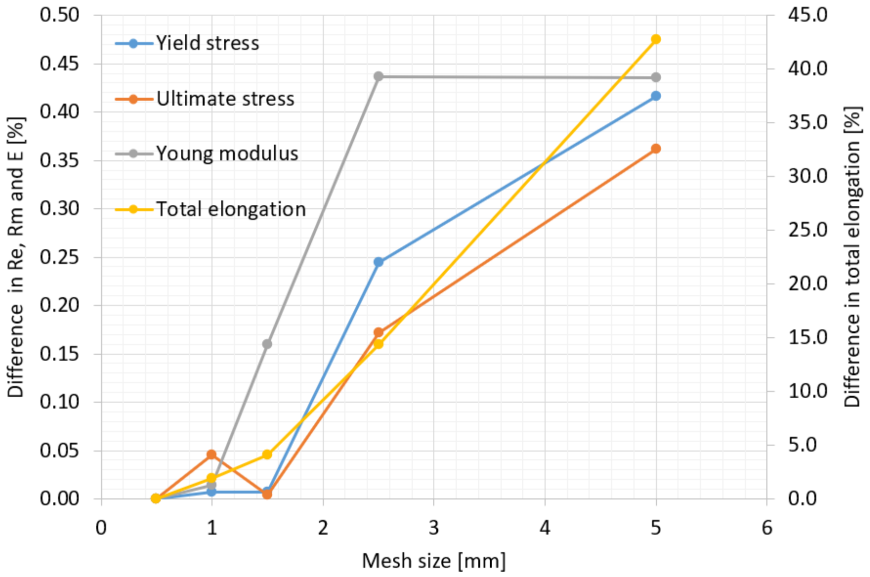

Figure 8.2. Mesh convergence studies.

The material properties of mild steel S235 obtained via tensile testing are as follows: yield stress $Re = 292.6\ MPa$, Young modulus $E = 207\ GPa$, ultimate tensile stress $R_u = 435\ MPa$ and total elongation $\delta = 35.2\ \%$. The output engineering stress-strain curve and input curve for the FE analysis compared to the experimental one are presented in Figure 8.3. Both numerical and experimental curves are almost identical with a minimal deviation. The first part of the input curve was obtained using Eqns 8.1 and 8.2 up to the ultimate tensile stress point (strain equal to 0.182). The calibration of the second part is done using Eqn 8.3 and the following parameters: $\varepsilon_{failure} = 0.9\ [-], K = 750\ MPa, n = 0.214\ [-]$. The element breaks when a defined failure strain is obtained. The proper modelling of the tensile behaviour in the FE analyses may be seen in Figure 8.4, where the necking phenomenon is visible.

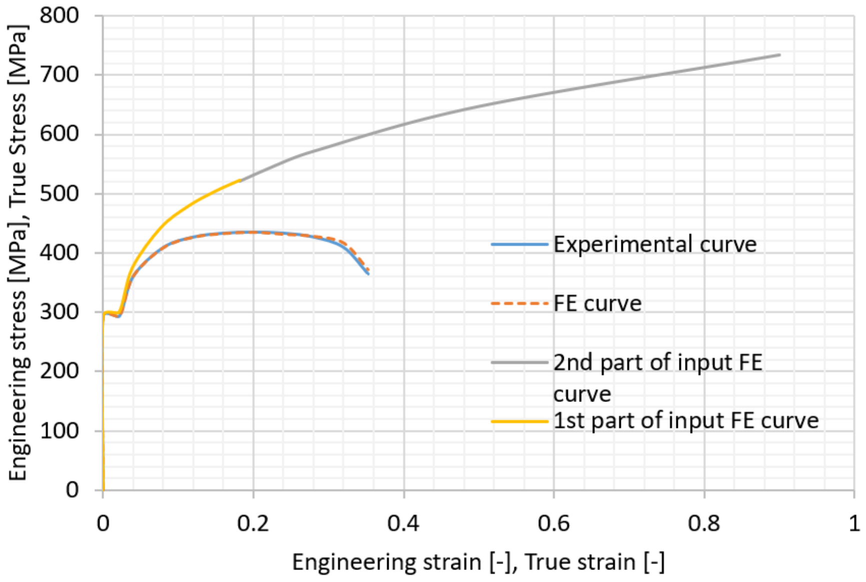

Figure 8.3. Stress-strain relationships for experimental [160] and numerical results.

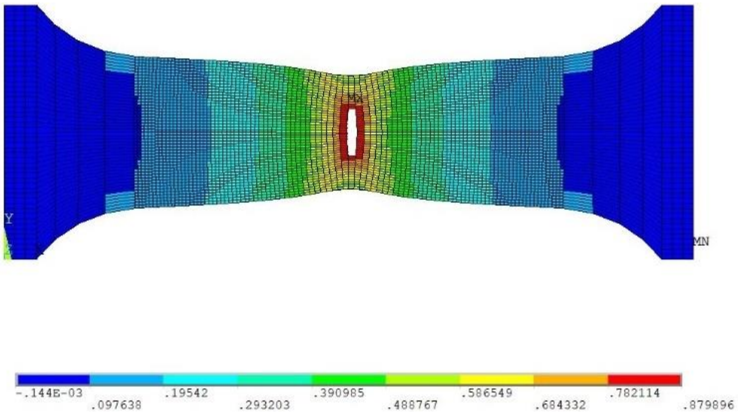

Figure 8.4. Strain distribution in specimen.

8.2. *Sensitivity studies [P7]*

Different parameters related to the geometry of the specimen and random field can influence the results of the current analysis. Thus, the sensitivity analysis is conducted. The analysed parameters of the specimen and random field are presented in Table 8.1. The ratio between maximum corrosion depth and mean corrosion depth is assumed here equal to 3 (the value was assumed based on the observations in [160]), and thus these two variables are changed at the same time considered as one factor. The correlation length cannot be less than 0.5 mm due to the specified element size. In the case of the upper value, with a correlation length above 2.5 mm, the number of pits is very low, which is not observed in reality. The number of corroded surfaces is one or two, which is the one-side or two-side corroded, respectively. To keep the same minimum and maximum thickness, the corrosion degradation depth of the one-side corroded plate is two times the corrosion depth of one of the surfaces in a two-side corroded plate. Additionally, the number of realizations of the corrosion field is studied to show the difference in the results between one sample and the average value from several samples.

Table 8.1. Parameters of sensitivity analysis.

Variable	Initial	Minimum	Maximum
Maximum thickness [mm]	5	3	8
Maximum corrosion depth [mm]	1	0.25	1.75
Mean corrosion depth [mm]	0.333	0.083	0.583
Correlation length [mm]	1.5	0.5	2.0
Number of realizations	1	1	9
Number of corroded surfaces	2	1	2

The One Factor at the Time (OFAT) methodology [270] is used to perform the sensitivity analysis. Only one factor is changed, whereas the rest of the variables are equal to the initial values presented in Table 8.1. Compared to advanced techniques of Design of Experiments [277], this methodology provides information about essential variables in a simple way, which is the main objective of the current analysis. Nevertheless, the multi-factorial analysis may be performed in further studies.

Figure 8.5 shows the influence of the maximum thickness on the mechanical properties. It could be noticed that with the increase of the maximum thickness, where the other corrosion descriptors remain unchanged, the mechanical properties are growing, which is caused by the ratio between minimal and maximum thickness. This ratio is much lower (for a 3 mm plate, it is 0.333, where for an 8 mm plate, it is 0.75). Any identical corrosion fields will significantly influence the stress distribution in the thin specimens compared to the thick specimens. The reduction in the yield stress ranges from 10 % in the case of an 8 mm specimen's thickness up to 40 % in a 3 mm thickness. In the Young Modulus and ultimate stress, the reductions are between 9 % and 33 %. The most sensitive parameter is the total elongation, which is reduced between 9 % up to 78 %. The fitting curves in all cases are of the 2nd order polynomial functions, and there are shown together with the Pearson correlation factor. It can be noticed that the correlation factors are very high, and thus, these curves can model the reduction of the mechanical properties in the range of thicknesses and the assumed values of the mean and maximum corrosion depths.

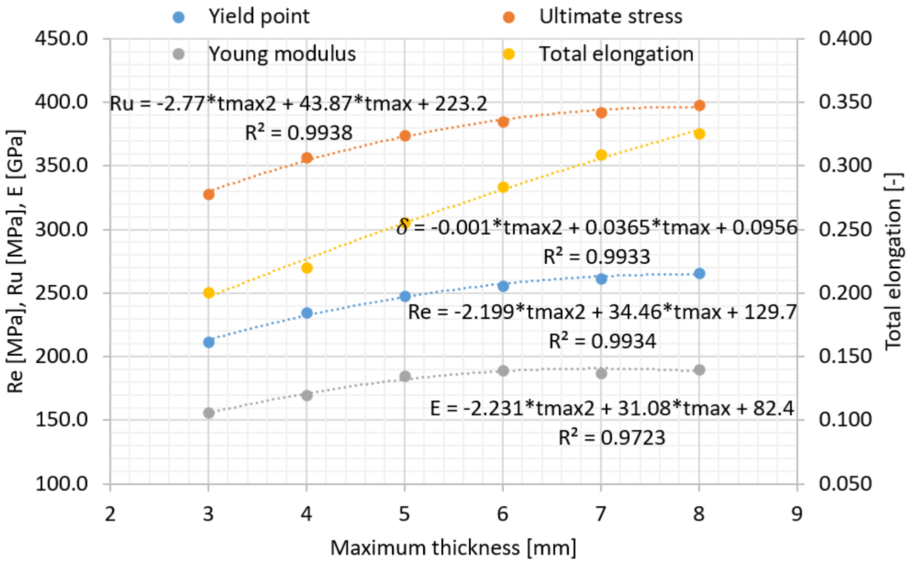

Figure 8.5. Mechanical properties in the function of maximum thickness.

Figure 8.6 shows the influence of the maximum corrosion depth and the mean corrosion depth in the mechanical properties of corroded specimens. It can be noticed that when the maximum corrosion depth is growing, all mechanical properties are decreasing. This is caused by the mean thickness reduction and the increase of the stress concentration factors in the pit regions. Reducing the yield stress varieties between 4% up to 29 % and ultimate stress is reduced between 3 % to 26 %. Similarly to the initial thickness, the most sensitive variable is the total elongation, which is decreased compared to its initial value between 4 % and 45 %. The less sensitive is the modulus of elasticity, which is reduced between 2 % and 22 %. All parameters may be modelled with the use of the linear approximation with the high correlation factor. It could be observed that the values of these functions for $h_{max} = 0$ are the values that should be equal to the initial mechanical properties. However, small deviations are observed.

In the case of different corrosion types (one-side or two-side), the results are presented in Table 8.2. One can observe that there are some changes in the mechanical properties. In the case of upper surface corroded only, the results are very similar to those obtained for two-side corrosion. In the case of the Young modulus and total elongation, the values are even slightly higher. However, in the case of lower surface corroded only, the values of the yield stress and ultimate stresses are 3% and 2% lower from two-side corrosion values, respectively. The Young modulus and total elongation are smaller by 4.5 % and 25 %, respectively. Additionally, the mean value from the two one-side corroded specimens was calculated, and the mechanical properties are lower from that obtained in the case of two-side corrosion degradation, although the same corroded surfaces were applied. Probably, the reduction is caused by higher stress concentration factors when compared with two-side corrosion.

Table 8.2. Results of sensitivity analysis.

Influencing factor	Value	Re [MPa]	Ru [MPa]	E [GPa]	δ [-]
Number of corroded surfaces	Upper surface corroded	246.8	374.0	190.5	0.272
	Lower surface corroded	241.4	366.5	176.9	0.204
	Mean	244.1	370.2	183.7	0.238
	Both surfaces corroded	247.8	374.0	184.8	0.256

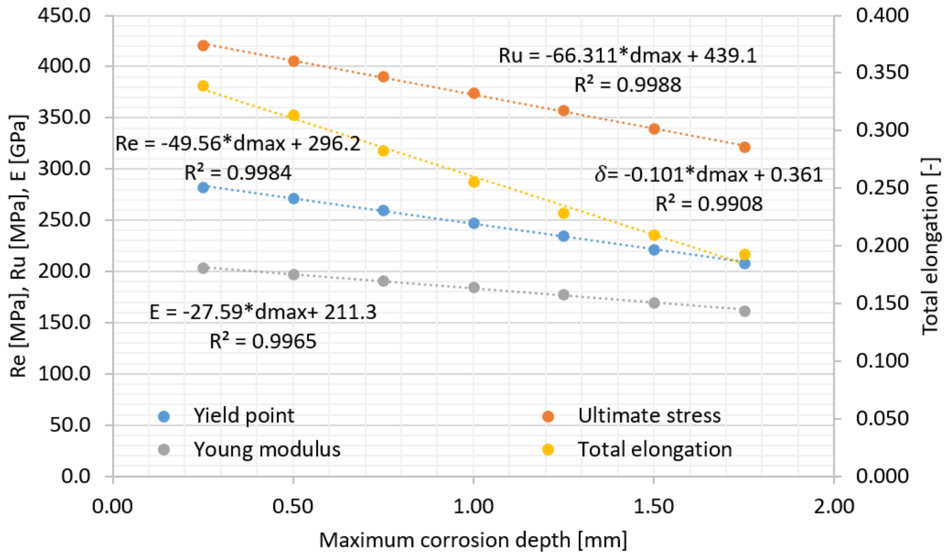

Figure 8.6. Mechanical properties in the function of maximum corrosion depth.

Both factors, the initial thickness and corrosion depth are investigated based on the corrosion degradation modelled with the same shape of random fields in both surfaces of corroded specimens (different between the surfaces). However, in the case of the correlation length and corrosion type, the results can deviate due to the different realizations of the specific random field. Thus, the influence of the number of random field realizations is investigated. The mechanical properties are calculated for the initial conditions with nine different random field realisations with the same characteristics (correlation length and mesh density). The deviations from the mean value for each realization are presented in Figure 8.7.

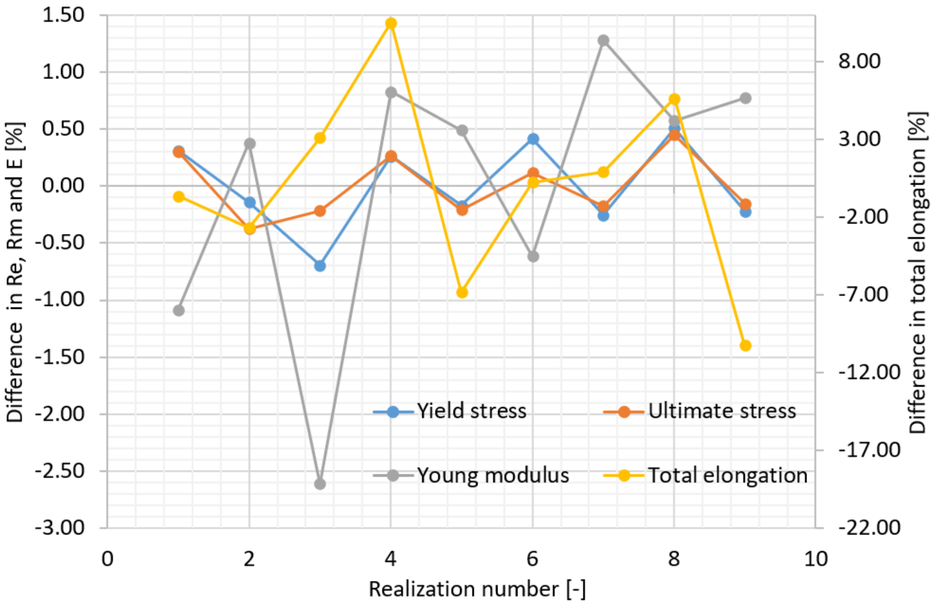

Figure 8.7. Deviations from the mean value for specific realization.

The analysis shows that both yield and ultimate stresses are almost independent of the realization number. The differences between the maximum and minimum values of these two variables are about 1 % concerning the mean value. In the case of the Young modulus, the deviations are in the order of 4 %, which is more significant. The biggest differences are in the total elongation, which reaches 20 % between the maximum and minimum value. Additionally, the correlation matrix has been developed, showing the correlation between variables. A strong correlation has been found between yield stress and ultimate tensile stress (0.84). A moderate correlation was found between yield stress and total elongation and between ultimate tensile stress and total elongation with values of 0.35 and 0.58. In the case of the Young modulus, the correlation with other variables was not noted.

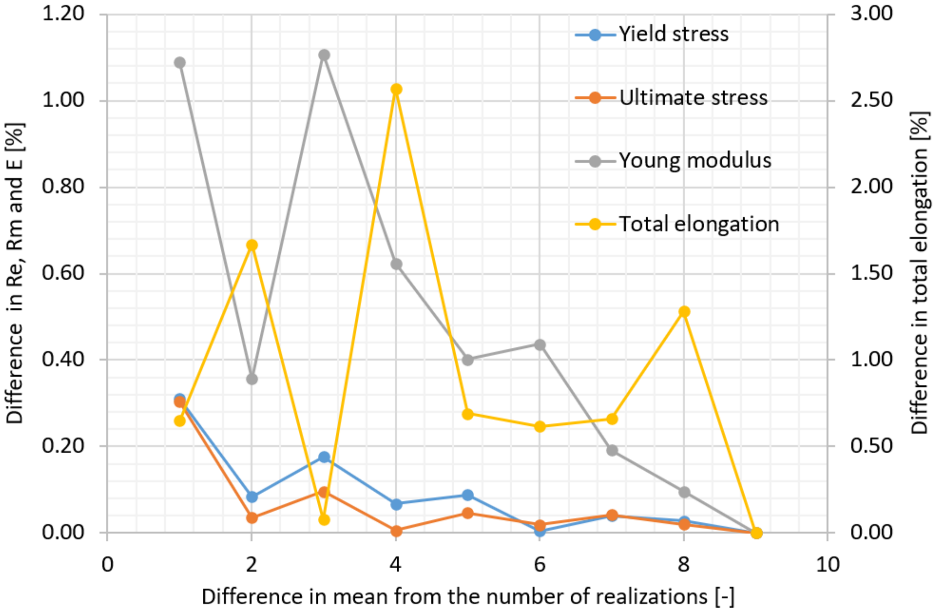

Figure 8.8. Convergence studies.

Due to the high level of variation in the total elongation and Young modulus case, additional convergence studies based on the previous results are performed. The reason for convergence studies is to see how many samples are needed to produce a confident mean value close to the mean value from a significant amount of samples. In other words, how many samples are needed to produce the representative mean values. The results of these studies are shown in Figure 8.8. The differences from *n* samples are calculated as follows (x is the selected variable and $\bar{x}$ is the mean value from 9 samples):

$$D_n = \left| \frac{\sum_{i=1}^{n} \frac{x_i}{n}}{\bar{x}} - 1 \right| * 100\ \% \tag{8.4}$$

The analysis shows that even one sample will be represented in yield stress and ultimate stress, and two samples and more will produce minimal deviations. In the case of the Young modulus, the mean from five samples will be quite representative and will result in a difference below 0.5 % from the mean of multiple samples. Additionally, in the case of these three variables, the deviations are converging. In the case of the total elongation, no specific convergence could be distinguished. Even the mean from 8 samples differs by about 1.3 % regarding the mean from 9 samples. In this case, more samples will be needed to achieve convergence. However, concerning the difference between the minimum and maximum value, the 2% deviation level seems to be quite representative. This level of deviation may be noticed above the mean from 5 samples.

Based on this study, one can choose the mean from a couple of samples, the most critical case or representative case, to simulate the corrosion field. In further studies, the representative realization for a specific correlation length will be chosen. The representative field is the one that results in mechanical properties closest to the mean from multiple samples. This approach will lead to the less computational effort.

It could be noticed that the total elongation is subjected to high uncertainties. Probably, the total elongation is dependent on a specific corrosion field, which could be seen in different failure schemes (Figure 8.9) for specimens with the same field descriptors. The failure modes for nine realizations are presented. Generally, the reduction of the total elongation is related to premature breaking due to the stress concentration in the region of the pit, which may be visible in the strain distribution of the corroded specimen. It can also be noticed that the breaking line is not perpendicular to the longitudinal direction of the specimen. Breaking may also not be located in the middle-length of the specimen, and it seems to be dependent on the minimum cross-sectional area's location.

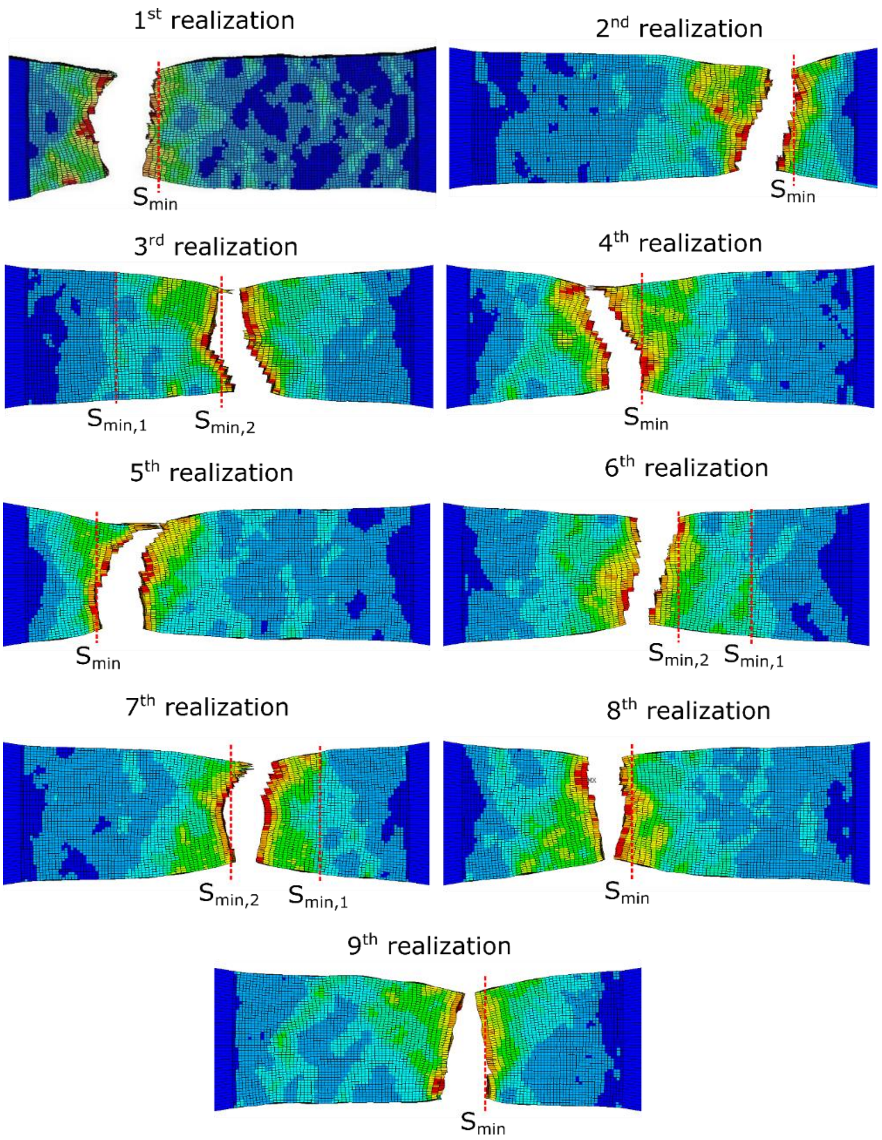

Figure 8.9. Failure schemes of specimens with different realizations of the random field.

The hypothesis that the breaking line is correlated with the minimum cross-sectional area is verified. The positions of the minimum cross-sections, together with actual breaking positions, are presented in Figure 8.9. If the first position of the minimum cross-sectional area is not coherent with the breaking position, the second smallest one is found.

It can be noticed that the positions of the minimum cross-sectional area are the same as the position of the breaking region. Thus, it can be concluded that the breaking will occur in the region of the minimum cross-sectional area of one of two minimum cross-sectional areas (in the case of three realizations). In the case of specimens, where the second smallest cross-sectional area broke, the stress concentration about pit regions could be the reason for that.

Figure 8.10 shows the impact of the correlation length of the random field on the mechanical properties. The representative fields for upper and lower corroded surfaces were chosen for each correlation length, as described previously. The correlation length has almost no influence on both yield stress and ultimate stress (the differences between maximum and minimum value are in the order of 2%). The minimal impact can be visible in the case of the Young modulus (difference of 7% between maximum and minimum value). However, it is hard to find any correlation with correlation length, represented by a small Pearson factor. It could be concluded that the deviations are stochastically originated. The only significant effect that can be noticed is concerning the total elongation. In this case, with the increase of the correlation length, the total elongation is reduced. Similarly to other factors, total elongation is the most sensitive variable.

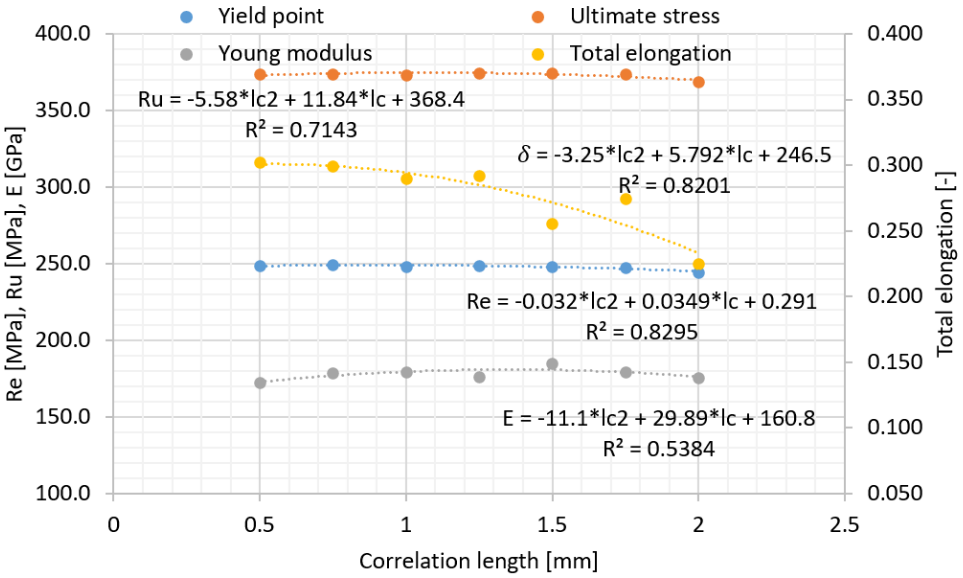

Figure 8.10. Mechanical properties as a function of the correlation length.

Based on the sensitivity analysis, one can conclude that the maximum thickness and mean corrosion depth are the most sensitive parameters that govern the reduction of mechanical properties. Almost no influence is visible in the correlation length and type of corrosion (one-side or two-side). The only variable that shows some sensitivity concerning the correlation length is the total elongation. However, the studies revealed that the total elongation is the most sensitive concerning all parameters, and it is subjected to high uncertainties, which was shown in the random field convergence studies. The Young modulus is also subjected to some uncertainty. The most certain parameters are the yield stress together with ultimate tensile stress. To see the influence of different factors, acting simultaneously, a multifactorial analysis needs to be conducted.

8.3. Validation with the experiment of thick specimens [P7]

The FE model of the specimen with the randomly generated corroded surfaces is presented in Figure 8.11.

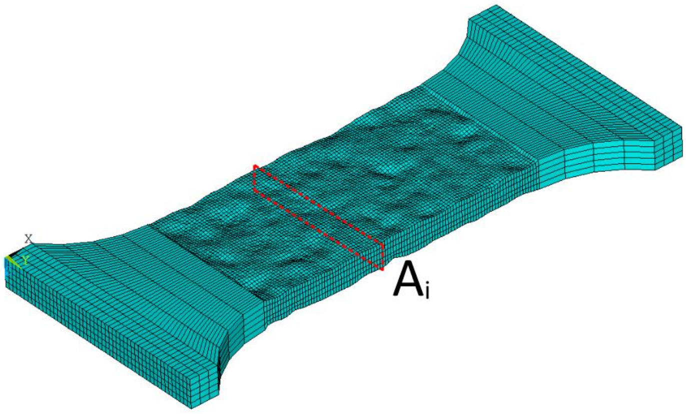

Figure 8.11. The specimen with randomly generated random fields of corrosion.

The specimens were taken from the steel truss (made from H-beam elements), exposed to natural environmental conditions. The nine specimens were taken and analysed from horizontal (H), sloping (S), and vertical (V) members. One specimen was cut from the top flange (TF), one from the bottom flange (BF), and one from the web (W) for each type of member. The random fields' basic parameters are equivalent to those measured experimentally, i.e. maximum and mean corrosion depths of both surfaces. The dimensions of the specimens and the maximum thicknesses of the specimens are satisfied as well. The material properties are calibrated to obtain the experimental stress-strain curve in the intact conditions, as presented in Section 8.1. The main dimensions and descriptors of the corrosion fields are presented in Table 8.3. All parameters are precisely identical in numerical simulations.

Table 8.3. Specimens descriptions.

Specimen	t_0 [mm]	t_{max} [mm]	$h_{u,max}$ [mm]	$\overline{h_u}$ [mm]	$h_{b,max}$ [mm]	$\overline{h_b}$ [mm]	t_{min} [mm]
HTF	9	7.98	0.331	0.113	1.253	0.515	6.4
HBF	9	7.93	0.945	0.361	1.106	0.399	5.88
HW	6.5	5.28	0.868	0.286	0.692	0.298	3.72
STF	9	7.86	0.437	0.134	1.282	0.466	6.14
SBF	9	7.8	0.737	0.228	0.91	0.341	6.15
SW	6.5	5.27	0.888	0.247	1.097	0.385	3.29
VTF	8	7.36	0.466	0.152	0.751	0.192	6.14
VBF	8	7.3	0.81	0.279	0.73	0.171	5.76
VW	6	5.42	0.593	0.163	0.487	0.179	4.24

The only parameter that is related to correlation length is the number of corrosion pits per square centimetre. Since the correlation length has no significant influence on mechanical properties, two different correlation lengths are chosen to simulate the corroded surfaces and make the analysis simpler. The correlation length of 1 mm was chosen to model the surfaces with a denser pitting distribution (above 10), whereas a correlation length of 1.5 mm was chosen to model the surfaces with a lower number of pits per square centimetre (below 10). The comparison of the experimentally measured and simulated surfaces is presented in Figure 8.12, and one can see that there are quite similar between each other. The comparison between surfaces in the experiment and numerical predictions is presented in Table 8.4.

Based on the sensitivity analysis, one can notice that at least a couple of samples is needed to produce accurate results. However, to avoid multiple calculations, two representative fields for each correlation length were chosen to produce results close to the mean from a couple of samples. One can notice small deviations in the minimum cross-sectional area between numerical and experimental predictions. There are originated from the differences between the real corrosion fields and randomly generated ones. When maximum corrosion depth and the mean corrosion depth are satisfied, the minimum cross-sectional area is the resulting value.

Table 8.4. Experimental and numerical corrosion field descriptors.

Specimen	DoD_u [%]	DoD_n [%]	DoD [%]	A_{min} $[mm^2]$	A_{min} numerical $[mm^2]$	$\frac{Pits}{cm^2}$ Upper surface	$\frac{Pits}{cm^2}$ Bottom surface	$c_{0,u}$ [mm]	$c_{0,b}$ [mm]
HTF	11.3	9.5	20.8	180.4	179.3	20.2	6.4	1	1.5
HBF	11.9	11.9	23.8	173.7	173.0	6.9	7.5	1.5	1.5
HW	18.8	10.5	29.3	115.3	112.6	9.4	11.5	1.5	1
STF	12.7	10.5	23.2	177.7	176.7	15.7	7.6	1	1.5
SBF	13.3	8.9	22.2	177.2	176.5	13.4	10.7	1	1
SW	18.9	14.7	33.6	112.1	110.2	8.6	6.8	1.5	1.5
VTF	8.0	8.9	16.9	173.4	172.4	15.3	14.6	1	1
VBF	8.7	10.5	19.2	168.5	167.5	11	13.3	1	1
VW	9.7	9.8	19.5	124.3	124.2	12.2	14.5	1	1

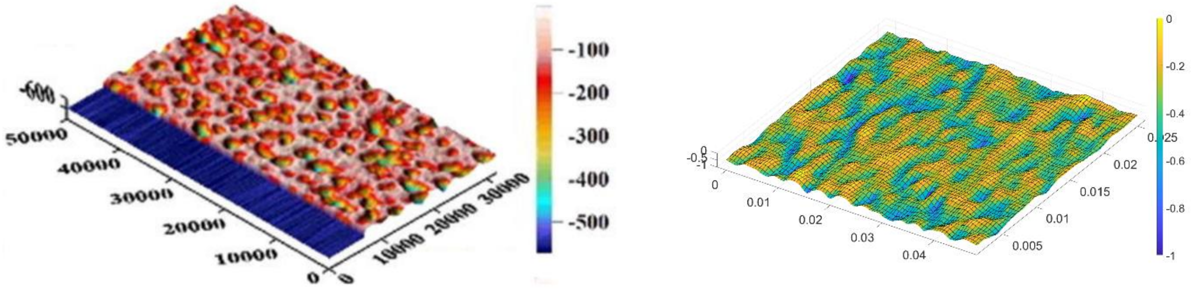

Figure 8.12. Real corrosion field of VW upper surface [160] (left) with randomly generated corrosion field (right).

The numerical analysis results using the random field approach compared to experimental tests are presented in Table 8.5. The lowest deviations between experimental and numerical results are in the case of the ultimate stress, where the mean error is 1 %. In the case of the Young modulus and yield stress, the mean error is about 2 %. The most significant mean error is for the total elongation, which is equal to 7%. However, only for severely corroded specimens (HW and SW), the error is 20 %. For the rest of the specimens, the error of total elongation does not exceed 6 %.

Table 8.5. Results of analysis – comparison between experiment and numerical predictions.

Specimen	R_e [MPa] [160]	R_e [MPa] num.	R_u [MPa] [160]	R_u [MPa] num.	E [GPa] [160]	E [GPa] num.	δ [%][160]	δ [%] num.
HTF	268.2	266.7	402.7	399.0	194.6	190.9	31.7	31.3
HBF	263.8	261.8	399.7	392.4	184.5	187.4	31.3	32.0
HW	250.7	256.8	384.5	385.6	189.7	188.7	24.1	28.9
STF	267.0	267.2	403.6	400.0	200.3	191.3	31.5	31.3
SBF	268.1	268.2	407.1	402.1	198.9	192.4	32.4	34.0
SW	242.4	252.0	388.2	380.3	187.3	179.7	21.6	26.0
VTF	264.8	277.7	415.6	413.6	203.9	198.1	32.3	34.3
VBF	264.5	272.9	412.0	407.1	200.7	194.5	31.8	33.7
VW	271.6	272.3	412.5	405.9	195.4	195.5	30.8	32.4
Error [%]	- 4.9		0.2 - 1.8		0.1 – 4.5		0.6 – 20.2	

One can notice that except for the total elongation, which is a very sensitive parameter, the deviations are not significant. They are much smaller than the deviations between experimental tests and results from different mathematical models presented in [160], which were in the order of 16 % for yield strength. Nevertheless, the deviations are in the same order with deviations between experimental and numerical results obtained in [160], where the FE analysis was performed, and the corrosion fields were identical with those measured experimentally. Additionally, the results of the proposed methodology are the results of a single random field realization, which is close to the mean value from a couple of samples. However, the sample that produces maximum or minimum mechanical properties can be more representative and closer to the real specimen. It is hard to produce two samples with the same corrosion field descriptors (maximum corrosion depth and mean corrosion depth).

The deviations between the numerical and experimental results may originate from the corrosion modelling differences and the material properties deviations in the experimental domain and uncertainty measurement. The results of tensile tests for intact specimens [271] show that the coefficient of variation in the case of the yield strength is 5 % and in the case of the ultimate stress is 1.5 %. From this perspective, the deviations between the numerical and experimental results are similar to these values. Thus, the results are compared with the numerical simulations of [160], where the same specimens with corrosion surfaces transmitted to the FE model were analysed. In this case, the input material properties are always the same. The results of the comparison are presented in Table 8.6.

Table 8.6. Results of analysis – comparison between the exact FE model and with randomly generated corrosion.

Specimen	R_e [MPa] [160] num.	R_e [MPa] num.	R_u [MPa] [160] num.	R_u [MPa] num.	E [GPa] [160] num.	E [GPa] num.	δ [%][160] num.	δ [%] num.
HTF	267.2	266.7	402.0	399.0	195.6	190.9	33.4	31.3
HBF	264.3	261.8	398.0	392.4	193.8	187.4	33.5	32.0
HW	249.2	256.8	388.6	385.6	185.7	188.7	26.8	28.9
STF	268.2	267.2	402.5	400.0	196.6	191.3	33.7	31.3
SBF	268.7	268.2	404.6	402.1	197.5	192.4	32.2	34.0
SW	248.2	252.0	390.1	380.3	183.1	179.7	24.6	26.0
VTF	275.0	277.7	411.4	413.6	200.0	198.1	33.6	34.3
VBF	271.2	272.9	408.8	407.1	199.2	194.5	34.0	33.7
VW	275.3	272.3	409.6	405.9	201.4	195.5	33.3	32.4
Error [%]	- 3.0		0.4 - 2.5		1.0 – 3.3		0.9 – 7.8	

It can be noticed that the error is smaller concerning the comparison between the experimental predictions and the random approach. Especially in the case of the total elongation, the maximum deviation is significantly reduced. The deviations shown in Table 8.6 are in the same order as the deviations between the exact FE model and experiment. Additionally, the deviations between the random field modelling and accurate FE modelling are in the order of the differences resulting from a couple of generations of the specific random field. One can notice that a single analysed specimen can be represented by the randomly modelled one with either the maximum mechanical properties or minimum between a couple of simulations. From that point of view, stochastic modelling provides accurate results concerning the corroded specimens' mechanical properties. Additionally, some specific FE modelling differences may impact the differences in the results. The comparison between experimental and numerical results of [160] compared to the presented methodology is shown in Figures 8.13 – 8.16.

The yield stress presented as a function of DoD is shown in Figure 8.13. One can notice that both curves, showing numerical predictions, are very close to each other, and there are modelled with the use of a linear approximation with highly correlated factors. In the case of the experimental curve, the best fitting curve is the polynomial one, and it deviates from the numerical predictions in the low values of DoD. However, the curves should tend to the initial value of the yield stress for DoD equals 0, which could be observed for numerical curves. Thus, the experimental curve's possible deviations may originate from the variability of the initial mechanical properties. Mainly, it could be noticed that two points for DoD close to 19 % differ significantly in the experimental results. In the case of numerical predictions, the two points are close to each other.

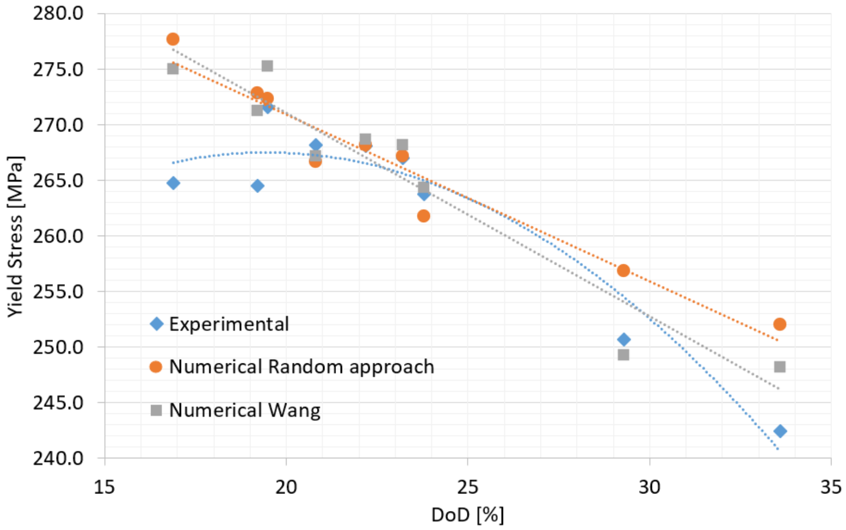

Figure 8.13. Yield stress in the function of DoD.

Figure 8.14 shows the ultimate stress as a function of DoD. In this case, all regression curves are linear with high correlation factors. It may be observed that all curves are very close to each other. However, the experimental curve shows slightly higher values compared to other ones. All curves tend to the value, which is very close to the initial ultimate stress when DoD equals 0.

The Young modulus presented as a function of DoD is presented in Figure 8.15. Similarly to the ultimate stress, the best regression curves are linear. In the numerical predictions, the coefficients of determination are high, whereas the coefficient of determination in the case of the experimental curve is quite low (0.52). The possible reason for that is the measuring uncertainty, which is related to the extensometer usage in the testing procedure. The deviations between the two numerical approaches may result from different parallel lengths taken to measure the elongation in the first part of the stress-strain curve. Additionally, the curves crossing the vertical axis for DoD equals 0 with values close to the initial Young modulus.

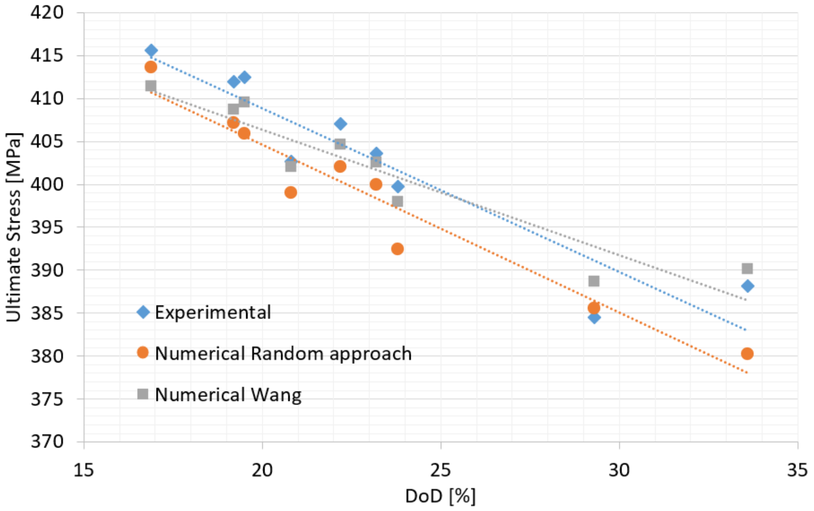

Figure 8.14. Ultimate stress as a function of DoD.

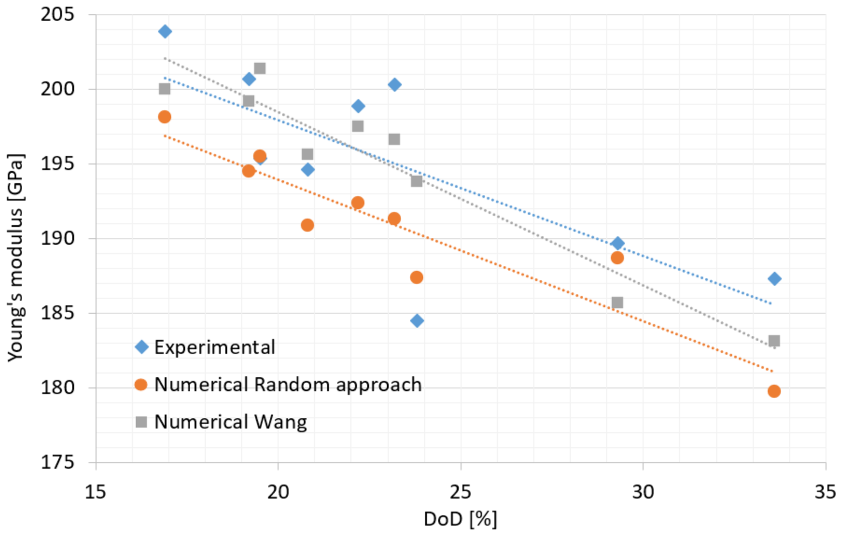

Figure 8.15. Young's modulus as a function of DoD.

Figure 8.16 shows the total elongation in the function of DoD. In this case, the polynomial fitting curves are used to model the change of the total elongation concerning the DoD. In all cases, the correlation factors are very high. Similarly to other mechanical properties, all three curves are quite similar. However, the methodology used in this study slightly overestimates the total elongation in the higher values of DoD. It may be explained with the representative random field that was chosen to model the corrosion fields. When the most critical random field is chosen, the values could be much closer to those obtained experimentally. For DoD equals 0, the numerical predictions using a random approach shows a value close to the initial total elongation. In other cases, these values are quite outstanding.

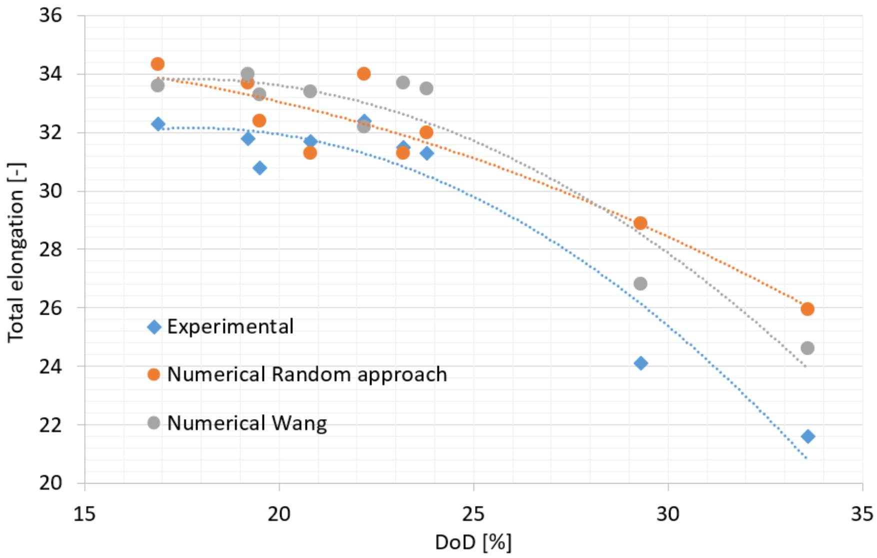

Figure 8.16. Total elongation as a function of DoD.

Based on the presented results, one can notice that the FE analysis of the corroded specimens with randomly generated corrosion fields is very close to the experiment. Additionally, the FE analysis with randomly generated corrosion degradation is almost identical to the FE analysis with real corrosion fields.

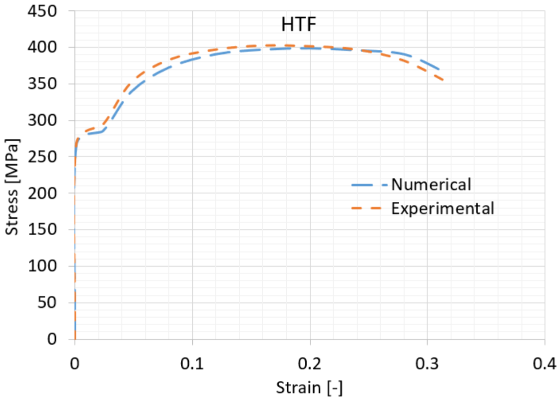
HTF
Stress [MPa]
450
400
350
300
250
200
150
100
50
0
0
0.1
0.2
0.3
0.4
Strain [-]
Numerical
Experimental

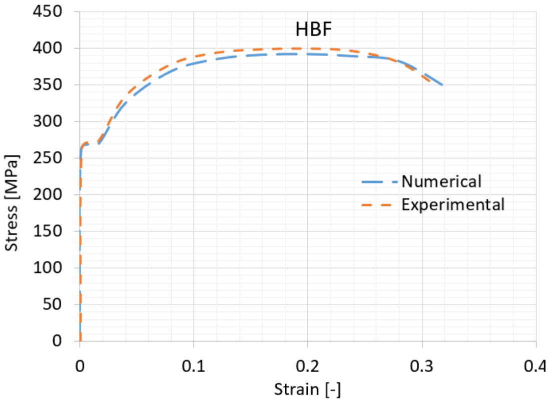
HBF
Stress [MPa]
450
400
350
300
250
200
150
100
50
0
0
0.1
0.2
0.3
0.4
Strain [-]
Numerical
Experimental

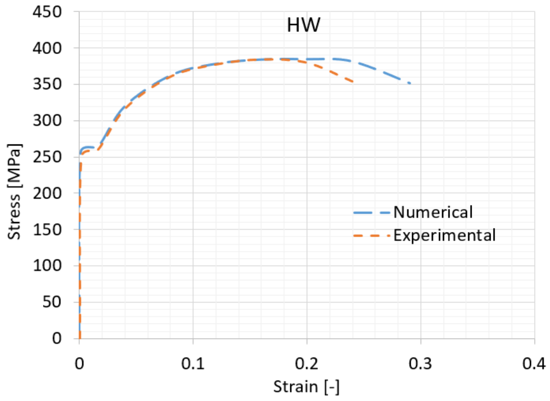
HW
Stress [MPa]
450
400
350
300
250
200
150
100
50
0
0
0.1
0.2
0.3
0.4
Strain [-]
Numerical
Experimental

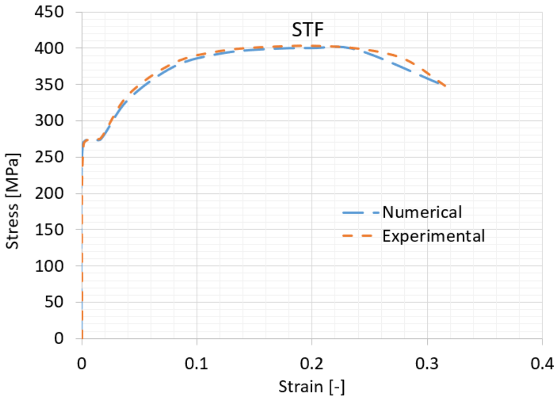
STF
Stress [MPa]
450
400
350
300
250
200
150
100
50
0
0
0.1
0.2
0.3
0.4
Strain [-]
Numerical
Experimental

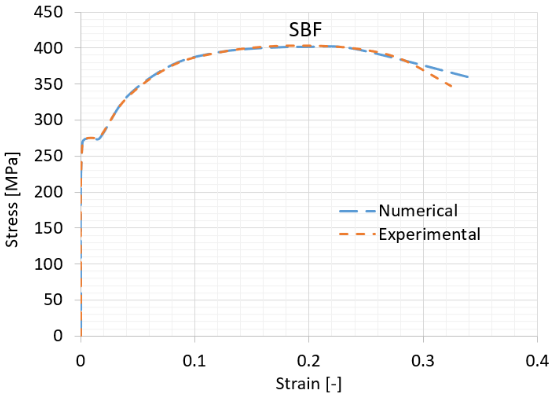
SBF
Stress [MPa]
450
400
350
300
250
200
150
100
50
0
0
0.1
0.2
0.3
0.4
Strain [-]
Numerical
Experimental

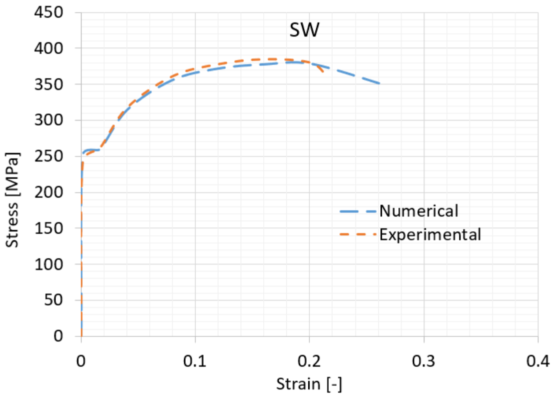
SW
Stress [MPa]
450
400
350
300
250
200
150
100
50
0
0
0.1
0.2
0.3
0.4
Strain [-]
Numerical
Experimental

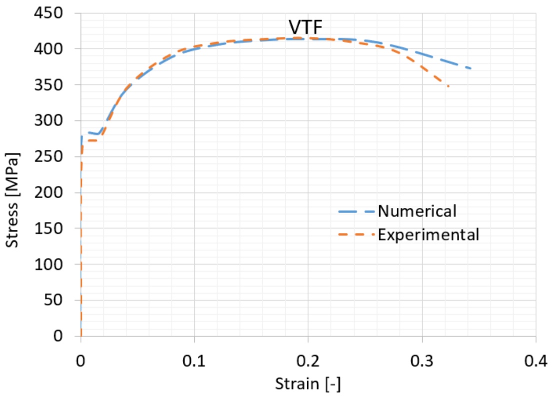
VTF
Stress [MPa]
450
400
350
300
250
200
150
100
50
0
0
0.1
0.2
0.3
0.4
Strain [-]
Numerical
Experimental

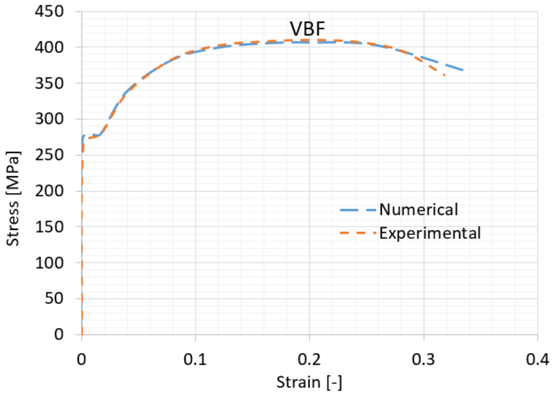
VBF
Stress [MPa]
450
400
350
300
250
200
150
100
50
0
0
0.1
0.2
0.3
0.4
Strain [-]
Numerical
Experimental

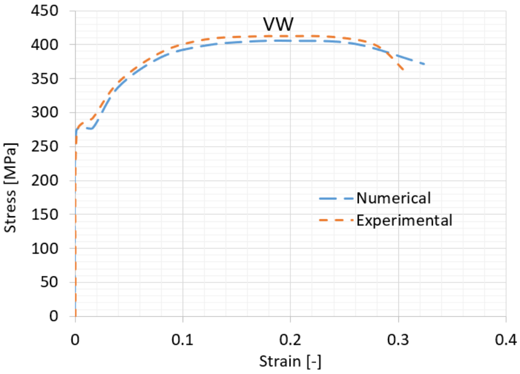

Figure 8.17. Stress-strain curves for all specimens.

The comparison between the experimental stress-strain curves and numerically obtained ones using the current methodology is presented in Figure 8.17. As it can be noticed, for all specimens, the curves are very similar to each other, which leads to the conclusion that not only mechanical properties are similar, but the general stress-strain response match as well.

8.4. Validation with experiments of very thin specimens [P8]

The corrosion field modelling using the random approach is compared to experimental results of very thin plates as reported in [161] (the initial thickness is 1 mm). Seven specimens were cut from a real structure and exposed to atmospheric corrosion conditions. However, only the maximum residual thickness and minimum cross-sectional area are provided due to the corrosion morphology analysis. Corrosion is one-side in this case. The dimensions of the gauge area of the specimens are 50x10 mm, and the specimen dimensions are identical, as presented in Figure 8.18.

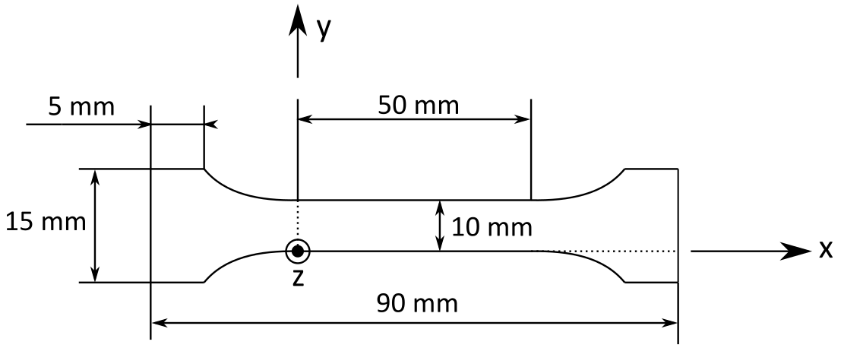

Figure 8.18. Specimen dimensions and system of coordinates.

The initial stress-strain relationship is calibrated similarly to the previous section, as presented in Figure 8.19. The primary material properties of referred material (mild steel S235) are yield stress, Young (elasticity) modulus, ultimate stress, and total elongation are 287 MPa, 178.5 GPa, 333 MPa, and 24.2 %, respectively. The first part of the true stress-strain relationship is established using Eqns 8.1 and 8.2 up to the true strain of 0.178, corresponding to the ultimate strain. The second part of the curve is calibrated with the experimental one using Eqn 8.3, leading to $\varepsilon_{failure} = 0.74\ [-], K = 550\ MPa, n = 0.19\ [-]$. It can be noticed that the FE element stress-strain relationship matches the experimental one and the basic mechanical properties are the same in both cases, although minimal deviations after reaching the ultimate point are visible.

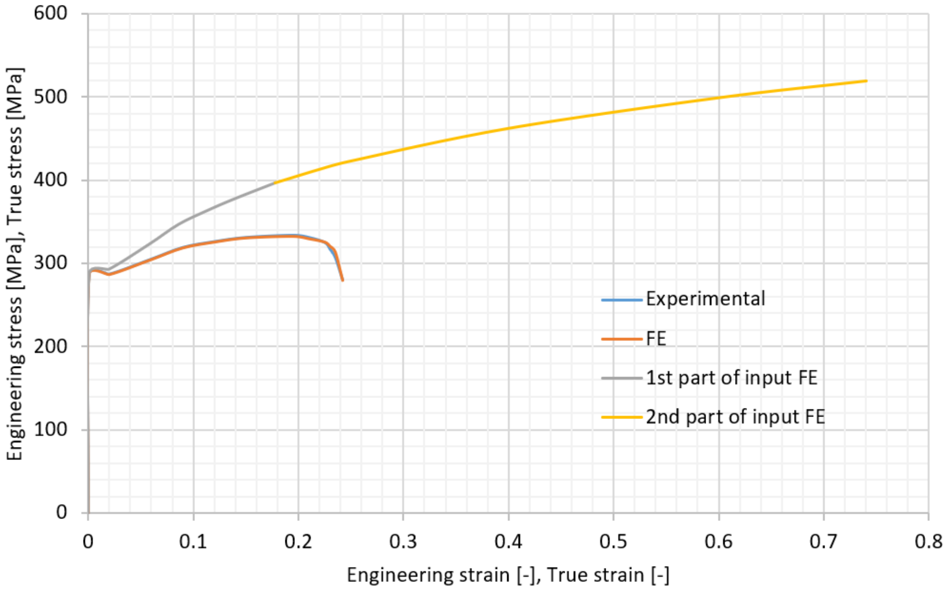

Figure 8.19. Experimentally and numerically developed stress-strain relationships.

Based on the corrosion morphology results, one can notice that the correlation is higher for severely corroded specimens. However, due to a lack of specific information on the corrosion field correlation, the correlation length of 0.6 mm is assumed for higher values of DoD (above 15 %), and the correlation length of 0.4 mm is assumed for lower values of DoD (below 15 %). In this way, the corrosion fields are similar to those obtained in the experiment. The comparison between a real corrosion field and a randomly generated one for a low value of DoD is presented in Figure 8.20, and the FE model of the corroded specimen is presented in Figure 8.21. The ratio between the maximum corrosion depth to mean corrosion depth was taken as 3 in this case. Due to the lack of mass measurements, the degree of degradation is calculated as a ratio between the minimum cross-sectional area to the initial cross-sectional area. Normally, the DoD values will be higher. The maximum residual thickness and minimum cross-sectional area are the same in the experimental and numerical models, as presented in Table 8.7.

Table 8.7. Specimens description.

Specimen	t_{max} [mm]	A_{min} $[mm^2]$	DoD [%]
F1	1.00	8.474	12.1
F2	1.01	9.006	6.6
F3	0.95	7.766	19.5
F4	1.00	8.32	13.7
F5	0.89	6.326	34.4
F6	0.85	5.94	38.4

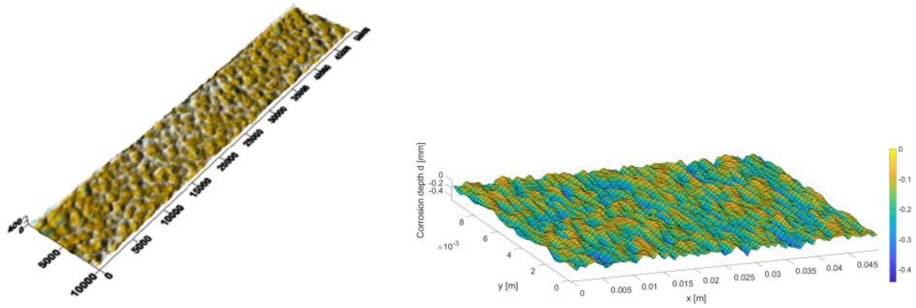

Figure 8.20. Corrosion field in the experiment (left) and randomly generated (right).

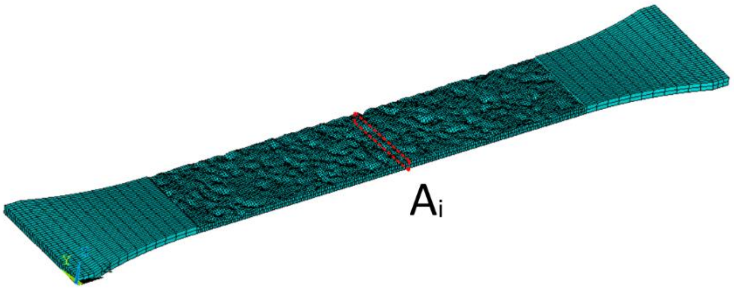

Figure 8.21. FE model of the corroded specimen.

The results of the analysis are presented in Table 8.8 and Figures 8.23 and 8.24. For each pair of experimental and numerical results, the relative error concerning the experimental one is presented.

Table 8.8. Results of analysis.

No	R_e [MPa] [161]	R_e [MPa] num.	Err. [%]	R_u [MPa] [161]	R_u [MPa] num.	Error [%]	E [GPa] [161]	E [GPa] num.	Error [%]	δ [-] [161]	δ [-] Num.	Error [%]
F0	286.9	286.9	-	333.4	333.4	-	178.5	178.5	-	0.242	0.242	-
F1	258.7	245.0	5.3	292.2	291.3	0.3	155.1	154.8	0.2	0.188	0.178	5.4
F2	263.0	255.0	3.1	311.3	300.7	3.4	168.7	159.8	5.3	0.217	0.190	12.4
F3	195.7	238.7	22.0	223.9	283.2	26.5	127.6	156.9	23.0	0.082	0.120	46.3
F4	215.3	240.3	11.6	254.4	286.7	12.7	150.1	152.4	1.5	0.136	0.166	22.2
F5	105.9	207.3	95.8	113.9	245.5	115.6	99.5	138.9	39.6	0.034	0.068	99.5
F6	79.8	203.6	155.2	92.9	240.7	159.2	97.2	138.1	42.1	0.019	0.061	223.3

Based on the presented results, it can be noticed that in the range between 0 % up to 15 % of DoD, the numerical predictions are quite similar to experimental results (F1, F2, and F4 specimen). The deviations can be originated from fluctuations of mechanical properties themselves [271]. However, for higher DoD values, the differences are very significant (F3, F5, and F6 specimen). Probably, in the case of very thin plates, not only the geometrical deviations of the corrosion field will cause mechanical properties reductions. The reduction of mechanical properties is very significant, especially for high values of DoD. In the numerical predictions, the mechanical properties (yield stress and ultimate stress) cannot be lower than those when we consider only the minimum thickness as residual material of specimen. Additionally, their reduction will be lower than this value. In this case, the maximum possible reduction can be calculated as equal to $1 - t_{min}/t_{max}$. The reduction should be below this value and above 0. In Table 8.8, the reductions in the experimental and numerical analyses concerning the maximum possible reductions are presented. In F1, F2, and F4 specimens, the reductions of yield and ultimate stresses are below the maximum possible level in both numerical and experimental domains. In F3, F5, and F6 specimens, the reductions in the experiments are above the maximum possible level or almost equal to it, whereas, in the numerical calculations, there are below this level. This led to the conclusion that general corrosion morphology is not the only factor that governs mechanical properties reduction for very thin plates. Very irregular breaking shapes can be observed for severely corroded specimens, such as presented in Figure 8.22. This type of breaking can be observed in the numerical model, where a tiny element size will be applied (about 0.1 mm or even smaller) and significantly increases the computational time. For this order of the element size, the lower correlation length values can be applied, and more localized phenomena will be observed. This will result in higher stress concentration factors in the pitted regions and possibly a higher reduction of mechanical properties. The other possible reason for the significant deviations can be the microstructure of steel, which cannot be captured by modelling the corroded surface.

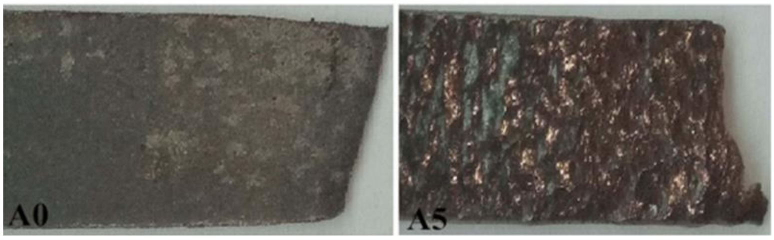

Figure 8.22. Comparison between non-corroded and severely corroded specimens [161].

Table 8.9. Reductions of yield stress and ultimate stress.

Specimen	Maximum possible reduction [%]	R_e red. exp. [%]	R_e red. num. [%]	R_u red. exp. [%]	R_u red. num. [%]
F1	34	10	15	12	13
F2	25	8	11	7	10
F3	35	32	17	33	15
F4	37	25	16	24	14
F5	55	63	28	66	26
F6	57	72	29	72	28

Figure 8.23 presents the yield stress as a function of DoD. Both numerical and experimental curves can be modelled with the use of a linear relationship. However, the significant deviations between them can be observed mainly due to deviations for the high values of DoD (above 20%). In the case of DoD up to 15 %, the deviations are in the range of the initial

mechanical properties variability. Very similar observations can be seen in the case of the ultimate stress (Figure 8.23 right).

The Young modulus, as a function of DoD, is presented in Figure 8.24. Deviations in the range between 0 % and 15 % of DoD are even smaller comparing to yield and ultimate stress. However, similarly to these two variables, the very significant deviations are for the DoD above 20 %.

Figure 8.24 also shows the total elongation as a function of DoD. Apart from that, the relative deviations between the two approaches are higher, as presented in Table 8.8, the inclination of curves seems to be more closely compared to other variables. The high relative deviations are mainly due to the very low values of the total elongation in the high values of DoD. For these specimens, the necking phenomenon is almost not visible. Lastly, one needs to consider the sensitivity of the total elongation for various factors, which was presented in Section 8.2.

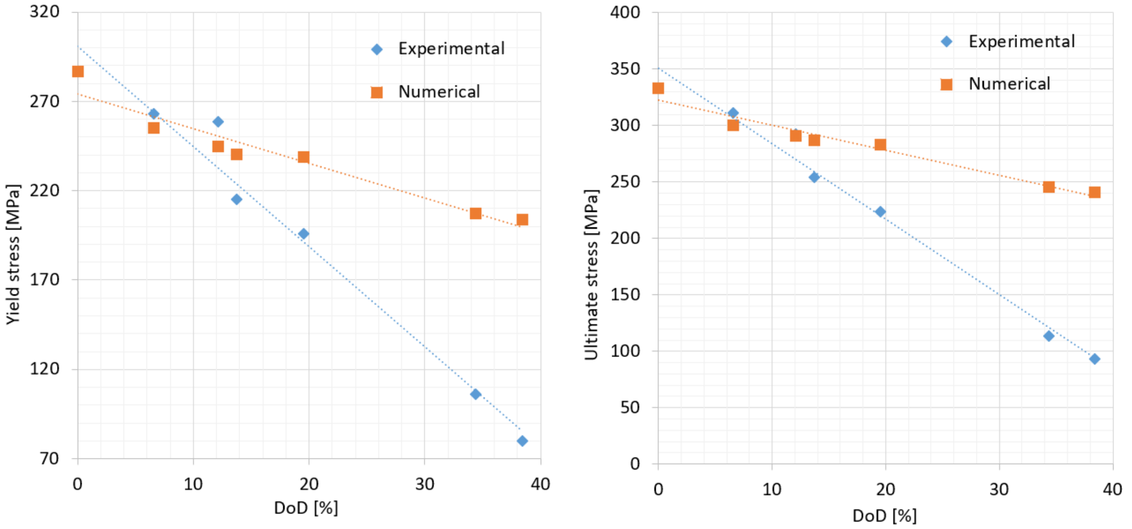

Figure 8.23. Yield (left) and ultimate (right) stresses in the function of DoD.

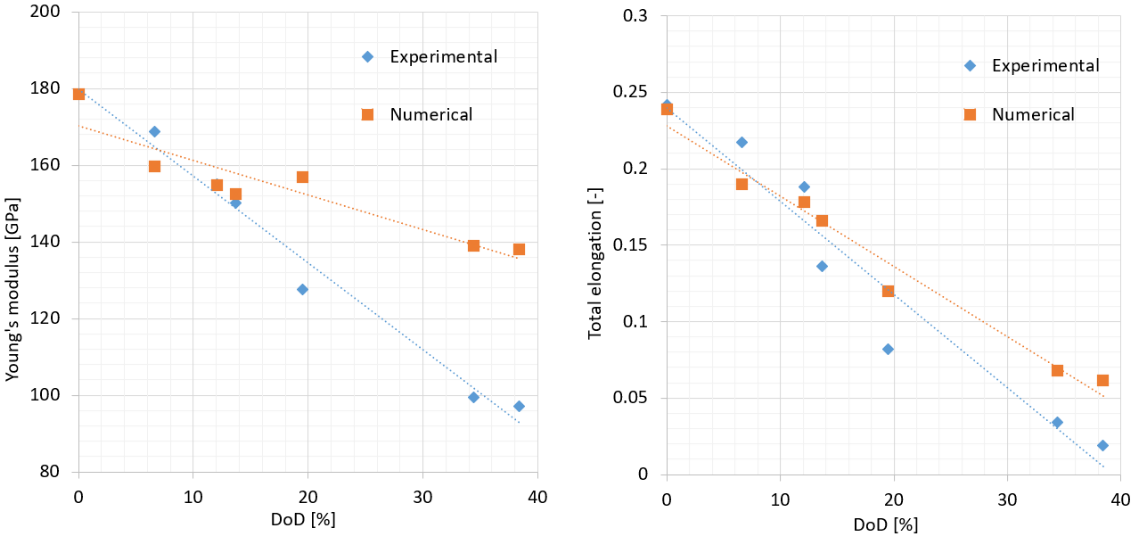

Figure 8.24. Young modulus (left) and total elongation (right) in the function of DoD.

Based on the presented results of the validation, it can be concluded that the corrosion degradation modelling with the use of the random approach predicts the mechanical properties reduction of very thin plates in the range between 0 and 15 % of DoD. Above this level, this approach significantly overestimates the mechanical properties. However, as it was discussed, the possible refinement of the mesh density can provide better results. The possible deviations can also be a result of the lack of corrosion morphology information. In this case, only the maximum thickness and minimum cross-sectional area are provided for each specimen. Lastly, the deviations can result from natural variations of the mechanical properties in the case of the experiment and the sensitivity of random field modelling to the design parameters.

The comparison between experimental and numerical results of the stress-strain relationships are presented in Figure 8.25. One can notice that apart from the deviations, the shapes are very similar.

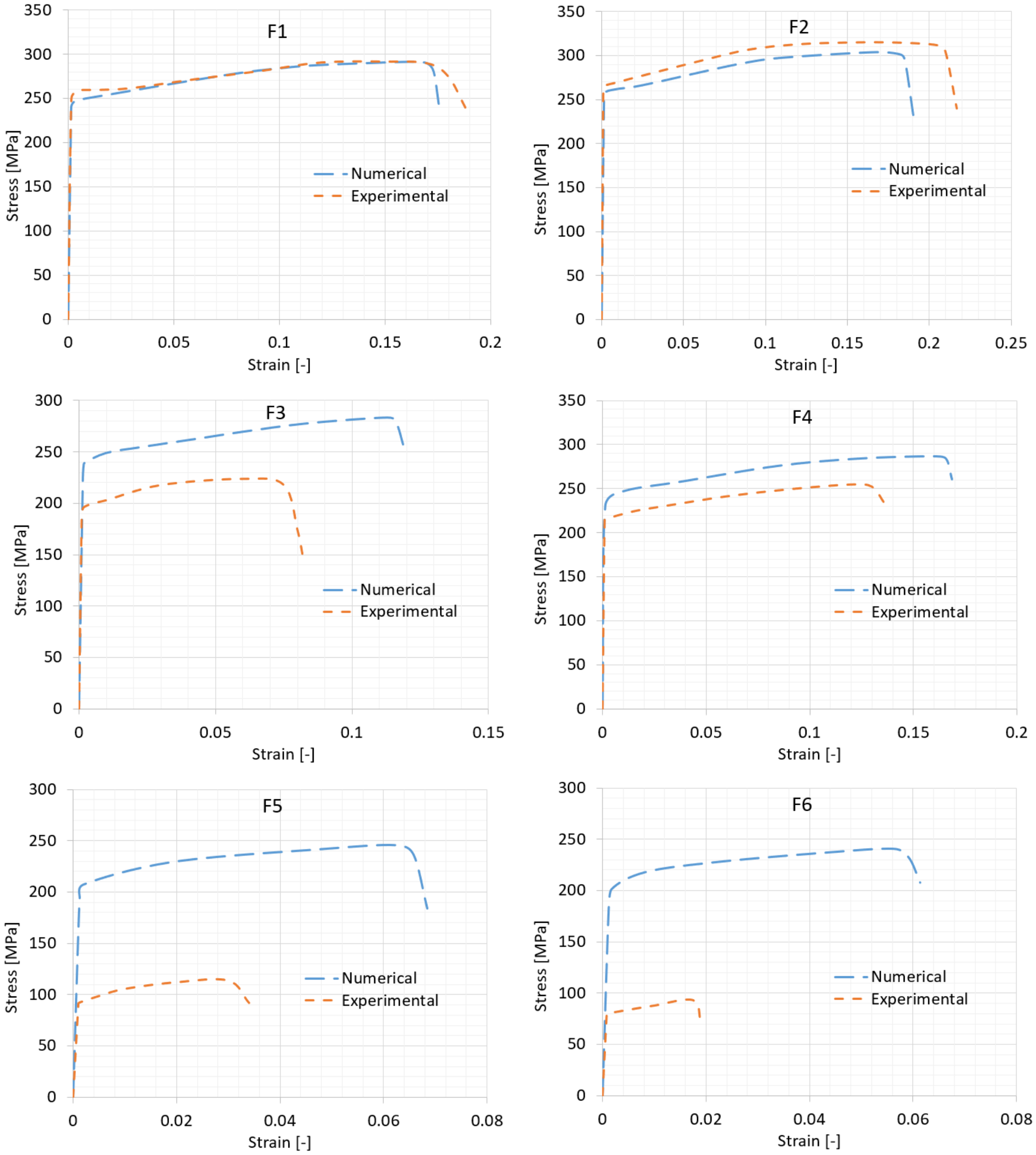

Figure 8.25. Stress-strain curves of experimental and numerical results.

8.5. *Validation with own experimental studies*

As presented in Section 6.5.2, the results of experiments are used in this section to validate the methodology further. Additionally, the FE computations with the measured fields of corrosion (see Appendix 1) are performed. The detailed information about corrosion characteristics for all specimens has been already provided in Table 4.8.

Similarly to previous cases, the initial stress-strain curves for FE analysis are calibrated using experimental results presented in Section 6.5.1, which are the mean values obtained from six or seven intact specimens for each thickness. The comparison between experimental and numerical stress-strain curves in intact conditions for three different thicknesses is presented in Figure 8.26.

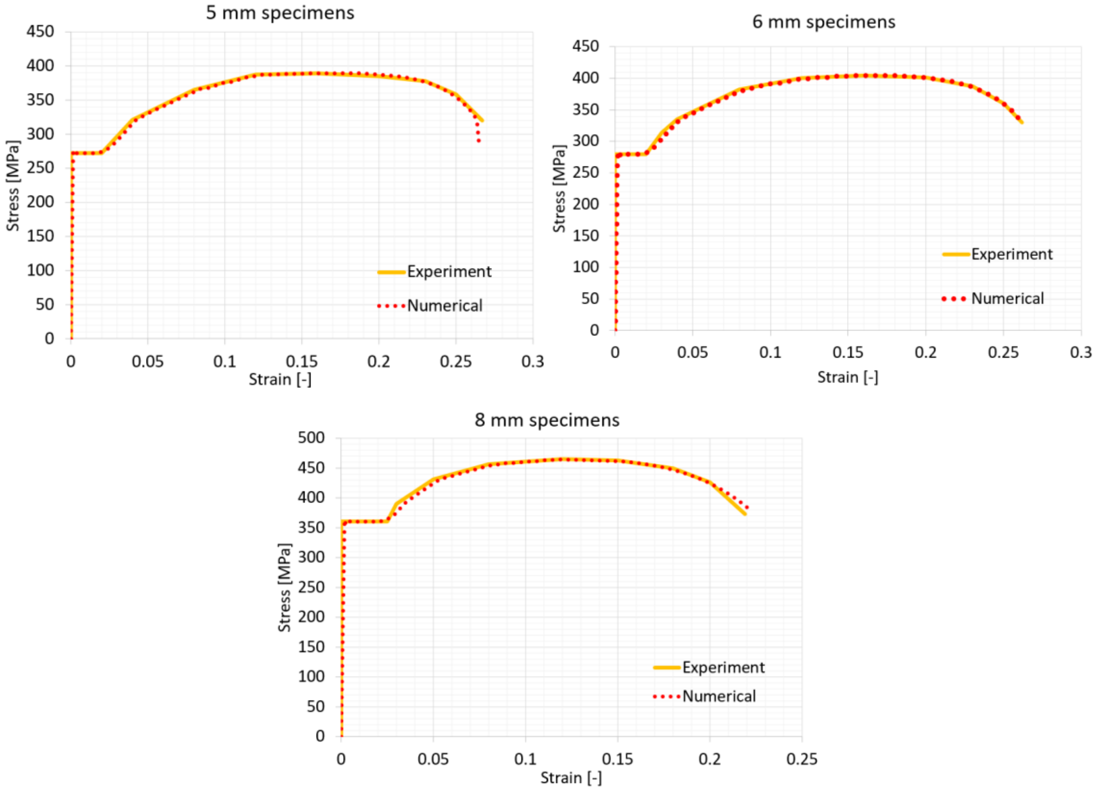

Figure 8.26. Comparison between the experimental and numerical stress-strain curve in intact conditions.

For each case presented in Table 4.8, the three runs of analysis with generated random fields are performed and mean values of mechanical properties are calculated. Compared to previous validation cases, where atmospherically corroded specimens were analysed, the marine immersed corrosion brings much strongly correlated random fields (see Appendix 1). Thus, the correlation length of 10 mm was used in most cases, up to 17 mm for several ones. The maximum corrosion depth and mean corrosion depth were identical for each random field concerning the measured corrosion characteristics.

The comparison between failure modes of tested specimens and FE computations with measured corrosion fields is presented in Appendix 2. It is noted that in almost all cases (except 5.6, 6.7 and 8.2 specimens), the failure positions have been identical. Further, in most of these cases, the exact failure behaviour has been captured as well. This indicates that the FE model could accurately predict corroded specimens' structural behaviour in marine immersed corrosion.

In Figure 8.27, the values of the obtained mechanical properties for various methods are compared, considering 5 mm specimens. In general, the FE computations (both with exact and randomly generated corrosion fields) showed higher decreases of mechanical properties. Since both FE models show very close results, the differences with the experiment are caused by the large scatter of mechanical properties in the non-corroded case (see Table 6.3). For yield stress, the maximum observed yield stress was higher by 30 MPa regarding the mean value. Thus, for several points, in an experimental domain, the observed mechanical properties in the corroded state were higher than the mean value in non-corroded specimens. A similar observation is captured in terms of ultimate tensile stress. In Young’s modulus, the experimentally obtained values were significantly higher concerning numerical ones. Some of the reasons were previously outlined in Section 6.5.2. Firstly, the extensometer could measure the strains inaccurately due to the un-uniformity of the corroded surfaces. Secondly, similarly to other mechanical properties, there was observed quite a high initial scatter. The closest results between the exact FE model and experiment were obtained for total elongation, and in this case, the initial scatter of this property was not that high. However, the model with randomly generated corrosion fields shown an even higher decrease of that parameter.

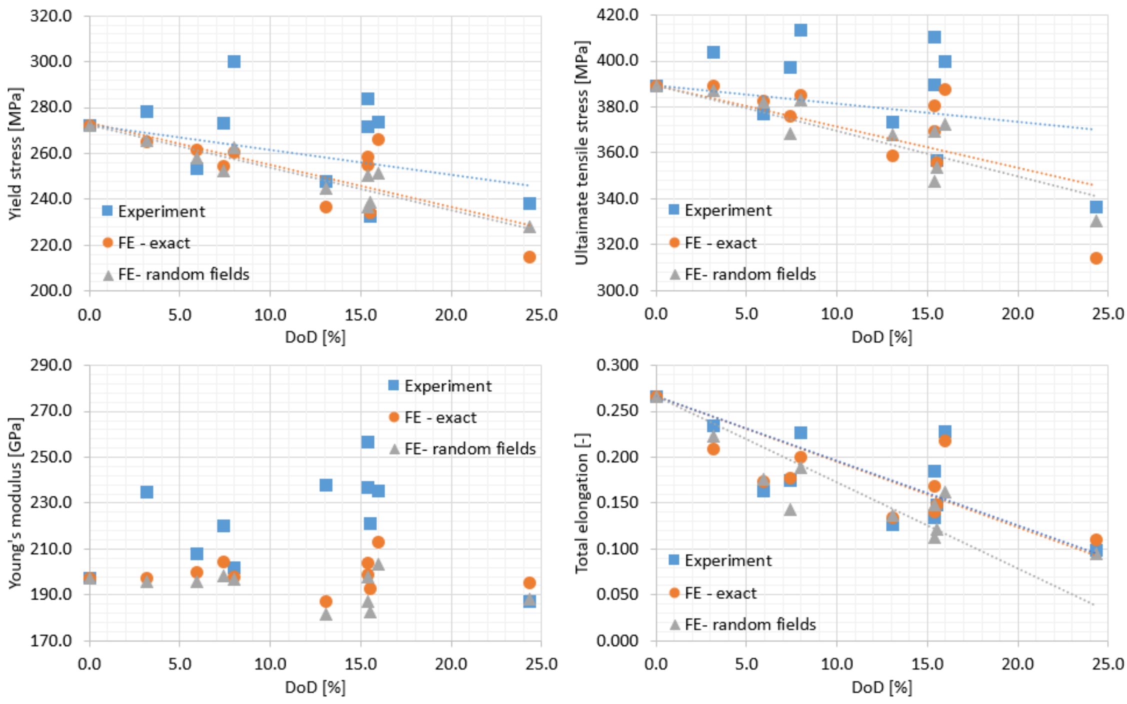

Figure 8.27. Mechanical properties changes – experimental and numerical results – 5 mm specimens.

The changes in mechanical properties considering various models and 6 mm specimens are presented in Figure 8.28. From the beginning, it is noted that excellent convergence has been obtained between numerical models. Thus, random fields accurately simulated the actual corrosion fields. Although a similar scatter of mechanical properties coming from tests has been visible as in the case of 5 mm specimens, the regressions were much closer between an experimental curve and FE computations, even that for some points, quite significant difference were visible. However, in this case, the scatter was compensated. Thus, for some points, the observed experimental values were lower than numerical ones, and for some points, it was oppositely. In ultimate tensile stress and total elongation, the regressions were almost identical. Only in yield stress, a slightly higher decrease of this parameter with corrosion development was obtained via FE computations. Similarly to 5 mm specimens, the unrealistic values of Young's modulus were obtained for several points in an experiment.

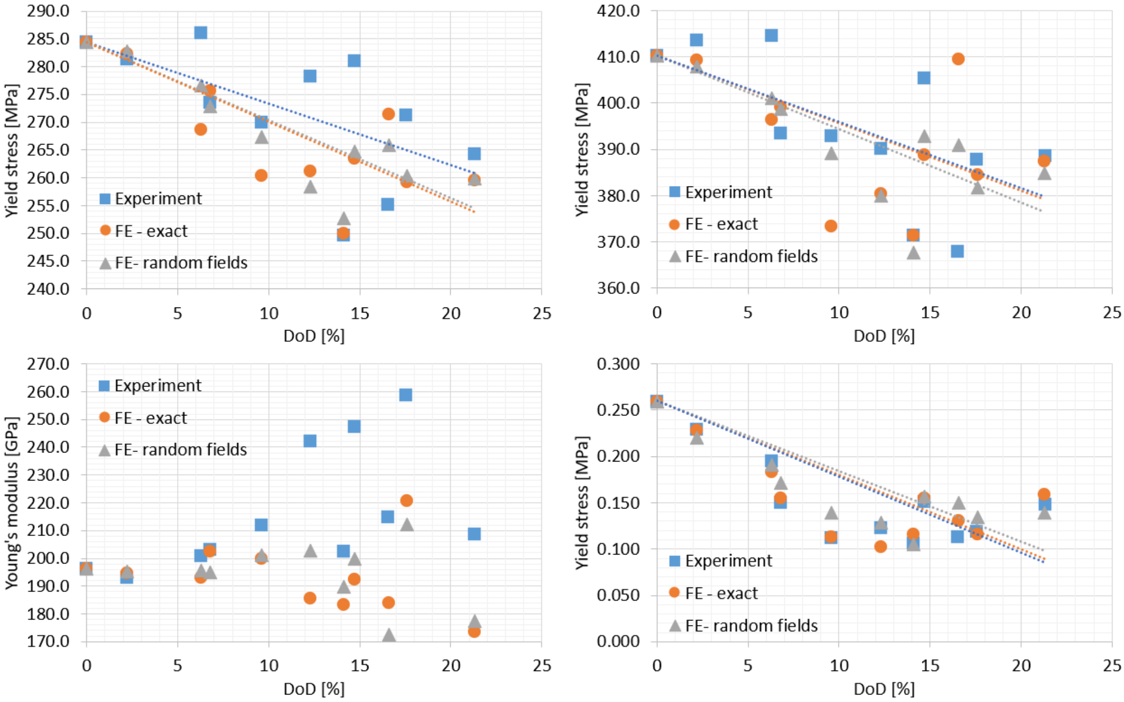

Figure 8.28. Mechanical properties changes – experimental and numerical results – 6 mm specimens.

Figure 8.29 presents the results of mechanical properties changes for 8 mm specimens. It is noted that very close results in terms of particular points and regressions were observed for experiment and numerical model with exact fields of corrosion. In 8 mm specimens, the observed initial scatter of mechanical properties was the lowest within thicknesses. However, a lower decrease of mechanical properties was observed for the numerical model with randomly generated random fields of corrosion. This indicates that for some specimens, the actual corrosion characteristics were not modelled accurately. The observed values of Young's modulus between numerical models were rather similar. However, experimental results were significantly higher.

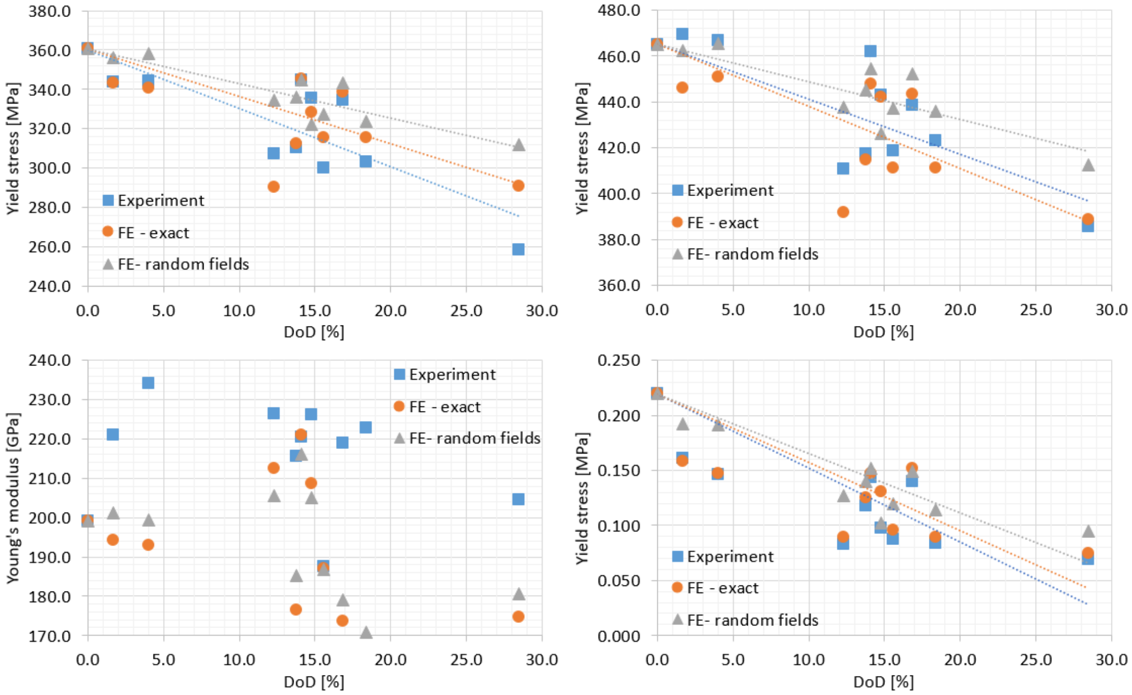

Figure 8.29. Mechanical properties changes – experimental and numerical results – 8 mm specimens.

Based on the presented results, it could be concluded that the FE modelling is very efficient to predict the decrease of mechanical properties with corrosion development and major differences when comparing to experimental results are due to the significant scatter observed for non-corroded specimens. The random fields are very efficient in simulating the real corrosion characteristics, although, for 8 mm specimens, the lower decrease of mechanical properties has been observed compared to the FE model with exact corrosion fields adopted.

8.6. Development of changes in mechanical properties for design purposes

It is noted that the changes in mechanical properties are different for different plate thicknesses. However, it was concluded that it is rather not a rule that with the increase of plate thickness, the mechanical properties decrease will be higher (see Section 6.5.2). Since the mechanical properties themselves are subjected to quite high scatter, it is reasonable to consider changes in mechanical properties obtained from various initial thicknesses. This will increase the total number of experimental points and derive some constitutive laws regardless of the specimen's initial thickness, which could be very useful in terms of design purposes.

Since different initial mechanical properties were obtained for different initial thickness, the relative values of mechanical properties with corrosion development are calculated. Thus, for a particular DoD, the observed value of the parameter is divided by its value in a non-corroded state. Since the results of Young's modulus are not credible, this parameter is assumed constant.

Figure 8.30 presents the collated results obtained from tested specimens (see Section 6.5.2). The regression curves have been derived, leading to general constitutive laws as presented in the Figure, and there were furtherly used in the analysis presented in Chapters 9 and 10.

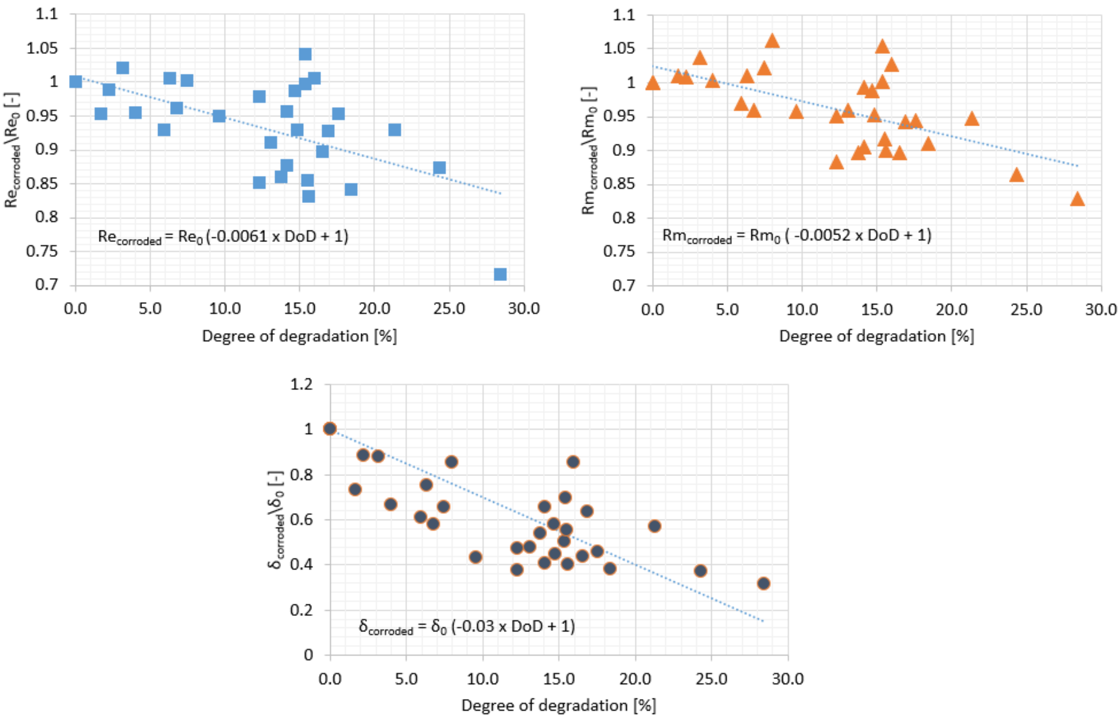

Figure 8.30. Changes in mechanical properties for design purposes.

Since particular points in Figure 8.30 are scattered from the regression curve, the standard deviation is calculated, which will be used in the reliability analysis presented in further part. The deviation for a particular point is calculated as a difference between the experimental value and the value predicted by the regression model. In Young’s modulus, the standard deviation is calculated based on the tests carried out for intact specimens (see Section 6.5.1).

The standard deviation results are as follows (Young's modulus – Eq. 8.5, Yield stress – Eq. 8.6, Ultimate tensile stress – Eq. 8.7, Total elongation – Eq. 8.8):

$$E_{StDev} = 0.0402\ E_0[GPa] \tag{8.5}$$

$$Re_{StDev} = 0.0556\ Re_0\ [MPa] \tag{8.6}$$

$$Rm_{StDev} = 0.0431\ Rm_0\ [MPa] \tag{8.7}$$

$$\delta_{StDev} = 0.145\ \delta_0\ [-] \tag{8.8}$$

8.7. Conclusions

The methodology presented in this chapter is revealed to be practical for evaluating the mechanical properties of corroded steel specimens. The random field modelling may provide the morphology of the corroded surface very similar to the real one. Except for the very thin plates, even for higher values of Degree of Degradation, the results are comparable to the experimental ones. This leads to the conclusion that the irregularities in the corroded surfaces are the factor that predominantly governs the mechanical properties reduction.

Random field modelling has another advantage. Using random field techniques, one can generate many samples, which is challenging in other cases due to the long duration of the corrosion process and very functional analysis of the corrosion morphology, and in this way, it is economically justified. Nevertheless, more experimental work should be done to validate the proposed methodology. The changes in the mechanical properties may vary depending on corrosion type and other factors (marine, atmospheric, etc.).

The corrosion degradation with the same average and maximum depth value will cause a much higher reduction of the mechanical properties in the thinner plates compared to thicker plates. Additionally, the reduction seems higher in the thinner plates for similar DoD than the thicker plates.

Based on the sensitivity analysis, it can be observed that the mechanical properties changes due to the corrosion process are susceptible to the initial thickness of plates as well as the maximum and mean corrosion depth values. Some sensitivity concerning the type of corrosion (one-side or two-side) is visible as well. In this case, the one-side corrosion will be the worst case. The corrosion field's correlation length was revealed to be not a very sensitive parameter within the considered range. However, the total elongation was slightly reduced for the higher values of the correlation length. The total elongation revealed to be subjected to a high level of uncertainties, and it is the most sensitive parameter concerning the input parameters. Thus, the higher deviations between the numerical predictions and experimental results in terms of this variable may be justified. Finally, one needs to be aware that presented foundlings are related to small-scale specimens subjected to tensile loading and yielding failure. The mechanical behaviour of corroded specimens with different scales and subjected to different types of loads need to be furtherly investigated.

The deviations between the numerical and experimental results may originate from the uncertainties in the initial mechanical properties. This is also supported by comparing the numerical predictions using the random approach and exact FE model of corroded specimens. In this case, where the input mechanical properties were identical, both models' deviations were minimal.

9. NUMERICAL ANALYSIS OF CORRODED STIFFENED PLATES SUBJECTED TO COMPRESSIVE LOAD

In this chapter, the numerical modelling of corroded stiffened plates is described and validated with the experimental results.

Concerning the material model, a bilinear stress-strain material relationship with hardening is employed. The material properties are considered as presented in Section 6.5 for both intact and corroded cases.

Before the numerical modelling of the corroded stiffened plates is presented, the model of an intact plate is validated with the experimental results.

9.1. Validation of the numerical model of compressed stiffened plates – intact specimens

9.1.1. Implementation of real imperfections [P6]

The initial imperfections are based on the photogrammetry measurements (see Section 6.4), and there are implemented by changing the z-coordinate of each finite element node. The FE analysis is conducted here without the application of corrosion degradation to compare the groups of thicknesses.

The post-collapse shapes of 5 mm specimens are presented in Figure 9.1. In all cases, the post-collapse is caused by local plate buckling followed by stiffener tripping. Nevertheless, the post-collapse shapes differ between each specimen, resulting from differences in initial imperfections distributions. The cross-section position, which is subjected to the highest plastic deformations, varies between specimens. In the case of specimen 5.2, it is even very close to the support. This indicates that the imperfections are different in terms of the maximum values presented in Section 6.4 and have different distributions along with the specimens.

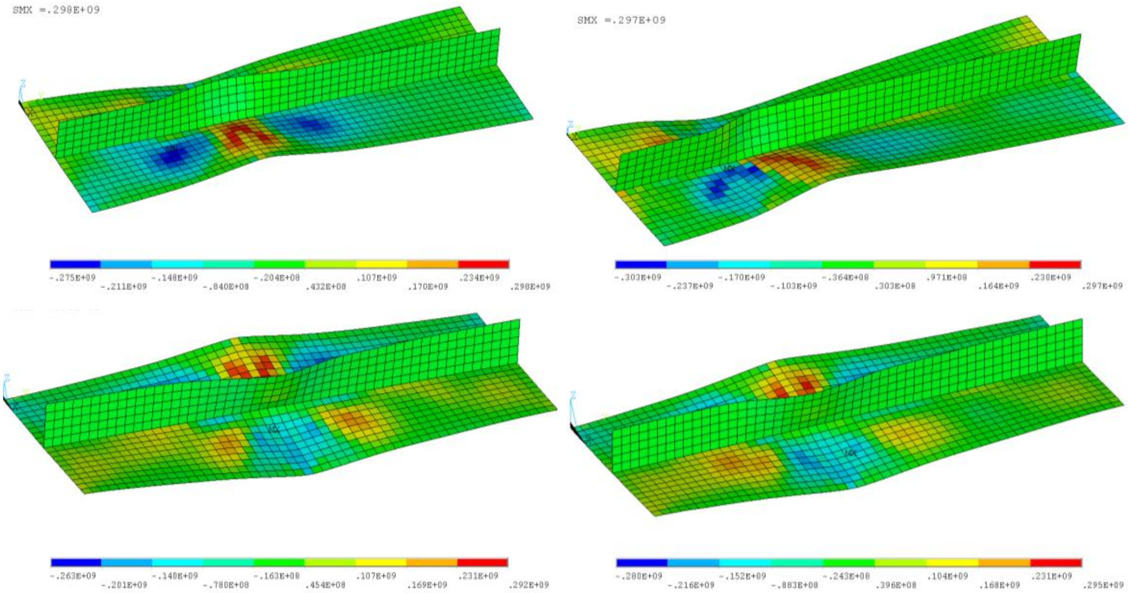

Figure 9.1. Post-collapse form of deformation in model with real imperfections – 5mm plates (5.1 -left up, 5.2 – right up, 5.3 – left bottom, 5.4 – right bottom). Normal stresses distribution in MPa.

The differences in force-displacement curves between specimens are noted too (see Figure 9.2), especially in the case of the post-collapse behaviour. The ultimate force varies between 406 kN for 5.1 specimens up to 410.1 kN for 5.2 specimens, so the impact of differences in imperfections on that value is not significant (about 1 % of difference). The initial inclinations of the force-displacement curves are different, and the specimen with the highest value of local imperfections (b_1, b_2) shows the lowest rigidity. In opposite, the most rigid is specimen 5.4, which has the lowest initial local imperfections. Further, for a specimen of the highest initial imperfections, the displacement where maximum force is reached is higher than in the case of other specimens. Additionally, for that case, the collapse is not so rapid, leading to a more smooth force-displacement curve in the region of maximum compressive force. In all cases, there is no explicitly visible bifurcation point where initial buckling occurred.

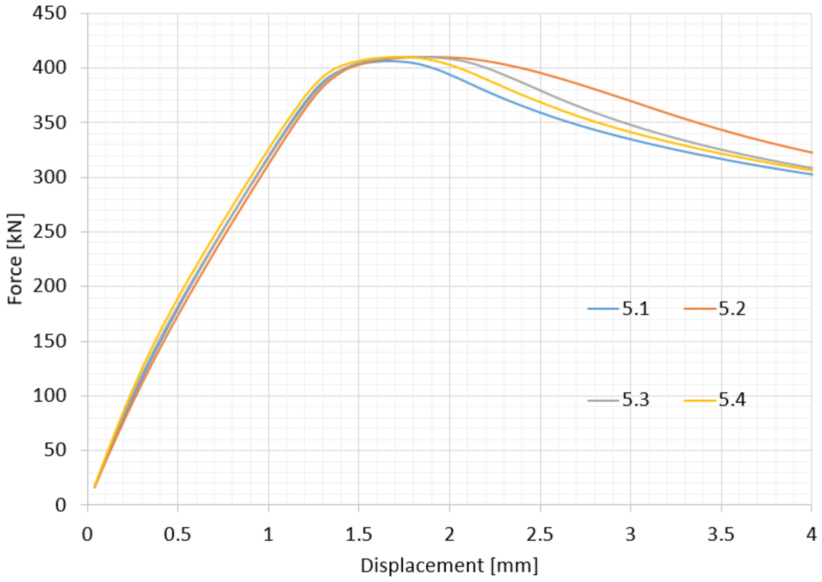

Figure 9.2. Force-displacement curves for 5 mm specimens.

The post-collapse shapes for 6 mm specimens are presented in Figure 9.3. The failure mode is plate buckling followed by stiffener tripping. Similarly to 5 mm specimens, the post-collapse shapes differ from each other. In each case, the position where maximum deflections after the collapse occurred is different. Additionally, in 6.2 specimens, the plate collapsed very near the support leading to different shape of the collapsed plate and a stiffener.

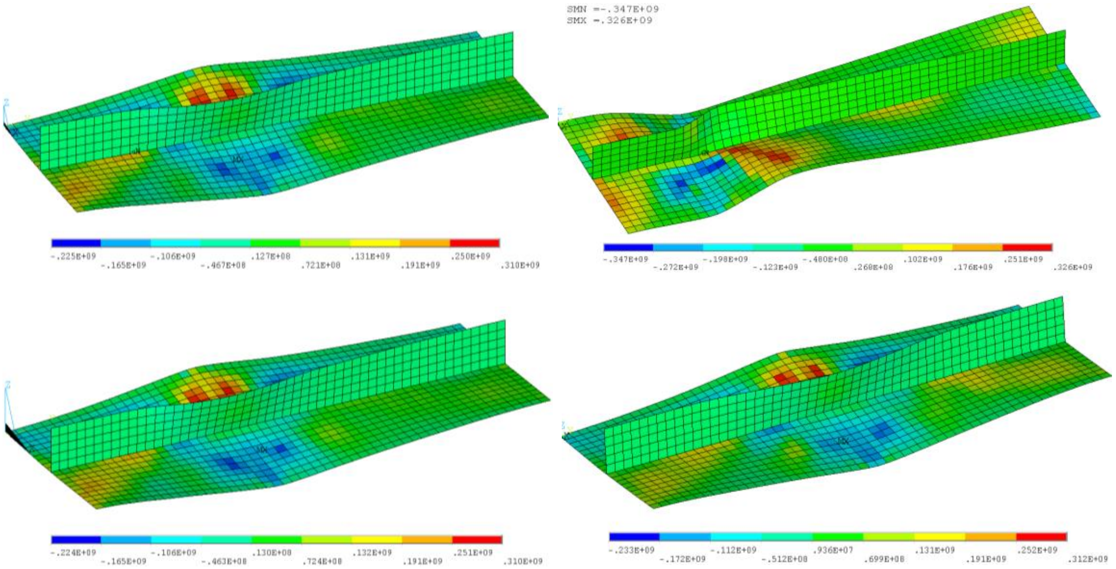

Figure 9.3. Post-collapse form of deformation in model with real imperfections – 6 mm plates (6.1 -left up, 6.2 – right up, 6.3 – left bottom, 6.4 – right bottom). Normal stress distribution in MPa.

In the case of force-displacement curves for 6 mm specimens (see Figure 9.4), the differences can also be visible. The ultimate force is between 546 kN and 546.7 kN. The specimen with the lowest local imperfections (6.4) has the biggest rigidity in the beginning, and the curve deviates from other ones. However, in this case, the deviations are smaller compared to 5 mm plates. In the case of post-collapse behaviour, only 6.2 specimen deviates from others. This is connected with different post-collapse shape observed for this specimen concerning others, as shown in Figure 9.3. It could be concluded that these deviations are originated from different initial imperfections distributions in the specimens, although the maximum values are rather similar. Similarly to 5 mm specimens, the clear bifurcation point cannot be traced.

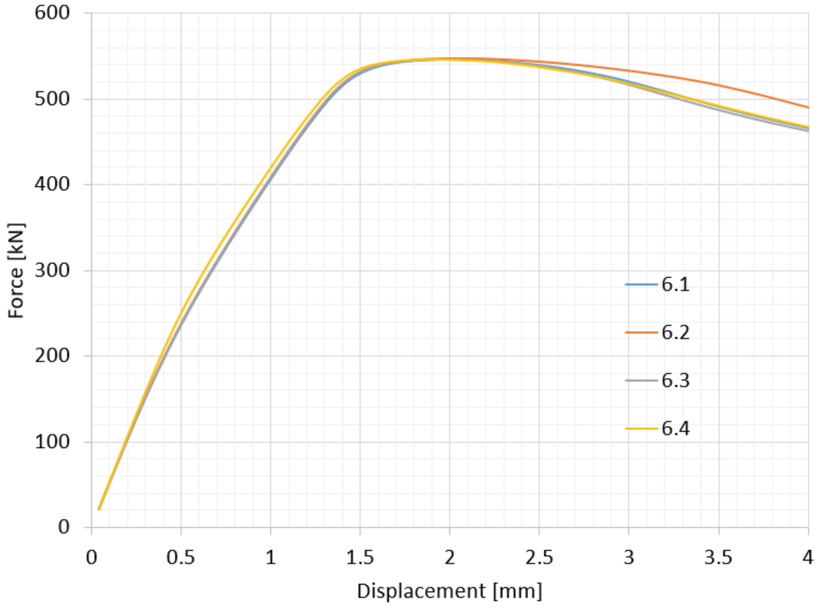

Figure 9.4. Force-displacement curves for 6 mm specimens.

The post-collapse forms of 8 mm specimens are presented in Figure 9.5. Based on the stress distributions, it could be noticed that in this case, the failure mode was a combination of local plate buckling and global column buckling. In that case, the post-collapse shapes are not differing much between the specimens. In all cases, the maximum plastic deflections occurred very close to the middle cross-section.

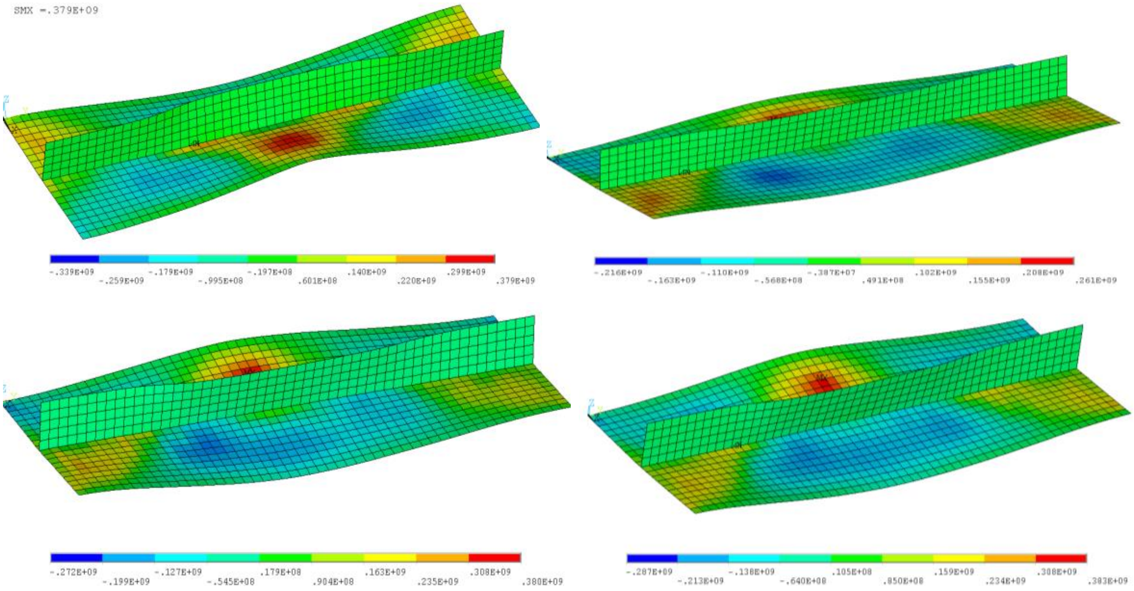

Figure 9.5. Post-collapse form of deformation in model with real imperfections – 8 mm plates (8.1 -left up, 8.2 – right up, 8.3 – left bottom, 8.4 – right bottom). Normal stress distribution in Pa.

The force-displacement curves for 8 mm specimens are presented in Figure 9.6. Similarly to post-collapse shapes, the force-displacement curves are not deviating between specimens much. However, in that case, the bifurcation point is observed, and some deviations in that region could be observed. The most explicitly it is visible for 8.2 specimen, due to the lowest local initial imperfections (only 0.25 mm and 0.11 mm). It is known that when imperfections are lower, the buckling behaviour is more rapid, and the bifurcation point is explicitly visible.

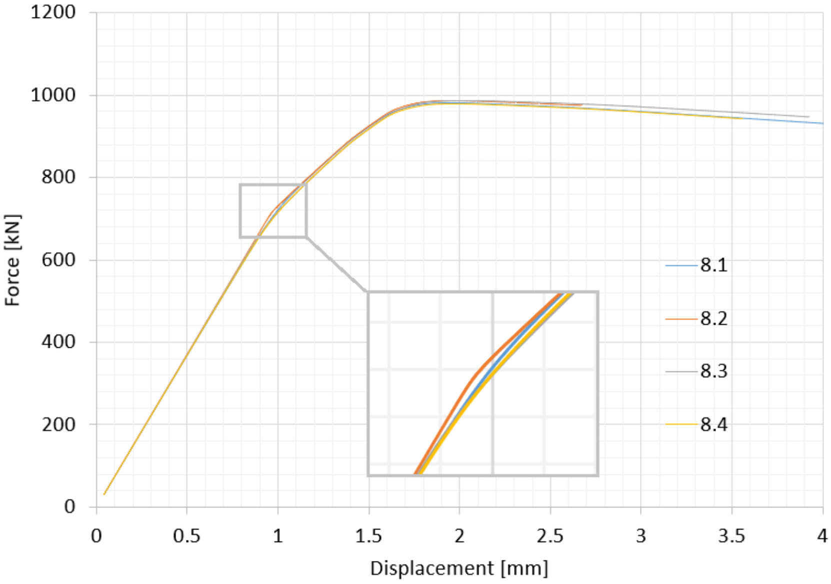

Figure 9.6. Force-displacement curves for 8 mm specimens.

In general, the differences in initial imperfections has a low impact on the value of the ultimate force. In the post-collapse shape, the differences are noted for thinner plates (5 mm, 6 mm), whereas for thicker plates, the shapes are very similar between each other. A similar observation could be noted by comparison of force-displacement curves.

The differences in maximum plastic deformations between the specimens indicate that the imperfections vary in terms of maximum value and the distributions along with the specimen. In the case of 5 mm and 6 mm specimens, the initial local imperfections with opposite signs of both side of stiffener lead to collapse without clearly visible bifurcation point since the collapsed form was similar to the initial shape of specimens. In the case of thinner 5/6 mm plates, both the deflection and the stress distribution have more of a local, concentrated character. Changes in deformation and stress are rapid and dramatic. Thicker plates manage to resist deplanation using their full length and width. The stress distribution is much milder, and the areas near supports are also affected. This phenomenon is not noticeable using artificially generated imperfections, which is discussed later in the text. The support area is nearly untouched by stress, concentrated mostly in the middle part of the plate regardless of its thickness.

Where initial imperfections are unknown, one needs to assume their value and shape using one existing technique. Thus, the results are compared with the Smith approach presented in Section 5.1.2.

Using the following model, the specimens with three different thicknesses are analysed, leading to post-collapse shapes, as presented in Figure 9.7. From the beginning, one can notice that in the case of the assumed shape of initial imperfections, the collapsed form is symmetrical with regards to the middle cross-section and maximum deflections occur in that place. In the plates with real imperfections, the usually non-symmetrical collapse was observed due to the unsymmetrical distribution of initial imperfections. In the case of failure modes, for plates with the assumed shape of imperfections, a local plate buckling is followed by stiffener tripping. In plates with real imperfections, similar modes are observed in 5 mm and 6 mm plates. However, for an 8 mm plate, the failure mode is rather the combination of local plate buckling and global column buckling. This could also be noticed when looking at stress distributions. In the case of an 8 mm plate with real imperfections, both compressive and tensile zone are quite extended along the plate length (see Figure 9.5), and in the case of the Smith approach, these zones are localised in the middle of the specimen with rather limited extension.

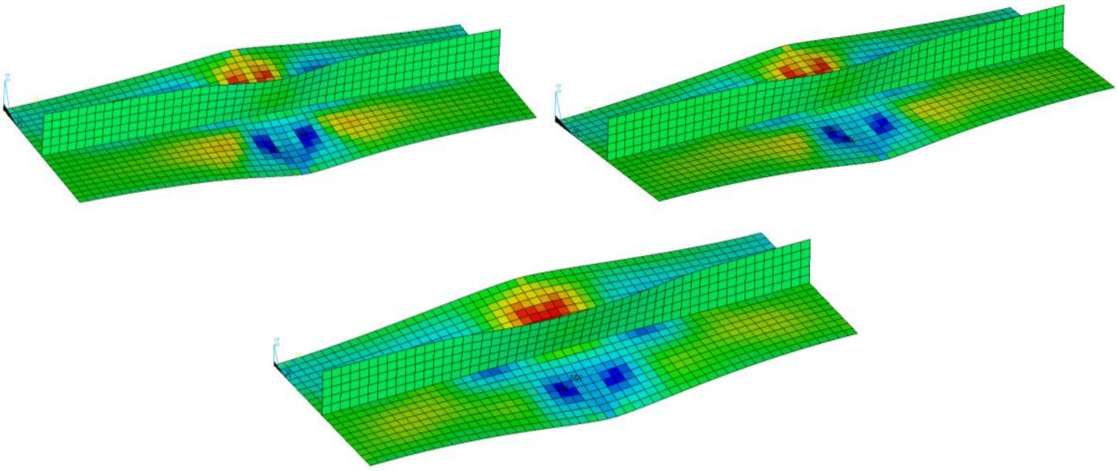

Figure 9.7. Post collapse shapes for imperfections based on smith approach (5 mm plate –left up, 6 mm plate – right up, 8 mm plate – bottom).

Due to the differences in the yield stresses due to different plate thicknesses, the normalised stress – mean strain curves are introduced instead of force-displacement curves. The stress is divided by material yield stress on the vertical axis, whereas, on the horizontal axis, the longitudinal displacement divided by plate length is presented. The comparison between mean response for stiffened plates with real measured imperfections and following the Smith approach is presented in Figure 9.8. It could be noticed that the differences are quite significant in the case of 5 mm and 6 mm plates. Firstly, in both cases, the clear bifurcation point is noted for plates with artificial imperfections, which could not be traced for plates with the measured imperfections. In the case of the measured imperfections, the collapsed shape was closer to the initial shape of the specimens; thus, the buckling was not so dramatic.

Additionally, the initial inclination of the stress-strain curve is significantly higher for the first case. Further, the point of the ultimate capacity is reached with smaller strain in plates analysed with artificial imperfections, and collapse is more rapid. In plates with real imperfections, the region of maximum stress is quite wide, and collapse is less rapid. With regards to the 8 mm plate, both curves are rather similar. The initial inclinations are almost the same, leading to the bifurcation point, which in case of artificial imperfections occur for slightly higher stress. The ultimate point cover in both curves and post-collapse behaviours are rather the same.

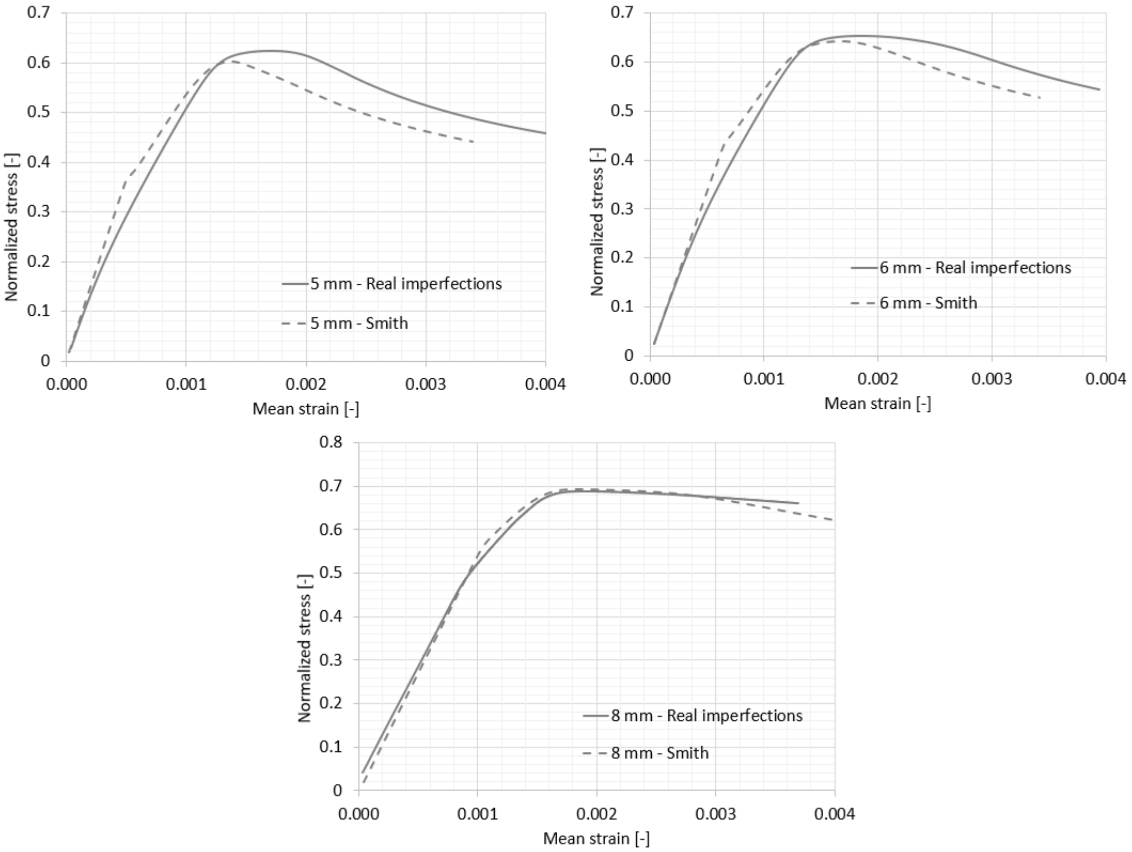

Figure 9.8. Comparison between stress-strain curves for specimens with real initial imperfections and generated using Smith approach.

Finally, the normalised ultimate stresses are compared in Table 9.1. It could be observed that there are no notable differences. In a 5 mm plate, the capacity is slightly higher in real imperfections, whereas it is the opposite for 6 mm and 8 mm plates.

Table 9.1. Results of normalised ultimate stress.

Thickness [mm]	Normalised ultimate stress [-]		Difference [%]
	Real imperfections – mean value	Artificial imperfections	
5	0.612	0.603	1.56
6	0.640	0.643	-0.47
8	0.687	0.694	-0.98

It has been observed that apart from the identical welding parameters were provided for each specimen, the imperfections varied between each other, leading to differences in both post-collapse shapes as well as force-displacement responses. The differences are more significant; the thinner plate is. This could be related to the increasing plate slenderness ratio, and for higher values of that parameter, the structural behaviour is more sensitive with regards to the initial imperfections level. Employing the real imperfections bring more variance to the deformation and stress distribution of different plate thickness. Although the ultimate force is hardly affected, the qualitative difference is easily noticeable to the eye. However, using different welding parameters, the differences in load-carrying capacity could be significantly higher too.

Comparing the proposed approach with the commonly used methodology of a priorly assumed shape and level of initial imperfections revealed some differences. Primary, the assumed shape of imperfections led to a symmetrical post-collapse shape of each specimen, which has not been observed for real imperfections due to uneven distribution. In the case of the Smith approach, the buckling has been more dramatic, and an explicit bifurcation point has been noted, and post-collapse behaviour has been more rapid.

9.1.2. Validation of boundary conditions [P4]

The FE model of the stiffened plate is presented in Figure 9.9. The boundary conditions are considered in two variants, namely clamped and simply supported one. The applied boundary conditions, referring to edges numbers, as shown in Figure 9.9, are summarised in Table 9.2. The loading is developed via an incremental increase of longitudinal displacement of edges 3 and 4.

Table 9.2. Applied boundary conditions.

Edge number	Simply supported conditions	Clamped conditions
1	$u_x = 0, u_y = 0$	$u_x = 0, u_y = 0, rot_z = 0$
2	$u_z = 0, u_y = 0$	$u_z = 0, u_y = 0, rot_x = 0$
3	$u_x = 0, u_y = coupled$	$u_x = 0, u_y = coupled, rot_z = 0$
4	$u_z = 0, u_y = coupled$	$u_z = 0, u_y = coupled, rot_x = 0$

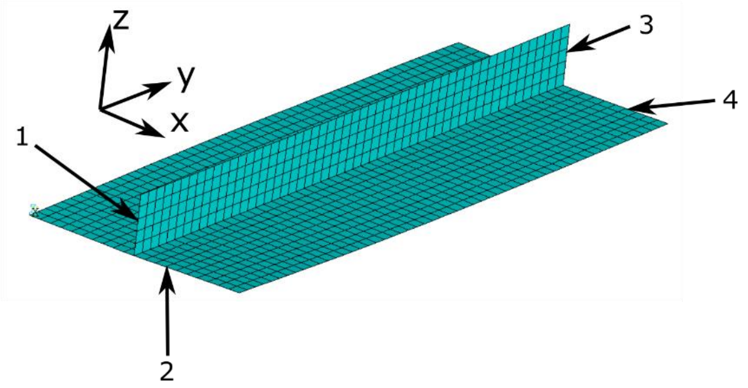

Figure 9.9. FE model of the stiffened plate.

The force-displacement responses estimated by the FEM and tests are compared. The ultimate strength has been reached, for the longitudinal shortening, between 5 and 7 mm. In the case of numerical results, this point has been reached with 2 mm of shortening. The readjustment of the test set-up may explain this until every part of the stiffened plate, supports, and hydraulic machine were in full contact, and experimental supports start be behaving like the ones generated by FEM. This problem was observed in different studies, e.g., [189,272,273]. Cui and Wang [273] suggested that when the displacement is measured only in the head, which transmits the load, the other supporting structure, since it is not perfectly rigid, is also subjected to some deflections, increasing the shortening in the measurements. The additional displacement transducer has been installed for measuring the relative displacement between the supports. It was found that there was a difference between both readings, and measurements between heads are more precise. Nevertheless, the longitudinal displacements are still significantly higher compared to the FE model.

The adjusted experimental force-displacement curves, together with the numerical model results, are presented in Figure 9.10. When comparing numerical and experimental results, the structural behaviour is quite similar after normalisation, including the pre-and post-collapse regime, especially when considering a 6 mm specimen. Nevertheless, in the case of both 5 mm and 8 mm specimens, some differences are notable. Generally, in pre-collapse behaviour, the curve inclination is smaller at the beginning of the loading process, up to the level of approximately 50 % of the maximum force. Furtherly, it is increasing, leading to a similar displacement at the point of maximum capacity. In the case of numerical curves, the exact bifurcation point cannot be distinguished.

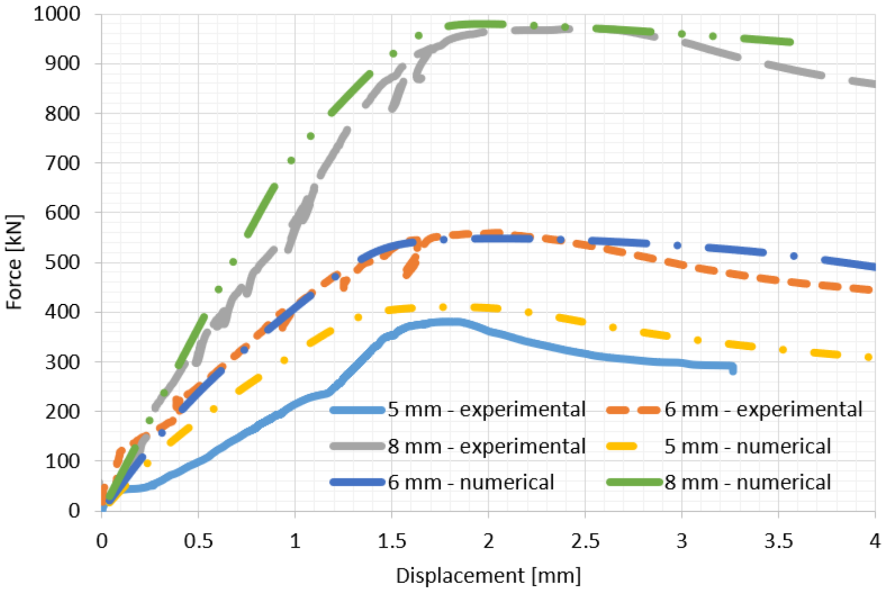

Figure 9.10. Force – displacement curves for 5 mm (left up), 6 mm (right up), and 8 mm (bottom) specimen.

The supports were designed to achieve the clamped boundary conditions leading to no displacement and no rotation, as discussed in Section 6.1. The force-displacement relationship from the experiment is compared with the numerical analysis of the linear structural response and eigenvalue buckling, taking into account both clamped as well as simply supported conditions (see Figure 9.11).

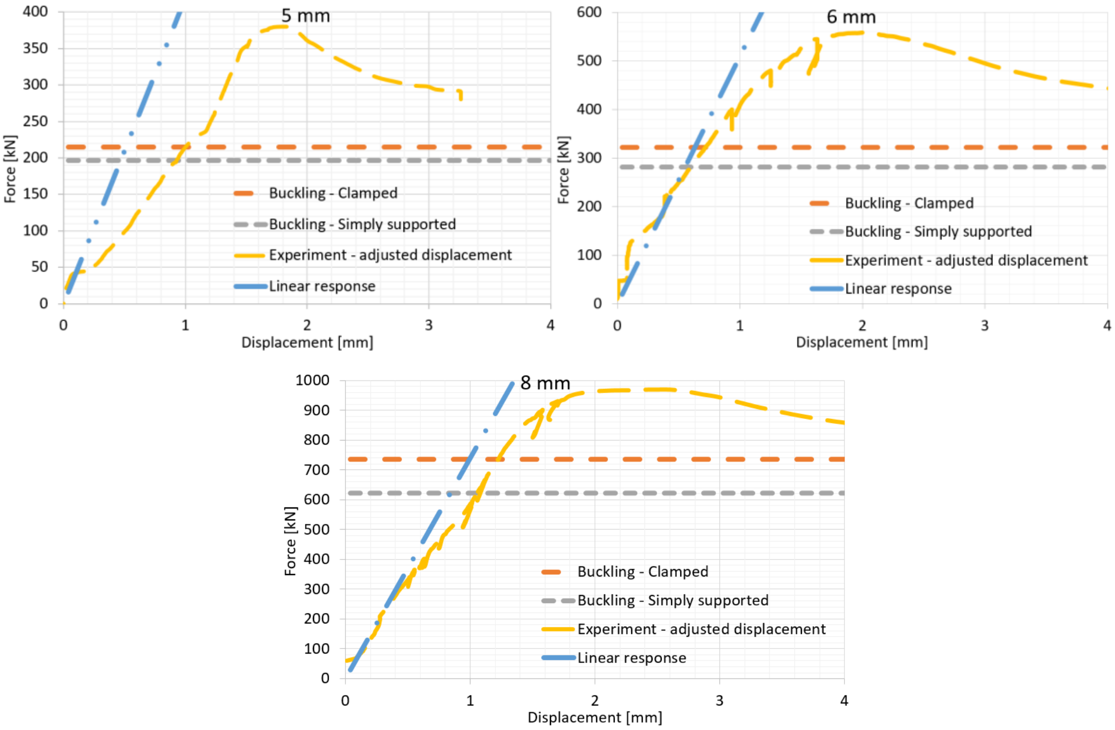

Figure 9.11. Force – displacement relationship for 5 mm (left up), 6 mm (right up), and 8 mm (bottom) specimen.

From the comparison presented in Figure 9.11, it is notable that there is no significant difference between critical force for both clamped and simply supported conditions. The reason for that is the restriction of an end-cross section of the stiffened plate from rotation, and the plate can rotate only locally. Due to that fact, the shape of the stiffened plate results in strong support itself, having a significant stiffness. Eventual clamping will additionally restrict the plate from a local rotation near the supports. The differences in the ultimate strength will be much higher for the non-stiffened plate. It could also be noticed that the differences in ultimate strength are even smaller when dealing with the nonlinear FE analysis (see Table 9.3). Thus, it may be concluded that the FE analysis predicts the ultimate strength of the stiffened plate accurately, and it is not so sensitive in the local rotation of the plate. The buckling capacity is lower than the estimated ultimate strength. When the elastic buckling occurs, the structural component will still carry some load to the structural collapse. It is also observed that the experimental curve's initial inclination is very similar to the linear response obtained in the numerical analysis. However, with the increase of the longitudinal displacement, the bending causing the high deflections of the plate occurs, leading to a drop of the force-displacement curve inclination.

The load-carrying capacity for both experimental and numerical results is very similar, as presented in Table 9.3. The ultimate load of the FE analysis with clamped boundary conditions is slightly closer to the experimental value for a 6 mm specimen. In the case of a 5 mm specimen, there are not notable differences. For an 8 mm specimen, the experimental value is between simply supported and clamped conditions in the numerical model. The differences between the simply supported conditions and clamped ones concerning FE analysis are increasing with the thickness increase. There are reaching about 3 % in the case of an 8 mm specimen thickness.

Nevertheless, based on these results, it could be concluded that the modelling is not very sensitive for a particular type of boundary conditions used.

Table 9.3. Ultimate force, experimental and numerical analyses.

Thickness [mm]	Ultimate force [kN]			Differences [%]	
	Experiment	Numerical - Simply Supported	Numerical - Clamped	Exp. – Simply Supported	Exp. - Clamped
5	380.2	407.4	410.1	7.2	7.3
6	552.3	539.5	548	-2.3	-0.8
8	953.9	950.4	979.7	-0.4	2.6

Furtherly, the post-collapse shapes of tested specimens are investigated. As it was analysed in Section 6.1, for the clamped boundary conditions (the gap between the specimen and supporting clamps will be small enough) and simply supported one, the post-collapse forms are quite different, as can be seen in Figure 6.3, where an example of a specimen of a 5 mm specimen thickness is presented. When clamped boundary conditions are employed, the one half-sine wave distortion during plate buckling loading occurs. The highest deflections are observed near the mid-cross-section along with the specimen. In simply supported specimens, the two half-sine wave displacement during plate buckling occurs with an excessive amount near the supports.

The post-collapse shapes of the experimentally tested specimens are presented in Figure 6.40. It may be noticed that the shape of the deformed specimens is relatively similar, and the collapse has been caused by the local plate buckling followed by stiffener tripping; i.e. global column buckling was not observed. In both 5 mm and 6 mm specimen thicknesses, the cross-section of the highest deflections occurred at some distance from the mid-cross-section, which was not observed in the initial numerical studies. In an 8 mm stiffened plate thickness, the extreme deflections occur very near the mid-cross-section. In all specimens, the one half-sine waves result from buckling, which shows that the supports behaved adequately, as was anticipated in pre-experimental studies.

The post-collapse shapes are compared with numerical investigations accounting for measured initial imperfections and considering clamped boundary conditions, as presented in Figure 9.12. In general, the deformation forms from both experimental and numerical studies are similar, i.e., the local plate buckling followed by stiffener tripping caused the collapse of the stiffened plates. The most identical deflection shapes are observed for a 6 mm specimen. In this case, the position of the highest deformations is similar and the form of the collapsed stiffener. In the case of a 5 mm specimen, the collapsed cross-section's position is not the same as in a FE analysis, which results in a slightly different shape of both collapsed plate and stiffener.

Regarding the 8 mm specimen, the position of the collapsed cross-section and shape of the collapsed plate are similar, and the only form of the damaged stiffener is different. As was presented in the next section, the differences in post-collapse shapes may result from the non-uniform distribution of mechanical properties within a single stiffened plate (see Section 9.1.3).

Other possible factors that may change the post-collapse behaviour are the welding-induced residual stresses.

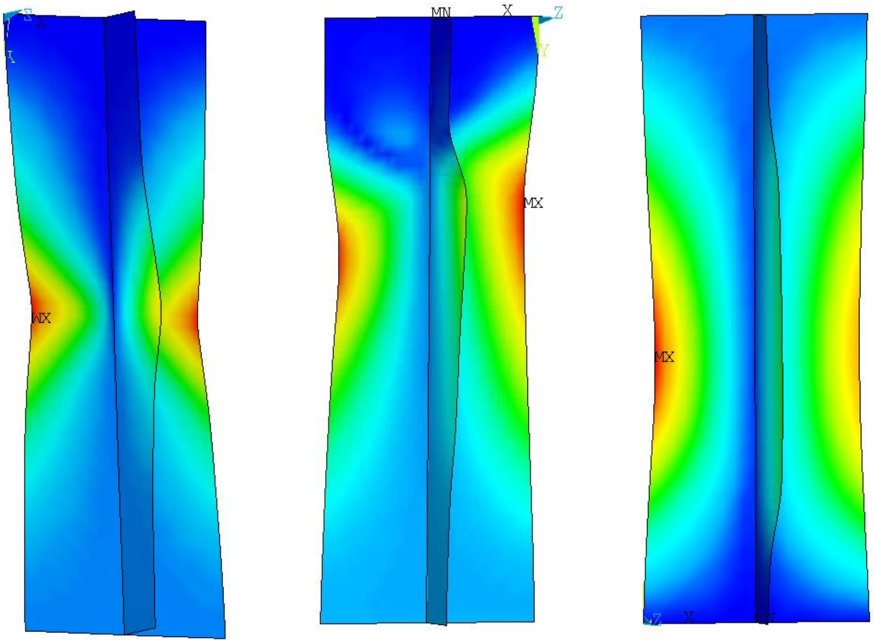

Figure 9.12. FE post-collapse shape for 5 mm (left), 6 mm (mid) and 8 mm (right) specimen.

Based on the analysis of the post-collapse forms of tested specimens, compared to pre-experimental FE analyses of supporting structure and the stiffened plate accounting for the initial geometrical imperfections, several conclusions may be derived. The designed supports can generate boundary conditions very close to the clamped ones, avoiding buckling forms with several half-sin waves. When comparing tested specimens with a FE analysis, the deformation forms are very similar, although, in the case of 5 mm and 8 mm specimens, some differences are observed.

It may be concluded that the rotations of the stiffened plate cross-sections in the supports were restrained. However, to investigate the clamped condition of plates locally, the lateral displacements near the supports were measured (see Section 6.2.3). When comparing the theoretical shapes of the buckled plate in the case of clamped and simply supported conditions (see Figure 9.13), one can notice that there are significant differences in the rotation of the edge near the support (φ_1 and φ_2). There is no rotation in the point of supports in the case of a clamped plate. When one measures the lateral displacement at a very close distance from the support, the rotation of the edge can be estimated as the deflection (w_1 and w_2) divided by the distance d, as it is presented in Figure 9.13.

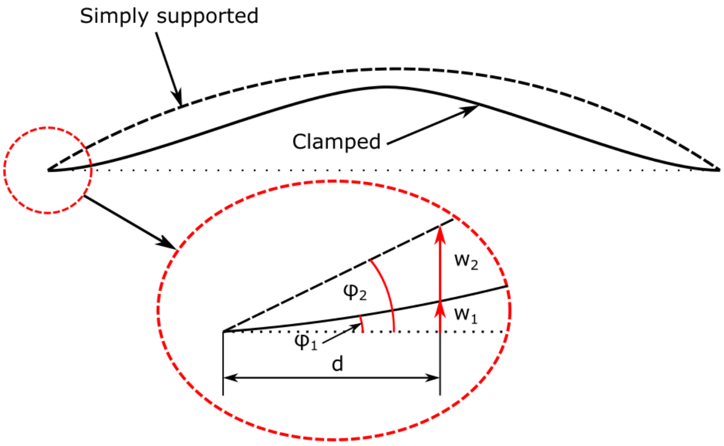

Figure 9.13. Displacement distribution of equally loaded simply supported and clamped plates.

To validate the boundary conditions, an analysis of the lateral plate displacements near the supports is carried out (d1, d2 (upper edge) and d4, d5 (bottom edge) using the displacement gauges presented in Figure 6.14. The measurements were compared with the FE analysis considering that the plate and stiffener are simply supported or clamped. The comparison for all lateral displacements in the function of longitudinal displacement for a 5 mm specimen is presented in Figure 9.14.

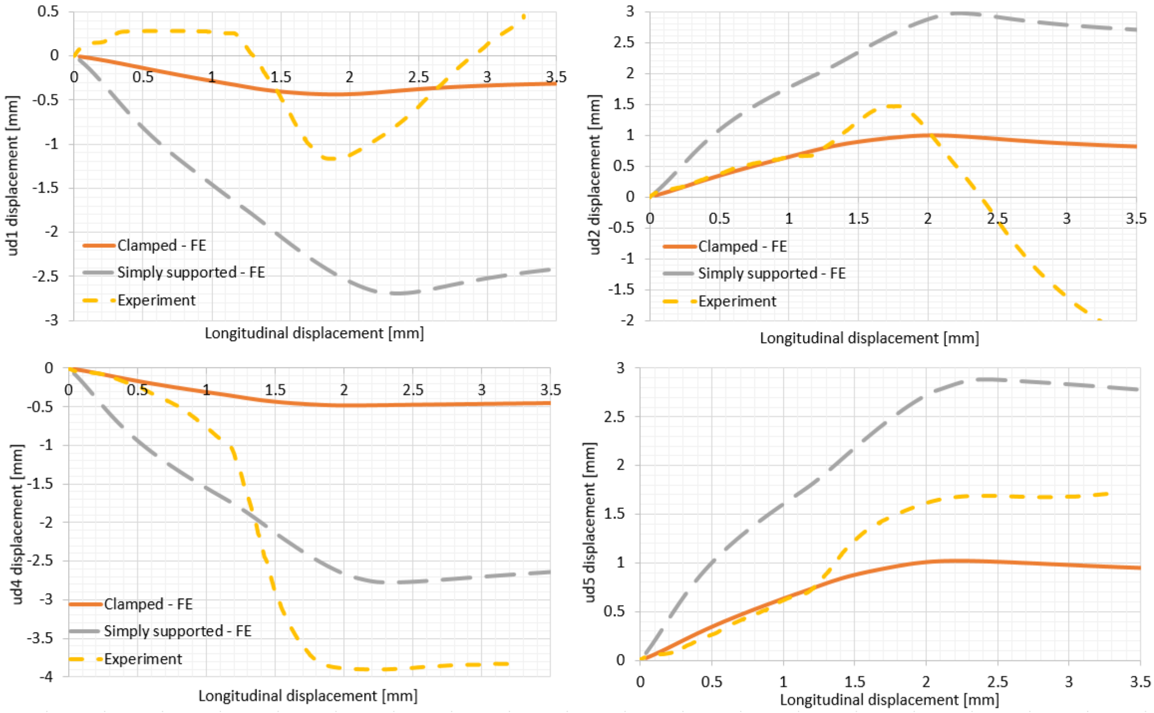

Figure 9.14. Displacements of the plate near support for 5 mm specimen.

One can notice that up to a 1.25 mm longitudinal displacement produced by a load before reaching the ultimate strength, the edges were almost without rotation. Up to that point, the behaviour was the same as for the FE analysis, considering the fully clamped conditions. After that point, the plate buckled elastically, increasing the deflections near the lower edge and decreasing the deflections near the upper edge. The FE analysis did not capture this phenomenon. Apart from that, the displacements near the supports increased but still closer to the clamped boundary conditions (ud1, ud2, and ud5). Only in the case of the plate corner (ud4), the displacement increased rapidly. After arriving at 2 mm longitudinal displacement, where the ultimate bending moment of the critical cross-section is achieved, and the response force starts decreasing, the displacement of the lower edge stabilized on a constant value, similarly to the one of the FE analysis. However, on the upper edge, the displacement started to increase in the opposite direction. The differences between the experimental set-up and FE model are mainly the reason for the different locations of the collapsed cross-section, which was observed in the middle of the specimen in the case of FE analysis. It was more close to the upper support in the case of the tested specimen. Thus, the differences are caused by different post-collapse shapes, governed by many factors, including the boundary conditions. The comparison of the lateral displacements of a 6 mm specimen is presented in Figure 9.15.

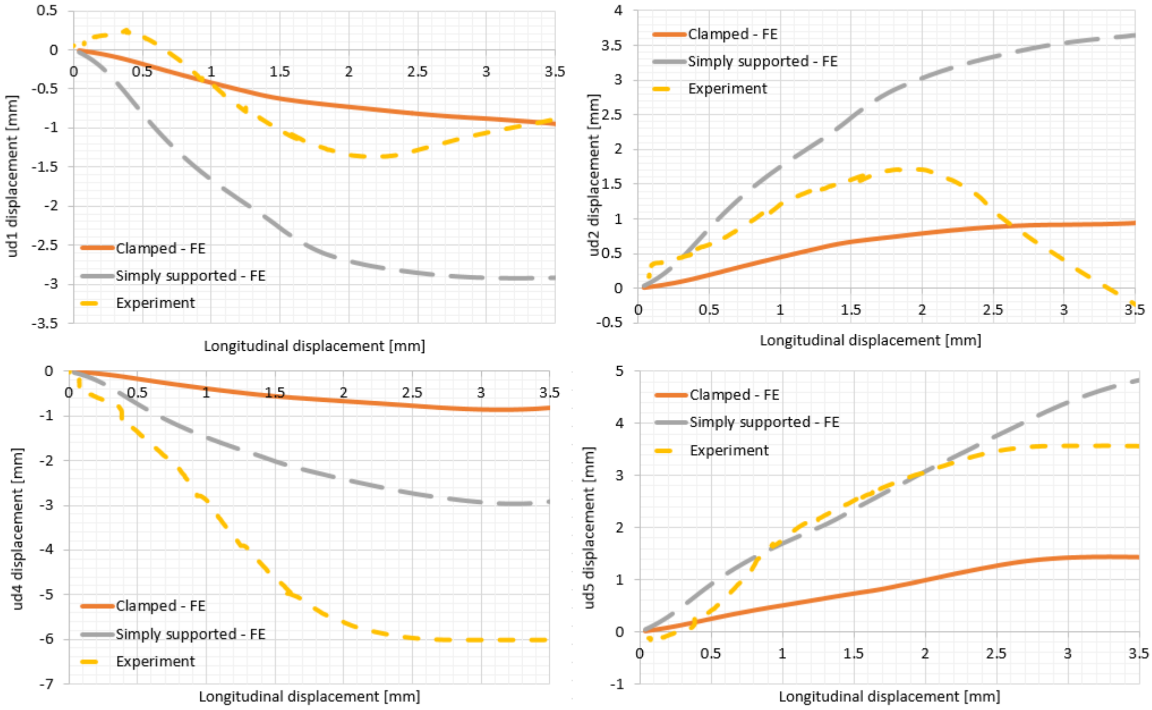

Figure 9.15. Displacements of the plate near the support for a 6 mm specimen.

As can be noticed, in the upper edge (ud1 and ud2, see Figure 9.15), the boundary conditions are very close to the clamped ones. However, in the bottom edge (ud3 and ud4), the structural behaviour is more comparable to the simply supported conditions. In the case of ud3 measurements, there were even more prominent than the results of the FE analysis considering the simply supported conditions. After reaching the ultimate strength, both displacements stabilized on a constant value. Additionally, for ud2 and ud3 gauges, the notable drop of the displacement at the beginning of the loading process is observed, which may be due to the initial adjustment of the specimen to the support resulting from possible misalignments between the specimen and support.

The comparison of the lateral displacements near the supports for the 8 mm specimen thickness is presented in Figure 9.16. It can be noticed for all measurements that for longitudinal displacement between 0 and 0.5 mm, some lateral displacements were captured, which was not observed in the FE analyses either with clamped or simply supported edges. Probably this was the result of an initial plate adjustment to the supports. After reaching that point, in the upper edges (ud1 and ud2), the displacements were very close to the clamped boundary conditions. However, the bottom edge (gauges ud4 and ud5) revealed the behaviour somewhat closer to the simply supported conditions. After reaching the ultimate strength (approx. 2 mm of the longitudinal displacement), the displacement near the upper edge decreased, whereas the displacement near the bottom edge stabilized on a constant level.

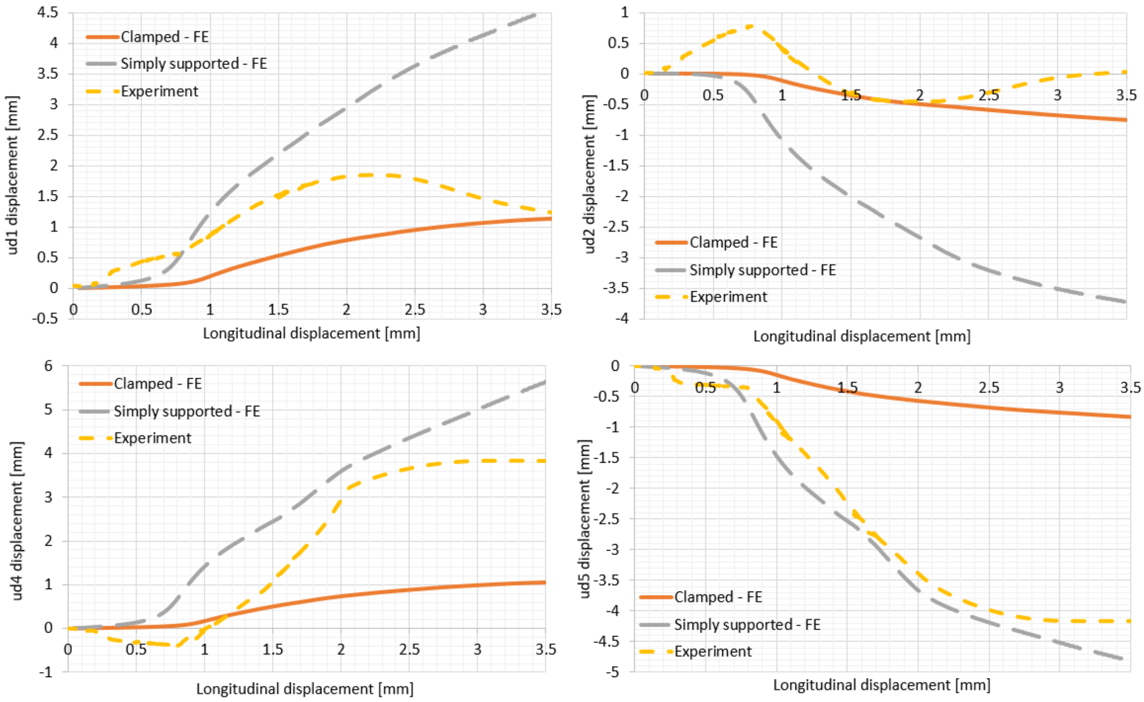

Figure 9.16. Displacements of the plate near the support for an 8 mm specimen.

Based on the detailed analysis of the lateral displacements of the plate near the supports, several general observations related to all specimens may be derived. It can be noticed that the displacements near the upper support (ud1 and ud2) were relatively very close to the results of the FE analysis with clamped boundary conditions. However, in displacements near the bottom support (ud4 and ud5), the behaviour was closer to the FE analysis with simply supported boundary conditions. The only exception was the 5 mm specimen, wherein in the case of ud5, the displacement was also very close to the clamped boundary conditions. Another observed phenomenon for all specimens was that the displacement near the upper support decreased after reaching the ultimate strength.

In contrast, the displacements near the bottom support stabilized on a constant level. Summarising, in all cases, the boundary conditions very close to the clamped ones were achieved, which was the intention of the design. The closest stiffened plate with clamped support behaviour was achieved for a 5 mm specimen. In the case of 6 mm and 8 mm specimens, the bottom support tended to simulate boundary conditions close to the simply supported ones.

One can distinguish many possible reasons that caused the differences between the experimental measurements and FE analyses. Firstly, both plate and stiffener were subjected to some misalignments. Thus, the absolute elimination of the gap between the supports and specimen is unachievable. Secondly, the loading process in the real machine is different from the one generated in the FE analysis. In experimental testing, the incremental loading has been produced by a hydraulic jack-up subjected to in the middle of the bottom support. In the upper support, the load has been transmitted via the upper head placed on the two side columns, leading to a more uniform response distribution in the specimen compared to the bottom edge. This led to the slightly unsymmetrical behaviour for the specimen, which was observed in measuring the lateral plate displacements. In the case of the FE analysis, the incremental loading was identical for both the bottom and upper edge of the specimen. Another problem related to the testing machine was raised about possible non-perfectly uniaxial loading with increased loading. This may lead to some eccentricity in loading and introduce an additional bending moment, causing higher lateral displacements of plates. Finally, it needs to be noted that the restraining of rotation in the FE analysis is also challenging.

Figure 9.17 compares the post-collapse shapes near the support for both FE analysis and tested specimen. It can be noticed that in the case of a FE analysis, the boundary conditions cause the restrain of the edge rotation, and deformed and unreformed edge are covering near the support. However, in the case of the experiment, the excessive lateral displacement of the plate near the mid-length region causes the local plate to bend near the support and creates a plastic hinge. One needs to note that the plastic hinge can be considered a simply supported condition, which explains the differences between the FE analysis and experiment in the lateral plate displacements, as reported in Figures 9.14 – 9.16.

The plastic hinges were observed near the bottom support for all specimens. Thus, the total restriction of the plate rotation near the support is impossible to be achieved, even when considering the welding of the transverse edge to the support. Based on that, it could be concluded that the ideal clamped conditions are rather non-achievable in both experimental testing and real ship structures.

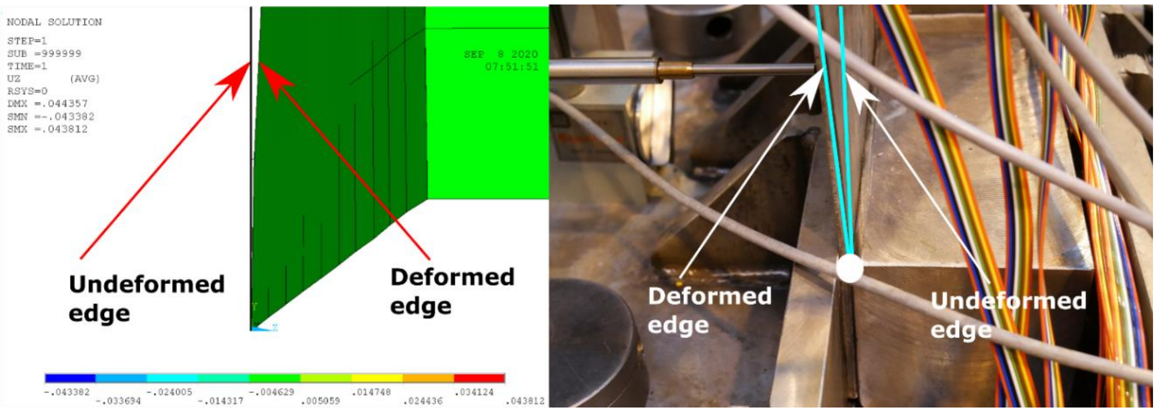

Figure 9.17. The post-collapse shape of a specimen in the support region, FE analysis (left), and tested specimen (right).

The presented section investigated the impact of the boundary conditions on the ultimate strength of stiffened plates with different thicknesses during experimental testing. Based on the experimental and FE analyses, several conclusions are derived. The experimental testing aimed to analyse the clamped boundary conditions' achievement, preceded by an advanced FE analysis of the support-specimen structural interaction. The experimentally estimated ultimate strength of the stiffened plate revealed to be very close to the FE analysis considering clamped boundary conditions. Nevertheless, even when the FE analysis considers simply supported conditions, the differences in estimating the ultimate strength is also minimal. The reason is that both the upper and lower cross-section of the specimen is restrained from out of plate rotation, and the shape of the stiffened plate results in strong support itself. Eventual clamping will additionally restrict the plate from a local rotation near the support. Thus, the developed FE models and performed analyses are credible in representing the experimental testing of the stiffened plate subjected to compressive load. The estimated ultimate strength is very similar compared to the one evaluated by the experiment.

Based on post-collapse shapes analysis, it can be concluded that the gap between the support and specimen has been minimized. In each specimen, the observed buckling shape was the one half-sine wave of loss of stability. This is consistent with the pre-experimental numerical investigations. Furtherly, similar post-collapse forms were noticed between the FE and experimental analysis, although some differences occurred. Based on that, it was concluded that the clamped boundary conditions were achieved. In each specimen, the local plate buckling, followed by stiffener tripping, was identified as a reason for the structural capacity loss.

The detailed analysis of lateral plate deflections near the supports and comparison with the FE analyses with both clamped and simply supported boundary conditions revealed that fully-clamped conditions were not achieved. Several possible reasons were identified, including the non-ideal force transition via the testing machine, the possible eccentricity of axial loading, the unfairness of both stiffened plates, and the supporting structure. Furtherly, by comparing the post-collapse shapes of specimens near the support, it was concluded that the total restriction of the plate rotation is challenging in experimental conditions, leading to the possible creation of plastic hinges. This will be valid also when one considers the real ship’s structural stiffened plates.

Finally, it is concluded that the clamped boundary conditions, as defined in the present study, have been achieved in terms of restraining the stiffened plate cross-sections from rotation in the supports. However, for some specimens, the plates were not fixed ideally in terms of local plate buckling, which will also be observed in real ship structures. The main advantage of the present support design is that it provides very stable support without welding. It is easily adjustable to specimens with different thicknesses and provides simplicity during specimen’s replacement. The FE analysis with clamped boundary conditions can predict the ultimate strength of stiffened plates with sufficient accuracy. However, it is noted that in real situations, the fully-clamped conditions will not occur either.

9.1.3. Impact of mechanical properties – intact plate [P9]

When one performs a validation of the numerical model within experimental results, the material properties coming from tensile tests of standard coupon specimens are typically taken as an input. The hypothesis, which is behind the origin of the presented study, states that the deviations of mechanical properties within a single specimen may also impact the collapse behaviour of structural components, such as stiffened plates.

In the presented section, the random field modelling is applied to model and analyse the spatial deviation of the mechanical properties within the stiffened plates made of different thicknesses. The results of tensile tests for intact specimens (see Table 6.3) are used as a basis for the current study, including mean values and standard deviations of mechanical properties. Furtherly, the random fields of both Young modulus and yield stress are generated considering different correlations and used in the FE model. The collapse behaviour of stiffened plates considering constant mechanical properties within the specimen and spatially distributed ones are analysed, and the discrepancy between the two model results are compared and discussed.

The generation of random fields accounts for different correlations. This includes a correlation length together for different correlations in the longitudinal and transverse directions of the field. Nevertheless, for one correlation, different random field realisations may result in a different structural response. Due to those reasons, the initial sensitivity analysis is performed for analysing the influence of the random field characteristics.

A 6 mm plate is chosen for the initial studies, and the considered random field correlation length varies between 0.1 m up to 0.316 m. The minimum correlation length cannot be less than the gauge length of the specimen as presented in Figure 6.29 because it is the minimum length of the specimen, where the material properties were evaluated. Above the maximum level of the correlation length, it was identified that the random field tends to be more uniform.

For each correlation length, four analyses are performed. For each run, a set of four random fields are generated considering two material properties separately for the plate and stiffener. Based on the analysis of the tensile tests, there was no found correlation between the Young modulus and yield stress. Due to that, the random fields are generated separately for both of these material properties.

The FE analyses considering different correlation length and realization are presented in Table 9.4. The results are compared with the initial reference case, where no deviations of the material properties are considered.

Table 9.4. Sensitivity analysis.

Correlation length [m]	Run No	Ultimate force [kN]	Normalized ultimate stress [-]	The difference with initial state [%]
Initial state	-	549.7	0.6442	0.00
0.316	1	543.2	0.6367	-1.17
0.316	2	542.3	0.6356	-1.34
0.316	3	551.3	0.6461	0.29
0.316	4	528.9	0.6199	-3.77

0.224	1	529.1	0.6202	-3.73
0.224	2	541.0	0.6341	-1.57
0.224	3	537.9	0.6305	-2.14
0.224	4	549.8	0.6444	0.02
0.100	1	540.3	0.6332	-1.71
0.100	2	546.7	0.6408	-0.54
0.100	3	540.5	0.6335	-1.66
0.100	4	540.7	0.6337	-1.63

One can notice that in almost all cases, the ultimate strength was reduced with regards to its initial value. For the extreme case, a reduction of 3.77 % was observed (4th run of a correlation length of 0.316 m). There cannot be an explicit correlation between the reduction of the ultimate strength and the correlation length. However, the extreme reductions of the ultimate strength are observed for rather strongly correlated fields. The random fields representing variations of the mechanical properties for the selected cases are presented in Figures 9.18 to Figure 9.20. The scales are normalized, i.e. the plotted value is multiplied by the mean value of the yield stress or Young modulus, respectively.

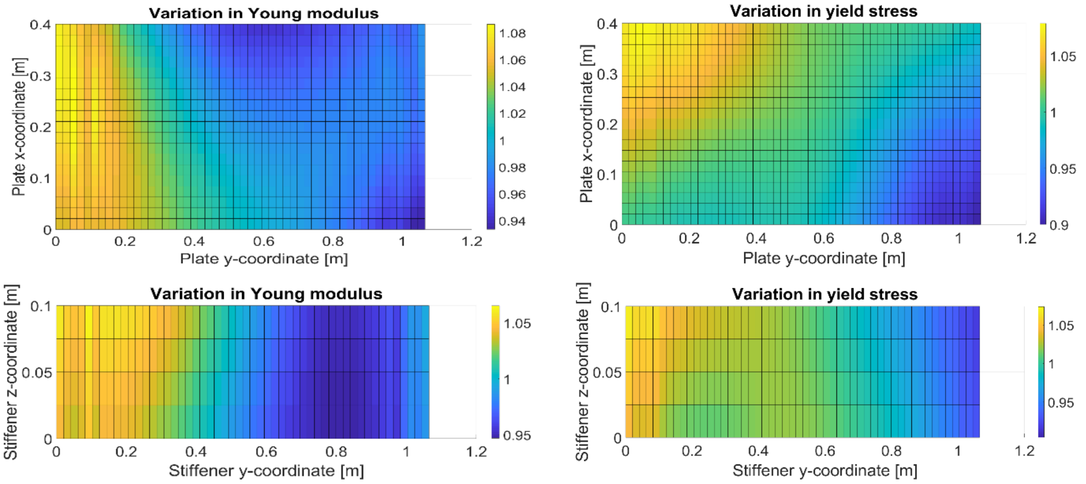

Figure 9.18. Random fields for the second run, correlation length of 0.316 m.

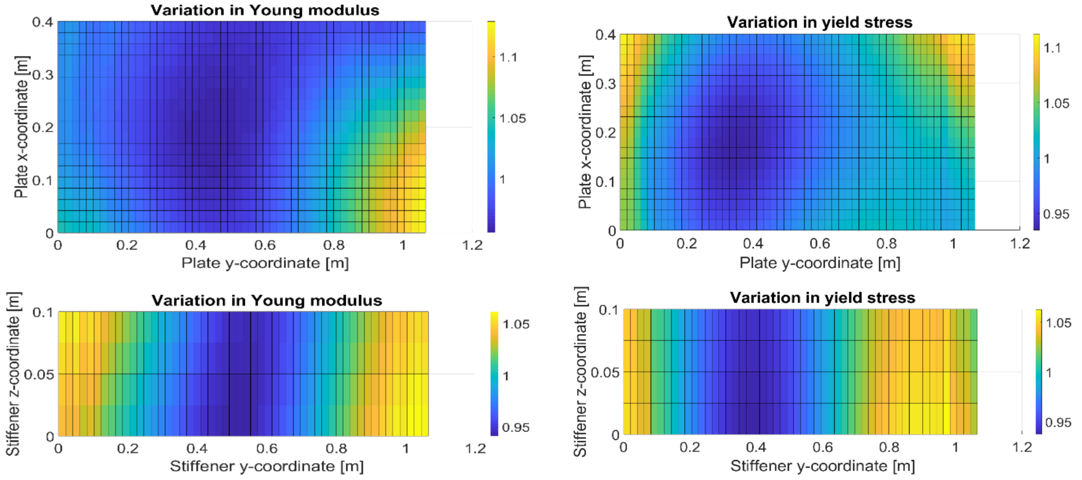

Figure 9.19. Random fields for the fourth run, correlation length of 0.316 m.

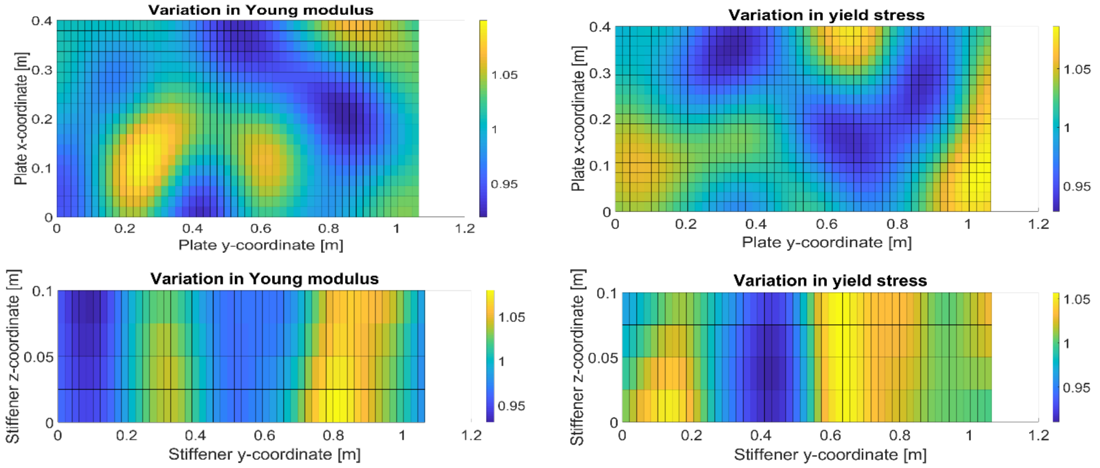

Figure 9.20. Random fields for the first run, correlation length of 0.1 m.

Based on the observations from the normal fields with a correlation length of 0.316 m, it could be seen that the minimum values of material properties are concentrated rather near the middle of the plate and stiffener for the fourth run. In the second run, the minimum and maximum values of the material properties are concentrated near the shorter edges. By comparing this with the ultimate strength reductions, it may be concluded that the first case is the weakest one. The middle sections of the stiffened plate are subjected to higher stresses during compressive loading. Thus, reducing the mechanical properties in that region leads to the highest decrease in the ultimate strength. As presented in Figure 9.20, there is more than one region of smaller values of the mechanical properties in the case of a smaller correlation. Thus, reducing the ultimate strength is not very severe, like in the most critical case with a high correlation. However, for a smaller correlation, the ultimate strength reductions are very similar, and there are not so spread. In the case of a higher correlation, some cases show higher ultimate strength than the initial case. For these examples, the higher values of the mechanical properties are observed in the mid-sections of the stiffened plate.

For further investigation, the post-collapse shapes for different cases are compared, as shown in Figure 9.21. It can be noticed that although the failure mode is similar for each case, which is a local plate buckling mode, followed by stiffener tripping, the position of the collapsed cross-section differs significantly between the cases. In the case of the initial state, the collapsed shape is symmetrical regarding the middle cross-section. When comparing the shapes with the distributions of the random fields, it can be noted that the positions of the collapsed cross-section occur near the regions of the lower values of the mechanical properties.

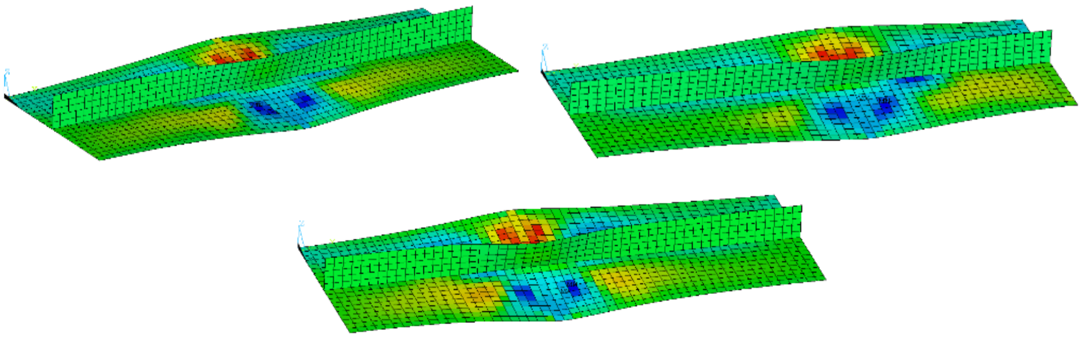

Figure 9.21. Post collapse shapes for 6 mm specimen – initial case (top), the second run of 0.316 m correlation (mid), fourth run of 0.316 m correlation (bottom).

For the selected cases, the force-displacement relationships are plotted (see Figure 9.22). It can be noticed that in the pre-collapse region, there is no significant deviation between the curves. In that region, the stresses are below the yield point. This also indicates that the variation of the Young modulus does not impact much the structural response since the initial inclination of the force-displacement curve does not deviate much. However, when the yield point is reached in the middle of the specimen, the deviations are visible, leading to a reduction of the ultimate force. Based on these observations, it can be concluded that the yield stress deviation is the main reason for the ultimate strength reduction of stiffened plates subjected to compressive loadings.

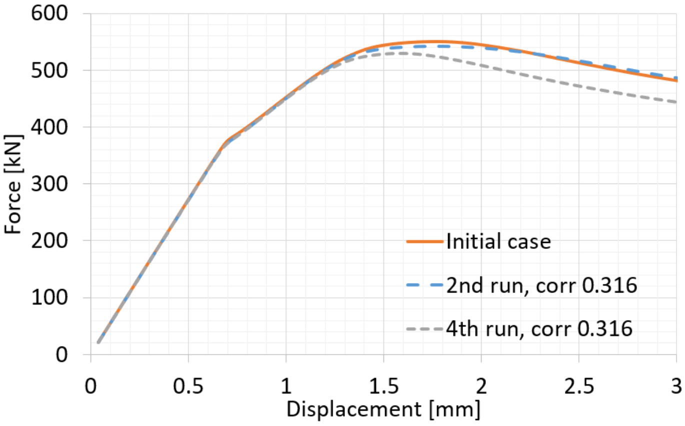

Figure 9.22. Force – displacement curves for different cases.

In random field modelling, the correlation can also be different in longitudinal and transverse directions for the plate and or stiffener. The additional analysis is performed, considering a very high correlation between mechanical properties in longitudinal and transverse directions. The resulting ultimate force was computed for both cases. A higher ultimate strength reduction is obtained for the mechanical properties variations in the longitudinal direction. A reduction of 3.59 % is very close to the maximum one obtained from the previous analysis. In mechanical properties, variating only in the transverse direction, the reduction is almost two times smaller and is about 2.09 %.

For most critical random fieldsets, as was found in sensitivity analysis, an analysis is carried out for a 5 mm, 6 mm, and 8 mm thickness of the plates, considering different correlation lengths, and the results of the analysis are presented in Table 9.5.

Table 9.5. Ultimate strength for stiffened plates.

Thickness [mm]	Correlation length [m]	Ultimate force [kN]	Difference with initial state [%]
5	Initial	406.9	0.00
	0.316	388.4	-4.57
	0.224	385.7	-5.22
	0.100	398.8	-1.99
6	Initial	549.7	0.00
	0.316	528.9	-3.77
	0.224	529.1	-3.73
	0.100	540.3	-1.71
8	Initial	1001.7	0.00
	0.316	984.0	-1.78
	0.224	989.7	-1.20
	0.100	992.1	-0.95

It can be seen that in the case of 5 mm- and 6 mm-thick plates, the reductions of the ultimate strength with regards to the non-homogenous distribution of mechanical properties is significant, whereas, for the 8 mm plate, it is rather small. This is caused by different variations of mechanical properties, as presented in Table 6.3. In an 8 mm plate, the coefficient of variation for both Young modulus and yield stress is around 3 %. In the case of ultimate strength reductions, similar observations may indicate that the higher correlation of the field causes a more significant ultimate strength reduction.

The comparison of the force-displacement curves for the initial and most critical cases for 5 mm and 8 mm plates is presented in Figure 9.23. In a 6 mm plate, the curves and discussion were already covered in the previous section. Concerning the 5 mm plate, similar observations can be noted. The initial inclination of the curve is not changed, although the CoV of the Young modulus for that plate reaches the level of 5 %. The differences start to occur near the ultimate strength point region. In the case of an 8 mm plate, there are very slight differences due to a very low level of variation of the mechanical properties.

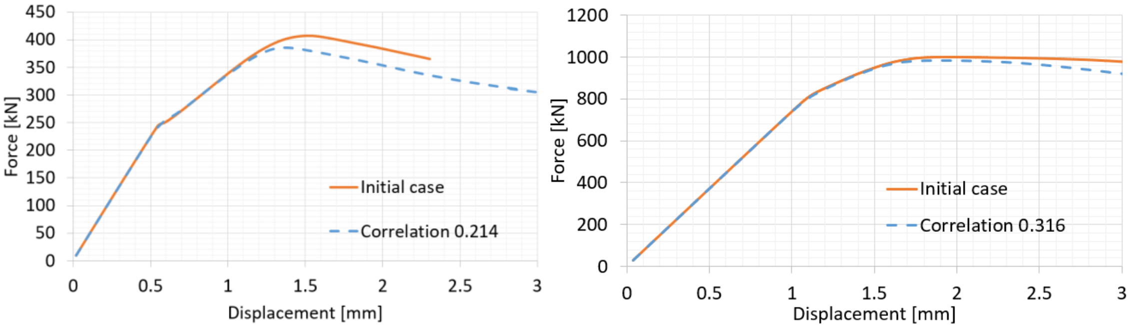

Figure 9.23. Force – displacement curves for 5 mm plate (left) and 8 mm plate (right).

Based on the force-displacement curves, it can be assumed that the deviation in the yield stress is the main reason for the ultimate strength reduction. This hypothesis is furtherly verified. In Figure 9.24, the mean ultimate strength reductions from Table 9.5 are compared with both Young modulus and yield stress coefficients of variation for particular plates, and the correlations are plotted.

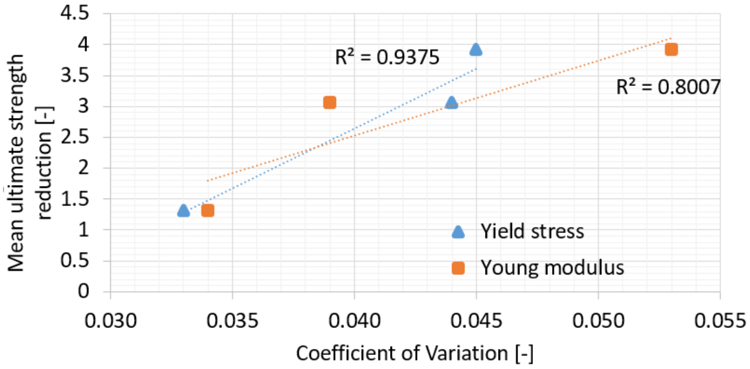

Figure 9.24. The relation between ultimate strength reduction and mechanical properties uncertainty level.

It can be noted that in the case of the yield stress variation level, the ultimate strength reduction is strongly correlated and the R^2 value is 0.94. In the case of the Young modulus, the correlation is lower but still rather strong. Based on these plots and previous observations regarding the force-displacement curves, it may be concluded that the ultimate strength reduction is mainly caused by the non – homogenous distribution of the yield stress, whereas the Young modulus deviation plays a secondary role.

The work presented in this section analysed the impact of the non – homogenous distribution of mechanical properties on the ultimate strength of stiffened plates subjected to a compressive load employing the random field methodology coupled with the nonlinear FE analysis. The statistical descriptors of the mechanical properties were obtained based on the tensile test of specimens, presented in Section 6.5.1.

In the first place, the present study revealed that non – uniform spatial distribution of the mechanical properties could cause a reduction of the ultimate strength of the stiffened plate up to

4.8 % for a 5 mm plate compared to the stiffened plate with a mean value uniformly distributed mechanical properties. This could be the possible source of the highest difference between the experiment and the FE model observed in Table 9.3.

The performed sensitivity analysis regarding the random field correlation length showed that the significant ultimate strength reduction is obtained for a more correlated field. Additionally, depending on the realization of a random field, the results are also subjected to deviations. Further, it was observed that the spatial variation of the mechanical properties might impact the ultimate strength and the post-collapse shapes of the stiffened plate and the force-displacement relationships.

Comparing the highly correlated longitudinal and transverse direction fields showed that the second one is the weakest case. A significant ultimate strength reduction is noted when the lower values of the mechanical properties are encountered in the region near the middle of the stiffened plate.

The investigation of the plate with different thicknesses revealed that the ultimate strength reduction is strongly correlated with the COV of the yield stress, whereas the deviations of the Young modulus plays a minor role.

The outcome of the present analysis has shown that the mechanical properties variation within a single stiffened plate causes additional variation regarding the FE analysis, which could be the possible source of difference between numerical investigations and experimental tests.

9.1.4. Comparison of strain measurements [P5]

To investigate the structural behaviour during the entire loading process, selected strain measurements in the middle cross-section (see Section 6.2.3) are compared with the FE results. The results for the 5 mm stiffened plate are presented in Figure 9.25.

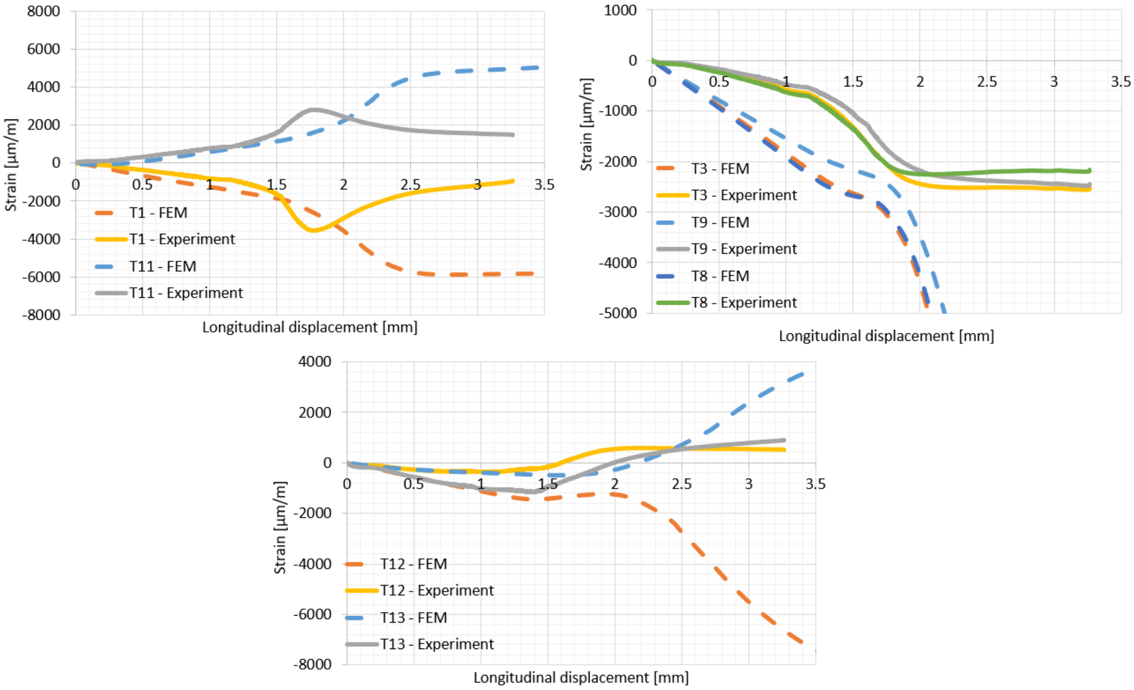

Figure 9.25. Strain development of a 5 mm specimen.

In the upper-left corner of Figure 9.25, the strain of the edge of the specimen is presented. It could be noticed that from the beginning of the loading process, the plate is subjected to bending. This is caused due to significant initial imperfections. Up to the level of the ultimate strength, the strain measurements are very similar. After reaching the highest compressive force status, the strain in the experimental test decreases, whereas the strain in the FE analysis is still increasing. This indicates that before the ultimate strength was reached, the most significant bending occurred in a similar place, i.e., the middle of the specimen, caused by the shape of the imperfect stiffened plate. However, after reaching that point, in the FE model, the collapse occurred in this cross-section leading to a significant strain. The highest deflections have shifted closer to the upper support (see Figure 6.40), leading to the plate bending in the middle cross-section in the opposite direction and decreasing the strain. In the upper-right corner of Figure 9.25, the strain near the connection between the plate and stiffener are presented. It is observed that the strain in the upper and lower surface of the plate are almost identical.

This indicates that the column buckling did not occur, and the local buckling of the plate dominates the collapse. The observations are consistent with the analysis of the post-collapse shape. However, when comparing the experimental and numerical results, the strain up to the moment of the ultimate strength is higher in the FE model, although they are similar at the point of the ultimate strength. The possible reason for that is the welding-induced residual stresses, which are not considered in the FE model. The strain in the edge of the stiffener is presented at the bottom of Figure 9.25. As can be observed, up to the moment when the maximum compressive force is reached, the strain readings are very similar for the experimental test and numerical computations.

It may be seen that the bending occurs from the beginning; however, the compressive forces are also transmitted. After reaching the ultimate strength point, significant bending occurs in the FE analysis, whereas in the experimental test, the edge is mainly subjected to axial compression. The reason for that is the same as in the case of plate bending. However, a different position of the critical cross-section is observed in the FE analysis and the experimentally tested specimen.

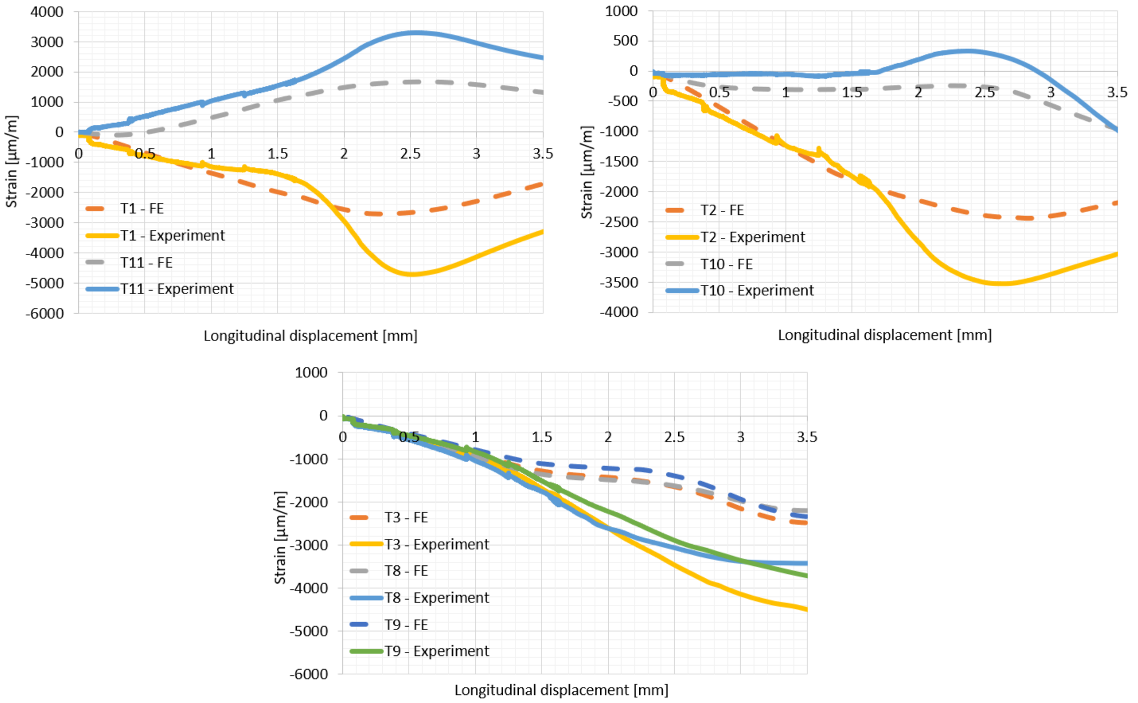

Figure 9.26. Strain development of a 6 mm specimen.

Figure 9.26 shows the strain development of a 6 mm specimen. The strain is one of the longitudinal plate edges shown in the upper-left corner in Figure 9.26. Similarly, as it was for a 5 mm specimen, the bending of the plate occurred from the very beginning of the loading process. However, in that case, when comparing the experimental and numerical measurements, the readings are very similar, which indicates that the structural behaviour during collapse was very similar, which was also observed in the post-collapse. In the pre-collapse regime, the strain is increasing almost linearly. The decrease of the strain after the region of the highest compressive force is caused due to the shift of the critical cross-section near the upper support.

Figure 9.26, upper-right corner, shows the strain development of the plate between the edge and stiffener. The observations are similar to those obtained for the gauges located on the edge of the plate. The only difference is that the plate transmits the axial compression, and the readings are unsymmetrical between the upper and bottom surface of the plate. The strain measured in the connection between the plate and stiffener is presented at the bottom of Figure 9.26.

Similarly to the specimen of a 5 mm thickness, there is no significant difference between the strain in the upper and bottom surface of the plate, which indicates that the local plate bending has been the primary cause of the collapse. Up to the level of ultimate strength, the experimental measurements and numerical predictions are quite similar. However, above the longitudinal displacement of 1.5 mm, the FE analysis strain is lower than the experimental test measurements.

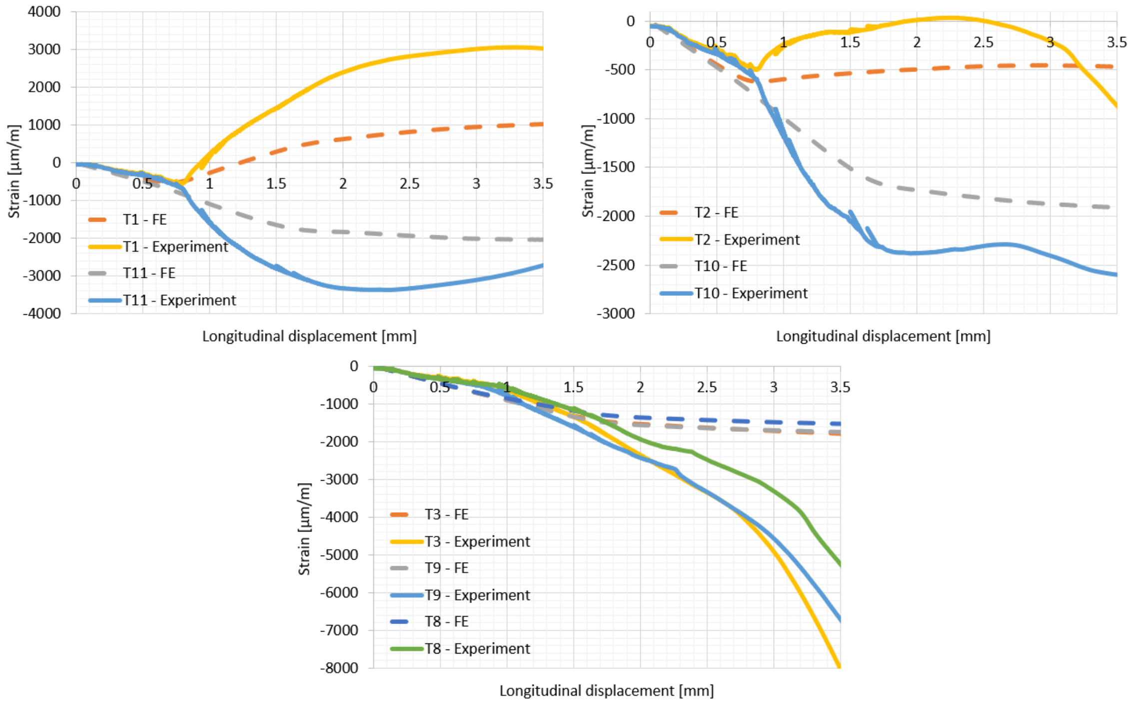

Figure 9.27. Strain development of an 8 mm specimen.

The strain development of an 8 mm stiffened plate is presented in Figure 9.27. It is observed that the structural behaviour was slightly different when compared to other specimens. In the upper-left corner of Figure 9.27, the strain in the side-edge of the specimen is compared. It may be noticed that up to the longitudinal displacement of approximately 0.75 mm, the plate was only subjected to the compressive load, and no bending has been observed. In that region, the strain in the FE analysis and tested specimen were the same. In the case of the 8 mm plate, the local imperfections of the plate were smaller with regards to its thickness, oppositely to the thinner specimens. Thus, in the beginning, only an axial thrust has been transmitted. After crossing that point, the buckling occurred, and the strains have increased rapidly due to the created local bending of the plate. It is also observed that the strain in the experimental test was considerably higher when compared to the numerical estimation.

Relatively similar observations can be seen when one considers the strain in the plate between the edge and the stiffener, as presented in the upper-right corner of Figure 9.27. However, the asymmetry of readings is observed due to the higher contribution of the membrane stresses in the plate edge (see Section 6.6.1). The strain in the middle of the specimen near the weld is presented at the bottom of Figure 9.27. Similarly to previous specimens, the strain in the upper and bottom surface of the plate is very close, showing that the local plate buckling has dominated the collapse. When the ultimate strength is reached, the readings of numerical analysis and experimental testing are very similar. After getting that level, the experimental measurements are significantly higher when compared to the FE analysis.

9.1.5. Comparison with other methods [P5]

The method used to estimate the ultimate strength of the ship hull girder is the incremental-iterative approach as adopted by the Common Structural Rules [5]. The hull girder ultimate strength is estimated based on the stress-strain responses of stiffened plate and plate elements treated separately. The normalized ultimate strength of any individual stiffened plate is defined as the minimum from several possible failure modes: plastic collapse, local plate buckling, local stiffener tripping, or global column buckling.

Additionally, the presented results are compared with the experimental results of Horne [47]. In this case, two flat-bar stiffened plates with the similar plate and column slenderness ratios were found. Finally, as developed by Paik and Thaymballi [281], the empirical formula is used to compare the results presented in the current work. Numerical and experimental test results as a function of the plate slenderness ratio are presented in Figure 9.28.

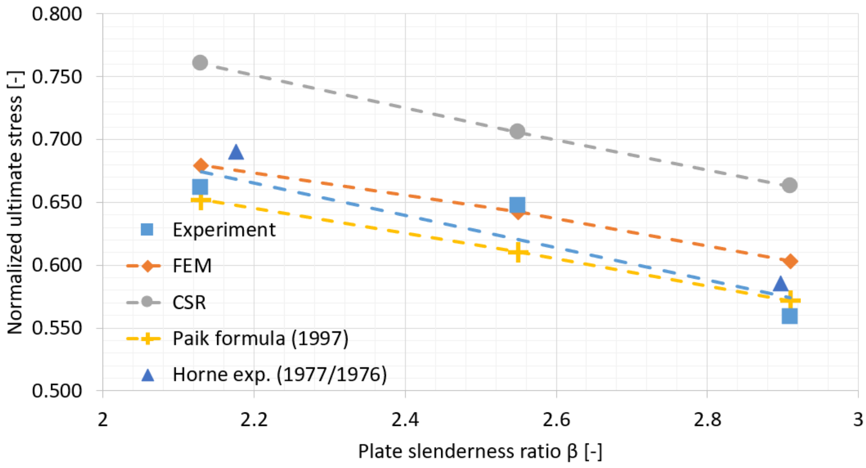

Figure 9.28. Comparison of numerical and experimental results.

It can be noticed that in the case of the stiffened plates of the lowest and highest value of the plate slenderness ratio, the presented analyses show results very close to the experimental results presented in [47]. In the case of Paik and Thaymballi’ s empirical formulation [274], the values of normalized ultimate strength are lower concerning the experimental investigations presented in the current work. However, when considering the CSR formulation, it can be noted that it overestimates the ultimate strength of up to 15 %.

9.1.6. Conclusions

The developed numerical model was revealed to be an excellent tool in predicting the structural behaviour of stiffened plates subjected to compressive load. As a result of the FE estimations, the achieved ultimate strength was very close to the experimental one. The post-collapse forms were very similar. However, some differences in the position of the collapsed cross-section where the highest deflections occurred and the shape of collapsed stiffener have been observed. The possible reasons are related to the non-ideal clamped boundary conditions in the experimental testing and uncertainties in the mechanical properties distribution within the specimen. The comparison of the strain in the mid-cross-section revealed that up to the point of ultimate strength, the agreement between the numerical and experimental results was good. After that point, a considerable difference was observed. In the case of 5 mm and 6 mm specimens, the bending of the plate occurred from the beginning of the loading process due to a high level of initial imperfections compared to the plate thickness. In the 8 mm specimen, the level of imperfections was not that high, and the local plate bending occurred above some compressive force.

The experimental and numerical investigations were compared with those published in the literature results, showing good agreement. However, it was revealed that the formulation used in the Common Structural Rules overestimates the ultimate strength of stiffened plates.

9.2. *Corroded stiffened plates with non-uniform thickness reduction – numerical modelling*

It is observed that even when considering general corrosion, considerable scatter of the thickness distribution occurs within the single specimen (see Section 4.4.2). To evaluate the ultimate strength of such specimens experimentally, corrosion tests are needed. However, there are time-consuming, and a limited number of samples is possible to obtain. Thus, efficient methods to generate the field of corroded plate surfaces artificially are needed. The presented Section incorporates random field modelling, as described in Section 7.3.

A two-stage corrosion model is adopted herein. In the first stage, the general corrosion loss is modelled using a random field considering the statistical descriptors of corroded plate thickness. In the second stage, the mechanical properties are changed to reflect the non-regularities of the corroded surface in the micro-scale based on the degradation level of a particular point of the plate surface. The numerical analyses, employing the non-linear FE method, are performed considering different plate thicknesses and corrosion degradation levels.

In the first part, the sensitivity studies with regards to random field realizations are performed. In the second part, predicting a decrease of strength for corroded stiffened plates tested in the current study is performed.

9.2.1. Sensitivity studies

For sensitivity studies, the constitutive models of changes in mechanical properties for design purposes in the function of corrosion degradation, as presented in Section 8.6, are used. For this assessment, the actual values of changes in mechanical properties for a particular thickness of plate are not crucial, and there will be applied in the next section for all range of thicknesses. Based on the sensitivity analysis regarding the ultimate strength of stiffened plates, as presented in Section 5.1.5, only the Young modulus and yield point variation are considered. Further, the Young modulus is kept constant within the degradation level, as described in section 6.5.2. The variations of the total elongation and ultimate tensile stress have insignificant influence.

To model the corrosion degradation, the thickness of each node is changed based on the generated random field. Then, the element's local degradation level is calculated based on the mean thickness of the four nodes. According to constitutive models, the mechanical properties of a particular element are changed based on the local degradation level.

To investigate the influence of different characteristics of a random field, sensitivity analysis is performed. The stiffened plate of 6 mm thickness and a corrosion level of 21 % is chosen to see the influence of parameter variations on the resulting ultimate strength. Two different characteristics of the random field are taken into account, namely correlation length and standard deviation. Additionally, the convergence studies were performed to see how many random field realizations concerning one case is enough to provide a stable mean value.

The correlation length was investigated within the level between 7 mm up to 316 mm. The minimum level is related to mesh discretization since the correlation highly below the element size will be not traced, and the thickness of the next two nodes will be not correlated. On the other hand, above a certain level of correlation length, the changes in corrosion depth can no more be distinguished. Thus, the maximum applicable correlation length was estimated as equal to 316 mm. The examples of random fields with different levels of correlation considering both plate and the stiffener are presented in Figure 9.29. It needs to be noted that the random fields for plate and stiffener are generated separately.

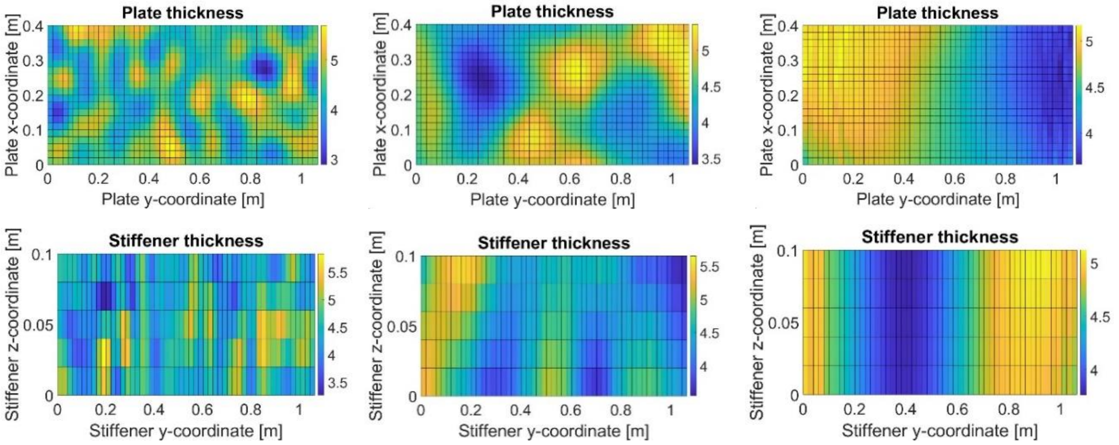

Figure 9.29. Random fields of corroded plates and stiffeners with low (left), moderate (mid), and high (right) correlation.

The random field methodology is advantageous. However, it requires a specific number of realizations. Although the two random fields of corrosion considering both plate and the stiffener will have identical statistical characteristics (correlation length and standard deviation), the resulting ultimate strength of stiffened plate could be different. Thus, instead of one specific realization, the mean value from several of them will be much more representative. To find the correct number of realizations that will result in a stable mean value, the so-called convergence studies need to be performed. The analysis is performed for a correlation length equal to 0.1 m. With the increase in the number of realizations, the mean value is calculated according to the equation:

$$\overline{x_n} = \sum_{i=1}^{n} \frac{x_i}{n} \tag{9.1}$$

where n is the number of realizations and x_i is the ultimate strength value for a specific realization. In Figure 9.30, the mean value of ultimate strength considering an increasing number of realizations is presented. It could be noticed that seven realizations provide stable mean value.

Nevertheless, the nine realizations for each correlation length were performed, and this number is chosen for further studies.

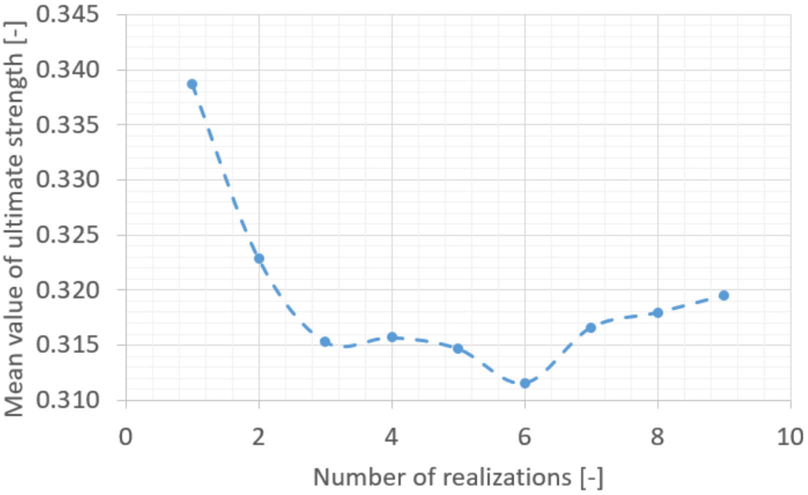

Figure 9.30. Convergence studies concerning realizations number (Correlation length of 0.1 m).

The normalized ultimate strength in the function of correlation length is presented in Figure 9.31, which is the ultimate force divided by cross-sectional area and yield stress. The normalized capacity is calculated always considering initial values of thickness and yield stress, even when corroded specimens are evaluated. For each correlation length, the box and whiskers plot is presented, showing mean values together with uncertainties. For this assessment, the standard deviation of 0.45 mm is taken into account.

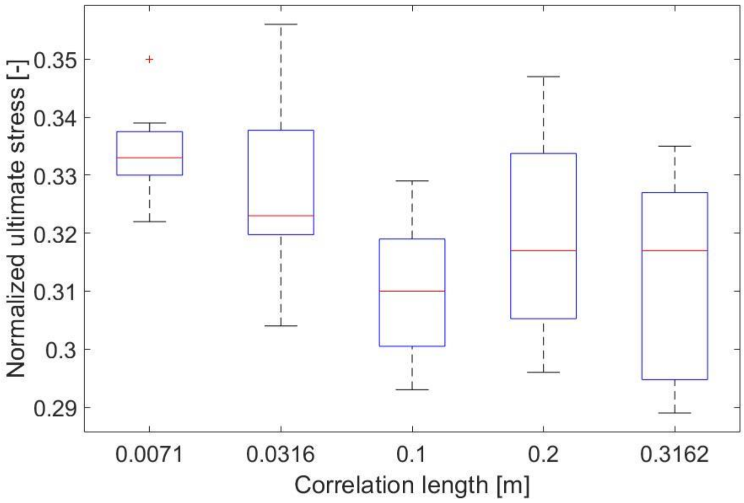

Figure 9.31. Box and whiskers plot of normalized ultimate strength grouped by correlation lengths.

It is notable that when the corrosion fields are more strongly correlated, the reduction of ultimate strength is more significant. The mean value of ultimate strength is quite similar within the range of correlation length between 0.1 m up to 0.316 m. Additionally, for lower correlation length, the scatter of the resulting ultimate capacity is lower. The most critical case appeared to be for the correlation length of 0.1 m, which resulted in a minimum mean value. However, in terms of a single realization, the most critical case was captured within the highest correlation value.

Finally, it is notable that the ultimate strength of corroded stiffened plates is subjected to quite high uncertainty. The difference between the maximum and minimum points within all realization reaches 20 % of the mean value. The degradation level governs the resulting ultimate strength, but the thickness distribution within the specimen is an essential parameter that changes the structural behaviour.

In the case of lower correlation length, the areas of high corrosion diminutions will be smaller compared to a more extended correlation, which can be observed in Figure 9.31. This leads to a different structural response. Actually, with a very high correlation, even an entire cross-section could have a smaller thickness concerning the mean value of corrosion degradation, leading to the premature collapse of the entire specimen.

This phenomenon can also be captured when one compares post-collapse shapes, as presented in Figure 9.32 for some selected cases of different correlation lengths. It is distinguishable that the position of the collapsed cross-section is quite different. In high correlation, the collapse could be very close to the loaded edges if the region of reduced thickness will occur in that place. Nevertheless, the failure mode is quite similar for all cases, and it is caused by the local plate buckling followed by stiffener tripping. The differences will also occur when comparing force-displacement curves discussed in the further part of this section.

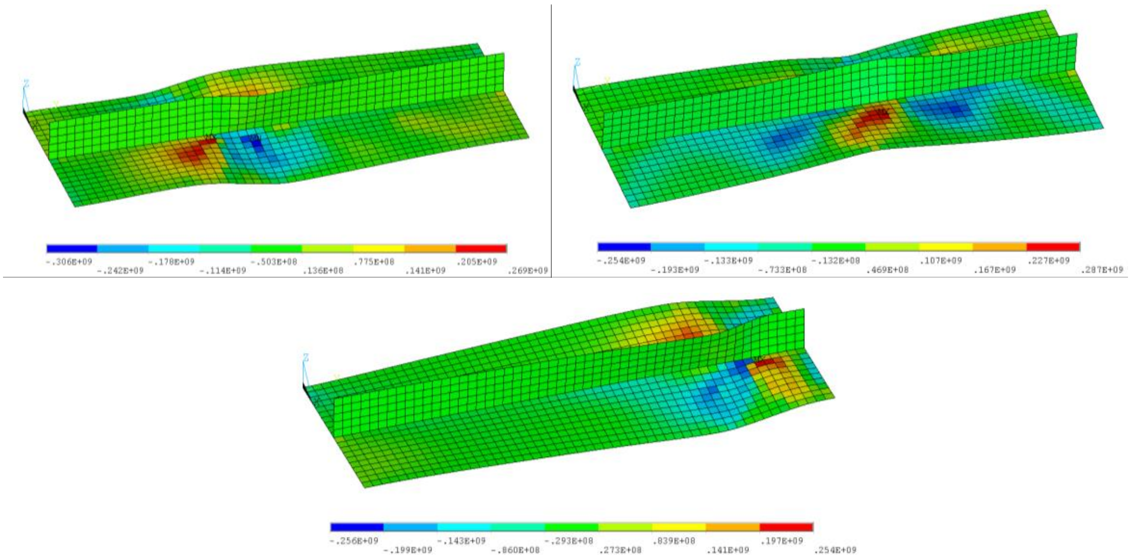

Figure 9.32. Post-collapse shapes of specimens with corroded fields of low correlation (left up), moderate correlation (right up), and high correlation (bottom), normal stresses [Pa].

The actual scatter of plate thickness could be different for some cases, depending on the corrosion environment [132]. Thus, the level of thickness standard deviation is investigated to see the possible impact on reducing ultimate strength. In each case of correlation length, the representative random field providing ultimate strength closest to the mean value from nine realizations was considered. For each correlation length, two standard deviation levels were investigated, namely the initial level of 0.45 mm and half of this value - 0.225 mm. The results are presented in Figure 9.33.

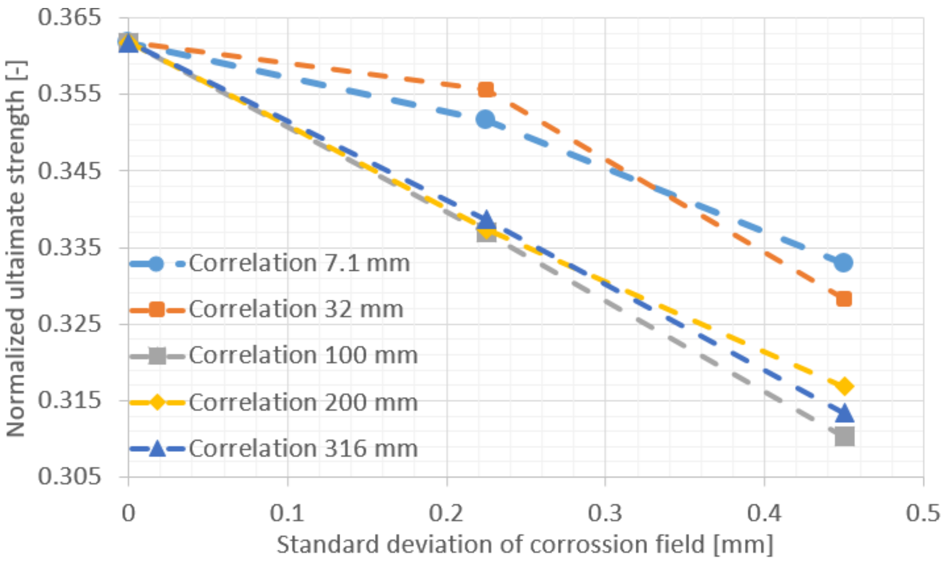

Figure 9.33. The influence of random field standard deviation on the reduction of ultimate strength.

In the beginning, one should notice that the ultimate strength for Standard Deviation equal to 0 is the basic model, where the uniform thickness reduction is assumed. In all cases, when considering thickness deviations within the specimen, the ultimate capacity occurred to be lower. Thus, the model where only uniform reduction of thickness is taken into account is revealed to be non-conservative. In higher correlation length (above 100 mm), the relationship between thickness standard deviation and ultimate strength is rather linear. However, in the case of lower correlations (7.1 mm and 32 mm), the dependency is more non-linear, and the reduction of ultimate strength tends to be more rapid with the increase of standard deviation.

Sensitivity analysis aimed to obtain the optimum values of random field characteristics used in further analysis. Based on the convergence studies, the nine realizations of the random field for specified values of standard deviation and correlation length were revealed to be enough to provide a stable mean value. The correlation length equal to 0.1 m revealed to be most dangerous in terms of ultimate strength reduction, and thus it will be considered in further analysis.

9.2.2. Prediction of decrease of strength of corroded stiffened plates

To evaluate the thickness variations within the stiffened plate, the standard deviation follows the relationship from Figure 4.29, based on the experimental results from Section 4.4.2. The mechanical properties for each thickness follow the relationships presented in Section 6.5.2.

The random fields with a distribution of thickness within the stiffened plate are generated based on the calculated uncertainty levels.

The structural behaviour of stiffened plates considering different thicknesses of the plate and the stiffener is studied. The three different thicknesses (5 mm, 6 mm and 8 mm) are taken into account. Two different levels of corrosion degree of degradation are considered, namely 10.5 % and 21 %. In Figures 9.34-9.36, the force-displacement curves considering 5 mm, 6 mm, and 8 mm thick stiffened plates, respectively, are presented. The upper bunch of curves in each Figure represent the 10.5 % level of corrosion degradation, whereas the lower bunch represents the high value of corrosion diminution.

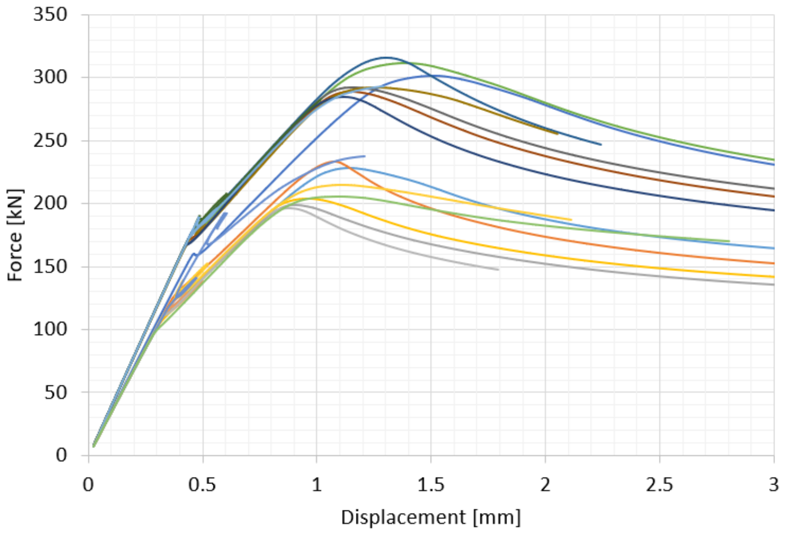

Figure 9.34. Force-displacement curves for 5 mm stiffened plates.

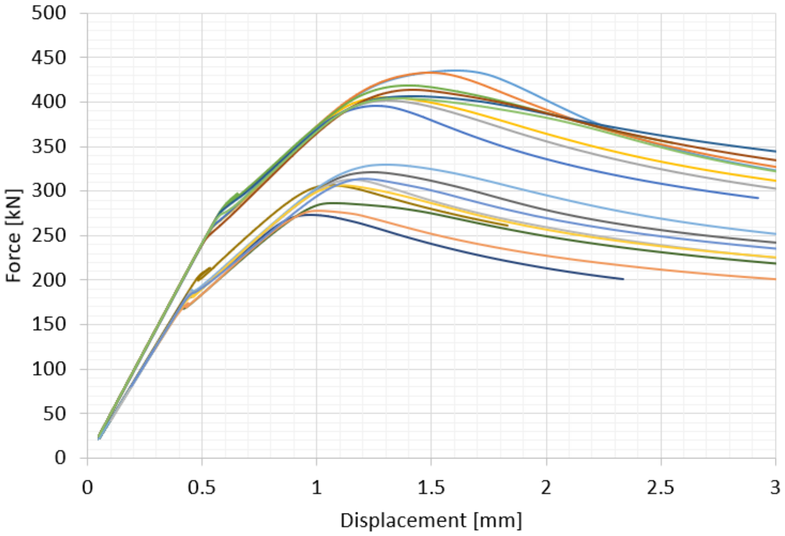

Figure 9.35. Force-displacement curves for 6 mm stiffened plates.

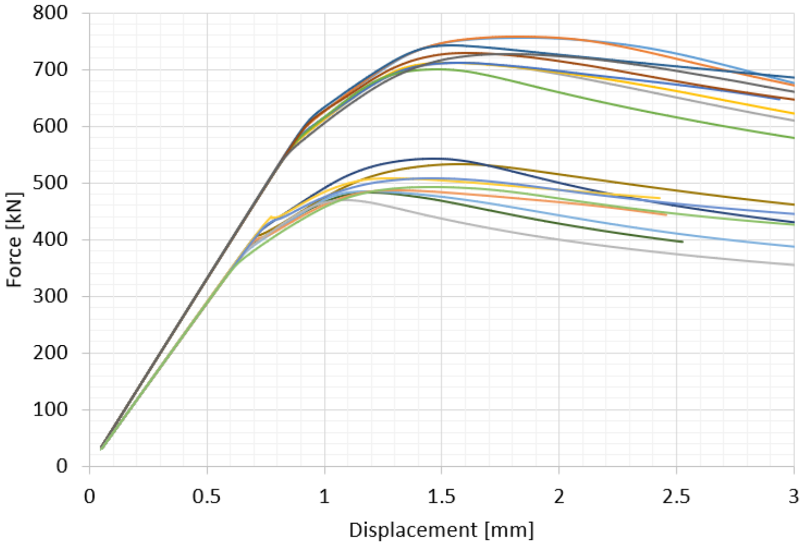

Figure 9.36. Force-displacement curves for 6 mm stiffened plates.

Notably, the behaviour is almost identical up to the bifurcation point in all cases, where buckling occurs. From that point, some scatter in terms of force value starts to be visible. After reaching the bifurcation point, the curves are scattered considering particular values of degree of degradation. However, the highest scatter is observed in the region where a stiffened plate reaches its maximum capacity, leading to significant differences in both values of ultimate strength and post-collapse behaviour. Depending on the particular thickness distribution on the plate, which is correlated with the distribution of mechanical properties, the plate will collapse in different positions of the cross-section concerning its longitudinal direction, which was already observed in Figure 9.32. One also needs to notice that with the increase of plate thickness, the scatter of ultimate strength becomes smaller. Apart from the thickness standard deviation being higher for thicker plates, the uncertainty level, compared to initial thickness, is lower for thicker plates.

The values of normalized ultimate strength, together with statistical characteristics, are summarised in Table 9.6.

Table 9.6. Ultimate strength of corroded stiffened plates.

Thickness [mm]	DoD [%]	Mean ultimate force [kN]	Normalized ultimate strength [-]		
			Mean value	St. Dev.	COV [-]
5	10.5	297.1	0.414	0.014	0.035
	21	214.0	0.298	0.022	0.072
6	10.5	412.7	0.484	0.016	0.034
	21	303.1	0.355	0.023	0.064
8	10.5	727.4	0.504	0.014	0.028
	21	501.0	0.347	0.017	0.049

Based on the presented results, one can conclude that with the increasing level of corrosion degradation, the resulting uncertainty of ultimate strength increases. This is related to the increasing thickness variation with corrosion development. The Coefficient of Variation is between 2.8 % up to 7.2%, which can be classified as rather high. The highest uncertainties are observed for the ultimate strength of 5 mm thick stiffened plates, whereas the capacity of 8 mm plates is subjected to the lowest uncertainty level. With the increase of plate thickness, the normalized ultimate strength increase as well, which is related to the increase of plate slenderness ratio. When compared to the intact specimens (see Section 9.1), the reduction of ultimate strength for severely corroded stiffened plates reaches the level of 50%.

The presented results are compared in the next section with the numerical model, where actual corrosion fields measured experimentally (see Section 4.4.2) are implemented.

9.3. Validation of the numerical models of compressed stiffened plates subjected to corrosion degradation

9.3.1. Detailed validation of a non-uniform model

The numerical model considering the combined effect of non-uniform thickness loss and subsequent reduction of mechanical properties is validated against experimental results. Thus, the thickness distribution is based on the measurements presented in Section 4.4.2. The initial imperfections are also implemented as measured, considering a particular specimen number.

Firstly, the force-displacement curves are adjusted for intact specimens, leading to the ultimate point being observed for the same longitudinal displacement. The comparison between numerical and experimental results for 5 mm plates is presented in Figure 9.37. In general, there is an observed bias between numerical and experimental results for all cases. A similar difference has been observed for an intact case, and possible reasons were discussed in Section 9.1.2. However, in terms of pre-and post-collapse behaviour, the curves are quite similar. It is noted that the initial inclination of curves is significantly lower in the case of an experiment, and after crossing 0.5 mm of displacement, the inclinations are similar to numerical predictions.

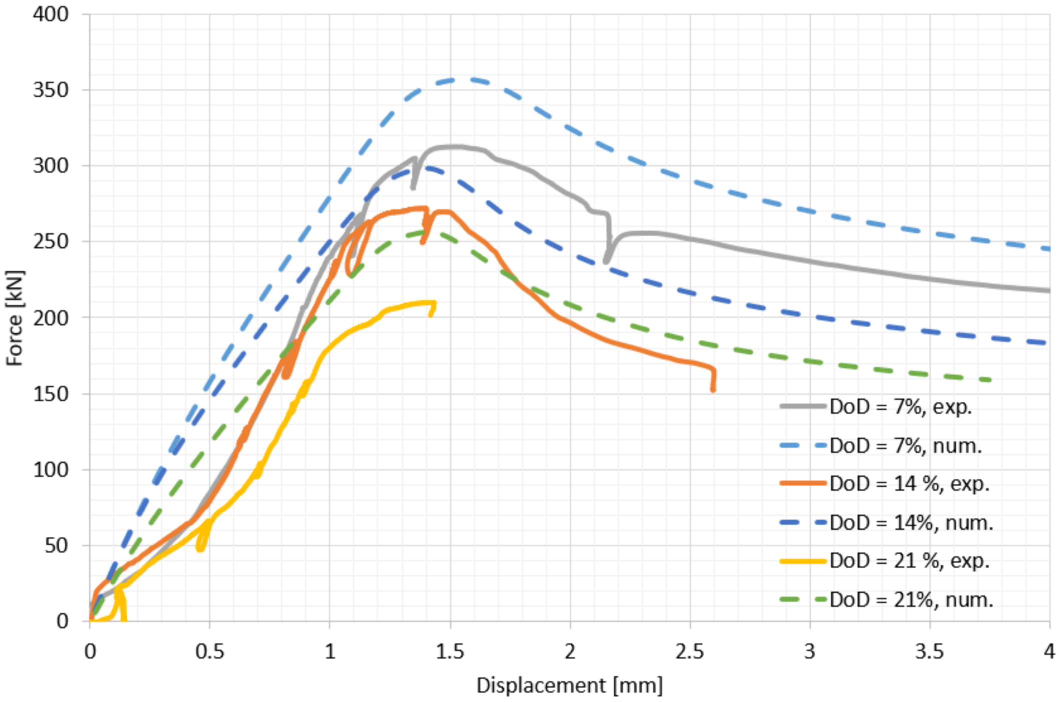

Figure 9.37. Force – displacement curves for 5 mm specimens.

The comparison between numerical and experimental results for 6 mm plates is presented in Figure 9.38. In the case of ultimate strength values, the higher ones are observed for the experiment in 7% and 14% of degradation level, whereas the lower value is observed for 21% of DoD. The force-displacement path is almost identical between experiment and numerical predictions for the specimen with the lowest corrosion diminution. In other specimens, the initial slope of the experimental curves is very low due to fixing the specimens in the supports. However, apart from that, pre-collapse behaviour is rather similar. The major differences after the collapse are observed only for the specimen with a medium level of corrosion severity.

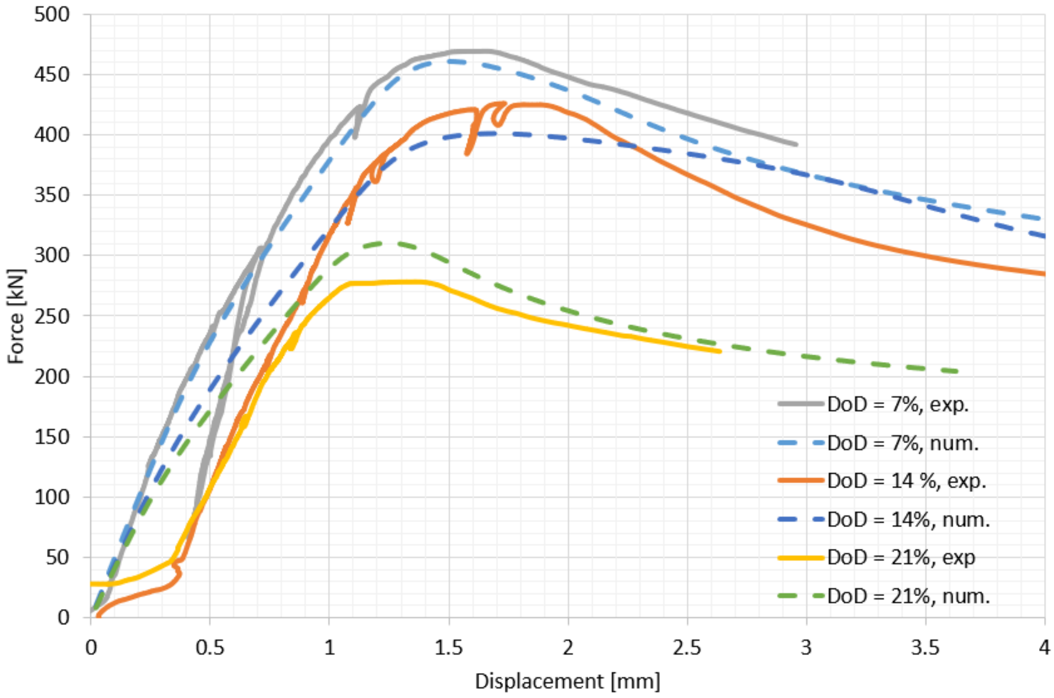

Figure 9.38. Force – displacement curves for 6 mm specimens.

The comparison between numerical and experimental results for 8 mm plates is presented in Figure 9.39. It is noted that in the case of 7% and 21% degradation level, the ultimate strength value is almost the same in the case of experimental and numerical results. However, some difference has been obtained for a degradation level of 14%. In pre-and post-collapse behaviour, the curves are very similar for 14% of DoD. For 21% of DoD, before reaching the ultimate point, the experimental and numerical path is very similar, whereas post-collapse behaviour is more dramatic for a numerical one. The most visible differences are observed for a degradation level of 7% within the entire force-displacement relationship.

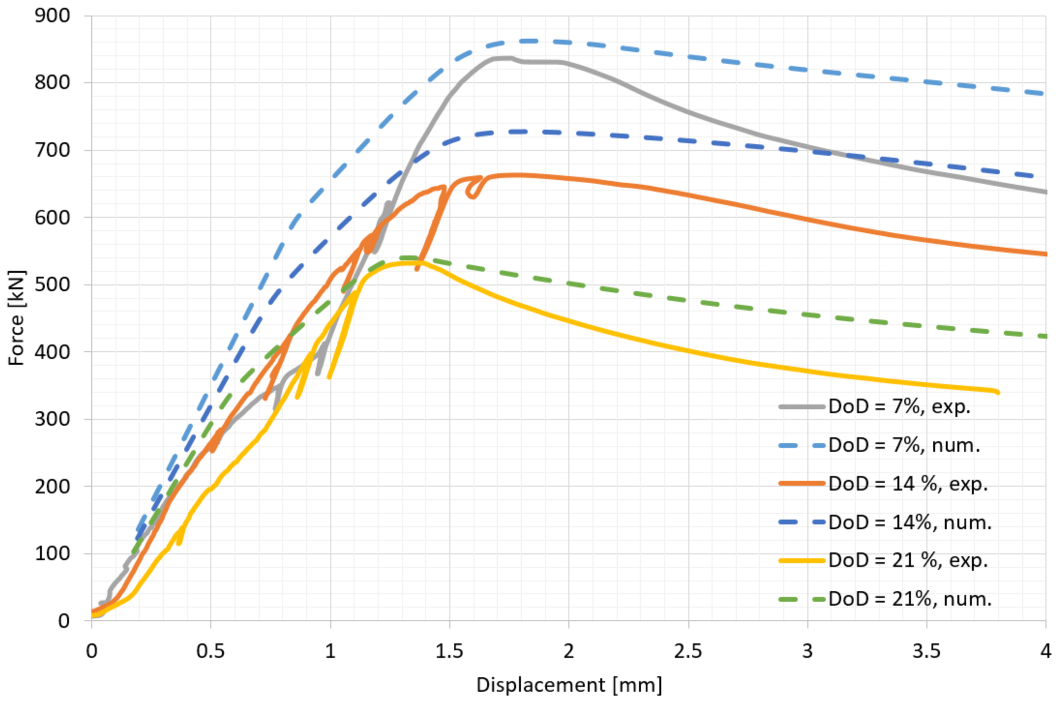

Figure 9.39. Force – displacement curves for 8 mm specimens.

The comparison of lateral displacements in the mid-cross section between experimental and numerical results is presented in Figure 9.40, regarding 5 mm specimens. The displacement gauges positions are presented in Figure 6.41. It is noted that excellent convergence has been obtained between the FE model and experiment. In each case, the displacements in both sides of the stiffener (ud2 and ud4) increased in the opposite direction, indicating local plate bending from the beginning of the loading process. Simultaneously, the lateral mid-displacement (ud3) was rather close to zero, indicating that local plate buckling and stiffener tripping was dominant failure mode. The only significant displacements in the connection of the plate and the stiffener were noted in a specimen with 14% of degradation level. However, it was captured only in an experimental domain. For all cases, the lateral displacements increased when ultimate capacity was reached and stayed constant after crossing that point.

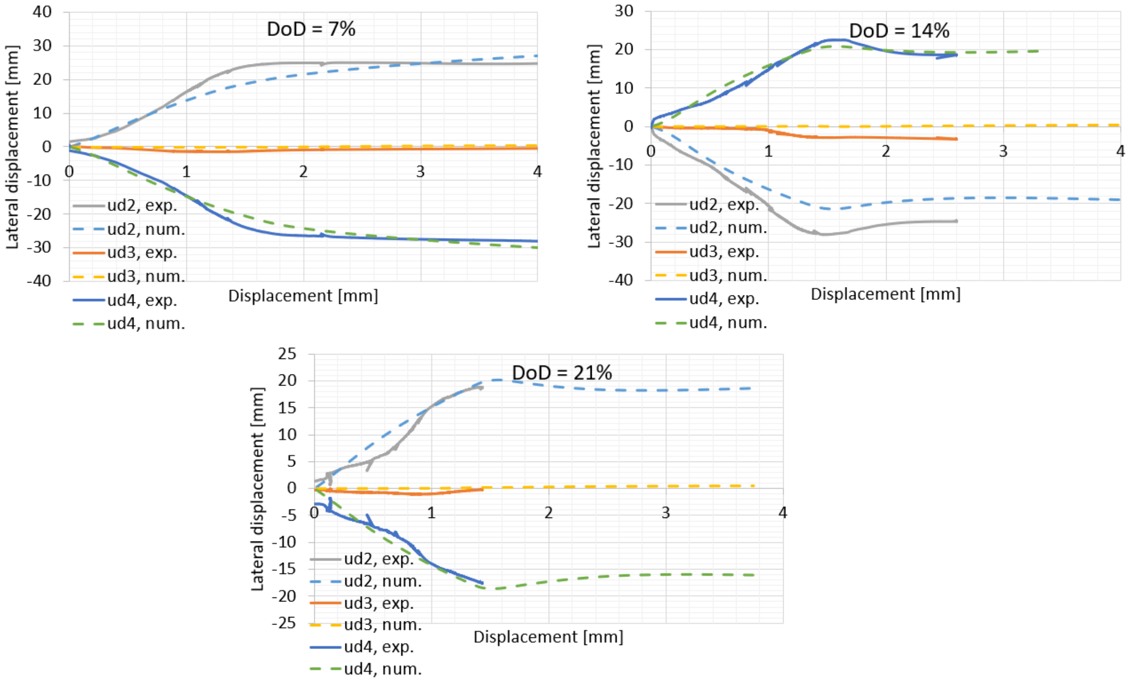

Figure 9.40. Comparison of lateral displacements – 5 mm specimens.

In Figure 9.41, the lateral displacements for 6 mm specimens are presented. It is observed that for DoD equal to 7% and 14%, the experimental readings and numerical predictions are similar. However, higher displacement values are noted in the case of an experiment. In these cases, the readings were increasing up to the level of ultimate strength value and then stabilised at a constant level. This indicates that the plate induced buckling was the main cause of the collapse. However, for a specimen with a degradation level of 7%, some level of global buckling occurred too in a tested specimen, which is noted in slightly increasing lateral mid-displacement. This was not observed in the FE model. In the case of a most severely corroded specimen, the global collapse mode has been observed in an experiment. The lateral displacements after collapse increased significantly in the same direction. However, the numerical model predicted another failure mode, similarly to previous specimens.

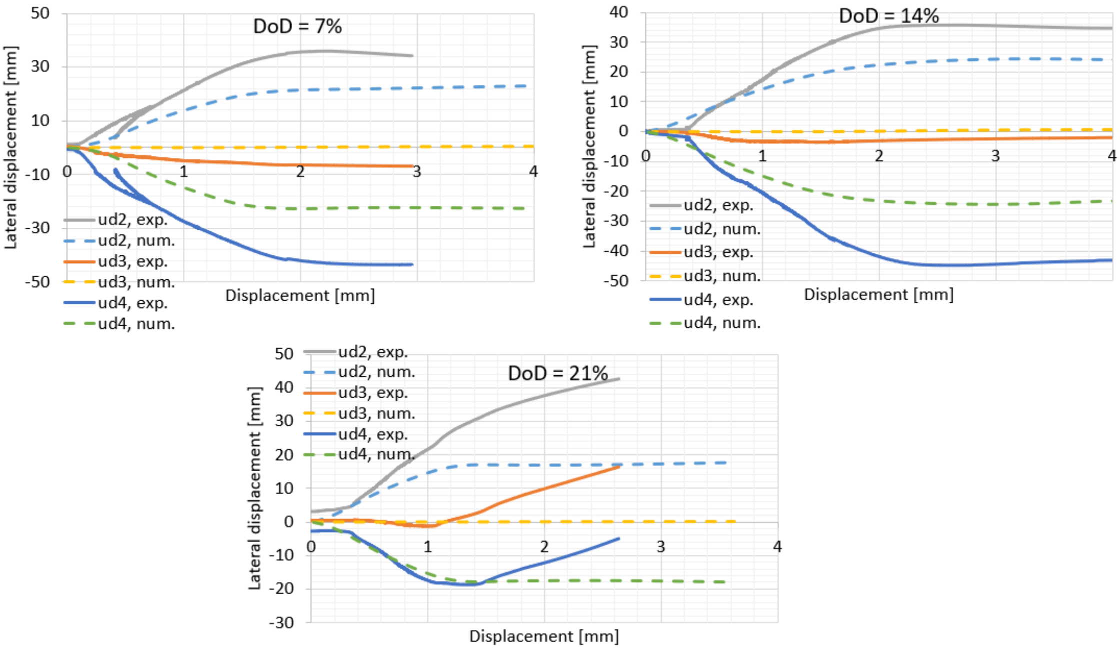

Figure 9.41. Comparison of lateral displacements – 6 mm specimens.

Figure 9.42 shows the lateral displacements obtained for 8 mm specimens. It is noted that similarly as in intact specimen, there was no local plate bending at the beginning of the loading process, and all displacements were very close to zero. However, with the corrosion development, when the plate on both sides of the stiffener starts to buckle occurred faster. This was observed for both numerical and experimental investigations. This observation is easily understandable since with the increase of corrosion level, the mean plate thickness decrease and slenderness ratio increase. Thus, the plate is more prone to buckle. For the specimen with the level of degradation of 21%, the plate is subjected to local bending almost from the beginning, similarly to stiffened plates of lower thickness values (5 mm and 6 mm).

Nevertheless, the buckling moment is slightly different for the FE model and tested specimens considering 14% and 21% of the degradation levels. In terms of lateral mid-displacement (ud3), some differences could be noted too. In the case of the experiment, some level of global bending occurred during failure, which was not captured in the FE model. Although the experimental displacements are slightly higher than the numerical ones, it could be concluded that a very good match has been achieved.

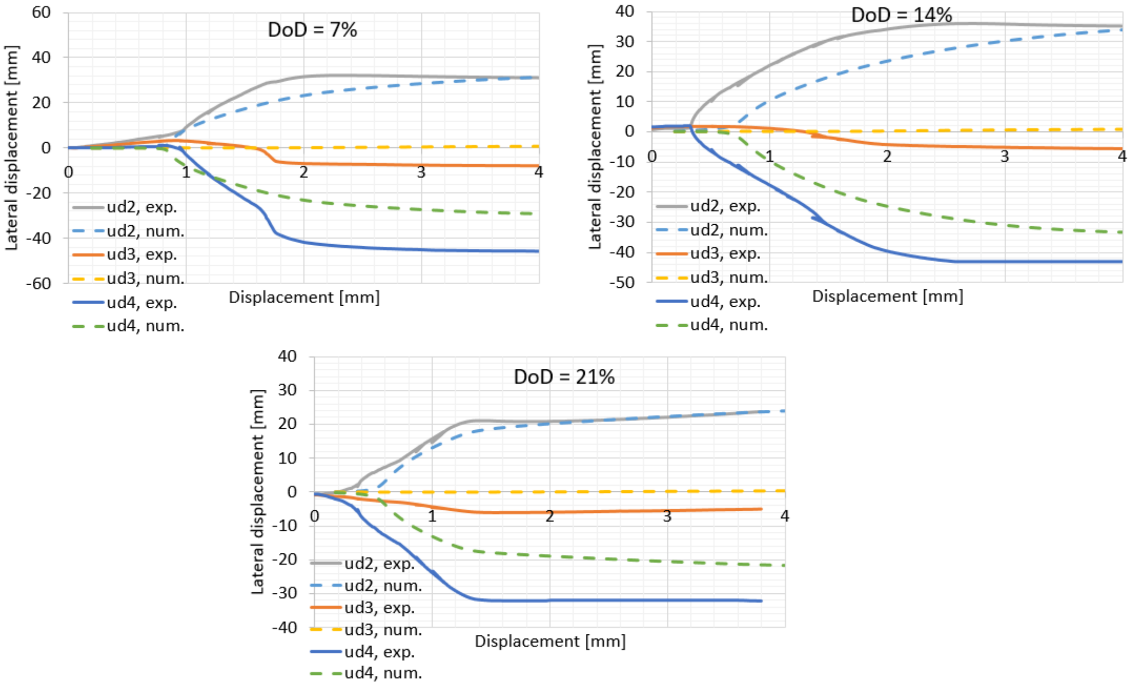

Figure 9.42. Comparison of lateral displacements – 8 mm specimens.

Finally, the post-collapse shapes of tested specimens (see Figures 6.46, 6.48, 6.49) are compared with the results of FE analysis. The failure modes from FE analysis for 5 mm specimens are presented in Figure 9.43. Similarly to the tested specimens, the post-collapse forms are unsymmetrical, not captured when thickness distribution will be uniform. The primary cause of the collapse is identical for both experiment and numerical model, i.e. local plate buckling followed by stiffener tripping. It is noted that only in a specimen with a 14% degradation level, the post-collapse forms are almost identical. In a specimen with a 7% of degradation level, the region of highest plastic deformations is closer to the upper support. For the specimen with a 21% level of degradation, the critical cross-section is on the opposite side of the experiment. The possible cause of differences could be the non-ideal capturing of real thickness distribution due to the uncertainty of the measuring technique. Secondly, as discussed in Section 9.1.3, the uneven distribution of mechanical properties could be the reason.

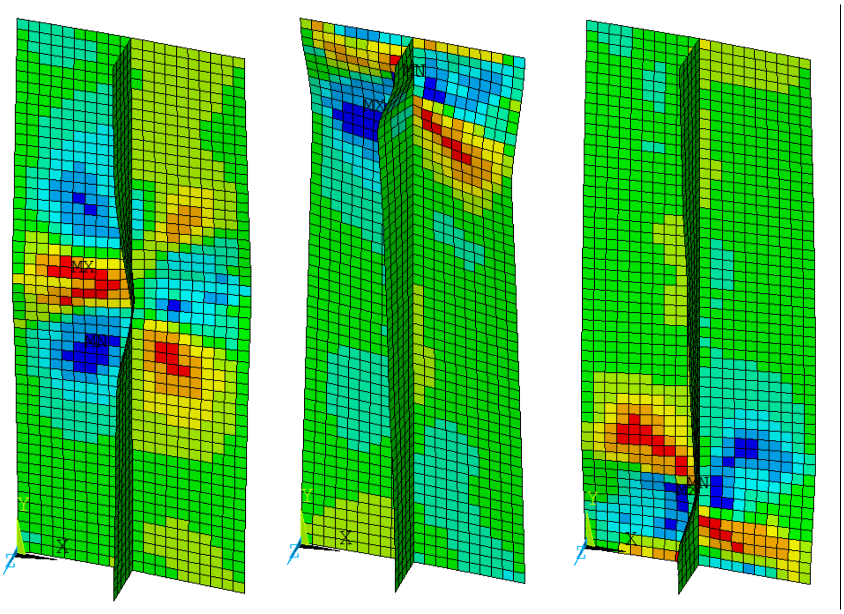

Figure 9.43. Post-collapse shapes – numerical analysis – 5 mm specimens (DoD = 7% - left, DoD = 14% - mid, DoD = 21% - right).

In Figure 9.44, the post-collapse shapes of 6 mm specimens obtained via numerical tool are presented. Compared with failure modes observed in tested specimens (see Figure 6.48), almost identical forms were observed for specimens with DoD levels of 7% and 14%. Thus, the local plate buckling followed by stiffener tripping caused the collapse, and the highest deformations were noted near the lower support. However, in the most severely corroded stiffened plate, the global buckling was primarily visible in a tested specimen, which was not captured in a numerical model. Nevertheless, the local plate buckling was observed in both cases near the upper support.

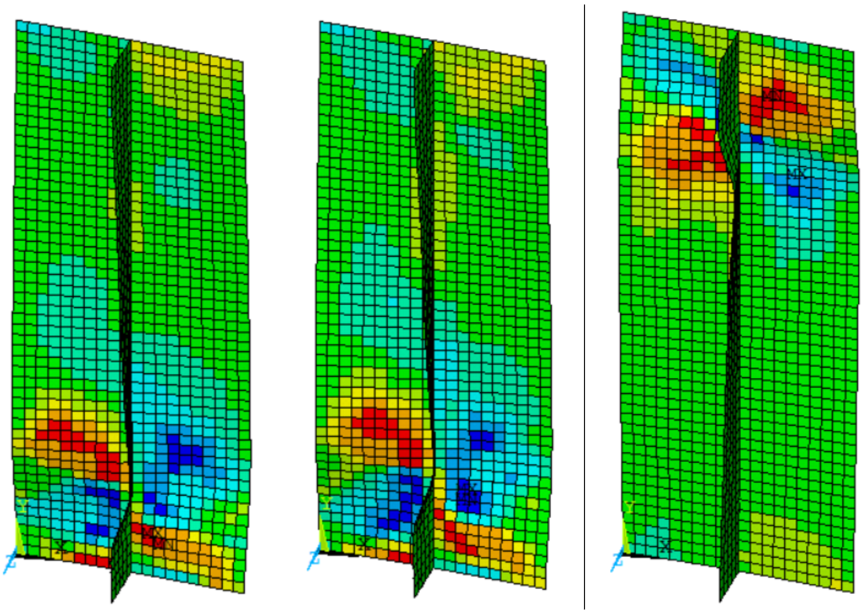

Figure 9.44. Post-collapse shapes – numerical analysis – 6 mm specimens (DoD = 7% - left, DoD = 14% - mid, DoD = 21% - right).

Figure 9.45 shows the failure modes of the 8 mm specimens from numerical analysis. It is noted that the post-collapse shapes are similar and unsymmetrical. In all cases, the local plate buckling was a primary cause of the collapse, which was also observed experimentally (see Figure 6.49). However, in the latter case, some level of global buckling was observed too. Nevertheless, the shapes of collapsed plates, including critical cross-section, were almost identical to those observed in tested specimens. In all cases, the highest plastic deformations occurred near the lower support.

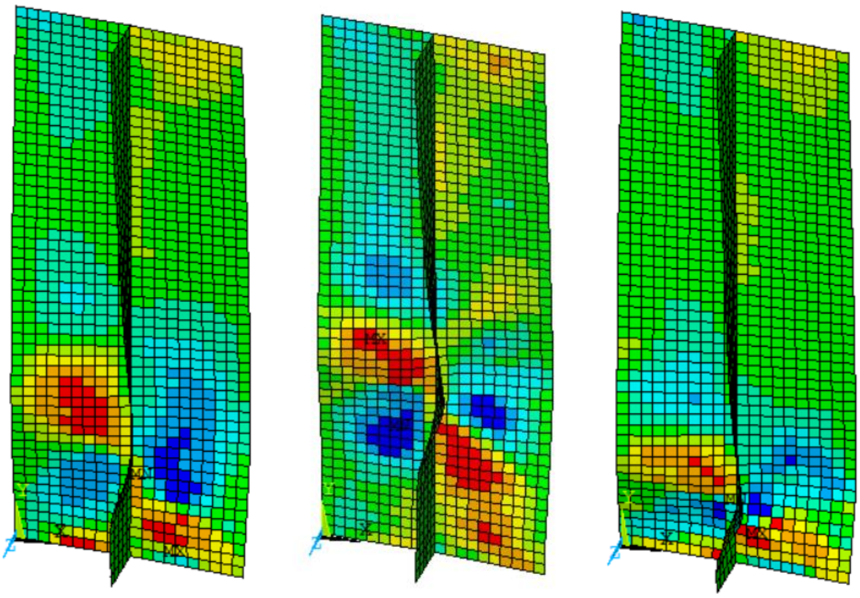

Figure 9.45. Post-collapse shapes – numerical analysis – 8 mm specimens (DoD = 7% - left, DoD = 14% - mid, DoD = 21% - right).

The presented comparison shows that the FE model, which includes real thickness distribution and changes in mechanical properties, properly simulates corroded stiffened plates' behaviour. Notably, in terms of 5 mm specimens, some bias in the ultimate strength value was observed, similar to the intact specimen. Nevertheless, in almost all cases, the force-displacement relationships, lateral displacements and post-collapse forms were very similar in the numerical model and experiment.

9.3.2. Comparison between different corrosion models

To verify the central research hypothesis, different corrosion models are compared with experimental results:

- non-uniform thickness loss with subsequent mechanical properties reduction (see Section 9.3.1);
- non-uniform thickness loss without changes in mechanical properties;
- uniform thickness loss with subsequent mechanical properties reduction;
- only uniform thickness loss.

For each model, the values of ultimate strength are plotted in function of degradation level. The comparison for 5 mm plates is presented in Figure 9.46. It is noted that the closest results to experimental ones were observed for the model with non-uniform thickness reduction and subsequent reduction of mechanical properties. Although some bias is observed, the regression curves inclinations are almost the same. The bias between experimental and numerical results is observed for intact specimen, too, and possible causes of this were already discussed in previous sections. The highest values of ultimate strength are observed when only mean thickness reduction is considered. The specimens with non-uniform distribution of thickness also showed lower results when compared to a uniform model.

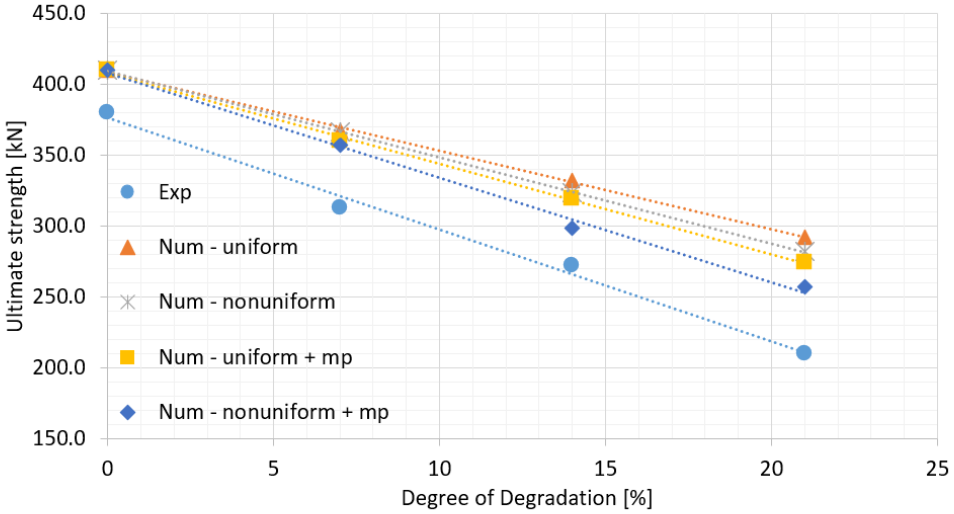

Figure 9.46. Comparison between different corrosion models – 5 mm stiffened plates.

In Figure 9.47, the comparison between different models for 6 mm stiffened plates is presented. It is noted that a very good match has been achieved between experimental results and the most sophisticated numerical model. All other models overestimated the values of ultimate strength. Notably, better results were achieved, where non-uniform thickness distribution was applied only compared to a uniform model with subsequent reduction of mechanical properties. This indicates the crucial role of the actual distribution of thickness in the stiffened plate.

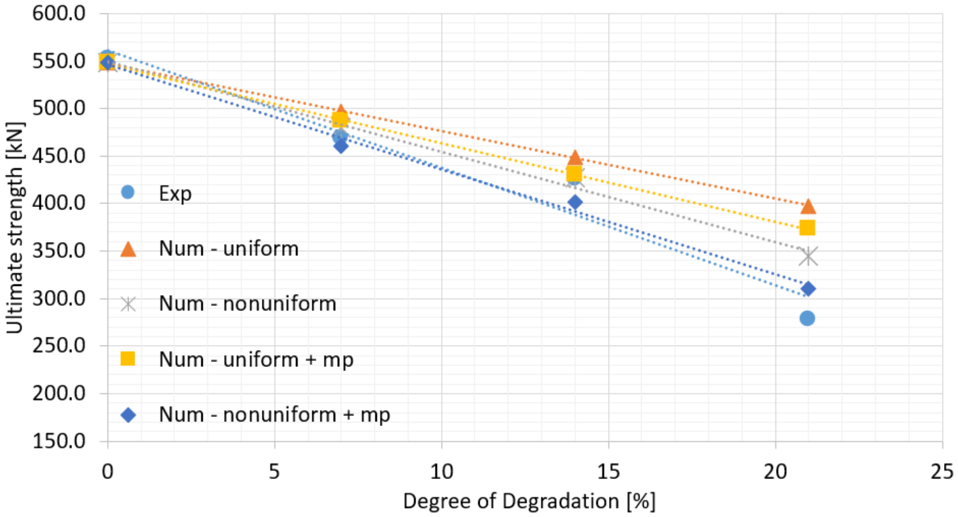

Figure 9.47. Comparison between different corrosion models – 6 mm stiffened plates.

The comparison of the results obtained for different models for 8 mm specimens is presented in Figure 9.48. Similarly to other thicknesses, the closest results to experimental ones were obtained for the model that considers the real thickness distribution and changes in mechanical properties. The inclination of both curves is the same; however, some small bias observed for the non-corroded specimen is observed. It is noted that with regards to other models, close results were also obtained for a model that considers uniform thickness loss and reduction of mechanical properties. Where non-uniform thickness loss is considered only, the results are away from the experiment. Thus, it was more crucial to consider the mechanical properties reduction rather than the actual thickness distribution in this case.

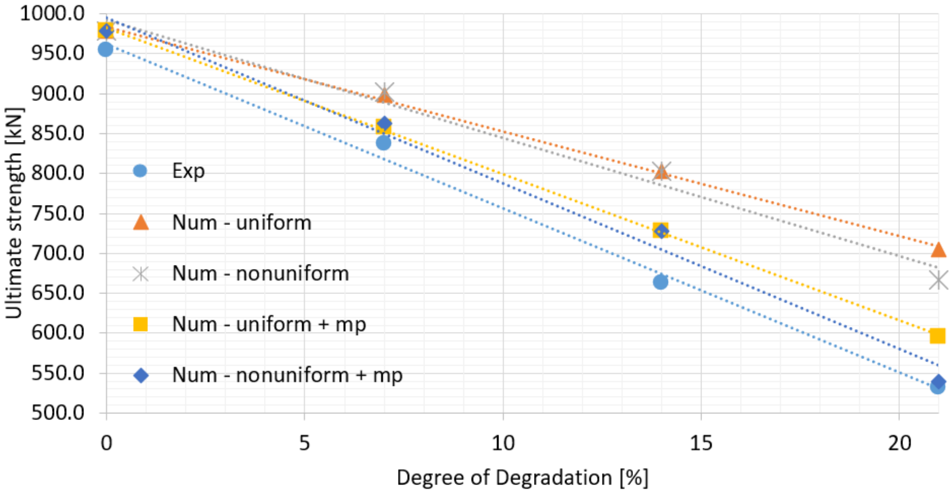

Figure 9.48. Comparison between different corrosion models – 6 mm stiffened plates.

From this analysis, it is evident that considering both uneven thickness distribution and mechanical properties changes. The results are closest to the experiment. This indicates that the central research hypothesis is verified positively. When the model considers only uniform thickness loss, not solely the value of ultimate strength will be overestimated, but the post-collapse form will not be captured accurately. For some stiffened plates, the more crucial was taking into account the changes in mechanical properties, whereas for others, the proper modelling of thickness distribution. However, only considering both of these factors simultaneously will capture the corroded compressed stiffened plate's behaviour most accurately.

9.3.3. Comparison between random field modelling and exact corrosion fields

In the presented section, the results of ultimate strength predictions that incorporated the random fields of corrosion (Section 9.2.2) are compared with numerical investigations that considered actual corrosion fields (Section 9.3.1). Namely, the maximum, mean and minimum results from random field analysis are compared with the exact FE analysis.

In Figure 9.49, the computations for 5 mm stiffened plates are presented and compared. It is noted that the results obtained via generated random fields are lower with regards to exact FE results. There is also observed quite a high scatter of random results. The closest results regarding accurate FE analysis were obtained for maximum values of ultimate strength from random field analysis. However, the random field analysis was performed for correlation length that produced the lowest ultimate strength values. Probably, in an experiment, other correlations were observed.

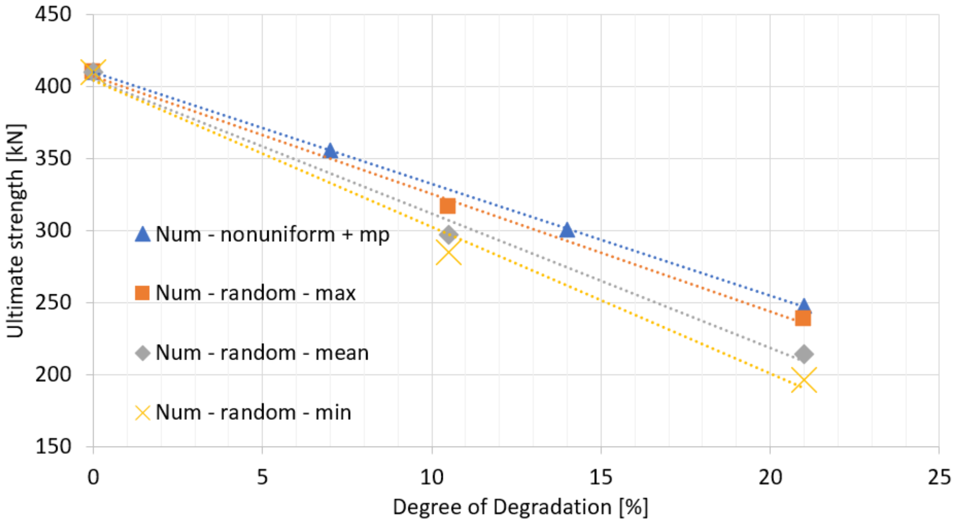

Figure 9.49. Comparison between random field analysis and exact FE computations – 5 mm stiffened plates.

The comparison for 6 mm plates is presented in Figure 9.50. In this case, the results obtained from accurate FE analysis are close to the mean values of ultimate strength resulting from computations with randomly generated corrosion fields. This indicates that the random fields are showing the possible case of real corrosion distribution.

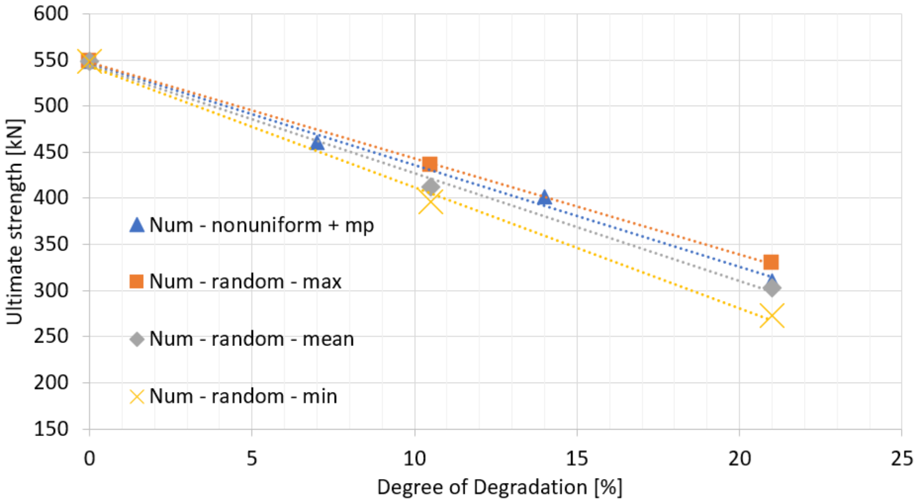

Figure 9.50. Comparison between random field analysis and exact FE computations – 6 mm stiffened plates.

In Figure 9.51, the comparison is made for 8 mm stiffened plates. It is noted that similarly to 5 mm plates, the exact results are closest to the maximum values from random field analysis. However, the numerical results obtained for generated corrosion fields are not subjected to very high scatter in this case.

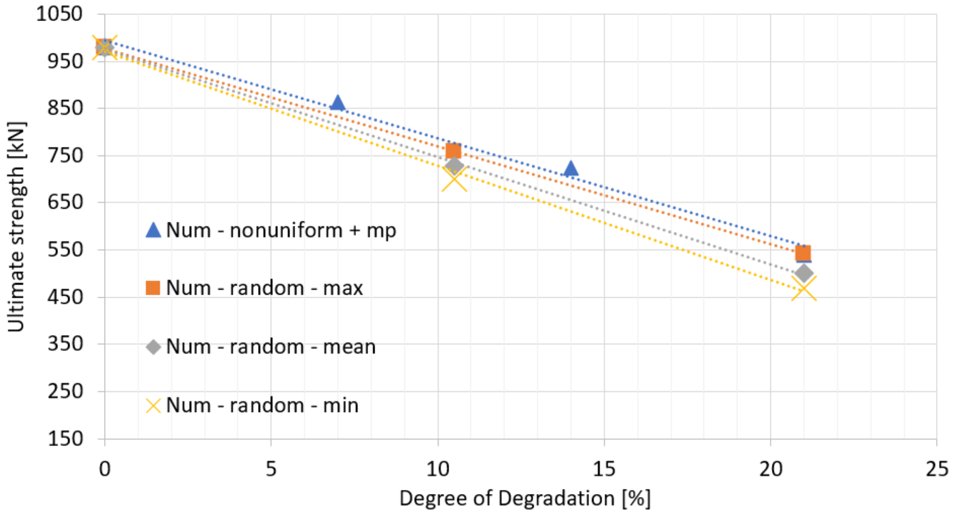

Figure 9.51. Comparison between random field analysis and exact FE computations – 8 mm stiffened plates.

Based on the presented analysis, it is observed that the exact FE results and results based on the random field analysis are close to each other. Although for 5 mm and 8 mm plates, the measured corrosion fields seem to be not so critical for the reduction of ultimate strength compared to randomly generated fields, there seems to be reasonable from the safety point of view, to take into account the representative random fields that result in the mean value of ultimate strength reduction. Especially in 6 mm plates, the exact FE analysis results were close to mean values of ultimate strength from random field analysis. Thus, such corrosion fields could exist in real conditions.

9.4. Conclusions

The model considering uniform thickness reduction in corrosion degradation revealed a non-conservative one compared to the model, which considers the non-uniformity of the thickness of the corroded plate. When only thickness change is considered corrosion development, the ultimate strength values can be overestimated even up to 30 % when considering the most severely corroded stiffened plate. It needs to be noted that this type of model is commonly used in design practice.

Based on the detailed validation with experimental results and comparison between different numerical models, it has been shown that only when the non-uniform distribution of thickness and changes in mechanical properties are taken into account, the results are similar to the one obtained via experiment. Thus, the research hypothesis has been verified positively.

The methodology that employs random fields is revealed to be fast and practical to model the corroded structural members. Compared to the time-consuming corrosion tests, when only a limited number of specimens are possible to be obtained, the presented model seems very useful.

10. FAST CLOSED-FORM APPROACH OF ULTIMATE STRENGTH ASSESSMENT USING DOE TECHNIQUES [P10]

The experimental results, together with numerical investigations presented in the Thesis, are highly time-consuming. In this view, it will be impossible to incorporate the advanced FE simulations with randomly generated fields of corrosion into engineering practice. For eventual design purposes, fast closed-form approaches are essential. One can derive such design equations directly from experimental results. However, to cover the broad scope of the plate slenderness ratios and column slenderness ratios, it requires a high number of specimens, which exceeds the number of specimens tested in this study. Thus, using an advanced numerical model seems reasonable, especially that it presented an excellent match regarding experimental results.

The initial mechanical properties are considered typical for design applications. The yield stress is considered equal to 235 MPa, Youngs modulus equal to 206 GPa and ultimate tensile stress equal to 400 MPa. The changes in mechanical properties follow the general constitutive lows developed in Section 8.6.

In corrosion degradation, the representative random field resulting in the results closest to the mean value from nine realizations is considered for each case. This will significantly reduce the number of needed computations.

Typically, the OFAT (One Factor At a Time) [270] technique was used to develop some closed-form approaches or sensitivity studies, i.e. only one parameter was changed, whereas the rest factors were kept unchanged. In terms of initial sensitivity studies, this technique seems to be good enough to examine the relevant parameters. However, this not allows investigating the possible interaction between factors. The DoE (design of experiments) [277] methodology seems to be most suitable to investigate that. Additionally, with comparison to OFAT analysis, the number of observations is significantly reduced. Outcomes of a DoE analysis are the response surface and the interactions between factors. The latter could be established considering the significantly lower number of observations when compared to classical regression analysis. The response surface may be linear or nonlinear, which depends on the assumed at the beginning experimental plan.

The ultimate strength of stiffened plates is mainly governed by two factors, i.e., the plate slenderness ratio and column slenderness ratio, as was discussed in previous parts of the thesis. Due to the non-linear relationship between ultimate strength and plate thickness, the Central Composite Design (CCD) experimental plan [275] is used to investigate the dependency between the ultimate strength of corroded stiffened plates and governing factors. In that plan, the selected factors are considered taking into account their maximum (+1), mean (0), and minimum (-1) values. Apart from both plate (factor A) and column (factor B) slenderness ratio, the level of corrosion degradation (factor C) is considered as a third factor. The total number of 15 cases has been analysed, considering factors values, as presented in Table 1. It needs to be noted that based on the plate and column slenderness ratios, the plate thickness (t_p) together with stiffener dimension (height h_s and thickness t_s) has been obtained. The estimated normalized ultimate strength (the ultimate force divided by the initial cross-section of the stiffener plate and yield stress value) are presented in Table 10.1.

Table 10.1. Ultimate strength of stiffened plates for DoE cases.

Case	Factor			t_p [mm]	h_s [m]	t_s [mm]	β [-]	λ [-]	DoD [%]	Normalized ultimate strength [-]
	A	B	C							
1	-1	-1	-1	11	0.25	13	1.23	0.135	0	0.975
2	-1	-1	1	11	0.25	13	1.23	0.135	10.5	0.542
3	-1	1	-1	11	0.07	10	1.23	0.7	0	0.906
4	-1	1	1	11	0.07	10	1.23	0.7	21	0.498
5	1	-1	-1	6	0.25	8	2.25	0.135	0	0.644
6	1	-1	1	6	0.25	8	2.25	0.135	21	0.330
7	1	1	-1	6	0.07	6	2.25	0.7	0	0.676
8	1	1	1	6	0.07	6	2.25	0.7	21	0.364
9	0	0	0	8	0.1	9	1.69	0.415	10.5	0.612
10	-1	0	0	11	0.1	11.5	1.23	0.415	10.5	0.730
11	1	0	0	6	0.1	7	2.25	0.415	10.5	0.505
12	0	-1	0	8	0.25	10	1.69	0.135	10.5	0.554
13	0	1	0	8	0.07	7.5	1.69	0.7	10.5	0.594
14	0	0	-1	8	0.1	9	1.69	0.415	0	0.892
15	0	0	1	8	0.1	9	1.69	0.415	21	0.440

Analysing the results presented in Table 10.1, one can first obtain the model's response factors' influence. However, firstly, the relevant and irrelevant factors need to be established. One of the most efficient methods is to use the half-normal probability plots [276]. If the factor is lying on the left-hand side of the dashed line, it is non-relevant. The three primary factors (A, B, C) and interactions between them are considered (A:B, A: C, B:C, A:B:C). Additionally, the primary factors' squares are considered too (A^2, B^2, C^2) to investigate the response surface's possible non-linearity. The half-normal probability plot of the considered study is presented in Figure 10.1.

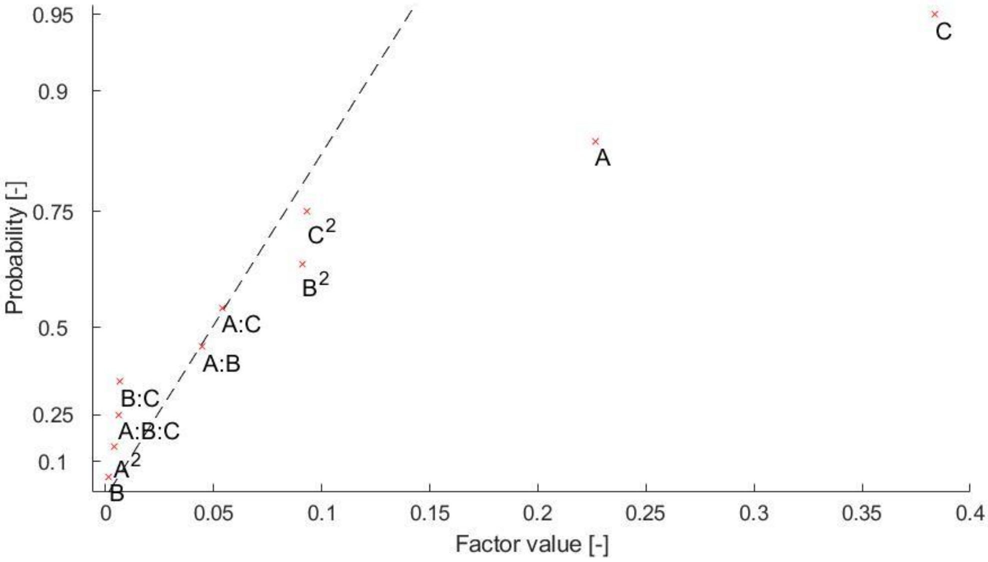

Figure 10.1. Half-normal probability plot.

As can be noticed, the factors that can be taken as important ones are (in the order of importance): C, A, C^2, B^2, A:C, A:B. The most important factor revealed to be the corrosion degradation level. The square value of corrosion level influences the results too. Further, the plate slenderness ratio significantly impacts the resulting stiffened plate capacity. An interesting observation can be made about the column slenderness, which does not impact ultimate strength when considering only the maximum and minimum value. However, the square of this factor was revealed to be an influential one. Two interaction factors were captured as important: the corrosion level and plate slenderness ratio and the column slenderness ratio and plate slenderness ratio. When the plate slenderness ratio is low, the decrease of the ultimate strength with corrosion development is less significant than the slenderer plates.

The different cases presented in Table 10.1 have different normalized ultimate strength, and the post-collapse shapes vary. In most cases, the plate induced failure lead to collapse (e.g., case 9 – see Figure 10.2, left). However, when the plate slenderness is significantly higher than the column one, the overall column buckling caused stiffened plate collapse (e.g., case 13 – see Figure 10.2, right).

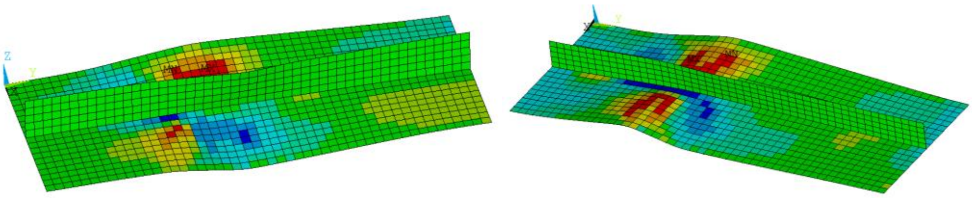

Figure 10.2. Post-collapse shape: case 9 (left) and case 13 (right).

Based on the factors obtained from the DoE analysis, the response surface to estimate the ultimate strength of corroded stiffened plates can be established. Considering only the most essential factors, a polynomial equation may be defined as:

$$\frac{\sigma_U}{Re} = 0.618 - 0.113 \cdot x_1 - 0.045 \cdot x_2^2 - 0.192 \cdot x_3 + 0.047 \cdot x_3^2 + 0.022 \cdot x_1 \cdot x_2 + 0.027 \cdot x_1 \cdot x_3 \quad (10.1)$$

where:

$$x_1 = \frac{\beta - 1.74}{0.51}; x_2 = \frac{\lambda - 0.4175}{0.2825}; \ x_3 = \frac{DoD - 10.5}{10.5} \quad (10.2)$$

The response surface considering the mean value of the column slenderness ratio is presented in Figure 10.3. It can be noticed that the ultimate strength decreases with the increase of both plate slenderness ratio as well as corrosion degradation level.

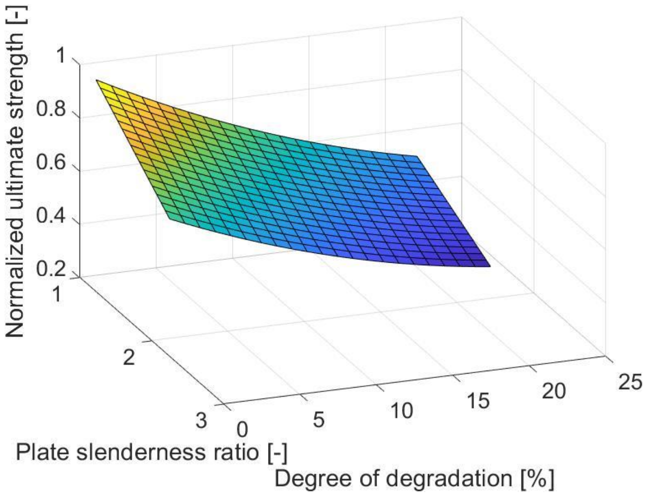

Figure 10.3. Response surface as a function of DoD and plate slenderness.

This chapter investigated the influence of different governing factors on corroded stiffened plates' ultimate strength employing the DoE technique. The corrosion degradation level and plate slenderness ratio are the primary factors that govern the load-carrying capacity. The observed reduction of the ultimate strength in a severely corroded stiffened plate reaching the level of 50% from the initial value, and it was slightly higher for thinner plates. However, the column slenderness ratio was also an essential factor, considering this parameter's square. It was found that apart from ultimate strength, the post-collapse shape will also vary depending on the governing factors. In the majority of the studied cases, the plate-induced failure was identified as a collapse mode. However, for the high plate slenderness ratio and low column one, the global column buckling occurred. As an analysis outcome, the response surface for fast estimation of the ultimate strength of corroded stiffened plates has been established, which may be used in the engineering practice, especially in the initial stages of the structural design process.

11. ULTIMATE STRENGTH RELIABILITY ANALYSIS OF AGEING SHIP STRUCTURES

As it was discussed, many sources of uncertainties are inherent in structural design. The introduction to uncertainty qualification has been provided at the beginning of Chapter 5. Despite the common view, the loading and load-carrying capacity of the structural members are not deterministic quantities. There can be random variables, and thus absolute safety (zero probability of failure) is non-achievable. The structures must be designed to provide the operation considering the specified probability of failure.

The structure reliability is its ability to comply with its design purpose for the specific design lifetime. Reliability is commonly understood to equal the probability that a structure will not fail to perform its intended function and can be considered a rational evaluation criterion. It provides a good basis for decisions about repair or replacement.

11.1. Reliability analysis

There are various methods to assess reliability. Four levels of reliability analysis can be classified [277]. Level I corresponds to the classical deterministic approach, inducing any uncertainty utilizing partial safety. In Level II, mean and standard deviation values are used to characterize each random variable. Level III describes the characteristics of random variables using the joint probability density function (first- or second-order reliability method). Finally, Level IV compares the prospect and integrity of a target structure with a reference structure using an engineering economic analysis, considering the costs and benefits associated with construction, as well as the consequences of structural failure and maintenance/repair. This method is used to obtain the target reliabilities.

11.1.1. Second-moment methods (Level II)

In second-moment methods, all failure modes are distinguished separately. This simplifies the procedure, but the value of acceptable risk must be defined separately for each mode of failure.

The first concept of this method was proposed by Freudenthal [278], and next, the reliability safety index was defined by Cornell [279] as:

$$\beta = \frac{E(M)}{\sigma(M)} \tag{11.1}$$

where $E(M)$ is the mean value of the safety margin, and $\sigma(M)$ is the standard deviation of the safety margin.

If the capacity R of the structure and the load effects S are independent variables, corresponding safety margin M is defined as:

$$M = R - S \tag{11.2}$$

and failure occurs when the margin becomes negative. The safety index β is given as:

$$\beta = \frac{E(R) - E(S)}{\sqrt{\sigma_R^2 + \sigma_S^2}} \tag{11.3}$$

Similarly to R and S are random variables, M has a probability density function as well as $p_M(M)$ As shown in Figure 11.1.

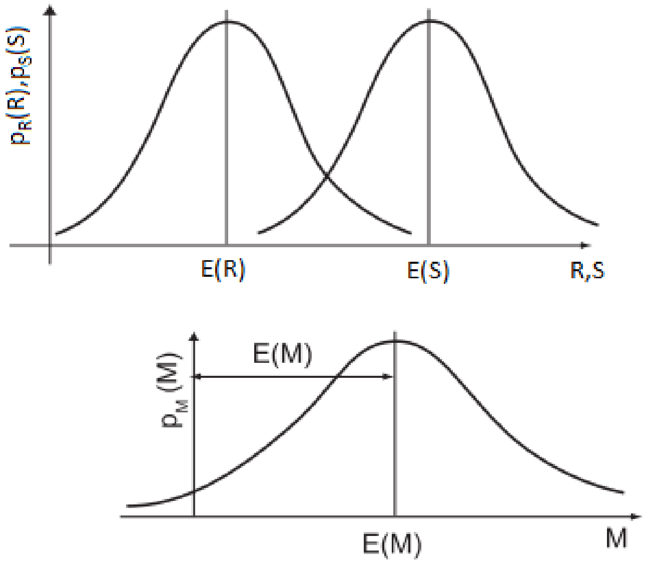

Figure 11.1. PDF of the safety margin.

The probability of failure is given as:

$$P_f = Prob[M < 0] = Prob\left[\frac{M - E(M)}{\sigma(M)} < -\frac{E(M)}{\sigma(M)}\right] \tag{11.4}$$

where $\sigma(M)/E(M)$ is a coefficient of variation (COV), and normalized margin of safety is $M_0 = \frac{M-E(M)}{\sigma(M)}$.

In these terms, the probability of failure becomes:

$$P_f = Prob\left[M_0 < -\frac{1}{V_M}\right] = Prob[M_0 \leq\ -\beta] \tag{11.5}$$

There is a direct relationship between the probability of failure and the safety index. The larger probability of failure, the smaller the safety index. If R and S are assumed to be normal random variables, then the equation above can be expressed as follows:

$$\beta = -\Phi^{-1}(P_f) \tag{11.6}$$

This approach may be generalized for cases where the limit state function $g(x)$ is a linear function of design parameters x_i. The safety margin can be expressed as:

$$M = b + \sum_i a_i X_i \tag{11.7}$$

or $M = a^T X + b$ in matrix notation.

Based on the safety index β definition and regarding the Ditlevsen and Madsen [280], it can be written as:

$$\beta = \frac{E(M)}{\sigma(M)} = \frac{E(M)}{\sqrt{\sum_{i=1}^{i=n} \sum_{j=1}^{j=n} a_i a_j \, Cov(X_i, X_j)}} \tag{11.8}$$

where $Cov(X_i, X_j)$ is the covariance of X_i and X_j defined as:

$$Cov(X_i, X_j) = E\left[\big(X_i - E(X_i)\big)\,\big(X_j - E(X_j)\big)\right] \tag{11.9}$$

For independent random variables, the safety index is equal to:

$$\beta = \frac{E(M)}{\sigma(M)} = \frac{E(M)}{\sqrt{\sum_i a_i^2 \sigma_{x_i}^2}} \tag{11.10}$$

If the limit state function $g(x)$ is nonlinear, the linearization in the design point takes place.

After the foundation work of Cornell [279], other second-moment methods were developed, e.g. Hasofer and Lind [281].

11.1.2. Full probabilistic methods (Level III)

The most accurate reliability methods employ complete probability distribution functions of all random variables (loads, load effects, and limit values).

In this approach, all probability distributions are determined either by measurements (full-scale or of a model) or by theoretical investigations. The distributions of loads and limit values are not easy to obtain due to their dependence on many variations (material properties, the accuracy of analysis).

The two most common full probabilistic methods are presented below: first-order reliability methods (FORM) and second-order reliability methods (SORM).

First-order reliability methods are improved approaches to the Hasofer-Lind method. All random variables are transformed into a set of independent and standard normal variables [237,280].

In the FORM approach, the failure set is approximated by first transforming the limit state surface into U space and then replacing it with its tangent hyperplane at the design point u^*.

The Rosenblatt transformation is used:

$$U_i = \Phi^{-1}\big(F_i(Z_i|Z_1, \dots, Z_{i-1})\big) \qquad i = 1,2, \dots, n \tag{11.11}$$

If the random variables are mutually independent, the transformation is:

$$U_i = \Phi^{-1}\big(F_i(Z_i)\big) \quad i = 1,2, \dots, n \tag{11.12}$$

The limit state surface $g(Z) = 0$ in Z space is transformed into a corresponding limit state surface $g(u) = 0$ in U space. The design point u^* has to be determined in U space, which lies on $g(u) = 0$, and it is closest to the origin of the U space. To find this point, the iterative procedure is applied:

$$u^* = \beta\alpha^* \tag{11.13}$$

where β is the first-order reliability index. Unit normal vector α^* to the failure surface at u^* is given as:

$$g(u) = \beta + \alpha^T u = 0 \tag{11.14}$$

The first order safety margin is:

$$M = g(U) = \beta + \alpha^T U \tag{11.15}$$

The approximate failure probability is:

$$P_f \approx \Phi(-\beta) \tag{11.16}$$

As described above, FORM approximates the failure set, replacing the limit state surface in the u-space by its tangent hyperplane at the design point (Figure 11.2). The accuracy of this method mainly depends on the accuracy of representation by linear approximation and can be improved by SORM.

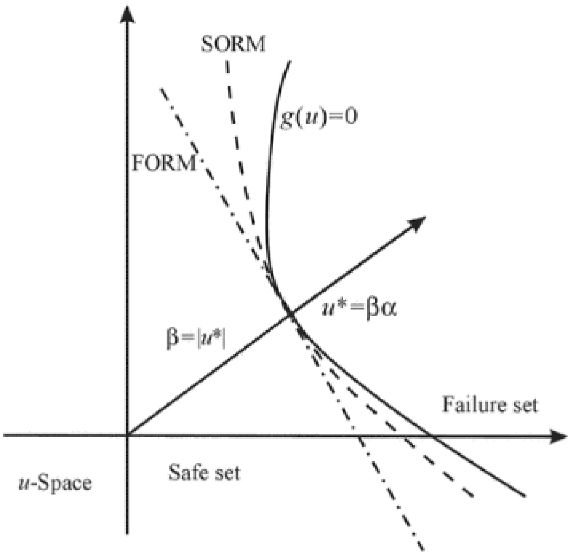

Figure 11.2. FORM and SORM [238].

In the second-order method, the approximation of the limit state surface is made by a hyper paraboloid with the same tangent hyperplane. The probability of failure is approximated as:

$$P_{f,SORM} \approx \Phi(-\beta)\prod_{j=1}^{n-1}\left(1-\beta_{k_j}\right)^{-\frac{1}{2}} + [\beta\Phi(-\beta)-\Phi(\beta)] \cdot \left\{\prod_{j=1}^{n-1}\left(1-\beta_{k_j}\right)^{-\frac{1}{2}} - \prod_{j=1}^{n-1}\left(1-(\beta+1)_{k_j}\right)^{-\frac{1}{2}}\right\} + (\beta+1)[\beta\Phi(-\beta)-\Phi(\beta)] \cdot \left\{\prod_{j=1}^{n-1}\left(1-\beta_{k_j}\right)^{-\frac{1}{2}} - Re\left\{\prod_{j=1}^{n-1}\left(1-(\beta+1)_{k_j}\right)^{-\frac{1}{2}}\right\}\right\} \#(11.17)$$

where i in the third term is the imaginary unit, Re() is the real part and $k_j (j = 1,2,\ldots,n-1)$ are the principal curvatures at the design point.

The corresponding reliability index is equal to:

$$\beta_{SORM} = -\Phi^{-1}\left(P_{f,SORM}\right) \qquad (11.18)$$

Comparing SORM and FORM, the estimate accuracy is higher in SORM by a second-order approximation.

11.2. Limit state functions

A fundamental part of the structural reliability analysis is component reliability based on the failure probability modelled by a single limit-state function [238]. The concept of structural reliability is illustrated in Figure 11.3, where the load and strength are modelled as random variables.

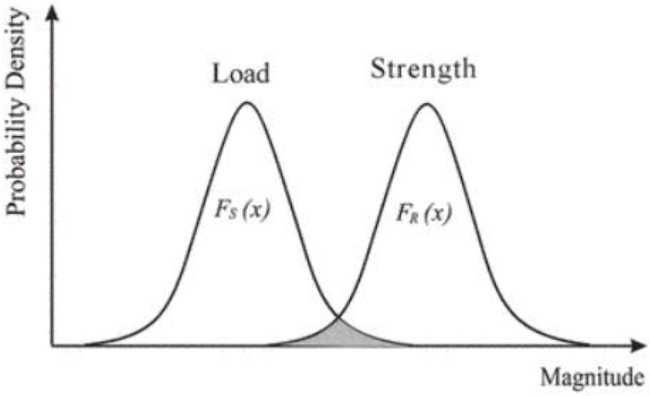

Figure 11.3. Concept of structural reliability [238].

Failure occurs when the load exceeds the strength. The probability of failure is equal to:

$$P_f = P(S \geq R) = \int_0^\infty F_S(x) F_R(x) dx \tag{11.19}$$

where $F_S(x)$ and $F_R(x)$ are probability density functions of load and strength, respectively.

The border between safe and failure states is called a limit state and is equal to $g(Z) = R - S$. There are three possible states of a structure:

$g(Z) < 0$ represents a failure state where loads S are greater than strength R.

$g(Z) > 0$ represents a safe state where strength R is larger than loads S.

$g(Z) = 0$ represents the limit state function.

These concepts are shown in Figure 11.4.

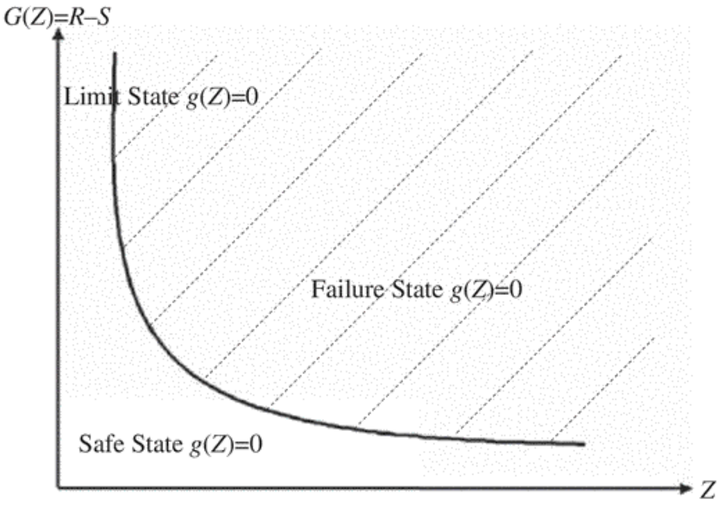

Figure 11.4. Limit state concept [238].

System reliability is considered where there is more than one limit-state function. Two types of basic systems exist, series systems and parallel systems. In the series system, the failure of one element causes the failure of the entire system (e.g. pipelines and risers). In the parallel system, failure of the system occurs due to the failure of whole elements.

The risk-based limit-state design combines probabilistic methods with FEM analysis, leading to a cost-effective and safe design.

11.3. Reliability analysis of ship hull girder

According to Mansour et al. [282], the limit state function of the hull girder can be expressed as follows:

$$g(X_i) = M_U - (M_{SW} + M_W) \tag{11.20}$$

The limit state functions for primary, secondary, and tertiary failure modes are presented in Table 11.1

Table 11.1. Limit state functions.

Failure mode	Hogging	Sagging
Primary (initial yield)	$G = M_{IY} - [M_{SW} + k_W M_W]$	$G = M_{IY} - [-M_{SW} + k_W(M_W + k_D M_D)]$
Primary (ultimate strength)	$G = M_U - [M_{SW} + k_W M_W]$	$G = M_U - [-M_{SW} + k_W(M_W + k_D M_D)]$
Secondary	$G = S_{U,2} - \frac{[M_{SW} + k_W M_W]}{SM_B}$	$G = S_{U,2} - \frac{[-M_{SW} + k_W(M_W + k_D M_D)]}{SM_B}$
Tertiary	$G = S_{U,3} - \frac{[M_{SW} + k_W M_W]}{SM_D}$	$G = S_{U,3} - \frac{[-M_{SW} + k_W(M_W + k_D M_D)]}{SM_D}$

where:

M_{IY} – initial yield vertical bending moment

M_U – ultimate vertical bending moment

M_{SW} – still-water bending moment for seagoing condition

M_W – vertical wave bending moment for in sagging or hogging condition

M_D – dynamic bending moment

k_W – load combination factor for still-water and wave/dynamic moments

k_D – load combination factor for wave and dynamic moments

SM_B – section modulus

S_U – ultimate stress

The procedure for reliability analysis should cover the following steps [238]:

Step 1: Definition of the basic geometry of the ship and scantlings and the environmental conditions.

Step 2: Definition of the limit-state functions, mainly four levels, for hull girder collapse, stiffened panels, buckling of plates between stiffeners, and fatigue of Critical Structural Details (CSD)

Step 3: Definition of random variables characteristic

Step 4: Selection of the proper reliability analysis method

Step 5: Calculation of the probability of failure for each failure mode

11.4. Reliability analysis of ship structures – a short review

One of the first attempts to employ probability-based methods in ship structural design was initiated by Mansour [283,284] and Mansour & Faulkner [285]. The first applications dealt with the safety of ship hulls subjected to wave-induced bending. Methodologies for single structural components were developed too.

A reliability assessment framework of ships under various operational conditions was developed in [286]. An oil tanker hull girder was analysed in [287] for different speeds, headings, and sea states. The reliability index was determined for intact and six damaged hull cases, where the limit state function was based on the hull girder's ultimate strength in the midship section. The reliability assessment of the ship structures accounting for the progressive and shock deuteriations has been presented in [288].

The reliability estimates of the hull girders subjected to the degradation effects, such as corrosion and cracking, were developed too. A time-variant reliability assessment is performed to see how the reliability index will change in time, which has an advantage over time-invariant solutions. Guedes Soares and Garbatov [289] presented the time-variant reliability formulation of maintained ship hulls with correlated corroded elements. It was found that when no correlation is considered between corrosion rates of neighbouring elements, it will lead to unconservative solutions. Another time-variant reliability analysis of the corroding ship hull could be found in [204]. The time-variant reliability analysis of steel plates accounting for corrosion pits nucleation and propagation has been presented in [290], and the model parameters were calibrated based on the existing results of exposure tests. Zayed et al. [291] performed a reliability analysis of ship hulls subjected to corrosion and maintenance, where ship loading uncertainties, random variables, and inspection events were considered. Teixeira et al. [183] performed an advanced uncertainty analysis, where an approach to assessing the ultimate strength of plates with random initial distortions, material, and geometrical properties and random corrosion degradation was presented. In [292], the reliability-based model of deteriorating ship structures subjected to multiple environmental conditions has been developed. The degradation effects have been considered a combined crack growth and corrosion in the ship's hull structural components. In most of these works, the corrosion has been considered a uniform thickness loss.

11.5. Reliability analysis of corroded stiffened plates [P11]

11.5.1. CSR approach

The method used to estimate the ultimate structural capacity may be found in detail in Common Structural Rules [5]. Nevertheless, the main assumptions are briefly introduced. Three different failure modes of the stiffened plate element, which is the typical part of ship cross-section, can be distinguished: beam-column buckling (CR1), torsional buckling (CR2), and web local buckling of the stiffener (CR3). The ultimate limiting capacity will be the minimum from the above three modes:

$$\sigma_U = \min(\sigma_{\mathrm{CR}1}, \sigma_{CR2}, \sigma_{CR3}) \tag{11.21}$$

The beam-column buckling failure mode is estimated as:

$$\sigma_{CR1} = \begin{cases} \sigma_{E1}; & \sigma_{E1} \leq \dfrac{Re}{2} \\ Re\left(1 - \dfrac{Re}{4\,\sigma_{E1}}\right); & \sigma_{E1} > \dfrac{Re}{2} \end{cases} \tag{11,22}$$

where σ_{E1} is the elastic Euler column buckling stress equal to:

$$\sigma_{E1} = \frac{\pi^2 E I_{b_{e1}}}{A_{b_e}} \tag{11.23}$$

where I_{b_e} is the moment of inertia of stiffener with a plating of width b_{e1} and A_{b_e} is the net sectional area of stiffener with a plating of a width b_e. Both of widths b_e and b_{e1} are dependent on the plate slenderness ratio.

The torsional buckling failure mode is equal to:

$$\sigma_{CR2} = \begin{cases} \sigma_{E2}; & \sigma_{E2} \leq \dfrac{Re}{2} \\ Re\left(1 - \dfrac{Re}{4\,\sigma_{E2}}\right); & \sigma_{E2} > \dfrac{Re}{2} \end{cases} \tag{11.24}$$

where σ_{E2} is the elastic Euler torsional buckling stress equal to:

$$\sigma_{E2} = \frac{E}{I_p}\left(\frac{\pi^2 I_\omega}{l^2} + 0.385 I_T\right) \tag{11.25}$$

where I_p and I_ω are the polar and sectional moments of the inertia of the stiffener about the point that the stiffener is welded to the plate, respectively, and I_T is the Saint Venant's moment of inertia of the stiffener.

The web local buckling mode is estimated as follows:

$$\sigma_{CR3} = \begin{cases} \sigma_{E3}; & \sigma_{E3} \leq \dfrac{Re}{2} \\ Re\left(1 - \dfrac{Re}{4\,\sigma_{E3}}\right); & \sigma_{E3} > \dfrac{Re}{2} \end{cases} \tag{11.26}$$

where σ_{E3} is the elastic Euler buckling stress of the stiffener:

$$\sigma_{E3} = 160000\left(\frac{t}{h}\right)^2 \tag{11.27}$$

where t and h are the thickness and height of the stiffener, respectively.

All three critical stresses will be a function of both the geometrical dimensions of the stiffened plate and the mechanical properties of the steel. In the main dimensions, the thickness is only treated as a random variable, whereas the length, breadth, and height of the stiffener are deterministic variables. In the case of the mechanical properties, both yield stress and Young modulus are random variables. As a result, the ultimate capacity will be a random variable too.

In the presented analytical model, one cannot control the initial imperfections level. The mean level of the initial imperfections is assumed in the model. However, it was shown in Section 5.1 that the variations of the initial imperfections cause significant variations in the ultimate capacity as well. Due to that fact, it cannot be neglected in the reliability analysis.

Since the uncertainty of initial imperfections cannot be implemented directly, it is introduced as a normal random variable $(\widetilde{X_I})$. The mean value and standard deviation of initial imperfections uncertainty are assumed to be equal to 1 and 0.05, respectively.

Together with initial imperfections, welding-induced residual stresses can also cause a reduction in the ultimate capacity. However, the level of reduction will depend on the size of the stiffened plate and the level of residual stresses. As proposed in [67], the maximum capacity reduction of the stiffened plates caused by the welding-induced residual stresses is about 10 %. In the presented study, the uncertainty level related to welding-induced residual stresses is introduced by a normal random variable $(\widetilde{X_R})$. The mean value is assumed to be equal to 0.95 and standard deviation is taken as 0.05.

Based on the presented assumptions, the limit state function is defined as follows:

$$g = \widetilde{X_R}\widetilde{X_I}\widetilde{\sigma_u} - \widetilde{\sigma_L} \qquad (11.28)$$

The acting stress $(\widetilde{\sigma_L})$ is assumed to be a normal random variable with the coefficient of variation (CoV) equal to 10%. The ultimate capacity is a log-normal random variable, with the CoV resulting from the uncertainties related to the thickness, yield stress, and Young modulus:

$$\widetilde{\sigma_U} = f\left(\tilde{t}, \widetilde{Re}, \tilde{E}\right) \qquad (11.29)$$

The mechanical properties in corrosion degradation were introduced in Section 8.6, together with their values of standard deviations. The mechanical properties are considered with nominal values for design purposes (see Chapter 10). In the case of thickness uncertainty, the standard deviations follow Equation 4.7, based on the measurements performed in operating ships. Similarly to previous studies, stiffened plate dimensions and thicknesses are considered as presented in Section 4.2.1.

The limit state function, together with the procedure for calculating the ultimate capacity, was adopted in the STRUREL software [293], and the FORM method [281] is used to estimate the Beta reliability index.

Two different models are analysed considering the corroded degradation conditions measured by the Degree of Degradation between 0 and 21 %. The first model (A) considers only thickness change, which is already adopted in the Classification Society Rules. Usually, the ultimate capacity check is performed for the net section without half of the corrosion additions. In this model, the mechanical properties are independent of DoD, and there are the same as for intact conditions. In the second model (B), the thickness reduction is followed by subsequent mechanical properties reduction.

Usually, the loads for stiffened plate elements composing the ship hull cross-section are coming from still water and wave-induced bending moments. However, in the presented section, only one stiffened plate element is analysed. For that reason, the acting stress is found to satisfy the initial level of the Beta reliability index. According to DnV [294], the target reliability level for a designed structure for a severe consequence of failure should be equal to 3.71. The loading that satisfies the target reliability value for the intact conditions is presented in Table 2 for various plate thicknesses.

Table 11.2. Acting stresses for different thickness levels.

Thickness t [mm]	Acting stresses σ_L [MPa]		Target reliability index [-]
	Mean value	Standard deviation	
5	96.48	9.65	3.71
6	106.4	10.64	3.71
8	121.4	12.14	3.71

Figure 11.5 presents the analysis results, where the Beta reliability index is in a function of DoD for both models and different thicknesses of the stiffened plate.

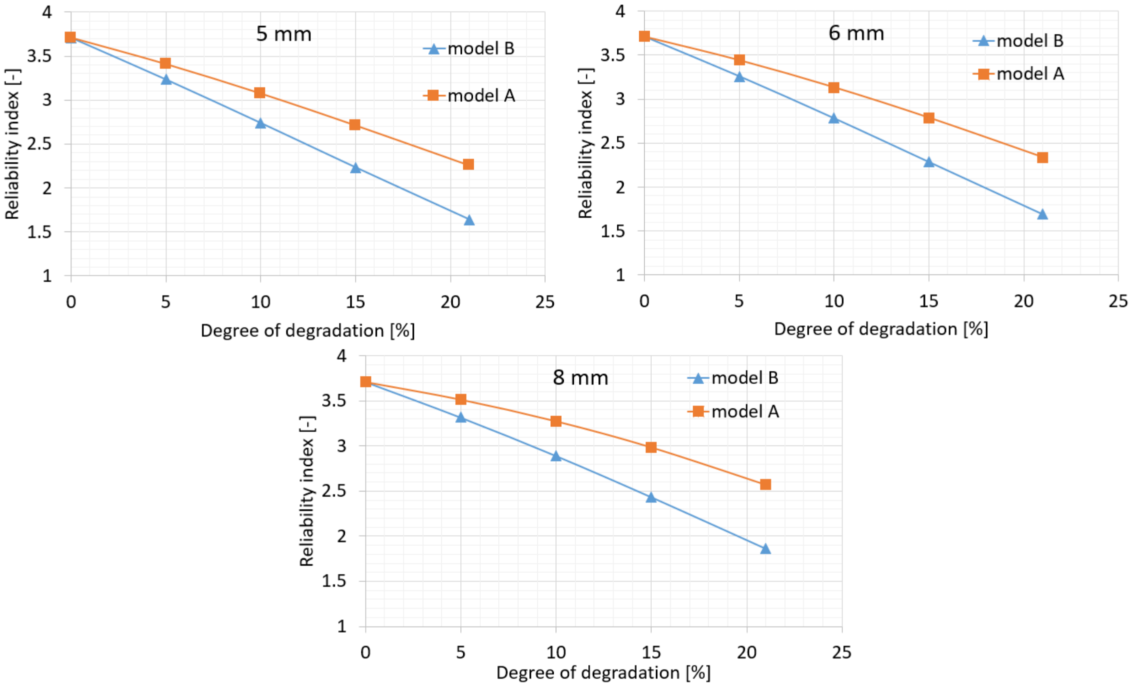

Figure 11.5. Reliability index values in function of DoD, t=5 mm (up), t=6 mm (mid) and t=8 mm (bottom).

One can notice that for all thicknesses, with the increase of DoD, the reliability level decreases. Additionally, for the higher values of DoD, the differences between model A and model B becomes significant. When considering the mechanical properties variations in the corrosion development, the Beta reliability level is significantly lower than the stiffened plate with a reduced thickness only. The differences between model A and model B are quite similar for each case of the stiffened plate. Nevertheless, for an 8 mm plate, the reliability index values are higher for the same DoD level than the thinner plates.

11.5.2. Influence of thickness uncertainty

The reliability analysis results presented in Section 11.5.1 are based on the thickness measurements related to stiffened plates corroded in laboratory conditions. Due to that, the thickness standard deviation is relatively high since plate were measured in many points. Additionally, in this case, the standard deviation is related to a particular Degree of Degradation. In normal ship exploitation conditions, such exact measurements are impossible. The corrosion measurements are reported during inspections, following specific time frames. Due to that, in practice, time-dependent corrosion degradation models are commonly used. This type of model could also be calibrated using data obtained from real measurements [295].

The equation to calculate the standard deviation of thickness depending on the corrosion depth value has been introduced in Equation 4.7, considering the measurements from ships. The comparison between standard deviations from the experiment and Equation 4.7 was presented in Figure 4.29.

The corrosion depth is modelled as a log-normal distribution [221]. Accordingly, the reliability limit state function is updated. The random variable of plate thickness is replaced as follows:

$$\tilde{t} = t_0 - \tilde{d} \tag{11.30}$$

where t_0 is the initial plate thickness.

The reliability analysis is carried out, and the differences for model B in the case of the standard deviation of thickness measurements based on the experimental investigations and in situ measurements are presented in Table 11.3.

Table 11.3. Reliability index as a function of thickness uncertainties.

DoD [%]	Initial thickness [mm]	Reliability index [-]		The difference [%]
		Experiments	Real measurements	
0	5	3.71	3.77	1.6
10	5	2.74	2.87	4.8
21	5	1.64	1.82	11.1
0	6	3.71	3.75	1.0
10	6	2.78	2.88	3.5
21	6	1.69	1.85	9.2

0	8	3.71	3.72	0.3
10	8	2.89	2.94	1.7
25	8	1.86	1.98	6.3

As it can be noticed, in the case of non-corroded plates, the thickness standard deviation is only slightly influencing the Beta reliability index. However, with corrosion development, the differences are growing. In the case of severely corroded plates (DoD = 21 %), the probability of failure significantly decreases for plates where the thickness is measured with lower uncertainties. Nevertheless, it could be observed that the differences are smaller for the higher initial thickness of the plate.

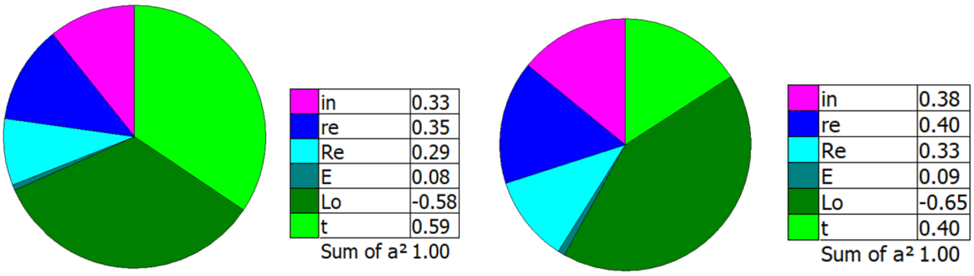

Figure 11.6. Sensitivity factors of reliability analysis, laboratory (left), and in situ (right) measurements.

The influence of the standard deviation of plate thickness on the reliability estimates is analysed. The sensitivity factors for specific analysis are presented in Figure 11.6, where the sensitivity factors for a 5 mm plate with 21 % of DoD are plotted in both cases. Figure 11.6 (left) shows the initial model where the sensitivity factor concerning the thickness (t) is equal to 0.59, and it is relatively high compared to other factors. Figure 11.6 (right) shows the model with a corrosion depth based on real measurements, and the sensitivity factor concerning the corrosion depth (t) is equal to 0.38. It could be concluded that with the decrease of the thickness standard deviation, the thickness related random variable becomes less critical in the reliability analysis. Based on the presented results, it may be noticed that the reliability analysis results are strongly dependent on the origin and level of uncertainties that are taken into account.

11.5.3. Probability of detection

In both models, as presented in sections 11.5.1 and 11.5.2, the resulting reliability index was based on the assumption that there are no inspections carried out. However, if the significant corrosion degradation exceeding the allowable level is found in normal conditions, such a structural component is replaced. In this way, only structural components that will be omitted during an inspection may fail.

To quantify the probability of corrosion degradation detection, the mathematical models as presented in [9] could be used. The conditional probability of detection consists of two terms. The first one is the probability of inspection (POI), and it is related to the probability that some structural components will be inspected. Typically, only selected areas are checked during the inspection, chosen as places most likely to have significant corrosion diminutions. Nevertheless, some severely corroded locations may be omitted. The second term is the unconditional probability of detection, which is related to the inspection itself. The corrosion degradation may be detected when it exceeds some threshold level d_{th}, which is related to testing equipment accuracy and environmental factors. The POD is given by:

$$POD(t) = P(d(t) \geq d_{th}) = 1 - F_{d(t)}(d_{th}) \tag{11.30}$$

When corrosion depth is given by log-normal distribution, the probability from Eqn 11.30 can be expressed as follows:

$$POD(t) = 0.5 - 0.5\,\mathrm{erf}\left(\frac{\ln(d_{th}) - \lambda_{d(t)}}{\varepsilon_{d(t)}\sqrt{2}}\right) \tag{11.31}$$

where $\lambda_{d(t)}$ and $\varepsilon_{d(t)}$ are defined as follows:

$$\lambda_{d(t)} = \ln\left(\frac{\bar{d}(t)}{\left(1 + \frac{\sigma_{d(t)}^2}{\bar{d}(t)^2}\right)^{0.5}}\right) \tag{11.32}$$

$$\varepsilon_{d(t)} = \sqrt{\ln\left(1 + \frac{\sigma_{d(t)}^2}{\bar{d}(t)^2}\right)} \tag{11.33}$$

where $\bar{d}(t)$ and $\sigma_{d(t)}$ are the mean value and standard deviation of the corrosion depth for a particular time, respectively.

Based on this, the conditional probability of detection results from the multiplication of POI and $POD(t)$ as:

$$POD_c(t) = POD(t) \cdot POI \tag{11.34}$$

The structural members that could be omitted during the inspection are those that cannot be detected. The conditional probability of non-detection is then:

$$PND_c(t) = 1 - POD_c(t) \tag{11.35}$$

The probability of failure of the structural component considering only the non-detected severely corroded plates is defined as:

$$P_{fND}(t) = P_f(t) \cdot PND_c(t) \tag{11.36}$$

where $P_f(t)$ is the probability of failure as calculated in reliability analysis.

Based on the probability of failure calculated by Eqn 11.36, the corrected Beta index can be calculated. To investigate the impact of the probability of detection on the resulting reliability index, the model from section 11.5.2 is analysed. The assumed probability of inspection is taken as 0.3, and the corrosion depth threshold value is taken as 0.8 mm.

The resulting $POD_c(t)$ curves are shown in Figure 11.7 for three different plate thicknesses. Since the curves are shown in the DoD domain, the time values are estimated using Eqn 4.6 based on the assumptions of the corrosion process as given in section 4.4.

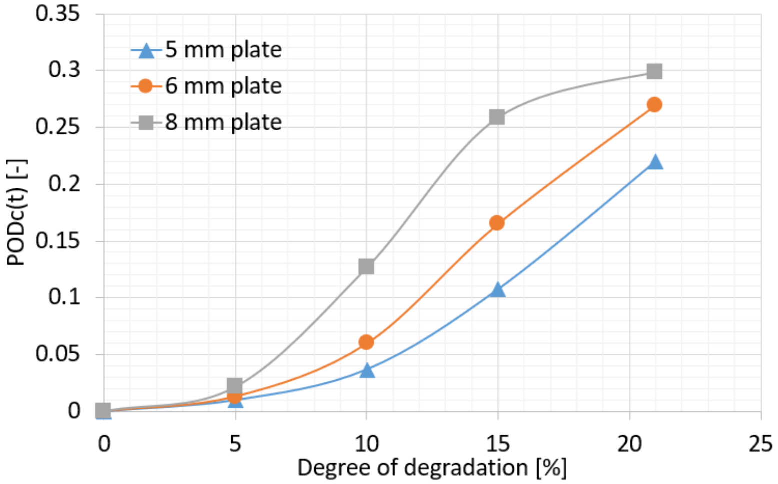

Figure 11.7. The conditional probability of detection.

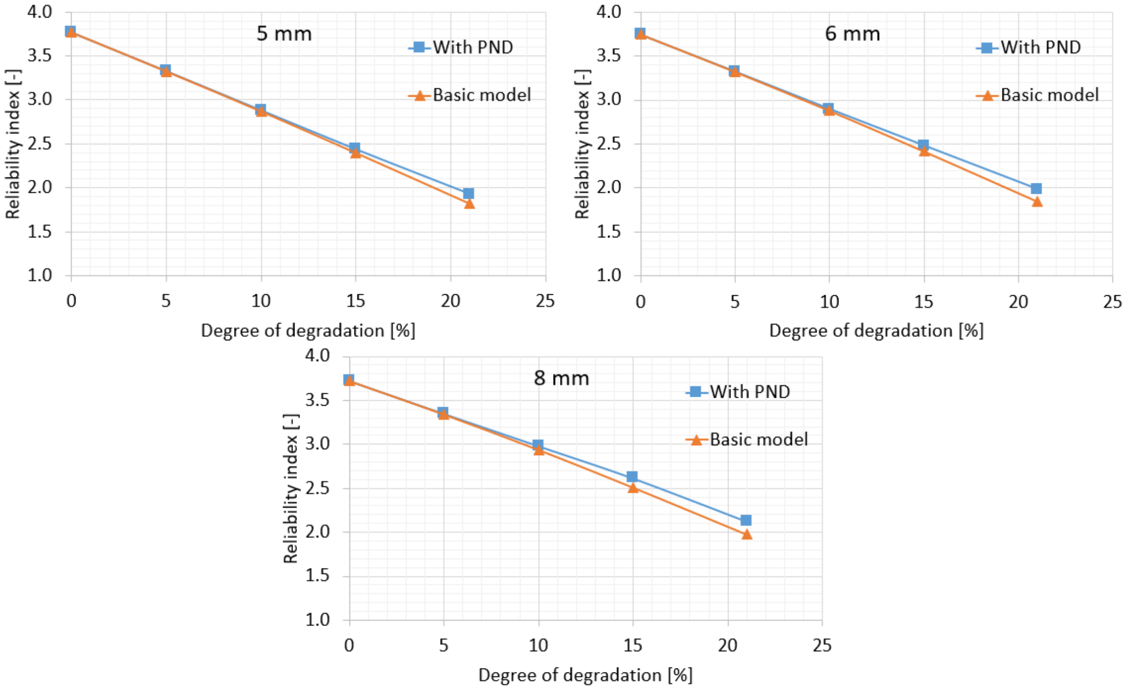

Figure 11.8. Reliability of corroded plates with and without consideration of corrosion detection.

As can be observed, the higher plate thickness leads to a higher probability of detection related to the corrosion detection threshold level. In the case of a 5 mm plate, the 25 %

degradation results in a 1.25 mm mean corrosion depth, wherein in the case of an 8 mm plate, the same degradation level leads to a 2 mm corrosion depth. In the first case, the relation between corrosion depth and threshold level is significantly lesser than the latter. The influence of the probability of detection on the resulting Beta index is presented in Figure 11.8.

As can be noticed, in all cases, the reliability increase is higher for high DoD levels. This is related to the probability of detection, which increases for higher DoD values, as presented in Figure 11.7. Additionally, the highest increase of the reliability index is observed in the case of an 8 mm plate.

11.5.4. Conclusions

The presented analysis showed a simplified approach to assess the ultimate strength and reliability of corroded stiffened plates with progressive uncertainties due to the nature of corrosion degradation. The approach presented here is fast and practical compared to the advanced non-linear FE analysis. When thickness reduction due to corrosion degradation is taken into account, and the subsequent decrease of mechanical properties are considered, the reliability index is significantly lower. In the second case, for severely corroded plates, the reliability index may even be 50% smaller than the intact plates: however, the reliability index reduction may be smaller for thicker plates.

Nevertheless, the outcome of the reliability assessment is highly sensitive to the initially defined random variables regarding their uncertainties. Two different uncertainty levels of plate thickness were investigated based on the laboratory measurements from the current Thesis and results of ship inspections. Different standard deviations of the corroded plate thickness led to quite different reliability estimates. In many cases, the initial uncertainty level is assumed, so further studies concerning the uncertainty qualification and confidence level are required.

Finally, when the probability of detecting corroded components during their inspection is taken into account, the reliability index is slightly higher than the reference model.

One also needs to note that the ultimate strength estimated by the FE method and experiment is lower compared to the CSR approach by approximately 9 % (see Section 9.1.5). Thus, the CSR results are non-conservative. A possible way to incorporate it into reliability analysis is to introduce the modelling uncertainty factor, in the form of a Gaussian random variable with a mean value equal to the ratio between ultimate strength values of FE analysis and CSR approach (similarly to the one developed in Section 5.1.7). The standard deviation of modelling uncertainty will be equal to the deviation of that ratio, respectively.

11.6. Reliability analysis of corroded hull girder based on experimentally estimated ultimate strength [P12]

The previous section presented the corrosion-dependent reliability related to a single stiffened plate element. In this section, the simple method to assess the ultimate strength of the entire hull girder based on the ultimate strength for an individual member is presented.

11.6.1. Time-dependent ultimate strength

Based on the experimental and numerical results, the ultimate time-dependent strength of stiffened plate has been derived. The specimens analysed in Section 6.6.2 could represent the stiffened plates from operating ships. However, in their basic dimensions, it will be rather to find the example. Nevertheless, the analysed stiffened plates will be geometrically similar to those operating in real ships. Notably, the 2 m long and 0.8 m wide stiffened plate together with the stiffener of 0.2 m height, with the thickness of 12 mm could be found in the deck of the tanker ship with the following main dimensions: length equal to 128 m, beam equal to 22.1 m and depth of 12.7 m. Thus, using dimensional theory, there is possible to estimate the ultimate strength of such a panel.

The analysis of the similarity between the model and real structure concerning the ship hull ultimate capacity was conducted in [201], and more information about the dimensional theory may be found in [296,297]. The scaling factors are as follows:

- the linear dimensions:

$$\frac{x}{x'}=\frac{y}{y'}=\frac{z}{z'}=\frac{l}{l'}=C_l \tag{11.37}$$

- stresses:

$$\frac{\sigma_x}{\sigma_x'}=\frac{\sigma_y}{\sigma_y'}=\frac{\tau_{xy}}{\tau_{xy}'}=\frac{\sigma}{\sigma'}=C_\sigma \tag{11.38}$$

- strains:

$$\frac{\varepsilon_x}{\varepsilon_x'}=\frac{\varepsilon_y}{\varepsilon_y'}=\frac{\gamma_{xy}}{\gamma_{xy}'}=\frac{\varepsilon}{\varepsilon'}=C_\varepsilon \tag{11.39}$$

- displacements:

$$\frac{u}{u'}=\frac{v}{v'}=\frac{w}{w'}=C_u \tag{11.40}$$

where l, σ, ε and u are the dimensions of real structure and $l', \sigma', \varepsilon'$, and u' are for the model respectively. The thickness term needs to be defined independently of the plane stress terms:

$$C_t=\frac{t}{t'} \tag{11.41}$$

The relations between the ship hull (real structure) and the model are as follows:

- length:

$$C_l=\frac{L_{structure}}{L_{model}}=\frac{B_{structure}}{B_{model}}=\frac{D_{structure}}{D_{model}}=2 \tag{11.42}$$

- thickness:

$$C_t=\frac{t_{stucture}}{t_{model}}=2 \tag{11.43}$$

- subjected force:

$$C_p=\frac{P_{real}}{P_{model}}=4 \tag{11.44}$$

- bending moment:

$$C_m = \frac{M_{structure}}{M_{model}} = C_p C_l = 8 \tag{11.45}$$

resulting in the same stresses in the model and real structure:

$$\sigma_{structure} = \sigma_{model} \frac{C_m}{C_l^2 C_t} = \sigma_{model} \tag{11.46}$$

Based on that, the ultimate stress is the same for the model and real structure.

Since the thickness scale is two and it is assumed that the corrosion depth follows the same time dependency in real structure and specimen, the degree of degradation (DoD) of the tanker ship model is:

$$t_{corroded} = t'_{corroded} \tag{11.47}$$

$$t = t_{netto} + t_{corroded} \tag{11.48}$$

$$DoD = \frac{t_{corroded}}{t} = \frac{t_{corroded}}{C_t t'} = \frac{DoD'}{C_t} \tag{11.49}$$

Since the stress scale is 1, the DoD-dependent ultimate-strength of the tanker ship is defined as:

$$\sigma_U(DoD) = \sigma_U\left(\frac{DoD'}{C_t}\right) = \sigma_U\left(\frac{DoD'}{2}\right) \tag{11.50}$$

The degree of degradation of the tanker ship plate is a function of the time derived from the corrosion degradation model presented in Section 4.2.8. The corrosion depth versus time is shown in Figure 4.7, where the coating life is not considered.

Based on that, the ultimate time-dependent strength of both model and tanker ship can be derived. The ultimate time-dependent strength of the tanker stiffened plate based on the experimental and numerical investigations is presented in Figure 9.46 (results for 6 mm stiffened plates). Thus, the ultimate strength is based on the regression curves presented there.

For the current analysis, the assumption is that the ultimate strength is equal to the initial member collapse strength (the collapse of the weakest stiffened plate in the cross-section, which initiates the progressive collapse). However, after the first stiffener plate collapse, the hull girder section still has some capacity [3], making the current assumption conservative.

The bottom and deck of the analysed tanker ship are made from high tensile steel with a yield stress of 315 MPa, and the Young modulus is 206 GPa.

11.6.2. Strength assessment

The deck section modulus of a real ship is $Z_d = 6.1\ m^3$ and the bottom section modulus is $Z_b = 10.9\ m^3$. Thus, the most critical in terms of ultimate strength will be the sagging condition and collapse of the deck panel. In the bottom panels, there are higher thicknesses to resist the local loads from external sea pressure.

The still water and wave-induced bending moments are estimated from the Common Structural Rules [5] in hogging and sagging condition, respectively, as follows:

$$M_{sw,h} = 324\,912\ kNm \tag{11.51}$$

$$M_{sw,s} = -228\,887\ kNm \tag{11.52}$$

$$M_{wv,h} = 423\,436\ kNm \tag{11.53}$$

$$M_{wv,s} = -488\,069\ kNm \tag{11.54}$$

In the Common Structural Rules [5], the ultimate strength limit state is formulated as:

$$\gamma_{sw} M_{sw} + \gamma_{wv} M_{wv} \leq \frac{M_U}{\gamma_R} \tag{11.55}$$

where $\mathrm{M_u}$ is the hull girder ultimate bending capacity and $\mathrm{\gamma_{sw}, \gamma_{wv}, \gamma_R}$ are the partial safety factors.

The ultimate capacity is estimated based on the experimental or numerical results and dimensional theory as:

$$M_u = \left(\frac{\sigma_U}{\sigma_Y}\right)_{experimental/FEM} Z_{d/b} Re \tag{11.56}$$

where $(\sigma_U/\sigma_Y)_{experimental/FEM}$ is the normalized ultimate capacity based on the experimental or numerical results, $Z_{d/b}$ is the section modulus of deck or bottom, and Re is the yield strength of a material.

11.6.3. Reliability analysis

To analyse the impact of the uncertainty in the ultimate strength assessment due to various governing parameters, the FORM [281] method is used here employing its algorithm.

The term formulated deterministically in Eqn 11.55 can be transformed into a limit state function:

$$\mathrm{g} = \widetilde{\mathrm{x_U}}\widetilde{\mathrm{M_U}} - \widetilde{\mathrm{x_{sw}}}\widetilde{\mathrm{M_{sw}}} - \widetilde{\mathrm{x_w}}\widetilde{\mathrm{x_s}}\widetilde{\mathrm{M_{wv}}} \tag{11.57}$$

where $\widetilde{\mathrm{M_U}}, \widetilde{\mathrm{M_{sw}}}, \widetilde{\mathrm{M_{wv}}}$ are the bending moments described as random variables, $\widetilde{\mathrm{x_U}}$ is the model uncertainty related to the ultimate strength, $\widetilde{\mathrm{x_{sw}}}$ is the uncertainty in the model of predicting the still water bending moment, $\widetilde{\mathrm{x_w}}$ is the uncertainty in the wave-induced bending moment due to the linear seakeeping analysis and $\widetilde{\mathrm{x_s}}$ takes into account nonlinearities in the sagging loading condition.

The statistical descriptors of the uncertainty coefficients presented in Eqn (21) are assumed to follow the Normal distribution function [298,299]:

$$\widetilde{x_U} \sim N\{1.1; 0.1\} \tag{11.58}$$

$$\widetilde{x_{sw}} \sim N\{1.0; 0.1\} \tag{11.59}$$

$$\widetilde{x_w} \sim N\{1.0; 0.1\} \tag{11.60}$$

$$\widetilde{x_s} \sim N\,\{1.0; 0.1\} \tag{11.61}$$

The First Order Reliability Method, FORM [281], is used to estimate the reliability index of the ultimate limit state. Since the ultimate capacity depends on time – the reliability index is also time-dependent.

The still water bending moment can be fitted to the Normal distribution as stipulated in [300], where the statistical descriptors are defined by regression equations based on about 2000 data points as a function of the length and the dead-weight ratio (W = DWT/Full Load). The estimated coefficients are shown in Table 11.4.

Table 11.4. Statistical descriptors of Still water bending moment [300].

	a_o	a_1	a_2
$Mean(M_{sw,max})=a_o+a_1.W+a_2.L$	114.7	-105.6	-0.154
$StDev(M_{sw,max})=a_o+a_1.W+a_2.L$	17.4	-7	0.035

The mean value and standard deviation of still water bending moment are estimated as:

$$\mathrm{Mean}(M_{sw}) = \frac{\mathrm{Mean}(M_{sw,max})M_{sw,CSR}}{100} \tag{11.62}$$

$$\mathrm{StDev}(M_{sw}) = \frac{\mathrm{StDev}(M_{sw,max})M_{sw,CSR}}{100} \tag{11.63}$$

where the $M_{sw,CSR}$ are the still water bending moments calculated with the formulas provided in Common Structural Rules [5].

The dead-weight ratio of the analysed tanker ship is 0.82 in the full-load condition, 0.61 in the partial load condition, and 0.41 in the ballast condition.

The still water bending moments for the analysed tanker ship under different loading conditions are shown in Table 11.5. The presented results concern moment values in sagging conditions since this case will be critical. The absolute values are presented since the sagging moment has a negative value.

Table 11.5. Still water bending moments.

Loading condition	$\mathrm{Mean}(M_{sw})$	$\mathrm{StDev}(M_{sw})$
Full-load	19 217	36 942
Partial	69 975	40 307
Ballast	118 316	43 512

The distribution of the extreme values of the wave-induced bending moment at a random point of time, over a specified period, can be represented as a Gumbel distribution as proposed by Guedes Soares et al. [301], considering that the wave-induced bending moment given by the Common Structural Rules [5] may be modelled as a Weibull distribution with a probability of exceedance of 10^{-8}.

The Gumbel distribution, for the extreme values of the vertical wave-induced bending moment, over the reference period T_r is derived based on the shape, $h$and scale, q factors of the Weibull distribution function as [301]:

$$\alpha_m = q(\ln(n))^h \tag{11.64}$$

$$\beta_m = \frac{q}{h}(\ln(n))^{\frac{1-h}{h}} \tag{11.65}$$

where α_m and β_m are the parameters of the Gumbel distribution, n is the mean number of load cycles expected over the reference period T_r for a given mean value period T_w. It is assumed that $T_w = 8\,sec.$ and T_w is equal to 1 year.

The number of load cycles n is calculated as:

$$n = \frac{p_i \cdot T_r \cdot 365 \cdot 24 \cdot 3600}{T_w} \tag{11.66}$$

where p_i is part-time in which the ship is in seagoing conditions.

The partial time factors and extreme values of the vertical wave-induced bending moment in hogging are shown in Table 11.6. Also, in this case, the absolute values are presented.

Table 11.6. Statistical descriptors wave-induced bending moment $M_{wv,h}$.

Loading condition	$p_i\,[-]$	$\alpha_m(M_{wv,s})$	$\beta_m(M_{wv,s})$
Full-load	0.4	586 985	19 840
Partial	0.1	523 393	20 062
Ballast	0.4	586 985	19 840
Harbour	0.1	-	-

The CoV of the ultimate capacity is based on the deviation between exact points and regression curves presented in Figure 9.46. It is equal to 0.0203 for the experimental one and 0.0054 for the FEM estimates. Additionally, due to the differences between experimental and FEM results, the bias factor is introduced:

$$x_{FEM} = \frac{\sigma_{U,FEM}}{\sigma_{U,exp}} \tag{11.67}$$

The bias factor is modelled as a random variable following the Normal probability function, $\widetilde{x_{FEM}} \sim \mathrm{N}\{0.995; 0.0148\}$Since both experimentally and numerically obtained capacities are fitted to the Normal probability function. The x_{FEM} is assumed constant for different corrosion degradation levels, and the mean value of the distribution is calculated as the mean of the fractions $\sigma_{U,FEM}/\sigma_{U,exp}$ for different time of exploitation. The standard deviation is calculated as the square root of the sum of squares of differences between the mean value and particular fractions. The limit state function for the ultimate capacity based on the FEM results is:

$$g = \widetilde{x_{FEM}}\widetilde{x_U}\widetilde{M_U} - \widetilde{x_{sw}}\widetilde{M_{sw}} - \widetilde{x_w}\widetilde{x_s}\widetilde{M_{wv}} \quad (11.68)$$

All random variables are considered here as non-correlated ones. When the reliability analysis is performed, the estimated reliability index needs to be compared with the target one. The target level is related to the failure cause and, according to DnV [294], is equal to $\beta = 3.09$ $(P_f = 10^{-3})$ for the less serious and $\beta = 3.71$ $(P_f = 10^{-4})$ for serious consequences of failure. The target reliability level is considered here as $\beta_{target} = 3.71$.

The required Beta index is based on the sum of probabilities of failure for different loading conditions:

$$\beta = -\Phi^{-1}(\Sigma P_{fi}) \quad (11.69)$$

11.6.4. Results and Discussion

For the analysed tanker ship, a more severe loading is the sagging case due to the still water bending moment's contribution compared to the hogging condition. The calculations performed for the sagging condition showed that the probability of failure is significantly smaller compared to the hogging condition.

The reliability safety indices for different load cases and the total Beta index are shown in Table 11.7.

Table 11.7. Reliability safety indices for different load cases, experiment.

Time (years)	Load Beta index [-]			Beta index [-]
	Full load	Ballast load	Partial load	
0	5.117	4.369	5.244	4.36
5	4.393	3.608	4.527	3.59
10	3.780	2.973	3.916	2.95
15	3.288	2.470	3.424	2.43
20	2.893	2.070	3.029	2.01
25	2.547	1.722	2.682	1.66

The reliability safety index results versus time for the ultimate capacity based on the experimental results are presented in Figure 11.9.

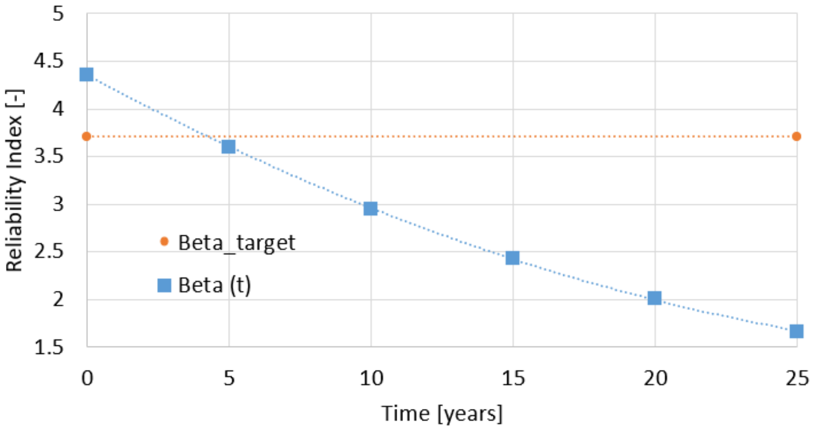

Figure 11.9. Reliability safety index of an analysed tanker ship based on the experimental results.

As it can be noticed, after four years of exploitation, without accounting for the coating life, the required reliability index is not satisfied. After this time, some maintenance action needs to be done. The most critical condition is the ballast one, and as it can be noticed, full and partial load conditions have almost no influence on the resulting reliability safety index.

Figure 11.10 shows the sensitivity analysis concerning the influence of different random variables. As it can be noticed, the most influencing variable is the model uncertainty of the ultimate capacity.

Figure 11.10. Sensitivity factors [-].

The reliability safety indices obtained based on the FEM are shown in Table 11.8. Very similar to the experimental results, the most critical condition which governs the resulting Beta index is the ballast one.

Table 11.8. Reliability safety indices for different load cases, FEM.

Time (years)	Load Beta index [-]			Beta index [-]
	Full load	Ballast load	Partial load	
0	5.168	4.389	5.285	4.38
5	4.548	3.722	4.677	3.71
10	4.021	3.160	4.162	3.14
15	3.594	2.708	3.746	2.68
20	3.247	2.343	3.410	2.31

25	2.939	2.016	3.112	1.97

The results of the Beta index versus time for the ultimate capacity based on the FEM results are presented in Figure 11.11.

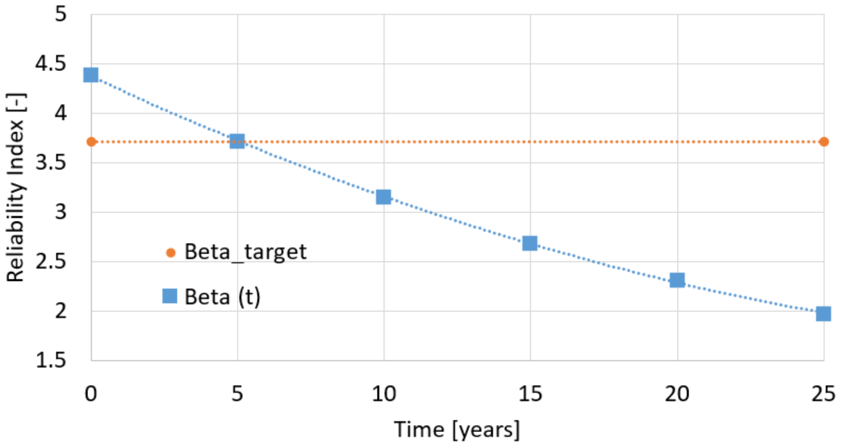

Figure 11.11. Reliability safety index of an analysed tanker ship based on the numerical results.

The service time, where the Beta index crosses the target value, is very similar to the results obtained based on the experiment, and it is about eight years.

Figure 11.12 shows the sensitivity analysis concerning reliability based on the FEM. Similarly to the experimental data, the most influencing parameters are the model uncertainty of the ultimate capacity and FEM calculations.

Figure 11.12. Sensitivity factors [-].

11.6.5. Conclusions

The results show that it is possible to estimate the ship cross-section's ultimate strength based on the experimental results and dimensional theory. Additional modelling uncertainties need to be considered to estimate the reliability safety index considering the FE model results. The reliability safety index was calculated as a function of the time, and the assumed target reliability safety index was crossed after around four years. The study revealed that the reliability analysis conducted in sagging condition, considering only the ballast load case for the present oil tanker, would give satisfying results.

The main limitation of this methodology is the assumption that the ultimate capacity is governed by the loss of capacity of the weakest stiffened plate. The presented methodology is flexible and can be furtherly used in more complex systems, e.g. ultimate capacity can be calculated using the Smith approach.

12. CONCLUSIONS AND FUTURE WORKS

The presented work investigated the impact of corrosion on the structural behaviour of small-scale specimens subjected to tensile loading and compressed stiffened plates. Both experimental and numerical investigations were performed.

The study significantly contributes to the knowledge regarding ship structural behaviour, especially when subjected to corrosion degradation. In particular, some most novel aspects are highlighted:

- the experimental set-up regarding the accelerated corrosion tests of large-scale structural elements has been developed especially for this study;
- the study was devoted to the corrosion of the ship's structural elements within the degradation level up to 20%, whereas previous works were concerned with rather high levels of degradation;
- the constitutive laws for changes in mechanical properties were developed, in terms of marine immersed corrosion degradation;
- the random field theory has been adopted for modelling of the corroded structural elements in different scales;
- a numerical model with regards to corroded stiffened plates was developed that accounted for a non-uniform loss of thickness with the subsequent changes of mechanical properties;
- the simple formulation that allows for fast estimation of the residual capacity of the corroded stiffened plates was developed;
- the reliability formulations for both stiffened plates and ship hull girder have been developed.

The most generic conclusion from the thesis is that the structural behaviour of corroded structural elements may be accurately captured when nonuniform corrosion distribution and changes in mechanical properties are considered simultaneously. The model that accounts only for mean thickness reduction is insufficient. It needs to be highlighted that such a model is commonly used in engineering practice, especially when it comes to structural rules issued by Classification Societies. Such a model could lead to significant overestimations in residual capacity, even in the degradation levels up to 20%, typically allowed during exploitation. Thus, the Thesis results could trigger the changes in rules that will result in safer structures.

In terms of changes in mechanical properties, it is observed that it is hard to develop some more generic constitutive laws. Based on different studies, it is evident that the decrease of mechanical properties will vary within the corrosion type, corrosion medium, etc. Further, the mechanical properties are subjected to significant scatter even in non-corroded conditions, and other possible factors could also contribute. Still, more experimental data will be needed to derive more general conclusions.

The random field modelling revealed to be an excellent tool to simulate the actual fields of corrosion. It was observed in both small-scale specimens as well as large-scale specimens. This is especially important that this technique allows for generating many cases without time-consuming and difficult corrosion tests. Further, by generating many cases, some more sophisticated studies showing uncertainty levels could also be conducted. Nevertheless, still, some more experimental data will be needed to calibrate the corrosion fields parameters properly.

The FE modelling revealed a very good tool in simulating the structural behaviour of corroded structural elements, such as stiffened plates. However, to achieve good results, one needs to account for many important issues, such as proper modelling of boundary conditions, implementing initial imperfections, selecting the element size, mapping the actual thickness distribution, accounting for changes in mechanical properties. Nevertheless, still, some differences with regards to the experiment were visible. Thus, implementation of other effects, such as eccentricity of the applied load, could be beneficial. The FE computations could also simulate accurately the behaviour of small-scale corroded coupons subjected to tensile testing. However, in such a case, the explicit dynamic solver needs to be used.

Based on the achieved results, the following directions of studies are planned to be carried out:

- impact of other degradation effects (e.g. locked cracks) into the behaviour of compressed structural elements will be investigated, and the simultaneous effect of corrosion degradation will be accounted for;
- more sophisticated reliability models will be developed that will be based on the results presented in the thesis;
- the studies looking for other techniques that could lead to the capturing of real corrosion fields of plates avoiding non-precise ultrasonic measurements will be carried out;
- the FE model of the corroded stiffened plate will be furtherly developed, accounting for different effects, such as change of local position shell midplane or accounting for uncertainties in mechanical properties also in the corroded state;
- the numerical studies of small-scale tensile specimens with random fields of corrosion will be continued with more variables considered (e.g. broader scope of initial thickness), which will lead to more general constitutive laws regarding changes in mechanical properties.

13. PUBLISHED WORKS

[P1] Woloszyk K, Garbatov Y. Accelerated large scale test set-up design in natural corrosion marine environment. In: Guedes Soares C, Santos TA, editors. Prog. Marit. Technol. Eng., CRC Press; 2020.

[P2] Woloszyk K, Garbatov Y. Uncertainty assessment of ultimate strength of corroded stiffened plates subjected to maintenance. In: Georgiev P, Guedes Soares C, editors. Sustain. Dev. Innov. Mar. Technol., CRC Press; 2019, p. 429–36.

[P3] Woloszyk K, Garbatov Y. FE analysis of support-specimen interaction of compressive experimental test. In: Georgiev P, Guedes Soares C, editors. Sustain. Dev. Innov. Mar. Technol., CRC Press; 2019, p. 423–8.

[P4] Woloszyk K, Garbatov Y, Kowalski J, Samson L. Numerical and experimental study on effect of boundary conditions during testing of stiffened plates subjected to compressive loads. Eng Struct 2021;235:112027.

[P5] Woloszyk K, Garbatov Y, Kowalski J, Samson L. Experimental and numerical investigations of ultimate strength of imperfect stiffened plates of different slenderness. Polish Marit Res 2020;27:120–9.

[P6] Woloszyk K, Bielski PM, Garbatov Y, Mikulski T. Photogrammetry image-based approach for imperfect structure modelling and FE analysis. Ocean Eng 2021;223:108665.

[P7] Woloszyk K, Garbatov Y. An enhanced method in predicting tensile behaviour of corroded thick steel plate specimens by using random field approach. Ocean Eng 2020;213:107803.

[P8] Woloszyk K, Garbatov Y. Random field modelling of mechanical behaviour of corroded thin steel plate specimens. Eng Struct 2020;212:110544.

[P9] Woloszyk K, Garbatov Y. Ultimate strength of stiffened plates subjected to compressive load and spatially distributed mechanical properties. Proceedings MARTECH 2020.

[P10] Woloszyk K, Garbatov Y. Design of experiments approach for ultimate strength assessment of corroded stiffened plates. Proc. 14th Int. Conf. Met. Struct., 2021, p. Accepted.

[P11] Woloszyk K, Garbatov Y. Reliability of corroded stiffened plate subjected to uniaxial compressive loading. Int J Marit Eng 2020;162 (A4):421–30.

[P12] Woloszyk K, Garbatov Y. Structural Reliability Assessment of Corroded Tanker Ship Based on Experimentally Estimated Ultimate Strength. Polish Marit Res 2019;26:47–54.

REFERENCES

[1] Okumoto Y, Takeda Y, Mano M, Okada T. Design of Ship Hull Structures. Berlin, Heidelberg: Springer Berlin Heidelberg; 2009.

[2] Interim Report of Committee on Large Container Ship Safety. Japan: 2013.

[3] Yao T, Fujikubo M. Buckling and ultimate strength of ship and ship-like floating structures. Elsevier; 2016.

[4] Ahmer Wadee M. Nonlinear Mathematics in Structural Engineering. Math Today 2007:104–6.

[5] International Association of Classification Societies. Common Structural Rules (BC & OT). 2018.

[6] United Nations Conference on Trade and Development. Review of maritime transport 2019. 2019.

[7] INTERCARGO. Bulk Carrier Casualty Report. Years 2010 to 2019 and trends. 2020.

[8] Zayed A, Garbatov Y, Guedes Soares C. Corrosion degradation of ship hull steel plates accounting for local environmental conditions. Ocean Eng 2018;163:299–306.

[9] Zayed A, Garbatov Y, Guedes Soares C. Non-destructive Corrosion Inspection Modeling of Tanker Structures. Vol. 2 Struct. Saf. Reliab., ASMEDC; 2008, p. 465–76.

[10] Flashback history: Tanker Prestige sinking (Video) 2015. https://www.vesselfinder.com/news/4776-Flashback-history-Tanker-Prestige-sinking-Video (accessed October 1, 2020).

[11] Bayatfar A, Kim BJ, Chen CP, Wang D, Boulares J, Gordo JM, et al. Report of Committee III.1: Ultimate strength. In: Guedes Soares C, Garbatov Y, editors. Ships Offshore Struct. XIX, London: CRC Press; 2015.

[12] Caldwell J. Ultimate longitudinal strength. Trans RINA 1965;107:411–30.

[13] Paik JK, Mansour AE. A simple formulation for predicting the ultimate strength of ships. J Mar Sci Technol 1995;1:52–62.

[14] Paik JK, Kim DK, Park DH, Kim HB, Mansour AE, Caldwell JB. Modified Paik–Mansour formula for ultimate strength calculations of ship hulls. Ships Offshore Struct 2013;8:245–60.

[15] Smith S. Influence of Local Compressive Failure on Ultimate Longitudinal Strength of a Ship's Hull. Proc Int Sym Pract Des Shipbuild 1977:73–9.

[16] Gordo JM, Guedes Soares C. Approximate method to evaluate the hull girder collapse strength. Mar Struct 1996;9:449–70.

[17] Yao T, Plamenn M, Nikolov I. Progressive Collapse Analysis of a Ship's Hull under Longitudinal Bending 1991.

[18] Yao T, Fujikubo M, Kondo K, Nagahama S. Progressive collapse behaviour of double hull tanker under longitudinal bending. Proc 4th int offshore polar Eng. Conf., Osaka, Japan: 1994, p. 570–7.

[19] Yao T, Nikolov P. Ultimate longitudinal strength of a bulk carrier. Proc 3rd int offshore polar Eng. Conf. vol. IV, 1993, p. 497–504.

[20] Benson S, Downes J, Dow RS. Compartment level progressive collapse analysis of lightweight ship structures. Mar Struct 2013;31:44–62.

[21] Benson S. Progressive collapse assessment of lightweight ship structures 2011.

[22] Li C, Ren H, Zhao Z, Zhao X, Zeng J, Xu D. An Approximate Calculation Approach for Ultimate Strength of Ship Hull Girder. Vol. 2B Struct. Saf. Reliab., ASME; 2013, p. V02BT02A018.

[23] Kutt LM, Piaszczyk CM, Chen Y. Evaluation of the longitudinal ultimate strength of various ship hull configurations. Soc Nav Archit Mar Eng 1985;93:21 p.

[24] Cook R, Malkus D, Plesha M, Witt R. Concepts and applications of finite element analysis. Wiley; 1974.

[25] Czujko J, Bayatfar A, Smith M, Xu M, Wang D, Lützen M, et al. Committee III.1: Ultimate Strength. In: Kaminski M, Rigo P, editors. Proc. 20th Int. Sh. Offshore Struct. Congr. (ISSC 2018) Vol. 1, IOP Press; 2018, p. 335–439.

[26] Kmiecik M, Guedes Soares C. Response surface approach to the probability distribution of the strength of compressed plates. Mar Struct 2002;15:139–56.

[27] Kmiecik M. Usefulness of the yield line theory in design of ship plating. Mar Struct 1995;8:67–79.

[28] Guedes Soares C, Kmiecik M. Simulation of the ultimate compressive strength of unstiffened rectangular plates. Mar Struct 1993;6:553–69.

[29] Tekgoz M, Garbatov Y, Guedes Soares C. Finite element modelling of the ultimate strength of stiffened plates with residual stresses. Anal. Des. Mar. Struct., CRC Press; 2013, p. 309–17.

[30] Taczala M, Jastrzębski T. Analysis of ultimate capacity of ship hulls with transversally stiffened plates. Arch Civ Eng 1999;45:357–68.

[31] Taczala M. Approximate method for evaluation of stress-strain relationship for stiffened panel subject to tension, compression and shear employing the finite element approach. Proc. MARSTRUCT 2009, 2nd Int. Conf. Mar. Struct. Des. Mar. Struct., 2009, p. 155–61.

[32] Taczala M. Methods for analysis of the ultimate capacity and structural response of stiffened panels. Mar. Technol. Eng. Vol. 2, 1st Int. Conf. Marit. Technol. Eng. MARTECH 2011, Lisbon, Portugal: Taylor & Francis Group,; 2011, p. 993–1109.

[33] Tanaka S, Yanagihara D, Yasuoka A, Harada M, Okazawa S, Fujikubo M, et al. Evaluation of ultimate strength of stiffened panels under longitudinal thrust. Mar Struct 2014;36:21–50.

[34] Yukio U, Rashed SMH. The idealized structural unit method and its application to deep girder structures. Comput Struct 1984;18:277–93.

[35] Paik JK, Thayamballi AK, Che JS. Ultimate Strength of Ship Hulls under Combined Vertical Bending, Horizontal Bending, and Shearing Forces. Trans Nav Archit Mar Eng 1996;104:31–59.

[36] Fujikubo M, Kaeding P, Yao T. ISUM Rectangular Plate Element with New Lateral Shape Functions (1st Report) - Longitudinal and Transverse Thrust. J Soc Nav Archit Japan

2000;187:209–19.

[37] Fujikubo M, Kaeding P. ISUM Rectangular Plate Element with New Lateral Shape Functions (2nd Report) - Stiffened Plates under Biaxial Thrust. J Soc Nav Archit Japan 2000;2000:479–87.

[38] Paik JK, Thayamballi AK. A concise introduction to the idealized structural unit method for nonlinear analysis of large plated structures and its application. Thin-Walled Struct 2003;41:329–55.

[39] Pei Z, Iijima K, Fujikubo M, Tanaka S, Okazawa S, Yao T. Simulation on progressive collapse behaviour of whole ship model under extreme waves using idealized structural unit method. Mar Struct 2015;40:104–33.

[40] Kell CO. Investigation of structural characteristics of destroyers Preston and Bruce, part 1 - description. Trans SNAME 1931;39:35–64.

[41] Lang DW, Warren WG. Structural strength investigations on the destroyer Albuera. Trans Inst Nav Arch 1952;94:243–86.

[42] Becker H, Goldman R, Pozerycki J. Compressive strength of ship hull girders Part I: Unstiffened plates. Ship Structure Committee, SSC-217; 1970.

[43] Valsgård S. Numerical design prediction of the capacity of plates in biaxial in-plane compression. Comput Struct 1980;12:729–39.

[44] Faulkner D. A Review of Effective Plating for Use in the Analysis of Stiffened Plating in Bending and Compression. J Sh Res 1975;19:1–17.

[45] Smith C. Compressive strength of welded steel ship grillages. Trans RINA 1975;118:325–59.

[46] Faulkner D. Compression tests on welded eccentrically stiffened plate panels. In: Dowling P, editor. Steel plated Struct., London: Crosby Lockwood Staples; 1977, p. 581–617.

[47] Horne M, Narayanan R. Ultimate capacity of stiffened plates used in girders. Proc Inst Civ Eng 1976;61:253–80.

[48] Dorman A, Dwight J. Tests on stiffened compression panels and plate panels. Int. Conf. Steel Box Girder Bridg., London: Institutes of Civil Engineers; 1973, p. 63–75.

[49] Gordo JM, Guedes Soares C. Compressive tests on short continuous panels. Mar Struct 2008;21:113–37.

[50] Gordo JM, Guedes Soares C. Compressive tests on stiffened panels of intermediate slenderness. Thin-Walled Struct 2011;49:782–94.

[51] Manuel Gordo J, Guedes Soares C. Compressive Tests on Long Continuous Stiffened Panels. J Offshore Mech Arct Eng 2012;134.

[52] Xu MC, Guedes Soares C. Experimental study on the collapse strength of wide stiffened panels. Mar Struct 2013;30:33–62.

[53] Kwon YB, Park HS. Compression tests of longitudinally stiffened plates undergoing distortional buckling. J Constr Steel Res 2011;67:1212–24.

[54] Choi BH, Hwang M, Yoon T, Yoo CH. Experimental study of inelastic buckling strength and stiffness requirements for longitudinally stiffened panels. Eng Struct 2009;31:1141–

53.

[55] Manco MR, Vaz MA, Cyrino JCR, Ramos NM, Liang DA. Experimental and numerical study of uniaxially compressed stiffened plates with different plating thickness. Thin-Walled Struct 2019;145:106422.

[56] Paik JK, Lee DH, Noh SH, Park DK, Ringsberg JW. Full-scale collapse testing of a steel stiffened plate structure under cyclic axial-compressive loading. Structures 2020;26:996–1009.

[57] Dowling P, Chatterjee S, Frieze PA, Moolani FM. Experimental and predicted collapse bahaviour of rectangular steel box girders. Int. Conf. steel box girder Bridg., London: Institutes of Civil Engineers; 1973, p. 77–94.

[58] Gordo JM, Guedes Soares C. Experimental evaluation of the ultimate bending moment of a box girder. Mar Syst Ocean Technol 2004;1:1–4.

[59] Gordo JM, Guedes Soares C. Experimental evaluation of the behaviour of a mild steel box girder under bending moment. Ships Offshore Struct 2008;3:347–58.

[60] Gordo JM, Guedes Soares C. Tests on ultimate strength of hull box girders made of high tensile steel. Mar Struct 2009;22:770–90.

[61] Gordo JM, Guedes Soares C. Experimental analysis of the effect of frame spacing variation on the ultimate bending moment of box girders. Mar Struct 2014;37:111–34.

[62] Yao T, Fujikubo M, Yanagihara D, Fujii I. Collapse test on 1/10-scale hull girder model of chip carrier in sagging. Proc 13th Int. offshore polar Eng. Conf., Honolulu, Hawaii, USA: 2003, p. 376–83.

[63] Wang J, S Zang. Ultimate Strength Experimental Research for Longitudinal Box Girders Module Model. Shipbuild China 2011;52:47–54.

[64] Gui-Jie S, De-Yu W. Ultimate strength model experiment regarding a container ship's hull structures. Ships Offshore Struct 2012;7:165–84.

[65] Wang C, Wu J, Wang D. Experimental and numerical investigations on the ultimate longitudinal strength of an ultra large container ship. Ocean Eng 2019;192:106546.

[66] Sun H-H, Guedes Soares C. An experimental study of ultimate torsional strength of a ship-type hull girder with a large deck opening. Mar Struct 2003;16:51–67.

[67] Gordo JM, Guedes Soares C. Approximate Load Shortening Curves for Stiffened Plates Under Uniaxial Compression. Proc Integr Offshore Struct - 5 1993:189–211.

[68] Ohtsubo H, Sumi Y. Report of special task committee VI.2-Ultimate hull girder strength. Proc. 14th Int. Sh. Offshore Struct. Congr., Elsevier; 2000.

[69] Hansen AM. Strength of midship sections. Mar Struct 1996;9:471–94.

[70] Dwight J, Little G. Stiffened steel compression flanges-a simpler approach. Struct Eng 1976.

[71] Dwight J, Ratcliffe A. The strength of thin plates in compression. SSIDA Symp. Thin-Walled Struct., 1967.

[72] Deng D, Liang W, Murakawa H. Determination of welding deformation in fillet-welded joint by means of numerical simulation and comparison with experimental measurements. J

Mater Process Technol 2007;183:219–25.

[73] Gannon L, Liu Y, Pegg N, Smith MJ. Effect of welding-induced residual stress and distortion on ship hull girder ultimate strength. Mar Struct 2012;28:25–49.

[74] Khan I, Zhang S. Effects of welding-induced residual stress on ultimate strength of plates and stiffened panels. Ships Offshore Struct 2011;6:297–309.

[75] Gannon L, Liu Y, Pegg N, Smith MJ. Nonlinear collapse analysis of stiffened plates considering welding-induced residual stress and distortion. Ships Offshore Struct 2016;11:228–44.

[76] Gannon L, Liu Y, Pegg N, Smith MJ. Effect of three-dimensional welding-induced residual stress and distortion fields on strength and behaviour of flat-bar stiffened panels. Ships Offshore Struct 2013;8:565–78.

[77] IACS. Common Structural Rules for Bulk Carriers. 2006.

[78] Chen B-Q, Guedes Soares C. A Simplified Model for the Effect of Weld-Induced Residual Stresses on the Axial Ultimate Strength of Stiffened Plates. J Mar Sci Appl 2018;17:57–67.

[79] Yi MS, Hyun CM, Paik JK. An empirical formulation for predicting welding-induced biaxial compressive residual stresses on steel stiffened plate structures and its application to thermal plate buckling prevention. Ships Offshore Struct 2019;14:18–33.

[80] Rodrigues LAS, Loayza L CR, Borges DJA, Baia PEC, Freitas EN, Braga EM. Welding procedures influence analysis on the residual stress distribution and distortion of stiffened panels welded via robotized FCAW. Thin-Walled Struct 2019;141:175–83.

[81] Smith MJ. Defence R&D Canada – Atlantic Ultimate strength assessment of naval and commercial ships 2008.

[82] Faulkner D. A Review of Effective Plating for Use in the Analysis of Stiffened Plating in Bending and Compression. J Sh Res 1975;19:1–17.

[83] Tall L, Rao N. Residual stresses in welded plates. Weld J 1961.

[84] Yi MS, Noh SH, Lee DH, Seo DH, Paik JK. Direct measurements, numerical predictions and simple formula estimations of welding-induced biaxial residual stresses in a full-scale steel stiffened plate structure. Structures 2021;29:2094–105.

[85] Tekgoz M, Garbatov Y, Guedes Soares C. Finite element modelling of the ultimate strength of stiffened plates with residual stresses. Anal. Des. Mar. Struct., CRC Press; 2013, p. 309–17.

[86] Tekgoz M, Garbatov Y, Guedes Soares C. Ultimate Strength Assessment of a Stiffened Plate Accounting for Welding Sequences. Proc. 11th Int. Symp. Pract. Des. Ships other Float. Struct. (PRADS 2013), 2013, p. 1089–95.

[87] Tekgoz M, Garbatov Y. Ultimate strength of a plate accounting for shakedown effect and corrosion degradation. Dev. Marit. Transp. Exploit. Sea Resour., CRC Press; 2013, p. 395–403.

[88] Kmiecik M, Jastrzębski T, Kużniar J. Statistics of ship plating distortions. Mar Struct 1995;8:119–32.

[89] Urbański T, Taczała M. Prediction of a transverse shrinkage of butt welded joints in shipyard conditions using the design of experimental approach. Int J Nav Archit Ocean Eng 2020;12:784–98.

[90] Urbański T, Banaszek A, Jurczak W. Prediction of Welding-Induced Distortion of Fixed Plate Edge Using Design of Experiment Approach. Polish Marit Res 2020;27:134–42.

[91] Dow RS, Smith CS. Effects of localized imperfections on compressive strength of long rectangular plates. J Constr Steel Res 1984;4:51–76.

[92] Ueda Y, Yao T. The influence of complex initial deflection modes on the behaviour and ultimate strength of rectangular plates in compression. J Constr Steel Res 1985;5:265–302.

[93] Smith C, Davidson P, Chapman J, Dowling P. Strength and Stiffness of Ships' Plating under In-plane Compression and Tension. Trans RINA 1988;130.

[94] Yu Y, Feng G, Li C, Ren H. Experimental and Numerical Investigation on the Ultimate Strength of Stiffened Plates with Scanned Initial Geometrical Imperfection. China Ocean Eng 2019;33:446–58.

[95] Özgüç Ö, Das PK, Barltrop N. The new simple design equations for the ultimate compressive strength of imperfect stiffened plates. Ocean Eng 2007;34:970–86.

[96] Pedram M, Khedmati MR. The effect of welding on the strength of aluminium stiffened plates subject to combined uniaxial compression and lateral pressure. Int J Nav Archit Ocean Eng 2014;6:39–59.

[97] Guedes Soares C, Luís RM, Teixeira AP, Quesnel T, Nikolov PI, Steen E, et al. Parametric study on the collapse strength of rectangular plates with localized imperfections under in-plane compression. Int Shipbuild Prog 2008;55:63–85.

[98] Estefen SF, Chujutalli JH, Guedes Soares C. Influence of geometric imperfections on the ultimate strength of the double bottom of a Suezmax tanker. Eng Struct 2016;127:287–303.

[99] Nikolov P. Collapse strength of damaged plating between stiffeners, maritime transportation and exploitation of ocean and coastal resources. Edited by C. Guedes 2007.

[100] Nikolov P. Collapse Strength of Damaged Plating. Vol. 2 Struct. Saf. Reliab., ASME; 2008, p. 79–88.

[101] Paik JK, Thayamballi AK, Park Y Il, Hwang JS. A time-dependent corrosion wastage model for seawater ballast tank structures of ships. Corros Sci 2004;46:471–86.

[102] Saad-Eldeen S, Garbatov Y, Guedes Soares C. Ultimate strength analysis of highly damaged plates. Mar Struct 2016;45:63–85.

[103] Witkowska M, Guedes Soares C. Ultimate strength of locally damaged panels. Thin-Walled Struct 2015;97:225–40.

[104] Xu MC, Guedes Soares C. Assessment of residual ultimate strength for wide dented stiffened panels subjected to compressive loads. Eng Struct 2013;49:316–28.

[105] Chujutalli JH, Estefen SF, Guedes Soares C. Experimental and numerical analysis of small-scale panels with indented stiffeners. J Constr Steel Res 2018;150:7–22.

[106] Chujutalli JH, Estefen SF, Soares CG. Indentation parameters influence on the ultimate strength of panels for different stiffeners. J Constr Steel Res 2020;170:106097.

[107] Ao L, Wu H, Wang D, Wu W. Evaluation on the residual ultimate strength of stiffened plates with central dent under longitudinal thrust. Ocean Eng 2020;202:107167.

[108] Park S-H, Kang E, Cho S-R, Jang Y-S, Baek N-K, Park D-K. Residual strength of stiffened plates having multiple denting damages. Dev. Collis. Grounding Ships Offshore Struct., CRC Press; 2019, p. 179–88.

[109] Saad-Eldeen S, Garbatov Y, Guedes Soares C. Strength assessment of steel plates subjected to compressive load and dent deformation. Struct Infrastruct Eng 2016;12:995–1011.

[110] Roy YA, Shastry BP, Rao GV. Stability of square plates with through transverse cracks. Comput Struct 1990;36:387–8.

[111] Shaw D, Huang YH. Buckling behavior of a central cracked thin plate under tension. Eng Fract Mech 1990;35:1019–27.

[112] Riks E, Rankin CC, Brogan FA. The buckling behavior of a central crack in a plate under tension. Eng Fract Mech 1992;43:529–48.

[113] Kumar YVS, Paik JK. Buckling analysis of cracked plates using hierarchical trigonometric functions. Thin-Walled Struct 2004;42:687–700.

[114] Paik JK, Satish Kumar YV, Lee JM. Ultimate strength of cracked plate elements under axial compression or tension. Thin-Walled Struct 2005;43:237–72.

[115] Babazadeh A, Khedmati MR. Ultimate strength of cracked ship structural elements and systems: A review. Eng Fail Anal 2018;89:242–57.

[116] Seifi R, Khoda-yari N. Experimental and numerical studies on buckling of cracked thin-plates under full and partial compression edge loading. Thin-Walled Struct 2011;49:1504–16.

[117] Shi XH, Zhang J, Guedes Soares C. Experimental study on collapse of cracked stiffened plate with initial imperfections under compression. Thin-Walled Struct 2017;114:39–51.

[118] Shi XH, Zhang J, Guedes Soares C. Numerical assessment of experiments on the residual ultimate strength of stiffened plates with a crack. Ocean Eng 2019;171:443–57.

[119] Saad-Eldeen S, Garbatov Y, Guedes Soares C. Experimental investigation on the residual strength of thin steel plates with a central elliptic opening and locked cracks. Ocean Eng 2016;115:19–29.

[120] Brighenti R. Numerical buckling analysis of compressed or tensioned cracked thin plates. Eng Struct 2005;27:265–76.

[121] Rahbar-Ranji A, Zarookian A. Ultimate strength of stiffened plates with a transverse crack under uniaxial compression. Ships Offshore Struct 2015;10:416–25.

[122] Cui C, Yang P, Xia T, Du J. Assessment of residual ultimate strength of cracked steel plates under longitudinal compression. Ocean Eng 2016;121:174–83.

[123] Bayatfar A, Khedmati MR, Rigo P. Residual ultimate strength of cracked steel unstiffened and stiffened plates under longitudinal compression. Thin-Walled Struct 2014;84:378–92.

[124] Xia T, Yang P, Hu K, Cui C. Combined effect of imperfections on ultimate strength of cracked plates under uniaxial compression. Ocean Eng 2018;150:113–23.

[125] Cui C, Yang P, Li C, Xia T. Ultimate strength characteristics of cracked stiffened plates subjected to uniaxial compression. Thin-Walled Struct 2017;113:27–38.

[126] Yu CL, Chen YT, Yang S, Liu Y, Lu GC. Ultimate strength characteristic and assessment of cracked stiffened panel under uniaxial compression. Ocean Eng 2018;152:6–16.

[127] Saad-Eldeen S, Garbatov Y, Soares C. Ultimate strength of a corroded box girder subjected to pure bending and a non-propagating crack. Towar. Green Mar. Technol. Transp., CRC Press; 2015, p. 373–80.

[128] Saad-Eldeen S, Garbatov Y, Soares C. Emergency repair of a single hull structure with locked cracks. Marit. Technol. Eng. III, CRC Press; 2016, p. 521–9.

[129] Babazadeh A, Khedmati MR. Empirical formulations for estimation of ultimate strength of cracked continuous unstiffened plates used in ship structure under in-plane longitudinal compression. Eng Fail Anal 2019;100:470–84.

[130] Xu MC, Garbatov Y, Guedes Soares C. Residual ultimate strength assessment of stiffened panels with locked cracks. Thin-Walled Struct 2014;85:398–410.

[131] Melchers RE. Development of new applied models for steel corrosion in marine applications including shipping. Ships Offshore Struct 2008;3:135–44.

[132] Guedes Soares C, Garbatov Y, Zayed A, Wang G. Corrosion wastage model for ship crude oil tanks. Corros Sci 2008;50:3095–106.

[133] Bai Y, Jin W-L. Reassessment of Jacket Structure. Mar. Struct. Des., Elsevier; 2016, p. 875–89.

[134] Wang Y, Wharton JA, Shenoi RA. Ultimate strength analysis of aged steel-plated structures exposed to marine corrosion damage: A review. Corros Sci 2014;86:42–60.

[135] Paik JK, Lee JM, Ko MJ. Ultimate compressive strength of plate elements with pit corrosion wastage. Proc Inst Mech Eng Part M J Eng Marit Environ 2003;217:185–200.

[136] Paik JK, Lee JM, Ko J. Ultimate shear strength of plate elements with pit corrosion wastage. Thin-Walled Struct 2004;42:1161–76.

[137] Ok D, Pu Y, Incecik A. Computation of ultimate strength of locally corroded unstiffened plates under uniaxial compression. Mar Struct 2007;20:100–14.

[138] Zhang Y, Huang Y, Wei Y. Ultimate strength experiment of hull structural plate with pitting corrosion damage under unaxial compression. Ocean Eng 2017;130:103–14.

[139] Huang Y, Zhang Y, Liu G, Zhang Q. Ultimate strength assessment of hull structural plate with pitting corrosion damnification under biaxial compression. Ocean Eng 2010;37:1503–12.

[140] Ok D, Pu Y, Incecik A. Artificial neural networks and their application to assessment of ultimate strength of plates with pitting corrosion. Ocean Eng 2007;34:2222–30.

[141] Feng L, He J, Hu L, Shi H, Yu C, Wang S, et al. A parametric study on effects of pitting corrosion on steel plate's ultimate strength. Appl Ocean Res 2020;95:102026.

[142] Jiang X, Guedes Soares C. Ultimate capacity of rectangular plates with partial depth pits

under uniaxial loads. Mar Struct 2012;26:27–41.

[143] Nakai T, Matsushita H, Yamamoto N, Arai H. Effect of pitting corrosion on local strength of hold frames of bulk carriers (1st report). Mar Struct 2004;17:403–32.

[144] Wang R, Ajit Shenoi R, Sobey A. Ultimate strength assessment of plated steel structures with random pitting corrosion damage. J Constr Steel Res 2018;143:331–42.

[145] International Association of Classification Societies. Recommendation 87. Guidelines for coating maintanance & repairs for ballast tanks and combined cargo/ballast tanks on oil tankers. 2015.

[146] Zhang J, Shi XH, Guedes Soares C. Experimental analysis of residual ultimate strength of stiffened panels with pitting corrosion under compression. Eng Struct 2017;152:70–86.

[147] Shi XH, Zhang J, Guedes Soares C. Numerical assessment of experiments on the ultimate strength of stiffened panels with pitting corrosion under compression. Thin-Walled Struct 2018;133:52–70.

[148] Zhang Y, Huang Y, Meng F. Ultimate strength of hull structural stiffened plate with pitting corrosion damage under unaxial compression. Mar Struct 2017;56:117–36.

[149] Rahbar-Ranji A, Niamir N, Zarookian A. Ultimate strength of stiffened plates with pitting corrosion. Int J Nav Archit Ocean Eng 2015;7:509–25.

[150] Sultana S, Wang Y, Sobey AJ, Wharton JA, Shenoi RA. Influence of corrosion on the ultimate compressive strength of steel plates and stiffened panels. Thin-Walled Struct 2015;96:95–104.

[151] Wang Y, Wharton JA, Shenoi RA. Ultimate strength assessment of steel stiffened plate structures with grooving corrosion damage. Eng Struct 2015;94:29–42.

[152] Panayotova M, Garbatov Y. Corrosion of steels in marine environment, monitoring and standards. Saf. Reliab. Ind. Prod. Syst. Struct., CRC Press; 2010, p. 369–413.

[153] Silva JE, Garbatov Y, Guedes Soares C. Ultimate strength assessment of rectangular steel plates subjected to a random localised corrosion degradation. Eng Struct 2013;52:295–305.

[154] Garbatov Y, Guedes Soares C, Parunov J, Kodvanj J. Tensile strength assessment of corroded small scale specimens. Corros Sci 2014;85:296–303.

[155] Kashani MM, Crewe AJ, Alexander NA. Nonlinear stress-strain behaviour of corrosion-damaged reinforcing bars including inelastic buckling. Eng Struct 2013;48:417–29.

[156] Zhang W, Shang D, Gu X. Stress-strain relationship of corroded steel bars. Tongji Daxue Xuebao/Journal Tongji Univ 2006;34.

[157] Fernandez I, Berrocal CG. Mechanical Properties of 30 Year-Old Naturally Corroded Steel Reinforcing Bars. Int J Concr Struct Mater 2019;13:9.

[158] Li L, Mahmoodian M, Li CQ. Effect of corrosion on mechanical properties of steel bridge elements. 9th Int. Conf. Bridg. MAINTENANCE, Saf. Manag., 2018.

[159] Li L, Li C-Q, Mahmoodian M. Effect of Applied Stress on Corrosion and Mechanical Properties of Mild Steel. J Mater Civ Eng 2019;31:04018375.

[160] Wang Y, Xu S, Wang H, Li A. Predicting the residual strength and deformability of corroded

steel plate based on the corrosion morphology. Constr Build Mater 2017;152:777–93.

[161] Nie B, Xu S, Yu J, Zhang H. Experimental investigation of mechanical properties of corroded cold-formed steels. J Constr Steel Res 2019;162:105706.

[162] Qin G, Xu S, Yao D, Zhang Z. Study on the degradation of mechanical properties of corroded steel plates based on surface topography. J Constr Steel Res 2016;125:205–17.

[163] Xu S, Zhang Z, Li R, Wang H. Effect of cleaned corrosion surface topography on mechanical properties of cold-formed thin-walled steel. Constr Build Mater 2019;222:1–14.

[164] Xu S, Zhang H, Wang Y. Estimation of the properties of corroded steel plates exposed to salt-spray atmosphere. Corros Eng Sci Technol 2019;54:431–43.

[165] Du YG, Clark LA, Chan AHC. Residual capacity of corroded reinforcing bars. Mag Concr Res 2005;57:135–47.

[166] Cairns J, Plizzari GA, Du Y, Law DW, Franzoni C. Mechanical properties of corrosion-damaged reinforcement. ACI Mater J 2005;102:256–64.

[167] Du YG, Clark LA, Chan AHC. Effect of corrosion on ductility of reinforcing bars. Mag Concr Res 2005;57:407–19.

[168] Palsson R, Mirza MS. Mechanical response of corroded steel reinforcement of abandoned concrete bridge. ACI Struct J 2002;99:157–62.

[169] Garbatov Y, Saad-Eldeen S, Guedes Soares C, Parunov J, Kodvanj J. Tensile test analysis of corroded cleaned aged steel specimens. Corros Eng Sci Technol 2018:1–9.

[170] Moreno E, Cobo A, Palomo G, González MN. Mathematical models to predict the mechanical behavior of reinforcements depending on their degree of corrosion and the diameter of the rebars. Constr Build Mater 2014;61:156–63.

[171] Fernandez I, Bairán JM, Marí AR. Mechanical model to evaluate steel reinforcement corrosion effects on σ-ε and fatigue curves. Experimental calibration and validation. Eng Struct 2016;118:320–33.

[172] Li D, Xiong C, Huang T, Wei R, Han N, Xing F. A simplified constitutive model for corroded steel bars. Constr Build Mater 2018;186:11–9.

[173] Ahmmad MM, Sumi Y. Strength and deformability of corroded steel plates under quasi-static tensile load. J Mar Sci Technol 2010;15:1–15.

[174] Appuhamy JMRS, Kaita T, Ohga M, Fujii K. Prediction of residual strength of corroded tensile steel plates. Int J Steel Struct 2011;11:65–79.

[175] Flaks VY. Correlation of pitting corrosion of aluminum plates and reduction of load-bearing capacity under tension. Sov Mater Sci 1978;14:75–8.

[176] Česen A, Kosec T, Legat A. Characterization of steel corrosion in mortar by various electrochemical and physical techniques. Corros Sci 2013;75:47–57.

[177] Wang Y, Xu S, Li H, Zhang H. Surface Characteristics and Stochastic Model of Corroded Structural Steel Under General Atmospheric Environment. Acta Metall Sin 2020;56:148–60.

[178] Xu S, Wang Y. Estimating the effects of corrosion pits on the fatigue life of steel plate

based on the 3D profile. Int J Fatigue 2015;72:27–41.

[179] Kainuma S, Jeong Y-S, Ahn J-H. Investigation on the stress concentration effect at the corroded surface achieved by atmospheric exposure test. Mater Sci Eng A 2014;602:89–97.

[180] Pidaparti RM, Rao AS. Analysis of pits induced stresses due to metal corrosion. Corros Sci 2008;50:1932–8.

[181] Wang Y, Xu S, Li A. Flexural performance evaluation of corroded steel beams based on 3D corrosion morphology. Struct Infrastruct Eng 2020:1–16.

[182] Mateus A, Witz J. On the post-buckling of corroded steel plates used in marine structures. Trans RINA 1998;140:165–83.

[183] Teixeira AP, Ivanov LD, Guedes Soares C. Assessment of characteristic values of the ultimate strength of corroded steel plates with initial imperfections. Eng Struct 2013;56:517–27.

[184] Reza Khedmati M, Mahdi Roshanali M, Mohammad Esmaeil Nouri ZH. Strength of steel plates with both-sides randomly distributed with corrosion wastage under uniaxial compression. Thin-Walled Struct 2011;49:325–42.

[185] Rahbar-Ranji A. Ultimate strength of corroded steel plates with irregular surfaces under in-plane compression. Ocean Eng 2012;54:261–9.

[186] Khedmati MR, Nouri ZHME, Roshanali MM. A comparative computational investigation on the effects of randomly distributed general corrosion on the post-buckling behaviour of uniaxially loaded plates. J Mech Sci Technol 2012;26:767–83.

[187] Teixeira AP, Guedes Soares C, Wang G. Probabilistic modelling of the ultimate strength of ship plates with non-uniform corrosion. J Mar Sci Technol 2013;18:115–32.

[188] Silva JE, Garbatov Y, Guedes Soares C. Reliability assessment of a steel plate subjected to distributed and localized corrosion wastage. Eng Struct 2014;59:13–20.

[189] Garbatov Y, Tekgoz M, Guedes Soares C. Experimental and numerical strength assessment of stiffened plates subjected to severe non-uniform corrosion degradation and compressive load. Ships Offshore Struct 2017;12:461–73.

[190] Woloszyk K, Kahsin M, Garbatov Y. Numerical assessment of ultimate strength of severe corroded stiffened plates. Eng Struct 2018;168:346–54.

[191] Mohammad ZH, Nouri E, Khedmati MR, Roshanali MM. Degradation of the compressive strength of unstiffened/stiffened steel plates due to both-sides randomly distributed corrosion wastage. Lat Am J Solids Struct 2010;7:335–67.

[192] Kim DK, Park DK, Kim JH, Kim SJ, Kim BJ, Seo JK, et al. Effect of corrosion on the ultimate strength of double hull oil tankers - Part I: stiffened panels. Struct Eng Mech 2012;42:507–30.

[193] Saad-Eldeen S, Garbatov Y, Guedes Soares C. Analysis of plate deflections during ultimate strength experiments of corroded box girders. Thin-Walled Struct 2012;54:164–76.

[194] Saad-Eldeen S, Garbatov Y, Guedes Soares C. Effect of corrosion degradation on

ultimate strength of steel box girders. Corros Eng Sci Technol 2012;47:272–83.

[195] Saad-Eldeen S, Garbatov Y, Guedes Soares C. Experimental assessment of the ultimate strength of a box girder subjected to severe corrosion. Mar Struct 2011;24:338–57.

[196] Saad-Eldeen S, Garbatov Y, Guedes Soares C. Corrosion-Dependent Ultimate Strength Assessment of Aged Box Girders Based on Experimental Results. J Sh Res 2011;55:289–300.

[197] Saad-Eldeen S, Garbatov Y, Guedes Soares C. Ultimate strength assessment of corroded box girders. Ocean Eng 2013;58:35–47.

[198] Saad-Eldeen S, Garbatov Y, Guedes Soares C. Experimental assessment of corroded steel box-girders subjected to uniform bending. Ships Offshore Struct 2013;8:653–62.

[199] Saad-Eldeen S, Garbatov Y, Guedes Soares C. Strength assessment of a severely corroded box girder subjected to bending moment. J Constr Steel Res 2014;92:90–102.

[200] P. Domzalicki, I. Skalski, C. Guedes Soares YG. Large Scale Corrosion Tests. In: P.K. Das, editor. Anal. Des. Mar. Struct., Taylor & Francis Group; 2009, p. 193–8.

[201] Garbatov Y, Saad-Eldeen S, Guedes Soares C. Hull girder ultimate strength assessment based on experimental results and the dimensional theory. Eng Struct 2015;100:742–50.

[202] Wang G, Boon B, Brennan FP, Garbatov Y, Ji C, Parunov J, et al. Committee V.6 Condition assessment of aging ships and offshore structures. In: Jang CD, Hong SY, editors. Proc. 17th Int. Sh. Offshore Struct. Congr., Seul: Seoul National University; 2009, p. 309–65.

[203] Guedes Soares C, Garbatov Y. Reliability of maintained ship hulls subjected to corrosion. J Sh Res 1996;40:235–243.

[204] Wirsching PH, Ferensic J, Thayamballi A. Reliability with Respect to Ultimate Strength of a Corroding Ship Hull. Mar Struct 1997;10:501–18.

[205] Akpan UO, Koko TS, Ayyub B, Dunbar TE. Risk assessment of aging ship hull structures in the presence of corrosion and fatigue. Mar Struct 2002;15:211–31.

[206] Paik JK, Lee JM, Hwang JS, Park Y Il. A Time-Dependent Corrosion Wastage Model for the Structures of Single-and Double-Hull Tankers and FSOs and FPSOs. Mar Technol SNAME News 2003;40:201–17.

[207] Horte T, Wang G, White N. Calibration of the hull girder ultimate capacity criterion for double hull tankers. Proc. 10th Int. Symp. Pract. Des. Ships Other Float. Struct. (PRADS'07), Oct., Citeseer; 2007, p. 1–5.

[208] Ivanov LD. A Probabilistic Assessment of all Hull Girder Geometric Properties at any Ship's Age. Int J Marit Eng 2007;149:15.

[209] Wang G, Lee A-K, Ivanov L, Lynch TJ, Serratella C, Basu R. A statistical investigation of time-variant hull girder strength of aging ships and coating life. Mar Struct 2008;21:240–56.

[210] Yamamoto N, Yao T. Hull Girder Strength of a Tanker under Longitudinal Bending considering Strength Diminution due to Corrosion. ClassNK Tech Bull (NK Tech Bull 2002;20:103–9.

[211] Baboian R. Corrosion Tests and Standards: Application and Interpretation-Second Edition. ASTM International; 2005.

[212] ASTM Norma G 52. Standard Practice for Exposing and Evaluating Metals and Alloys in Surface Seawater. Annu B ASTM Stand 2006.

[213] Melchers RE. Corrosion uncertainty modelling for steel structures. J Constr Steel Res 1999;52:3–19.

[214] Weiss RF. The solubility of nitrogen, oxygen and argon in water and seawater. Deep Sea Res Oceanogr Abstr 1970;17:721–35.

[215] Pedeferri P. Corrosion Science and Engineering. Cham: Springer International Publishing; 2018.

[216] Guedes Soares C, Garbatov Y, Zayed A. Effect of environmental factors on steel plate corrosion under marine immersion conditions. Corros Eng Sci Technol 2011;46:524–41.

[217] Kirk W, Pikul S. Seawater Corrosivity Around the World: Results from Three Years of Testing. In: Baloun CH, editor. Corros. Nat. Waters, 100 Barr Harbor Drive, PO Box C700, West Conshohocken, PA 19428-2959: ASTM International; 2009, p. 2–36.

[218] Melchers RE. Probabilistic Models for Corrosion in Structural Reliability Assessment—Part 2: Models Based on Mechanics. J Offshore Mech Arct Eng 2003;125:272–80.

[219] Laque FL. Marine corrosion causes and prevention. Wiley; 1975.

[220] Yamamoto N, Ikegami K. A Study on the Degradation of Coating and Corrosion of Ship's Hull Based on the Probabilistic Approach. J Offshore Mech Arct Eng 1998;120:121–8.

[221] Guedes Soares C, Garbatov Y. Non-linear time dependent model of corrosion for the reliability assessment of maintained structural components. A A Balkema, Saf Reliab 1998;2:929–936.

[222] Guedes Soares C, Garbatov Y. Reliability of maintained, corrosion protected plates subjected to non-linear corrosion and compressive loads. Mar Struct 1999;12:425–45.

[223] Kee Paik J, Kyu Kim S, Kon Lee S. Probabilistic corrosion rate estimation model for longitudinal strength members of bulk carriers. Ocean Eng 1998;25:837–60.

[224] Qin S, Cui W. Effect of corrosion models on the time-dependent reliability of steel plated elements. Mar Struct 2003;16:15–34.

[225] Garbatov Y, Guedes Soares C, Wang G. Nonlinear Time Dependent Corrosion Wastage of Deck Plates of Ballast and Cargo Tanks of Tankers. J Offshore Mech Arct Eng 2007;129:48–55.

[226] Garbatov Y, Guedes Soares C. Corrosion wastage modeling of deteriorated bulk carrier decks. Int Shipbuild Prog 2008;55:109–25.

[227] Xiao L, Peng J, Zhang J, Ma Y, Cai CS. Comparative assessment of mechanical properties of HPS between electrochemical corrosion and spray corrosion. Constr Build Mater 2020;237:117735.

[228] Zhang S. A review and study on ultimate strength of steel plates and stiffened panels in axial compression. Ships Offshore Struct 2015:1–11.

[229] Colt J, Westers H. Production of Gas Supersaturation by Aeration. Trans Am Fish Soc

1982;111:342–60.

[230] Clay CH, Kovari J, editors. Inland Aquaculture Engineering: Lectures Presented at the ADCP Inter-regional Training Course in Inland Aquaculture Engineering, Budapest, 6 June-3 September 1983. Rome: Food & Agriculture Org.; 1984.

[231] Venkatesan R, Venkatasamy MA, Bhaskaran TA, Dwarakadasa ES, Ravindran M. Corrosion of ferrous alloys in deep sea environments. Br Corros J 2002;37:257–66.

[232] Zakowski K, Narozny M, Szocinski M, Darowicki K. Influence of water salinity on corrosion risk—the case of the southern Baltic Sea coast. Environ Monit Assess 2014;186:4871–9.

[233] Cegla F, Gajdacsi A. Mitigating the effects of surface morphology changes during ultrasonic wall thickness monitoring. AIP Conf. Proc., 2016, p. 170001.

[234] Garbatov Y, Guedes Soares C, Wang G. Nonlinear Time Dependent Corrosion Wastage of Deck Plates of Ballast and Cargo Tanks of Tankers. J Offshore Mech Arct Eng 2006;129:48–55.

[235] Dowdy SM, Wearden S, Chilko DM. Statistics for research. Wiley-Interscience; 2004.

[236] Wang X, Moan T. Stochastic and deterministic combinations of still water and wave bending moments in ships. Mar Struct 1996;9:787–810.

[237] Melchers R. Structural Reliability Analysis and Prediction. Chichester, UK: John Wiley & Sons Ltd; 2017.

[238] Bai Y, Wei-Liang J. Marine Structural Design (2nd ed.). vol. 10. 2016.

[239] Guedes Soares C, Scotto M. Modelling uncertainty in long-term predictions of significant wave height. Ocean Eng 2001;28:329–42.

[240] Ang A-S, Cornell C. Reliability Bases of Structural Safety and Design. J Struct Div 1974;100:1755–69.

[241] Ditlevsen O. Model uncertainty in structural reliability. Struct Saf 1982;1:73–86.

[242] Garbatov Y, Tekgoz M, Guedes Soares C. Uncertainty assessment of the ultimate strength of a stiffened panel. MARSTRUCT-2011, 2011, p. 659–68.

[243] Stefanou G. The stochastic finite element method: Past, present and future. Comput Methods Appl Mech Eng 2009;198:1031–51.

[244] Garbatov Y, Parunov J, Kodvanj J, Saad-Eldeen S, Guedes Soares C. Experimental assessment of tensile strength of corroded steel specimens subjected to sandblast and sandpaper cleaning. Mar Struct 2016;49:18–30.

[245] ANSYS. Online Manuals, Release 19 2019.

[246] Metropolis N, Ulam S. The Monte Carlo Method. J Am Stat Assoc 1949;44:335–41.

[247] Olsson A, Sandberg G, Dahlblom O. On Latin hypercube sampling for structural reliability analysis. Struct Saf 2003;25:47–68.

[248] Tekgoz M, Garbatov Y, Guedes Soares C. Ultimate strength assessment of welded stiffened plates. Eng Struct 2015;84:325–39.

[249] Timoshenko SP, Gere JM. Theory of elastic stability. 1961.

[250] Villavicencio R, Guedes Soares C. Numerical modelling of the boundary conditions on beams stuck transversely by a mass. Int J Impact Eng 2011;38:384–96.

[251] Chmielewski M, Piotrowski L, Augustyniak B. A fast procedure of stress state evaluation in magnetically anisotropic steels with the help of a probe with adjustable magnetizing field direction. Meas Sci Technol 2017;28:045903.

[252] Li C, Dong S, Wang T, Xu W, Zhou X. Numerical Investigation on Ultimate Compressive Strength of Welded Stiffened Plates Built by Steel Grades of S235–S390. Appl Sci 2019;9:2088.

[253] Lo Brutto M, Spera MG. Image-based and range-based 3D modelling of archaeological cultural heritage: the Telamon of the Temple of Olympian Zeus in Agrigento (Italy). ISPRS - Int Arch Photogramm Remote Sens Spat Inf Sci 2012;XXXVIII–5:515–22.

[254] Koelman HJ. Application of a photogrammetry-based system to measure and re-engineer ship hulls and ship parts: An industrial practices-based report. Comput Des 2010;42:731–43.

[255] Garbatov Y, Guedes Soares C, Masubuchi K. Residual Stresses and Distortion in Welds. Ref. Modul. Mater. Sci. Mater. Eng., Elsevier; 2016.

[256] ISO. Metallic materials - Tensile testing - Part 1: Method of test at room temperature. Int Stand ISO 6892-1 2009.

[257] Jankowski R, Walukiewicz H. Modeling of two-dimensional random fields. Probabilistic Eng Mech 1997;12:115–21.

[258] Górski J, Winkelmann K. Generation of random fields to reflect material and geometric imperfections of plates and shells. Shell Struct. Theory Appl. Vol. 4, CRC Press; 2017, p. 537–40.

[259] Górski J, Mikulski T, Oziębło M, Winkelmann K. Effect of geometric imperfections on aluminium silo capacities. Stahlbau 2015;84:52–7.

[260] Teixeira ÂP, Guedes Soares C. Ultimate strength of plates with random fields of corrosion. Struct Infrastruct Eng 2008;4:363–70.

[261] Garbatov Y, Guedes Soares C. Spatial Corrosion Wastage Modelling of Steel Plates Subjected to Marine Environments. Vol. 9 Offshore Geotech. Torgeir Moan Honor. Symp., American Society of Mechanical Engineers; 2017.

[262] Ghanem RG, Spanos PD. Stochastic Finite Elements: A Spectral Approach. New York, NY: Springer New York; 1991.

[263] Li C, Der Kiureghian A. Optimal Discretization of Random Fields. J Eng Mech 1993;119:1136–54.

[264] Mathworks. Matlab R2019b 2019.

[265] Constantine P. Random Field Simulation 2012. https://www.mathworks.com/matlabcentral/fileexchange/27613-random-field-simulation (accessed November 26, 2019).

[266] DNVGL-CG-0285. Ultrasonic thickness measurements of ships. DNV GL; 2016.

[267] ANSYS Inc. ANSYS LS-DYNA User's Guide 2019.

[268] Bäker M. How to get meaningful and correct results from your finite element model 2018.

[269] Kwesi Nutor R. Using the Hollomon Model to Predict Strain-Hardening in Metals. Am J

Mater Synth Process 2017;2:1–4.

[270] Daniel C. One-at-a-Time Plans. J Am Stat Assoc 1973;68:353–60.

[271] Li Z, Pasternak H. Experimental and numerical investigations of statistical size effect in S235JR steel structural elements. Constr Build Mater 2019;206:665–73.

[272] Kim U-N, Choe I-H, Paik JK. Buckling and ultimate strength of perforated plate panels subject to axial compression: experimental and numerical investigations with design formulations. Ships Offshore Struct 2009;4:337–61.

[273] Cui J, Wang D. An experimental and numerical investigation on ultimate strength of stiffened plates with opening and perforation corrosion. Ocean Eng 2020;205:107282.

[274] Paik JK, Thayamballi AK. Empirical formulation for predicting the ultimate compressive strength of stiffened panels. Proc. Int. Offshore Polar Eng. Conf., 1997.

[275] Montgomery DC. Design and Analysis of Experiments. John Wiley & Sons Ltd, USA; 2006.

[276] Daniel C. Use of Half-Normal Plots in Interpreting Factorial Two-Level Experiments. Technometrics 1959;1:311–41.

[277] Paik JK, Frieze PA. Ship structural safety and reliability. Prog Struct Eng Mater 2001;3:198–210.

[278] Freudenthal AM. Safety and the Probability of Structural Failure. Trans Am Soc Civ Eng 1956;121:1337–75.

[279] Cornell CA. A Probability-Based Structural Code. ACI J Proc 1969;66:974–85.

[280] Ditlevsen O, Madsen HO. Structural reliability methods. Wiley and Sons; 1996.

[281] Hasofer AM, Lind NC. Exact and Invariant Second-Moment Code Format. J Eng Mech Div 1974;100:111–21.

[282] Mansour A, Wirsching P, Luckett M, Plumpton A. Assessment of Reliability of Existing Ship Structures 1997.

[283] Mansour A. Methods of computing the probability of failure under extreme values of bending moment. J Sh Res 1972:113–23.

[284] Mansour AE. Probabilistic design concepts in ship structural safety and reliability. Trans SNAME 1972;80:64–97.

[285] Mansour AE, Faulkner D. On applying the statistical approach to extreme sea loads and ship hull strength. Trans RINA 1972;114:273–314.

[286] Decò A, Frangopol DM, Zhu B. Reliability and redundancy assessment of ships under different operational conditions. Eng Struct 2012;42:457–71.

[287] Saydam D, Frangopol DM. Performance assessment of damaged ship hulls. Ocean Eng 2013;68:65–76.

[288] Liu Y, Frangopol DM. Time-dependent reliability assessment of ship structures under progressive and shock deteriorations. Reliab Eng Syst Saf 2018;173:116–28.

[289] Guedes Soares C, Garbatov Y. Reliability assessment of maintained ship hulls with correlated corroded elements. Mar Struct 1997;10:629–53.

[290] Han X, Yang DY, Frangopol DM. Time-variant reliability analysis of steel plates in marine environments considering pit nucleation and propagation. Probabilistic Eng Mech

2019;57:32–42.

[291] Zayed A, Garbatov Y, Guedes Soares C. Reliability of ship hulls subjected to corrosion and maintenance. Struct Saf 2013;43:1–11.

[292] Moan T, Ayala-Uraga E. Reliability-based assessment of deteriorating ship structures operating in multiple sea loading climates. Reliab Eng Syst Saf 2008;93:433–46.

[293] RCP Consult GmbH. STRUREL User Manual 2018.

[294] DnV. Structural Reliability Analysis of Marine Structures. Classif Notes No 306 1992.

[295] Hifi N, Barltrop N. Correction of Prediction Model Output--Application to General Corrosion Model. Int J Marit Eng 2014;156:363–74.

[296] Buckingham E. Dimensional analysis. Phys Rev 1914;4(345):12–23.

[297] Harris HG, Sabnis GM. Structural modeling and experimental techniques. CRC Press; 1999.

[298] Guedes Soares C, Teixeira A. Structural reliability of two bulk carrier designs. Mar Struct 2000;13:107–28.

[299] Garbatov Y, Sisci F, Ventura M. Risk-based framework for ship and structural design accounting for maintenance planning. Ocean Eng 2018;166:12–25.

[300] Guedes Soares C, Moan T. Statistical analysis of stillwater load effects in ship structures. Soc Nav Archit Mar Eng 1988;96.

[301] Guedes Soares, C., Dogliani, M., Ostergaard, C., Parmentier G, & Pedersen PT. Reliability Based Ship Structural Design. Trans Soc Nav Archit Mar Eng 1996;104:359–89.

FIGURES LIST

TABLES LIST

APPENDIX 1 – THE SCANNED CORROSION FIELDS OF SMALL-SCALE SPECIMENS

5 mm specimens

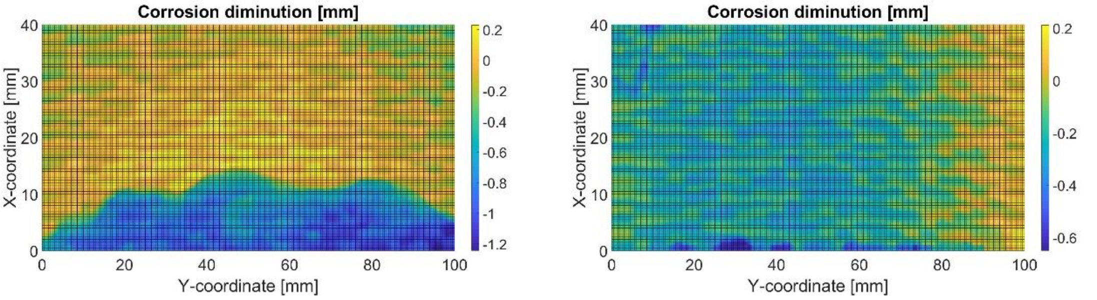

5.1 specimen – top (left) and bottom (right) surface

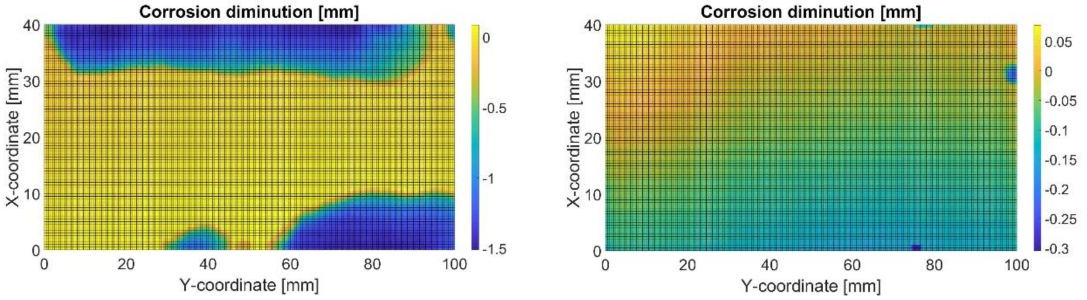

5.2 specimen – top (left) and bottom (right) surface

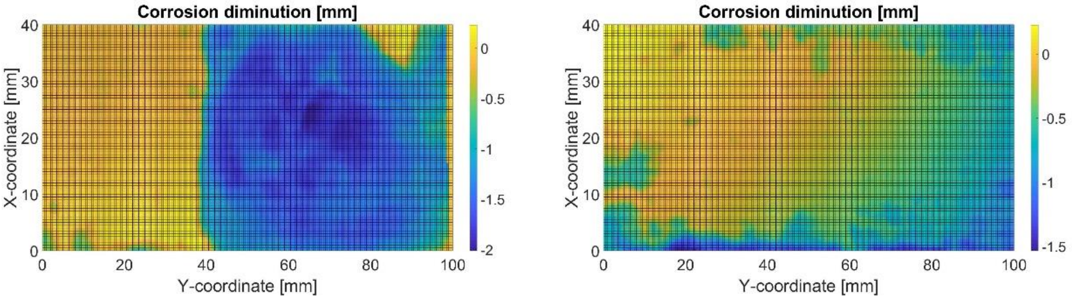

5.3 specimen – top (left) and bottom (right) surface

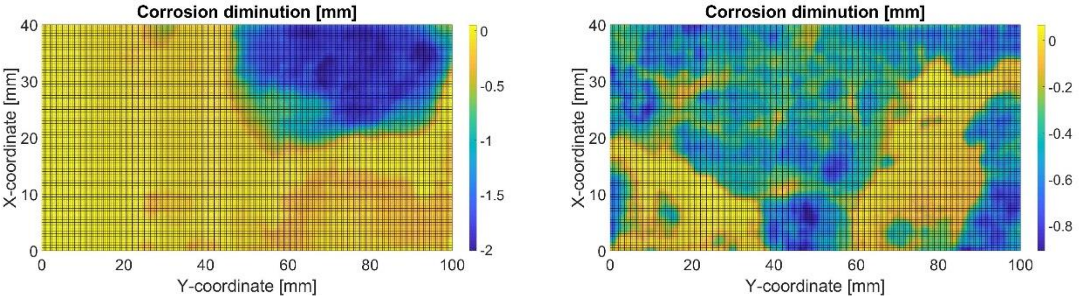

5.4 specimen – top (left) and bottom (right) surface

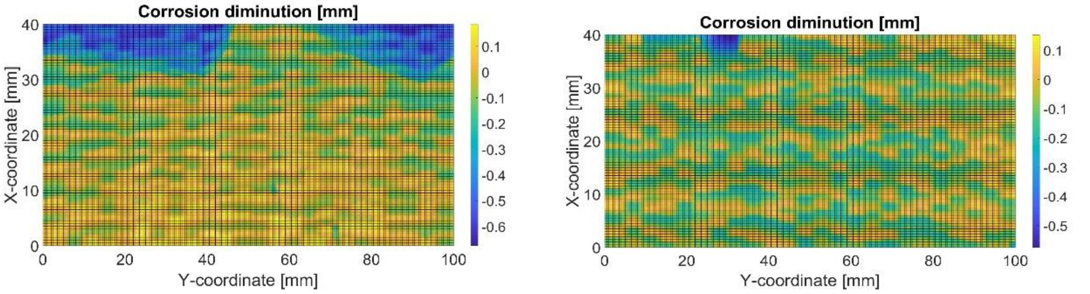

5.5 specimen – top (left) and bottom (right) surface

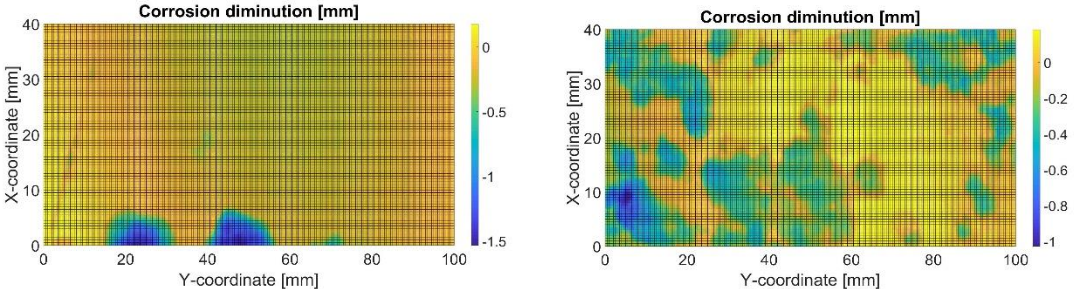

5.6 specimen – top (left) and bottom (right) surface

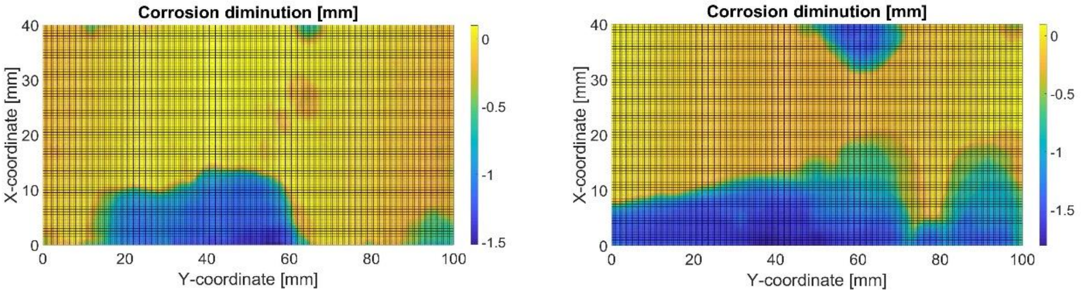

5.7 specimen – top (left) and bottom (right) surface

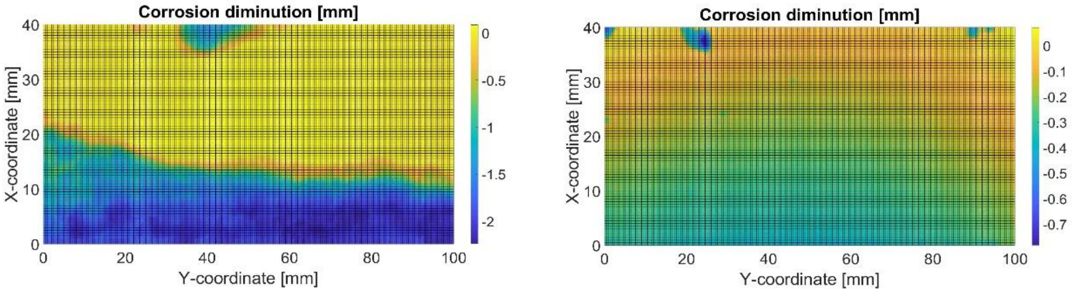

5.8 specimen – top (left) and bottom (right) surface

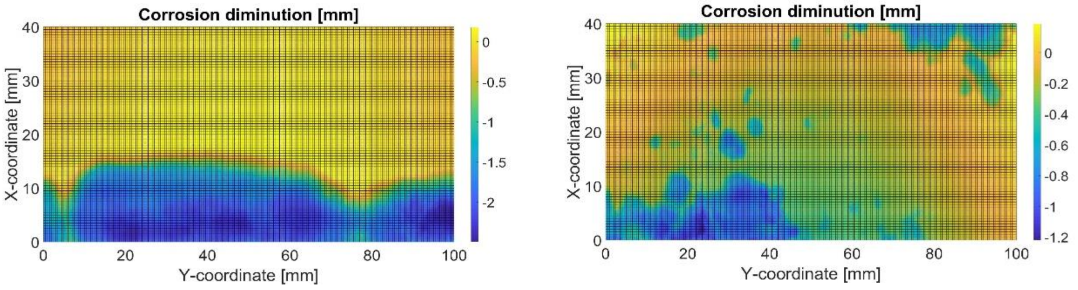

5.9 specimen – top (left) and bottom (right) surface

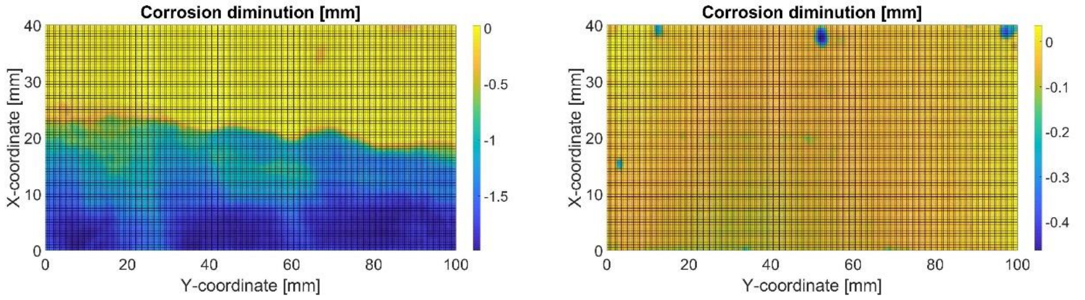

5.10 specimen – top (left) and bottom (right) surface

6 mm specimens

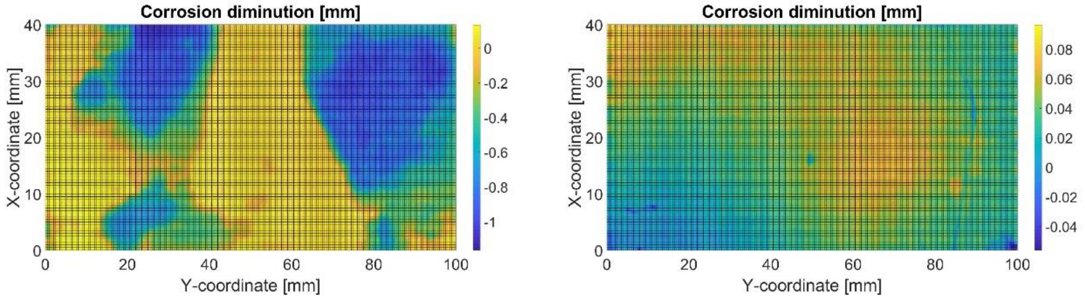

6.1 specimen – top (left) and bottom (right) surface

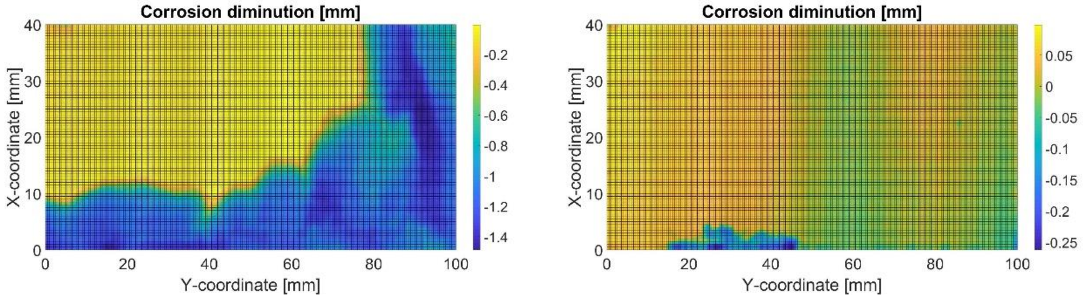

6.2 specimen – top (left) and bottom (right) surface

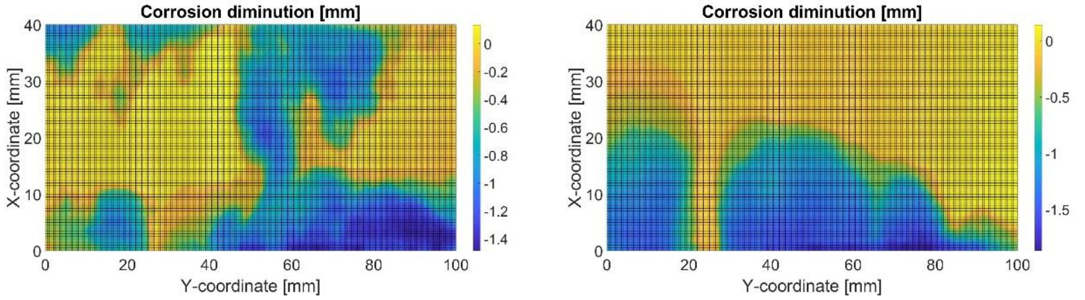

6.3 specimen – top (left) and bottom (right) surface

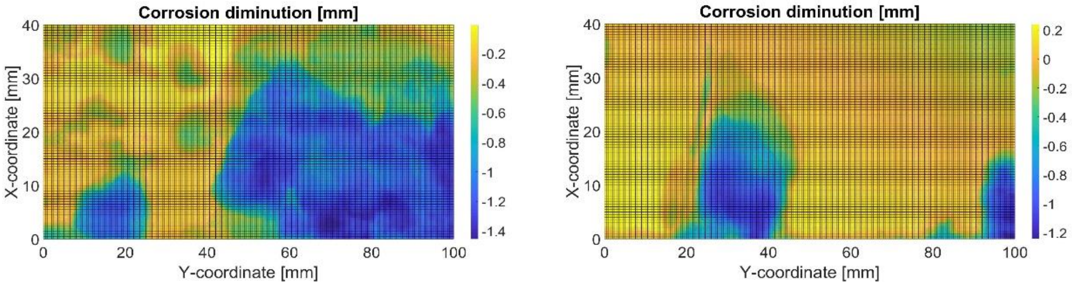

6.4 specimen – top (left) and bottom (right) surface

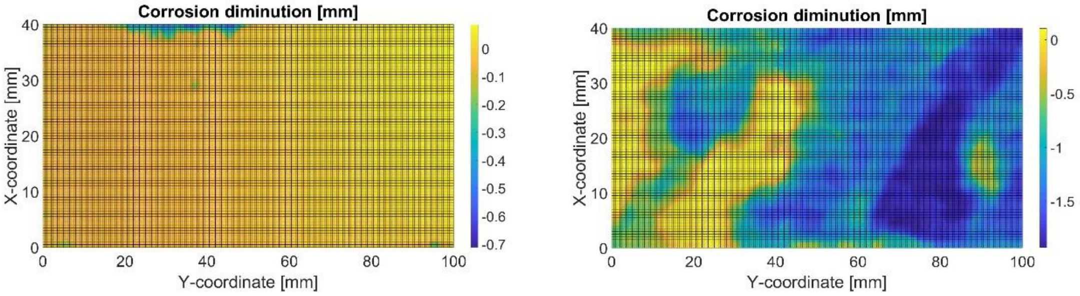

6.5 specimen – top (left) and bottom (right) surface

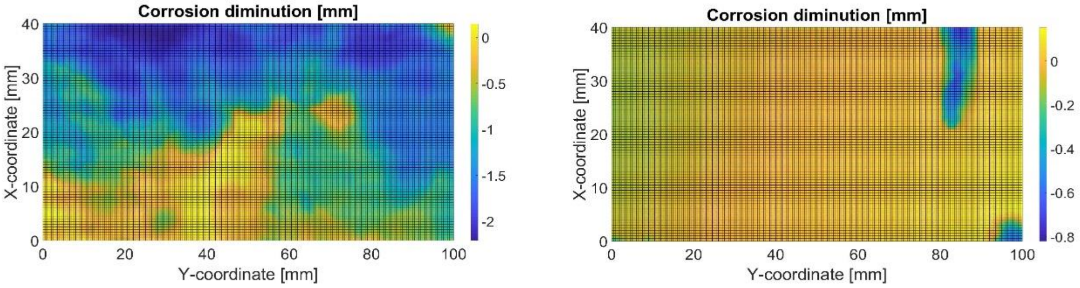

6.6 specimen – top (left) and bottom (right) surface

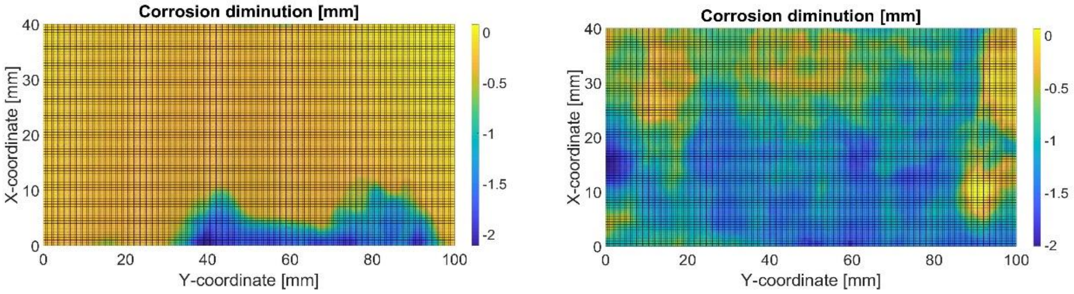

6.7 specimen – top (left) and bottom (right) surface

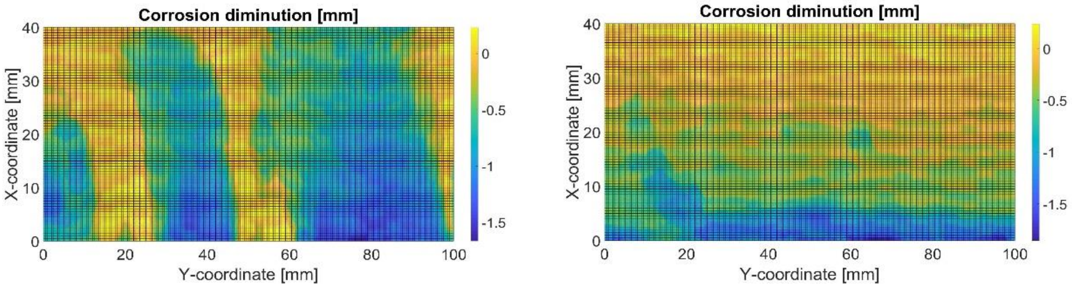

6.8 specimen – top (left) and bottom (right) surface

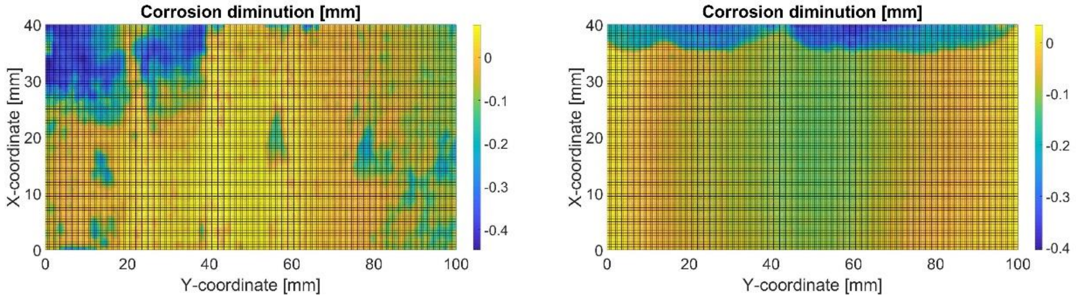

6.9 specimen – top (left) and bottom (right) surface

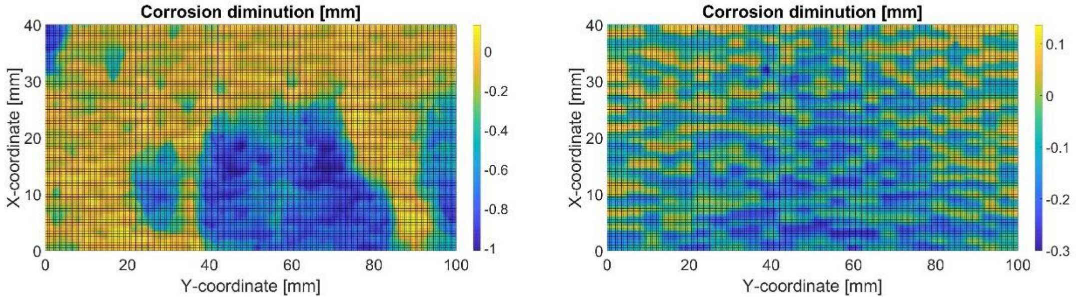

6.10 specimen – top (left) and bottom (right) surface

8 mm specimens

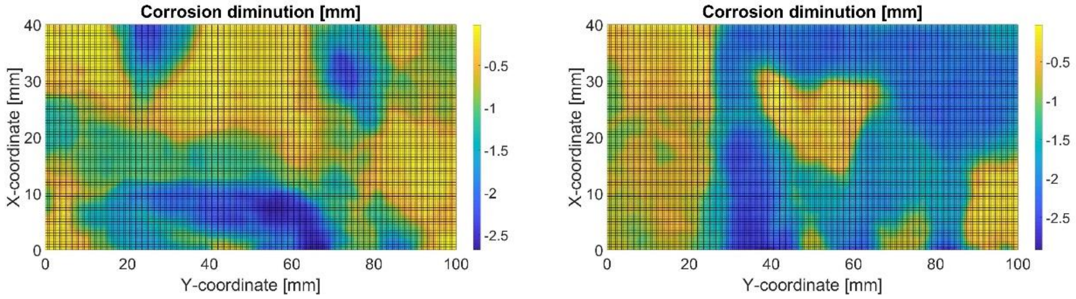

8.1 specimen – top (left) and bottom (right) surface

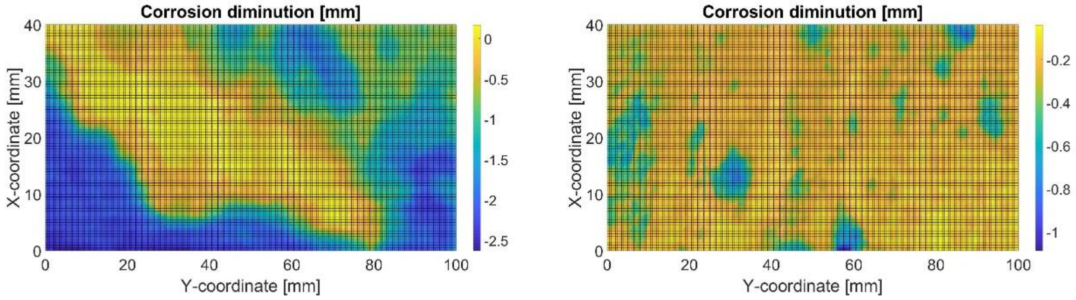

8.2 specimen – top (left) and bottom (right) surface

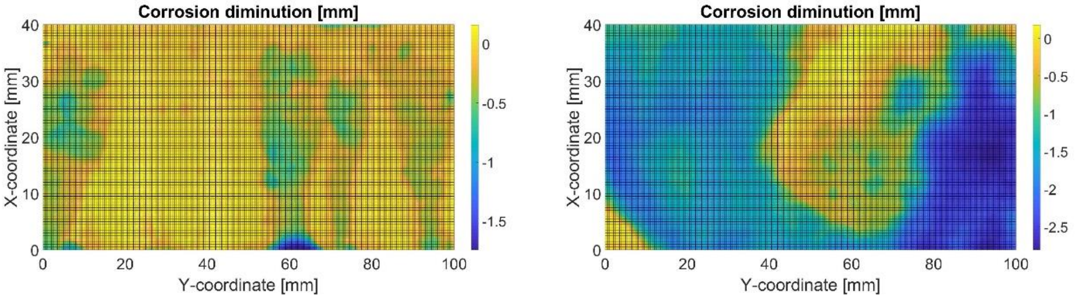

8.3 specimen – top (left) and bottom (right) surface

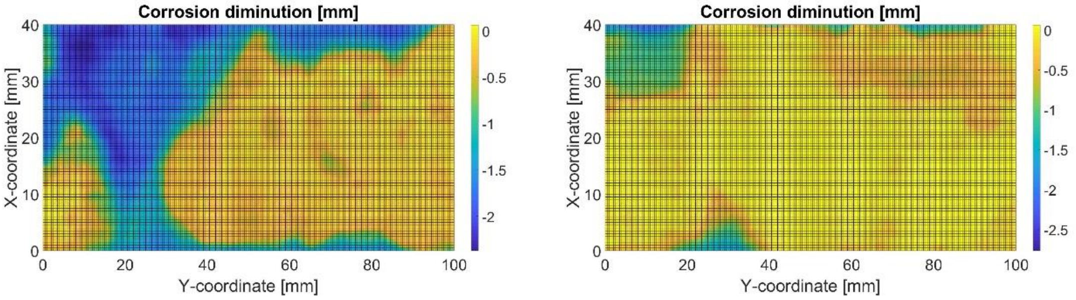

8.4 specimen – top (left) and bottom (right) surface

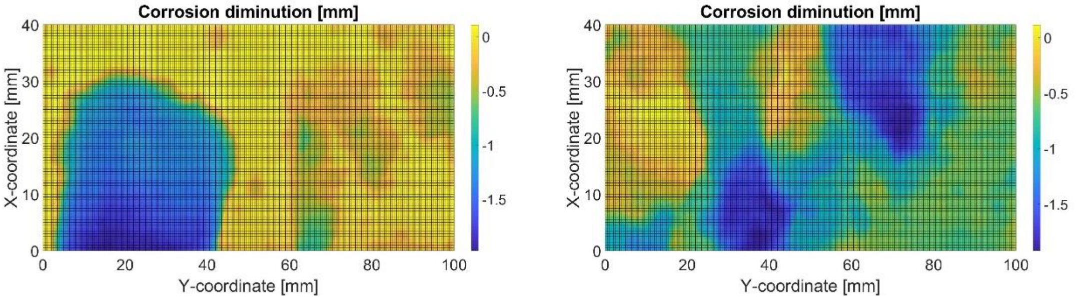

8.5 specimen – top (left) and bottom (right) surface

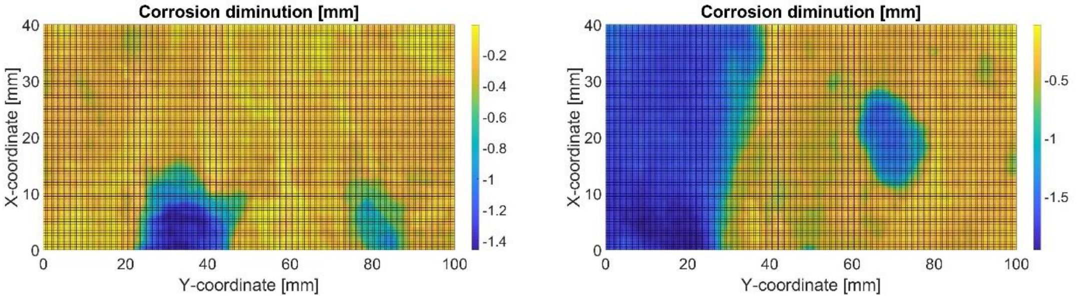

8.6 specimen – top (left) and bottom (right) surface

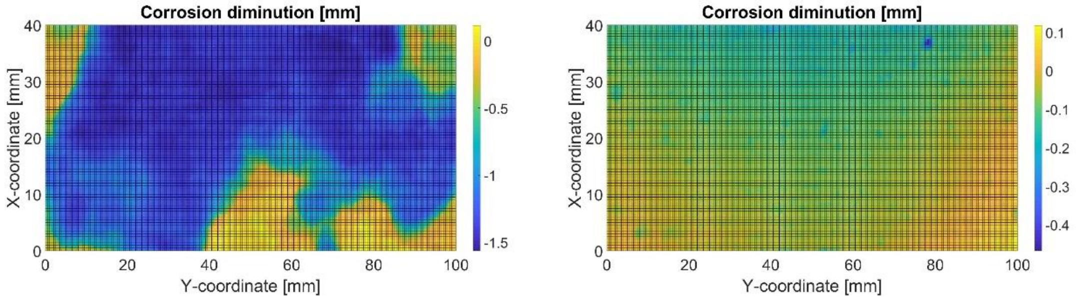

8.7 specimen – top (left) and bottom (right) surface

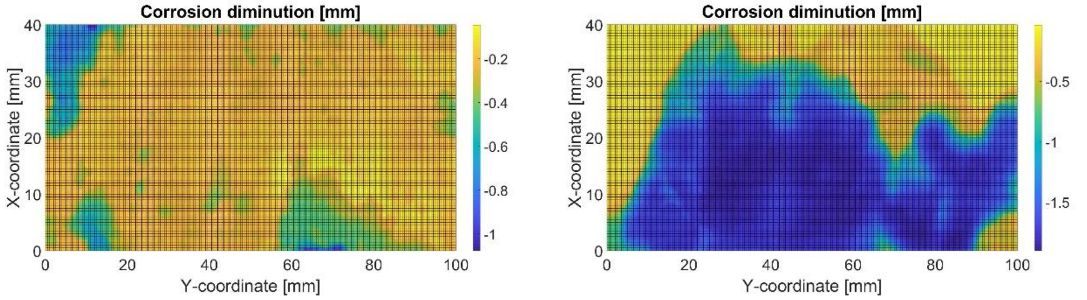

8.8 specimen – top (left) and bottom (right) surface

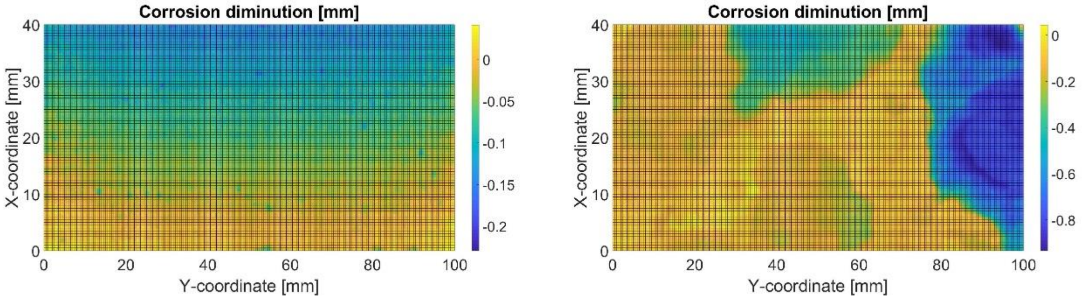

8.9 specimen – top (left) and bottom (right) surface

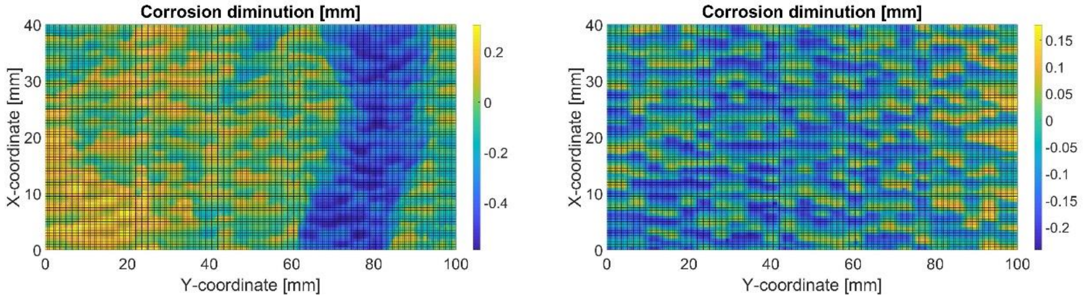

8.10 specimen – top (left) and bottom (right) surface

APPENDIX 2 – SMALL-SCALE SPECIMENS AFTER FAILURE – EXPERIMENTAL AND NUMERICAL RESULTS

5 mm specimens

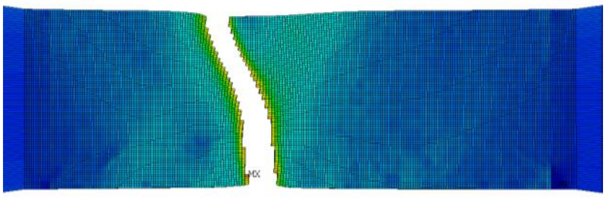

5.1 specimen – FE (top) and experimental (bottom) failure mode

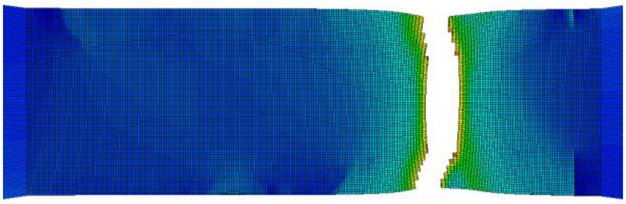

5.2 specimen – FE (top) and experimental (bottom) failure mode

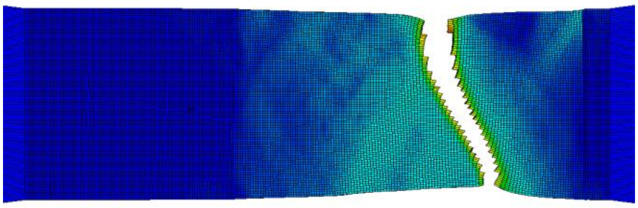

5.3 specimen – FE (top) and experimental (bottom) failure mode

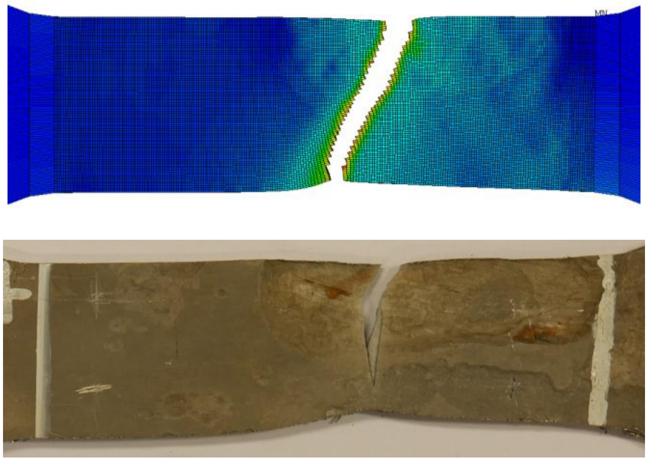

5.4 specimen – FE (top) and experimental (bottom) failure mode

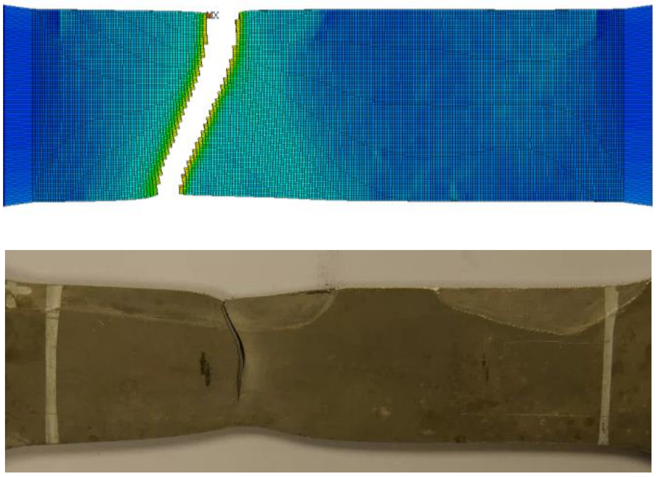

5.5 specimen – FE (top) and experimental (bottom) failure mode

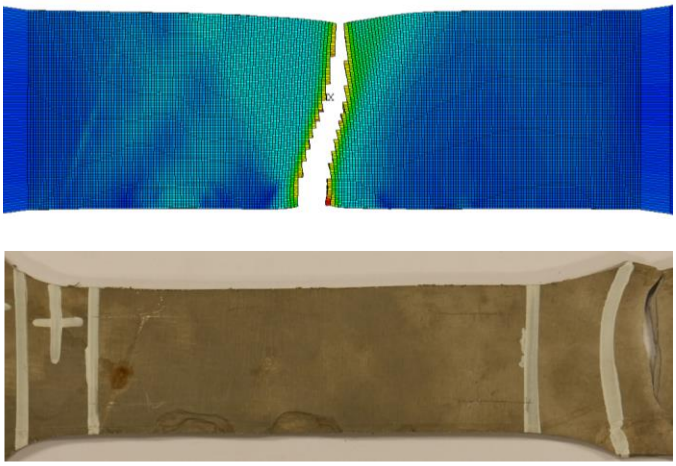

5.6 specimen – FE (top) and experimental (bottom) failure mode – the experimental specimen failure near the support due to the excessive corrosion in that region

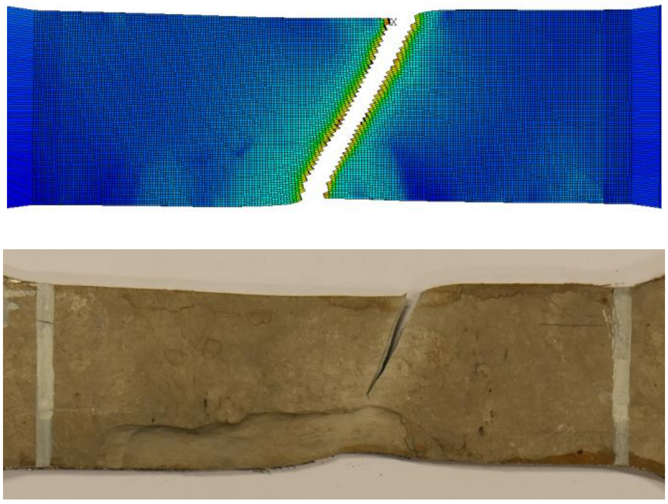

5.7 specimen – FE (top) and experimental (bottom) failure mode

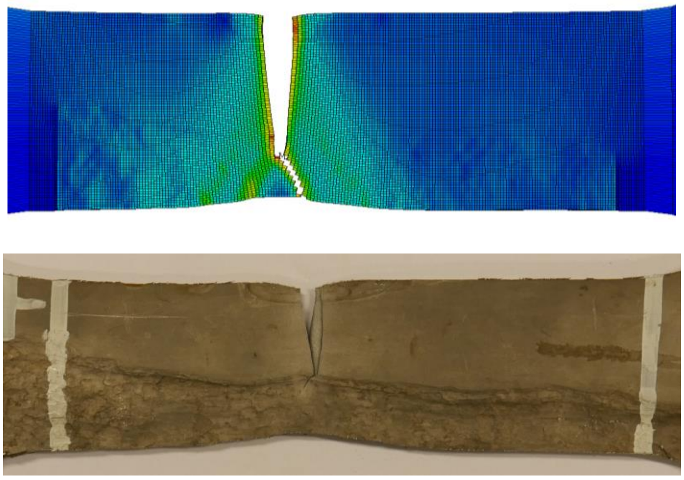

5.8 specimen – FE (top) and experimental (bottom) failure mode

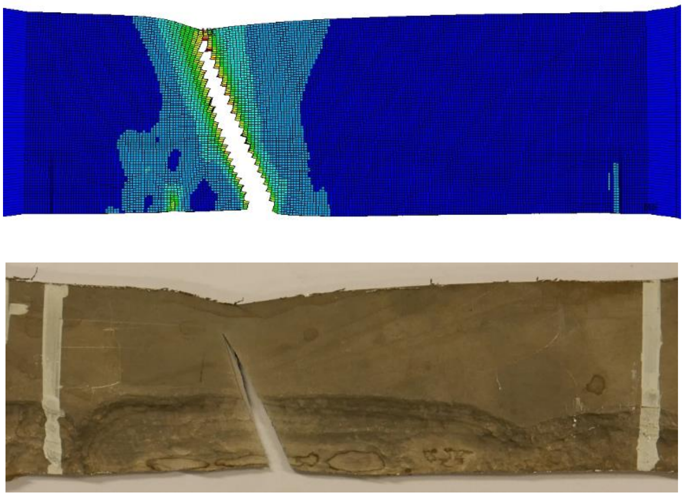

5.9 specimen – FE (top) and experimental (bottom) failure mode

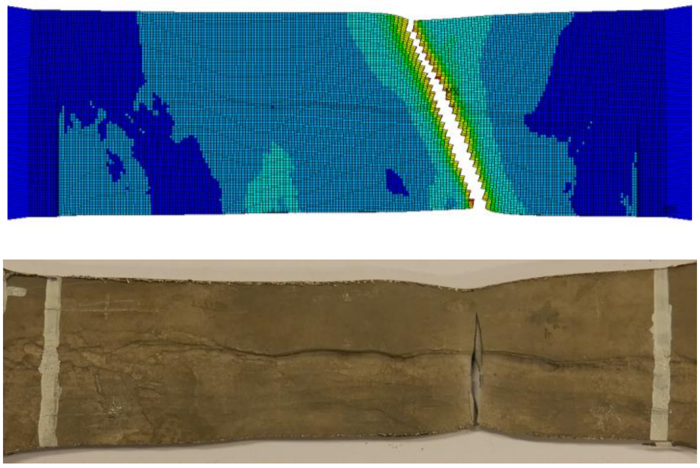

5.10 specimen – FE (top) and experimental (bottom) failure mode

6 mm specimens

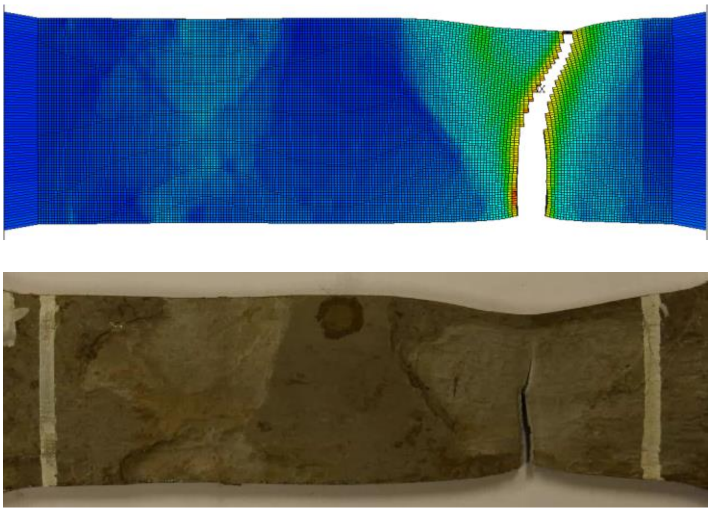

6.1 specimen – FE (top) and experimental (bottom) failure mode

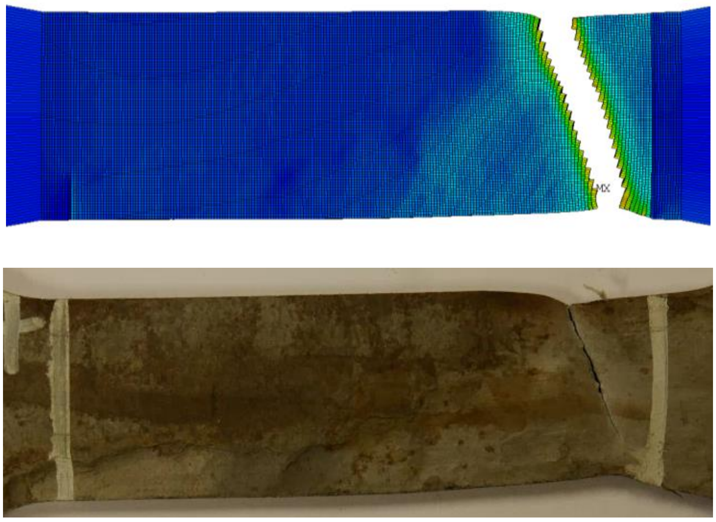

6.2 specimen – FE (top) and experimental (bottom) failure mode

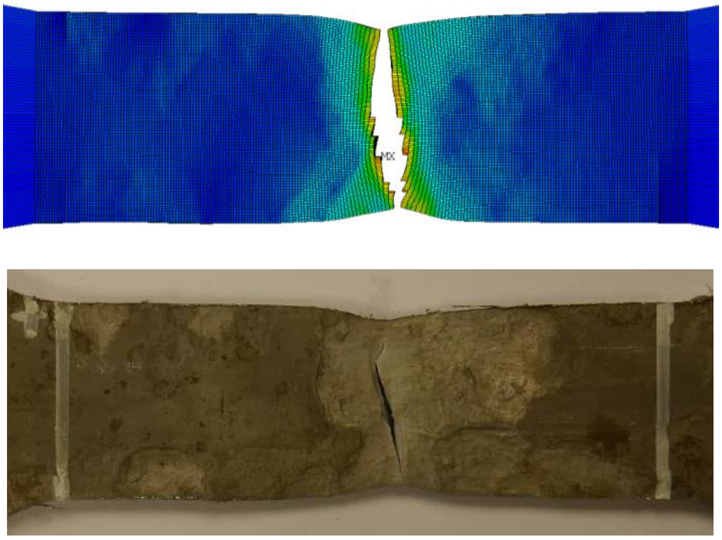

6.3 specimen – FE (top) and experimental (bottom) failure mode

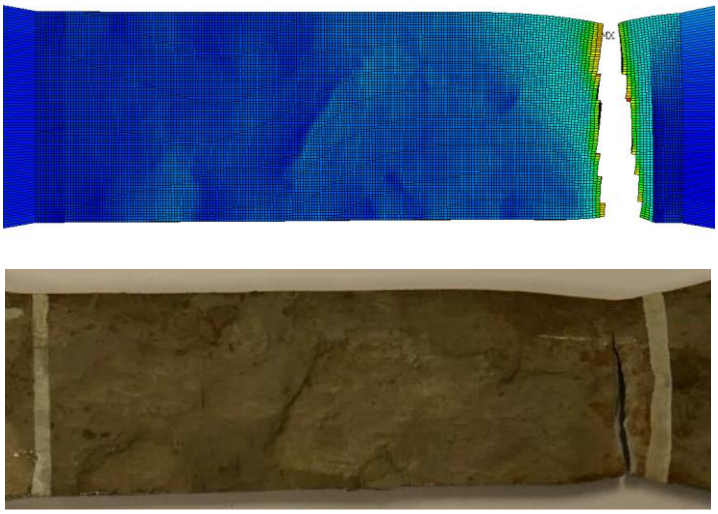

6.4 specimen – FE (top) and experimental (bottom) failure mode

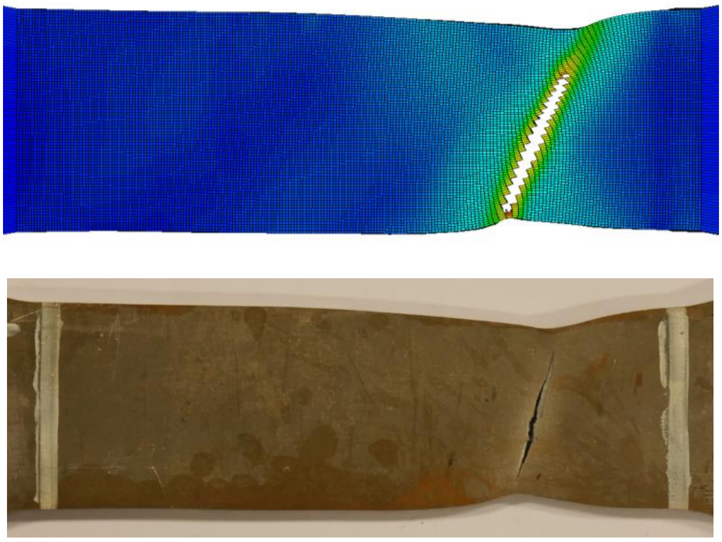

6.5 specimen – FE (top) and experimental (bottom) failure mode

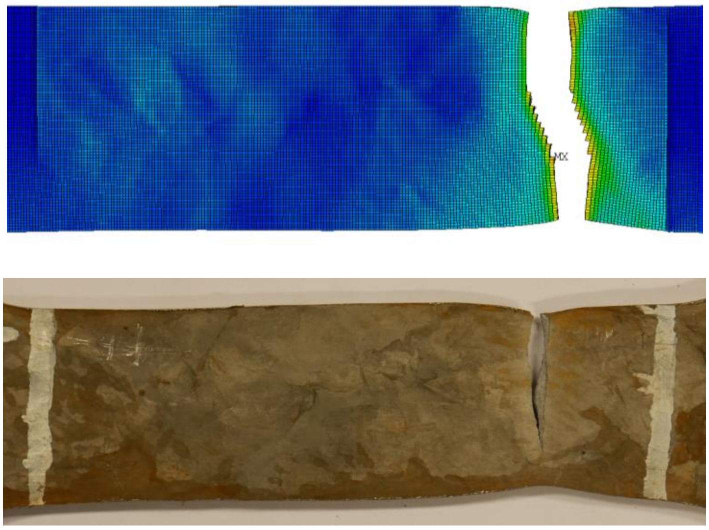

6.6 specimen – FE (top) and experimental (bottom) failure mode

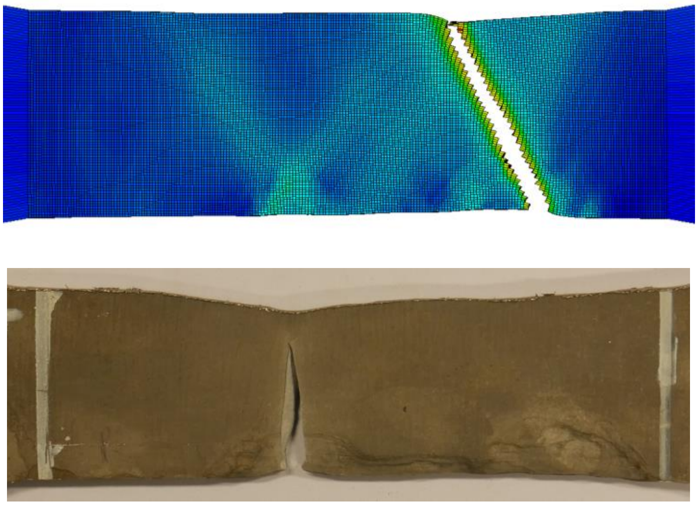

6.7 specimen – FE (top) and experimental (bottom) failure mode

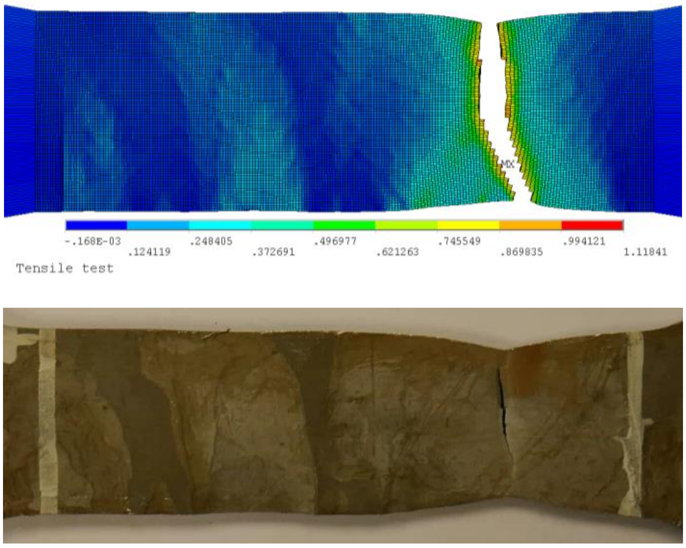

6.8 specimen – FE (top) and experimental (bottom) failure mode

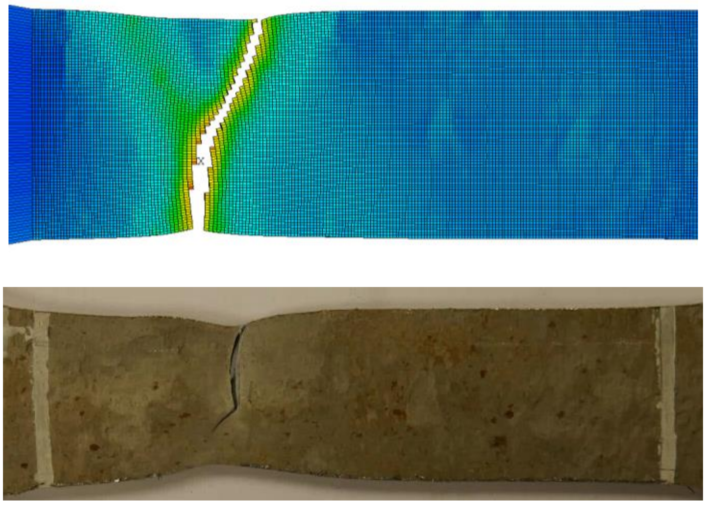

6.9 specimen – FE (top) and experimental (bottom) failure mode

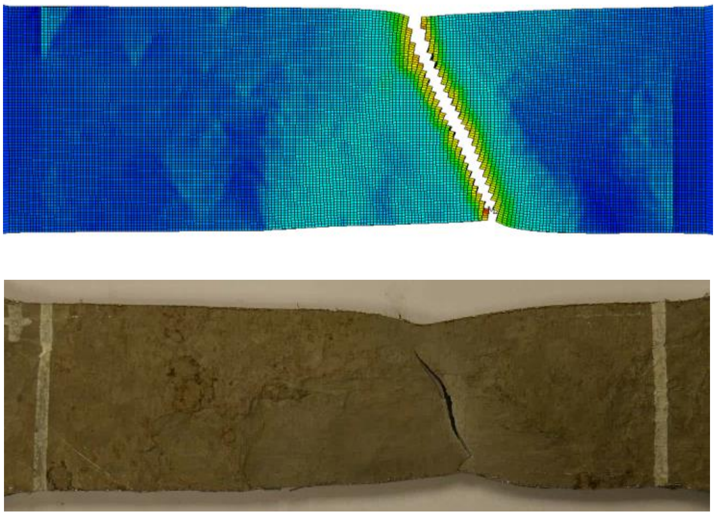

6.10 specimen – FE (top) and experimental (bottom) failure mode

8 mm specimens

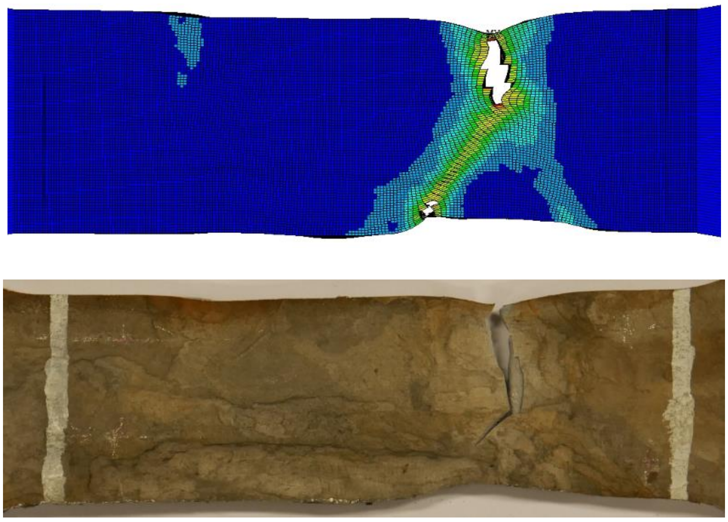

8.1 specimen – FE (top) and experimental (bottom) failure mode

8.2 specimen – FE (top) and experimental (bottom) failure mode

8.3 specimen – FE (top) and experimental (bottom) failure mode

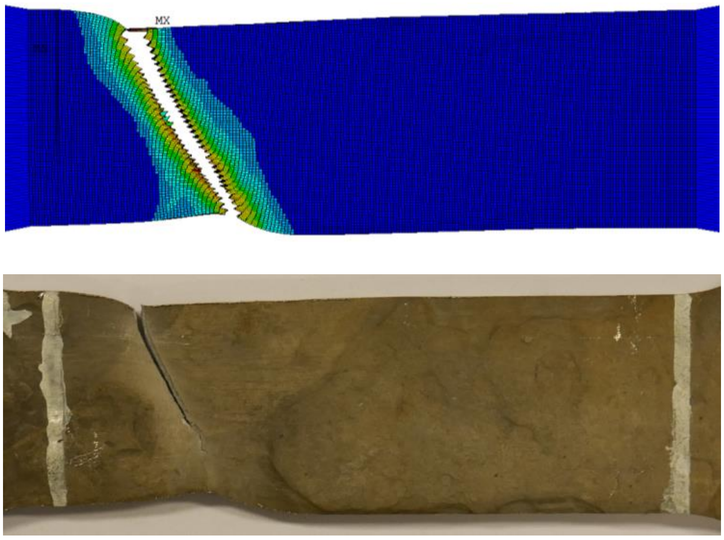

8.4 specimen – FE (top) and experimental (bottom) failure mode

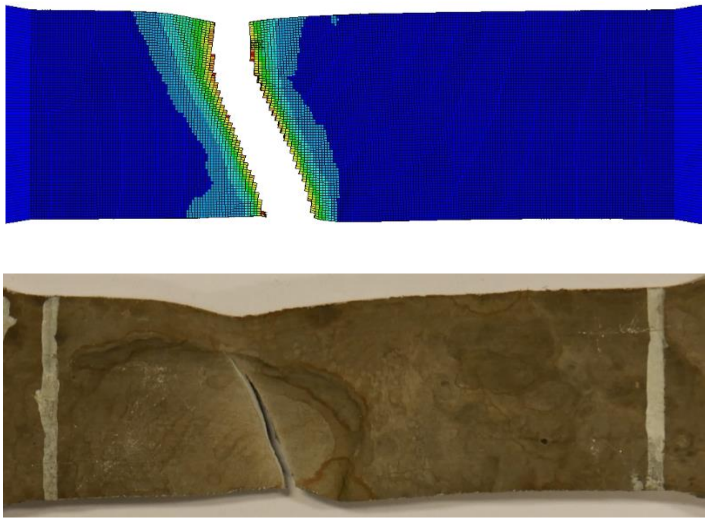

8.5 specimen – FE (top) and experimental (bottom) failure mode

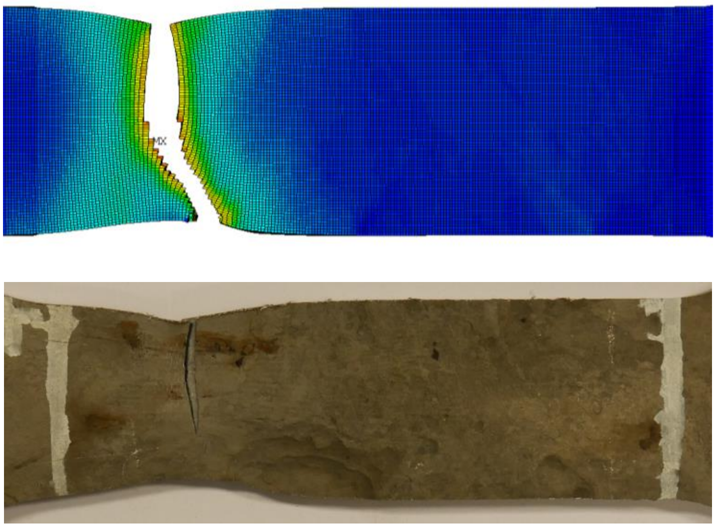

8.6 specimen – FE (top) and experimental (bottom) failure mode

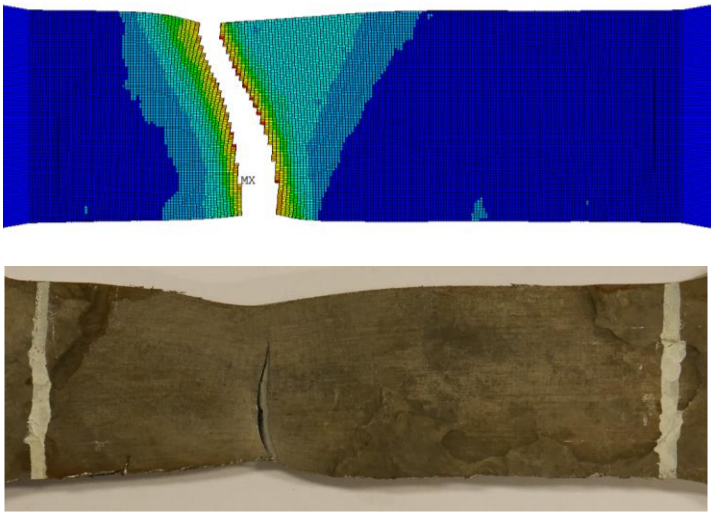

8.7 specimen – FE (top) and experimental (bottom) failure mode

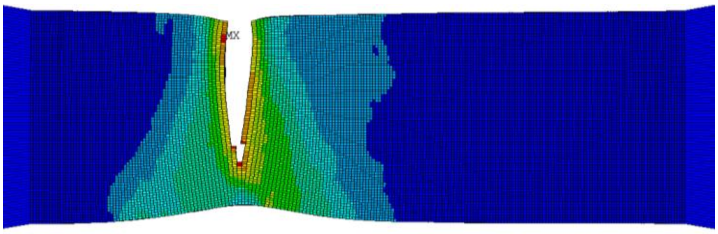

8.8 specimen – FE (top) and experimental (bottom) failure mode

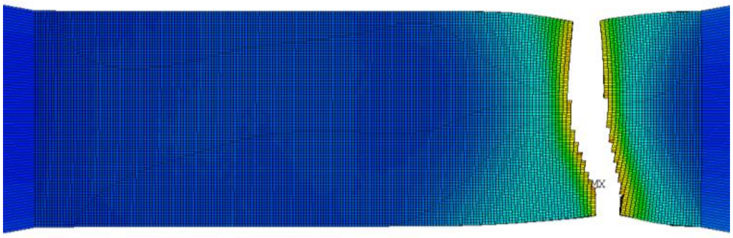

8.9 specimen – FE (top) and experimental (bottom) failure mode

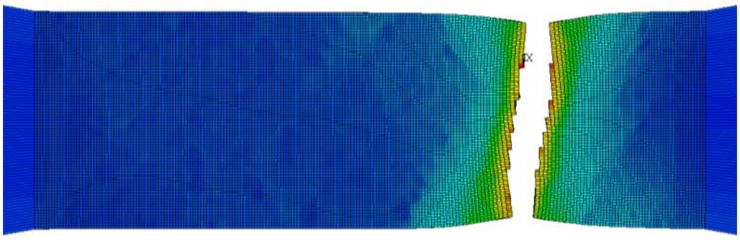

8.10 specimen – FE (top) and experimental (bottom) failure mode